Numerical Modelling of the Hydrodynamics and Suspended Sediment Transport in the Passaúna Reservoir

Zur Erlangung des akademischen Grades einer

DOKTORIN DER INGENIEURWISSENSCHAFTEN (Dr.-Ing.)

von der KIT Fakultät für

Bauingenieur-, Geo- und Umweltwissenschaften

des Karlsruher Instituts für Technologie (KIT)

genehmigte
DISSERTATION
von
Gonzalez Otero, Wendy Johana

Tag der mündlichen Prüfung: 25. Mai 2023

Referent: Prof. Dr.-Ing. Dr.h.c.mult. Franz Nestmann
Korreferent: Prof. Dr.-Ing. Tobias Bleninger

Karlsruhe (2023)

Abstract

Reservoirs are designed to achieve a wide range of tasks such as water supply, flood protection, hydropower generation and/or recreation. The construction of reservoirs around the world is constantly rising due to the increasing water scarcity and energy demand. Nowadays, their construction is concentrated in developing countries and emerging economies, including South America (Zarfl et al., 2015). 2010 approximately 60% of the reservoirs worldwide were situated in the tropical and subtropical zones (Selge and Gunkel, 2013). Ensuring the water quantity and quality in storage reservoirs is the most important management goal to be achieved by public water companies. The present work deals with the characterization of the hydrodynamics and suspended sediment transport through field measurements and numerical modelling in the subtropical Passaúna Reservoir at the west margin of the city of Curitiba in Brazil .

The numerical simulation of the water quality in reservoirs has increasingly become an invaluable tool to scientist and practicioners in the management of those water bodies. The hydrodynamics including the thermal structure of the reservoir have to be calibrated in order to have a reliable model to later simulate the transport of substances. Within the framework of this dissertation a numerical model for the Passaúna Reservoir was developed using the software Delft3D. The influence of numerical and physical parameters like the wind drag coefficient, the number of layers, the background mixing coefficients and additional variables related to the heat fluxes on the thermal structure and flow velocities are investigated and compared with field measurements. In the studied ranges of the parameters, the Dalton number affected the most the calculated temperatures. The horizontal flow velocity was most influenced by the change in the user defined background vertical viscosity. Moreover, the existence of density driven currents and their simulation with the model are evaluated. The performances of Z-and Sigma-layered systems are studied as well. The Z-model better simulated the stratification of the water column and the Sigma-model offered a more realistic prediction of the density currents. The inclusion or exclusion of wind in the numerical model showed to have an effect on both the thermal structure and the flow velocities in the reservoir.

The transport and deposition of suspended sediments in reservoirs not only affect the life span and the storage capacity of these water bodies but also influence the quality of the water. Wind and temperature influence the hydrodynamics of lakes and reservoirs affecting the shape and magnitude of the velocity profiles and also inducing mixing and stratification in the water column. The effect of those two factors on the transport of suspended sediments is here investigated through numerical simulations applied to the mentioned reservoir. Furthermore, the sensitivity of the simulations results to two vertical grid systems implemented in Delft3D: Z- and sigma-coordinates systems was tested. The amount of deposited sediments, the deposition pattern and the suspended sediment concentrations (SSC) profiles were investigated for the scenarios with the inclusion or exclusion of wind and/or water temperature. It was found that the numerical results in terms of transport of suspended sediment are affected by the selection of the vertical coordinate system. Moreover, it was shown that the inclusion of temperature and wind in the numerical simulations is relevant and produced different results. This work is a basis for the setup of other models in similar

reservoirs, in environments where both fine sediment transport and thermal stratification processes are relevant.

Kurzfassung

Stauseen dienen einer breiten Palette von Aufgaben wie der Wasserversorgung, dem Hochwasserschutz, der Stromerzeugung aus Wasserkraft und/oder der Naherholung. Aufgrund der zunehmenden Wassermangel- und Energienachfrage nimmt der Bau von Stauseen weltweit ständig zu. Heutzutage konzentriert sich der Bau von Stauseen auf Entwicklungs- und Schwellenländer, einschließlich Südamerika (Zarfl et al., 2015). 2010 befanden sich etwa 60 % der Stauseen weltweit in den tropischen und subtropischen Zonen (Selge and Gunkel, 2013). Die Sicherstellung der Wassermenge und -qualität in den Stauseen ist das wichtigste Managementziel, das von den öffentlichen Wasserbetrieben erreicht werden muss. Die vorliegende Arbeit beschäftigt sich in ihrem mit der Charakterisierung der Hydrodynamik und des Schwebstofftransports durch Feldmessungen und numerischen Modellierung im subtropischen Passaúna-Stausee am Westrand der Stadt Curitiba in Brasilien.

Die numerische Simulation der Wasserqualität in Stauseen ist für Wissenschaftler und Anwender bei der Bewirtschaftung dieser Gewässer zu einem äußerst wertvollen Instrument geworden. Die Hydrodynamik einschließlich der thermischen Struktur des Stausees muss kalibriert werden, um ein zuverlässiges Modell für die spätere Simulation des Stofftransports zu erhalten. Im Rahmen dieser Dissertation wurde ein numerisches Modell für den Passaúna-Stausee anhand der Software Delft3D entwickelt. Der Einfluss von numerischen und physikalischen Parametern wie dem Windwiderstandskoeffizienten, der Anzahl der vertikalen Schichten, den Hintergrundmischungskoeffizienten und zusätzlichen Variablen, die mit den Wärmeflüssen zusammenhängen, die thermische Struktur und die Strömungsgeschwindigkeiten wird untersucht und mit Feldmessungen verglichen. In den untersuchten Parameterbereichen beeinflusste die Dalton-Zahl die berechneten Temperaturen am stärksten. Die horizontale Strömungsgeschwindigkeit wurde am stärksten durch die Änderung der benutzerdefinierten vertikalen Hintergrundviskosität beeinflusst. Darüber hinaus wurden die Existenz dichtegetriebener Strömungen und ihre Simulation mit dem Modell bewertet. Die Leistungen von Z- und Sigma-Schichtsystemen werden ebenfalls untersucht. Das Z-Modell simulierte die Schichtung der Wassersäule besser und das Sigma-Modell bot eine realistischere Vorhersage der Dichteströmungen. Die Einbeziehung bzw. der Ausschluss von Wind in das numerische Modell wirkte sich sowohl auf die thermische Struktur als auch auf die Strömungsgeschwindigkeiten im Reservoir aus.

Der Transport und die Ablagerung von Schwebstoffen in Stauseen wirken sich nicht nur auf die Lebensdauer und die Speicherkapazität dieser Wasserkörper aus, sondern beeinflussen auch die Qualität des Wassers der Stauseen. Wind und Temperatur beeinflussen die Hydrodynamik von Seen und Stauseen, indem sie sich auf die Form und die Größe der Geschwindigkeitsprofile auswirken und zu einer Durchmischung und Schichtung in der Wassersäule führen. Die Auswirkung dieser beiden Faktoren auf den Transport von Schwebstoffen in Stauseen wird hier durch numerische Simulationen für den genannten Stausee untersucht. Außerdem wird die Sensitivität der Simulationsergebnisse auf zwei in Delft3D implementierte vertikale Gittersysteme untersucht: Z- und Sigma-Koordinatensysteme, getestet. Die Menge der abgelagerten Sedimente, das Depositionsmuster und die Profile der Schwebstoffkonzentrationen (SSC) wurden für die Szenarien mit oder ohne Einbeziehung von Wind und/oder Wassertemperatur untersucht. Es wurde festgestellt, dass die numerischen Ergebnisse in Bezug auf den Transport von Schwebstoffen durch die Wahl des vertikalen Koordinatensystems beeinflusst werden. Darüber hinaus wurde gezeigt, dass die Einbeziehung von Temperatur und Wind in die numerischen Simulationen relevant ist und zu unterschiedlichen Ergebnissen führen wird. Diese Arbeit bildet eine Grundlage für den Aufbau anderer Modelle in ähnlichen Stauseen, in denen sowohl der Feinsedimenttransport als auch thermische Schichtungsprozesse von Bedeutung sind.

Acknowledgements

First of all, I would like to thank my supervisor Prof. Dr.-Ing. Dr.h.c.mult. Franz Nestmann for the opportunity to work at his (former) institute and by his side not oly during my doctoral studies but also within the frame of further Projects and as a lecturer in his courses. Dear Franz, you always believed in my capacity of working in sciences and your passion for the water sciences motivates me in my work every day. I also want to thank my colleague and boss Dr.-Ing. Frank Seidel, who always believed in my scientific skills and who allowed flexible work-schedules for me to work on my dissertation. To my co-supervisor Prof. Dr.-Ing. Tobias Bleninger, for always having time for my questions and for the great work within the frame of the MuDak-Project. Furthermore, I would like to thank Prof. Dr. Mário Franca, who gave me the opportunnity to complete my dissertation at his institute and keep working in further projects.

Thanks to my colleagues Christin Kannen and Andreas Müller for the many talks about the not-so-delights and perks of the doctoral research. The mutual support among us kept us going through dark covid-filled times.

Thanks to all members of the MuDaK-Project team. Without your work in the data acquisition and scientific discussions, my plans would have not succeeded. Special thanks to Dr.-Ing. Mayra Ishikawa and Dr.-Ing. Liege Wosiacki, who always were excellent project partners in the adventure of thermal stratification and suspended sediments dynamics. Muito obrigada, Colegas!. To all my former students/HiWis over the years a big thank you, Dankeschön, Obrigada and Gracias. Diogo, Maseh, Christoph, Javier, Toprak, Anne and Maria thanks for the support with the data and analysis within the frame of the MuDak-Project, your help was invaluable.

I want to thank my dear friends and colleagues Dr.-Ing. Michele Trevisson and Dr.-Ing. Irina Klassen, who always offered me moral and academic support in the course of my research. Also thanks to my friend Carolin Nanz for their constant support, no matter what.

The biggest Thanks goes to my family. My husband Andreas, who literally walked and fought by my side all these difficult years full with covid-restrictions and with so many things I can not even start to count. Danke, Andi! To my parents-in-law Annemarie and Klaus, who always supported me in my carreer and during the difficult times of parenthood. Annemarie und Klaus ohne euch, wäre diese Diss niemals möglich gewesen, Danke!. Thanks to my parents and sister in Colombia, who have been there for me since I can remember. Gracias mami, papi y Mayra; la distancia y un oceáno entre nosotros no ha evitado que siempre sienta su apoyo. Last and never ever least, thanks to my twins Noah und Nicolas, who are my motor and who constantly make me think: Wasser ist Faszination! Gracias Nicolas y Noah, cuando ya puedan leer esta tésis sólo quiero que mantengan algo en la mente, lo mismo que yo mantuve, sobre todo al final:

"Have no fear of perfection; you will never reach it"
-Marie Curie

Contents

List of Figures

List of Tables

1. Introduction

In many regions around the world, reservoirs represent the main source for ensuring the reliable storage of drinking water, energy production and river flood protection. 2019 the International Commission on Large Dams ICOLD estimated the number of reservoirs with a minimum dam height of 15 m or a dam height in the range 5 to 15 m impounding a water volume of minimum 3 Mio m^3, to be around 57985. These reservoirs generate 24% of the world's electricity and provide water for 30% of the global irrigation areas (ICOLD, 2019).

Sediment transport is a fundamental aspect in the management of impounded water bodies, such as reservoirs and lakes, since sediments can affect both the quantity and quality of the water stored in them. At the same time the sediment transport is, among other factors, affected by the hydrodynamics of the water body. The latter also influences the stratification and mixing processes taking place in the reservoir. The hydrodynamics and suspended sediment transport in reservoirs are the two main issues treated in the present work.

1.1. Issue and Relevance

Ensuring the quality and the quantity of water is one of the most important aspects (if not the most) in the management of storage reservoirs. The quality of the water in the reservoir is strongly affected by the temperature and hydrodynamics of the flow. At the same time vertical temperature gradients cause stratification and mixing processes in the water column. Stratification determines in great part the distribution of heat and substances in the reservoir. Some water quality issues influenced by the hydrodynamics of the reservoir are eutrophication and dissolved oxygen depletion (Polli, 2017). Another aspect affecting the water quality in reservoirs is the presence of high suspended sediments concentrations. It increases the turbidity of water, diminishing the light penetration and decreasing food availability for aquatic organisms (Klassen, 2017). Also the finest fractions of the suspended sediments can act as a source of pollution due to its capacity to absorbe substances such as heavy metals, methane, phosporous and further contaminants (Hillebrand, 2008).

The amount of water that should be storaged and hence the volume of the reservoir that should be available for it depends on hydrological variablity (Annandale et al., 2016). Climate change is increasing the hydrological variability in most places on earth. Which leads us to the constuction of more and larger reservoirs. The amount of water that can be storaged in the reservoir is strongly influenced by sedimentation, since deposited sediment reduces the usable storage volume. The deposition of the sediment entering the reservoir is favoured by the low transport capacity of the flow due to the low velocities regime prevailing in those environments. The storage loss due to sedimentation not only affects the drinking water supply but also other relevant reservoir-related aspects such as hydropower generation. For instance; the amount of energy will be reduced and the cost of the maintenace for the turbines increases (abrasion due to the presence of sediment in the outflowing water) (Annandale et al., 2016).

The average annual sedimentation rate of reservoirs around the world has been calculated to be of approximately 1% of the initial storage volume (Mahmood, 1987; ICOLD, 2009). This value is just a rough average and its purpose is to serve as orientation, since sedimentation rates vary for each region around the world and they are a function of the hydrology and the land use in the watershed (Haun et al., 2013). Countries like China and Tanzania present high sedimentation rates of approximately 2.9 and 3.27% respectively. Taking into account the world average, low sedimentation rates can be found in countries like Egypt and Germany with 0.05 and 0.17% respectively. Ohter nations like France and Nepal present sedimentation rates of 1.08 and 1%, corresponding to the world average (ICOLD, 2009). In addition to the above mentioned points, the accumulation of sediment in reservoirs also implies the lack of it downstream of the dam, disrupting the natural conditions of the ecosystem and producing erosion. The construction of dams affects the sediment balance downstream of the reservoir, even at further locations e.g. at the coast.

The volume of sediment deposited in the reservoir for a given period of time is a key piece of information to be determined. As important as the amount of deposited sediments is the sedimentation pattern, which is the spatial distribution of the deposited sediment in the reservoir. Knowledge of these two relevant aspects is essential to plan adequate sediment management strategies. When a free flowing river enters a reservoir, the sediment carried by the flow starts to deposit. The bed load and the coarsest fractions of the suspended load are deposited almost instantly forming delta deposits. The finest fractions of sediment are normally maintaned in suspension and are transported further into the reservoir by stratified or non-stratified flow (Morris and Fan, 1998). Even though general depositions patterns can be defined for storage reservoirs, they always differ as function of the hydrodynamics, the characteristics of the incoming sediments and the geometry of the reservoir.

Numerical modeling is being increasingly used as a tool for the development of management strategies and the decision-making processes in water bodies systems. Although sediment transport in reservoirs can be modeled with good agreement with the measured data (see Hillebrand et al. 2016; Haun et al. 2013; Zhang and Wu 2019; Omer et al. 2015; Schleiss et al. 2014), the amount of input parameters for setting up, calibrating and validating the model is high and requires the implementation of measurements campaigns and monitoring of the water body. However, in many regions of the world validation and input data are strongly limited in an adequate spatial and temporal resolution due to financial restrictions and lack of time. Consequently very complex and basically powerful CFD-software packages are feeded with default parameters, which in most cases do not represent the reality and thus lead to poor quality simulation results and prediction capacity of the model.

For an adequate modelling of the sediment transport, the reproduction of the hydrodynamics (see Chanudet et al. 2012a; Polli and Bleninger 2019a; Weber 2017) in the water body is essential. In the case of storage reservoirs the flow velocities are usually low and the flow is governed by density currents caused by temperature and/or suspended solid concentration gradients. The interaction between the transport of sediments and stratified flows in reservoirs is complex and its satisfactory simulation has a direct repercussion in the simulation of the water quality. The inclusion of density currents caused by temperature has not been widely included in the numerical modelling of suspended sediment transport due to its complexity and high data demand.

1.2. Objectives

The main objective of the present work is to identify the processes and parameters governing the quality of the results of the numerical modelling of the hydrodynamics and sediment transport in reservoirs including the relevance of considering thermal stratification and wind in the simulations. In order to achieve this aim, the following research questions are intended to be answered within the frame of this work:

Question 1 What are the main processes influencing the numerical simulation of temperature stratification patterns and flow velocities in a reservoir? (see chapters 3 and 4)

Question 2 What are the main processes influencing the numerical simulation of deposited sediment volume, sedimentation patterns and suspended sediment concentrations in a reservoir? (see chapters 3 and 5)

Question 3 How can the complexity of the input data for the numerical model be reduced without affecting the quality of the simulation results? (see chapter 6)

To answer the aforementioned questions, the study of field measurements and numerical modelling of the described processes were conducted. As study case a sub-tropical reservoir has been selected; the Passaúna reservoir in Brazil. For this water body a 3D-numerical model will be developed using the software Delft3D (Deltares, 2014). The findings of this work should help engineers in the planning of measurements campaigns and the modelling (mainly modelling setup) of the hydrodynamics and suspended sediment transport in reservoirs.

The measurements and the modelling presented in this dissertation were carried out within the framework of the MuDak-Project (Multidisziplinäre Datenakquisition als Schlüssel für ein global anwendbares Wasserressourcenmanagement) at KIT funded by the Federal Ministry of Education and Research BMBF.

1.3. Structure of the Work

Figure 1.1 shows an overview of the present's work structure. This dissertation consists of two main parts. The first one is the analysis of the existing field measurements for the studied reservoir. The second part deals with the numerical modelling of hydrodynamics, suspended sediment transport and the reduction of their complexity.

Chapter 2 describes the theoretical background necessary to understand the analyses and results showed in the main body of the work (Parts I and II). The chapter starts with an overview of the hydrodynamics equations and approaches available to describe the movement of the fluid (e.g. Navier-Stokes equations, turbulence closure models). Afterwards a brief review of the reservoir lymnology is performed. Hereinafter a description of sediment characteristics and the suspended sediment transport is presented. The chapter concludes with the description of the sedimentation processes in storage reservoirs.

Main issue of the chapter 3 is the analysis of the measurements performed in the studied water body: the Passaúna Reservoir. Also a clasification of the reservoir is performed in this chapter based on physical indices and parameters. The measurements presented here are the basis for the numerical modelling of the next chapters.

In chapter 4 the setup of the three dimensional numerical model in Delft3D is described. Followed by a calibration of the hydrodynamics based on water temperature and velocities. Additionally, sensitivity analysis regarding the input physical parameters are performed. The effects of using sigma or Z-layers configurations are studied in this chapter as well.

Issue of chapter 5 is the simulation of the suspended sediment transport. Sensitivity analysis regarding the parameters for the setup of the morphological model are carried out. For the Passaúna Reservoir a calibration regarding the deposition volume and the measured suspended sediment concentrations are presented. Another important part of this chapter is the modelling of suspended sediment transport including wind and temperature effects.

In chapter 6 the possibilities to reduce the complexity of the 3D numerical model are studied. The complexity reduction analyses are performed in the Passaúna Reservoir as well.

The present dissertation concludes with chapter 7, which summarizes the main conclusions of this work and also points out some aspects to be taken into account for further studies on the discussed topics.

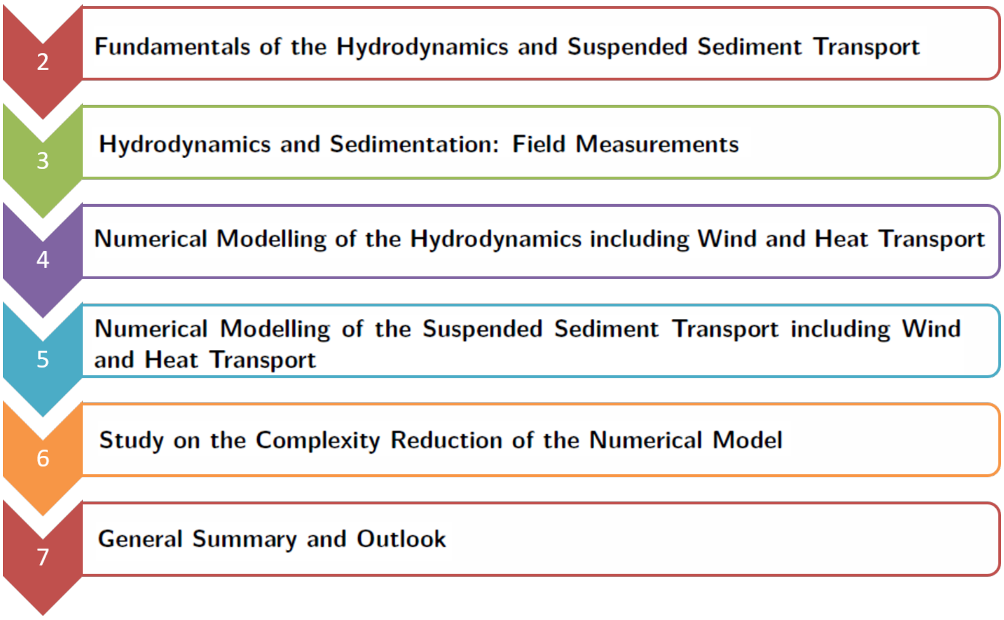

Figure 1.1.: Overview of the structure of the work

2. Fundamentals of the Hydrodynamics and Suspended Sediment Transport

Content of the present chapter is the description of the principal aspects concerning the hydrodynamics and suspended sediments, focussing on impounded water bodies. The chapter starts with the equations defining a hydrodynamic system in which temperature and density are relevant parameters.
The main aim of this chapter is to show a comprehensible overview of the physical processes taking place in reservoirs. Further aim of this chapter is to show the simplifications that are generally assumed regarding the main equations in order to be able to solve them. This chapter refers to the approaches implemented in the software Delft3D used within the framework of the present research project.

2.1. General Description of the hydrodynamics in Reservoirs

The **Navier-Stokes Equations** describe the movement of water in any water body and hence they are the main equations to be solved when studying the hydrodynamics of a reservoir. This system of non-linear partial differential equations expresses the conservation of mass and momentum of a flow field (Johnson, 1981) and reads as follows:

$$\frac{\partial u}{\partial x} + \frac{\partial v}{\partial y} + \frac{\partial w}{\partial z} = 0 \tag{2.1}$$

$$\frac{\partial u}{\partial t} + u\frac{\partial u}{\partial x} + v\frac{\partial u}{\partial y} + w\frac{\partial u}{\partial z} = -\frac{1}{\rho}\frac{\partial p}{\partial x} + \nu\left(\frac{\partial^2 u}{\partial x^2} + \frac{\partial^2 u}{\partial y^2} + \frac{\partial^2 u}{\partial z^2}\right) + g_x \tag{2.2}$$

$$\frac{\partial v}{\partial t} + u\frac{\partial v}{\partial x} + v\frac{\partial v}{\partial y} + w\frac{\partial v}{\partial z} = -\frac{1}{\rho}\frac{\partial p}{\partial y} + \nu\left(\frac{\partial^2 v}{\partial x^2} + \frac{\partial^2 v}{\partial y^2} + \frac{\partial^2 v}{\partial z^2}\right) + g_y \tag{2.3}$$

$$\frac{\partial w}{\partial t} + u\frac{\partial w}{\partial x} + v\frac{\partial w}{\partial y} + w\frac{\partial w}{\partial z} = -\frac{1}{\rho}\frac{\partial p}{\partial z} + \nu\left(\frac{\partial^2 w}{\partial x^2} + \frac{\partial^2 w}{\partial y^2} + \frac{\partial^2 w}{\partial z^2}\right) + g_z \tag{2.4}$$

where:

x, y, z	spatial coordinates	$[m]$
u, v, w	components of the velocity vector in x, y and z direction	$[m/s]$
ρ	fluid density	$[kg/m^3]$
t	time	$[s]$
P	pressure	$[N/m^2]$
ν	kinematic viscosity of the fluid	$[m^2/s]$
g	gravity acceleration	$[m/s^2]$

Equation 2.1 is the continuity equation, which is based on mass conservation. Equations 2.2 to 2.4 correspond to the momentum conservation in the x, y and z spatial directions, they are derived based on Newton's second law of movement. The version of the Navier-Stokes Equations presented here assumes the fluid to be non-compressible and also adopts the Boussinesq approximation. Boussinesq pointed out that for most hydrodynamics problems the density variations are small and they can be ignored in all terms of the equations with exception of the variability in the gravitational or buoyancy term (Johnson, 1981). It means that ρ is considered a constant in all terms except in the body force term. The components included or balanced in the equations 2.2 to 2.4 can be directly related with the following terms (Musall, 2011):

- **local acceleration**: caused by the temporal variation of the velocity. It corresponds to the first term on the left hand side of the equations. If a steady state of the flow is consider, the local acceleration vanishes.
- **convective acceleration**: caused by the spatial variation of the velocity. It corresponds to the remaining three terms on the left hand side of the equations.
- **pressure gradient**: due to variations in the pressure in the three spatial coordinates. First term on the right side of the equations.
- **viscous stresses**: caused by the resistance that the fluid layers present to the motion i.e. fuid viscosity. This resistance appears due to velocity gradients in the fluid. It refers to the terms between the parentheses on the right hand side of the equations.
- **body forces**: these forces act on the volume of the fluid. In general only the gravitational force is included in the equations (like presented in this work), nevertheless other body forces such as the coriolis can affect the fluid system. For small systems such as reservoirs the coriolis force can be ignored. The gravitational force corresponds to the last term on the right hand side of the equations.

In Delft3d (and in most of the software in the CFD field), it is assumed that the ratio between the horizontal length scale is much larger that the vertical one. Given this, it is valid to assume that the effect of the acceleration in the vertical direction is much smaller than the accelation caused by the gravity field and thus the momentum equation in the vertical direction is reduced to the hydrostatic pressure equation. These conditions are known as the shallow water assumption. There is also the option to ommit this assumption by making use of the non-hydrostatic presure approach. The shallow water assumption was applied within this work.

When studying systems in which thermal effects are relevant an additional equation has to be written, i.e. the **advection-diffusion equation**, which is based on the conservation of energy. This equation reads:

$$\frac{\partial T}{\partial t} + u\frac{\partial T}{\partial x} + v\frac{\partial T}{\partial y} + w\frac{\partial T}{\partial z} = S + \frac{\partial}{\partial x}\left(D_t\frac{\partial T}{\partial x}\right) + \frac{\partial}{\partial y}\left(D_t\frac{\partial T}{\partial y}\right) + \frac{\partial}{\partial z}\left(D_t\frac{\partial T}{\partial z}\right) \tag{2.5}$$

where:

T	water temperature	$[°C]$
S	source and sink terms	$[°C/s]$
D_t	Diffusion coefficient	$[m^2/s]$

The advection-diffusion equation describes the transport of heat in the water body. It includes the factors that can cause a change in the temperature of the water i.e. by advection of the flow field, by molecular diffusion and/or as a result of source or sinks of heat (e.g. inflows or heat exchange at the reservoir free surface) (Johnson, 1981).

In order to completely describe the hydrodynamic system, a further equation is needed: a **equation of state**. Such an equation describes the density variations as a function of physicochemical characteristics of the water e.g. temperature, pressure, suspended solid concentration and salinity (Imboden and Wuest, 1995). As water cools down a volumen contraction takes places leading to a rise in its density. The density of fresh water reaches a maximum of $1000 kg/m^3$ at $4°C$(exactly $3.98°C$). Between $0°C$ and $4°C$ water expands slightly (Wiberg et al., 2014). Figure 2.1 shows the variation of the water density with temperature.

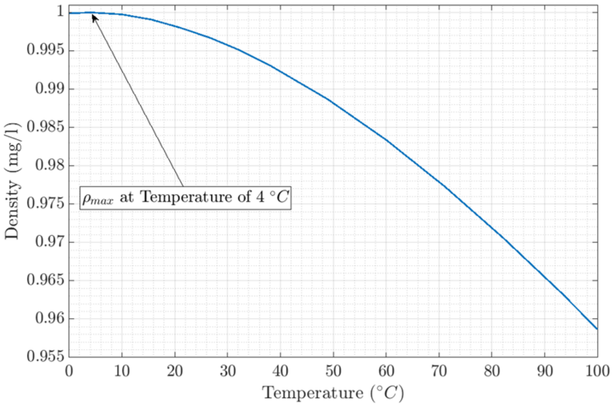

Figure 2.1.: Variation of the water density as a function of the water temperature (after data by Fierro and Nyer 2007).

Many formulations for an equation of state exist. One of the first derived equations based on empirical data was formulated by Carl Eckart (Eckart, 1958a). The formulation is based on measuremnents of the water density for two salinities and 5 temperatures. It also contains the pressure as a variable, but at low pressures the effect on density variation can be ignored (Deltares, 2014). The equation is applicable for temperatures between 0 and $40°C$ and salinities between 0 and $40 ppt$. The formulation reads as follows:

$$\rho = \frac{1000 P_0}{\lambda + \alpha_0 P_0} \tag{2.6}$$

with:

$$\lambda = 1779.5 + 11.25T - 0.0745T^2 - (3.8 + 0.01T)s \tag{2.7}$$

$$P_0 = 5890 + 38T - 0.375T^2 + 3s \tag{2.8}$$

where:

T	water temperature	$[°C]$
s	salinity	$[ppt]$
α_0	0.6980	$[-]$

As already mentioned fresh water reaches its maximum density at a temperature of 4 $°C$. This physical characteristic is not reproduced by the Eckart state equation, which can be problematic when dealing with thermal stratification in deep lakes. A further formulation is the international equation of state for seawater UNESCO (UNESCO, 1981). This equation gives the most widely accepted representation of the relation between the water density as a function of temperature, salinity and pressure (Wright, 1997). However the UNESCO equation is computationally expensive for the application in numerical models in which the density has to be calculated very often (Wright, 1997). The formulation is described through the following equations (Deltares, 2014):

$$\rho = \rho_0 + As + Bs^{\frac{3}{2}} + Cs^2 \tag{2.9}$$

with:

$$\begin{aligned}\rho_0 = {} & 999.842594 + 6.793952 \cdot 10^{-2}T - 9.095290 \cdot 10^{-3}T^2 \\ & + 1.001685 \cdot 10^{-4}T^3 - 1.120083 \cdot 10^{-6}T^4 + 6.536332 \cdot 10^{-9}T^5\end{aligned} \tag{2.10}$$

$$\begin{aligned}A = {} & 8.24493 \cdot 10^{-1} - 4.0899 \cdot 10^{-3}T + 7.6438 \cdot 10^{-5}T^2 \\ & - 8.2467 \cdot 10^{-7}T^3 + 5.3875 \cdot 10^{-9}T^4\end{aligned} \tag{2.11}$$

$$B = -5.72466 \cdot 10^-3 + 1.0227 \cdot 10^{-4}T - 1.6546 \cdot 10^{-6}T^2 \tag{2.12}$$

$$C = 4.8314 \cdot 10^{-4} \tag{2.13}$$

The Navier-Stokes equations, the Advection-Diffusion equation and the Equation of State are in total six equations which totally describe the hydrodynamic system by finding the values of six flow-defining variables: u, v, w, P, ρ and T.

The solution of the Navier-Stokes equation also describes the **turbulence** present in the flow. Turbulence is well characterized by its non-steadiness, three-dimensionality, non-periodical behaviour and by the presence of eddies of different sizes (Laurien and Oertel, 2013). The most widely used macroscopic model to describe turbulence is the so-called Kolmogorov-Richardson energy cascade. In this model, a homogeneous and isotropic distribution of turbulence is assumed. The model states that during the development of turbulence, large vortices are formed, which extract kinetic energy from the flow. The large vortices decay into smaller vortices, to which the energy of the larger vortices is transferred. This process will continue until the smallest vortices reach the so-called Kolmogorov length. At this point, the kinetic energy cannot be passed on and consequently it is dissipated into heat by viscous friction (Köhler, 2010; Hu et al., 2018).

One of the main roles of turbulence is to transfer kinetic energy from large eddies to smaller ones until the Kolmogorov-micro-scale is reached and energy dissipates by internal friction induced by the molecular viscosity. To quantify turbulece, two main parameters are used in the field of hydrodynamics i.e. the turbulent kinetic energy *TKE* and the turbulent energy dissipation ϵ. The *TKE* describes the amount of energy $[J]$ per unit mass $[kg]$ which is contained in the velocity fluctuations of all three velocity components (Wuest and Lorke, 2009) (see equation 2.14).

$$TKE = \frac{1}{2}\left(\overline{u'^2} + \overline{v'^2} + \overline{w'^2}\right) \quad [m^2/s^2] \tag{2.14}$$

The turbulent energy dissipation rate $\epsilon[m^2/s^3]$ is a measure of the intensity of turbulent motions and the rate of dissipation of *TKE* by viscocity effects(Wuest and Lorke, 2009).

As stated by Wuest and Lorke (2009), another method to describe turbulence is the characterization of the different sizes of eddies caused by it. The largest eddies in stratified flows are defined by the *Ozmidov length scale* L_O (see equation 2.15) and the smallest ones are limited by the *Kolmogorov length scale* L_K (see equation 2.16).

$$L_O = \left(\frac{\epsilon}{N^3}\right)^{1/2} \quad [m] \tag{2.15}$$

Typical magnitude range of L_O for lakes and reservoirs comprehends values between 0.1 and 10 m (Wuest and Lorke, 2009). Eddies larger than L_O are attenuated by the stratification of the water body. By observing equation 2.15 is evident that the more stable the stratified flow becomes, the smallest the magnitud of L_O will be.

$$L_K = \left(\frac{\nu^3}{\varepsilon}\right)^{1/4} \quad [m] \tag{2.16}$$

For the case of embeded water bodies, the Kolmogorov length scale L_K ranges between 1 and 10 mm. For scalar properties of the fluid flow such as temperature, the molecular diffusivity is smaller than the kinematic viscosity and as consequence fluctuations of temperature are observed at smaller lenght scales than L_K (range: 0.4 to 4 mm).Actually there is no way to make a clear difference between large scale from small scale motion since large scale energy of motion is at some point lost to turbulence then again turbulence influences large scale motion (Imboden and Wuest, 1995)

As already mentioned, the Navier-Stokes equations are capable to fully describe the movement of water including the turbulence. In order to completely model turbulence, eddies all sizes should be taken into account, while solving the NSE directly. This approach is known as the **Directly Numerical Simulation DNS** of turbulence. The size of the smallest eddies that should be simulated by the DNS can be approximated using the Kolmogorov-length λ_k:

$$\lambda_k = \frac{h}{Re^{\frac{3}{4}}} \tag{2.17}$$

where:

h	water depth	$[m]$
Re	Reynolds number	$[-]$

Musall (2011) shows through an example the enormous computational requirements of a DNS for the simulation of a water body; in a 1 km long and 100 m width river reach with flow velocity of 1 m/s and depth of 10m, considering a kinematic viscosity of the water of $10^{-6}m^2/s$, a Reynolds number of 10^7 is obtained. For this example, a Kolmogorov-length of 50μm can be calculated. Given the dimensions of the river reach, a total of around $8 * 10^{18}$ calculation points would be necessary in order to include the smallest eddies in the simulations. This enormous number of calculation points added to the fact that the time step should be chosen small enough to simulate the fastest fluctuations, would make of this simulation an impossible task to complete, even for modern computers.

In general, the turbulenter the flow regime (high Re) the highest the number of computational points (low λ_k) required to solve directly the Navier-Stokes equations. Rivers and also reservoirs normally present a turbulent flow regime, which makes of the DNS an inapproapiate method to apply to those water bodies, even with today's high capacity computers.

A second approach in oder to solve the turbulence in a flow the **Large Eddy Simulation** or LES simulates directly only the largest eddies and the smallest are modeled by local averaging or filtering of the Navier-Stokes equations, the so called sub-grid-scale (SGS) models. The large eddies extract most of the kinetic energy from the flow and cause most of the turbulent mixing and momentum transfer (Zhiyin, 2015), this makes LES a method that delivers good results for simulating turbulent flows.

For most engineering problems, the accurate description of the turbulent fluctuating motion is not a priority. Instead, the description of the mean turbulent flow is of primary interest. A further approach in the modelling of turbulence considers the velocity vector to be the sume of a time averaged value and a temporal fluctuation component (see Figure. 2.2).

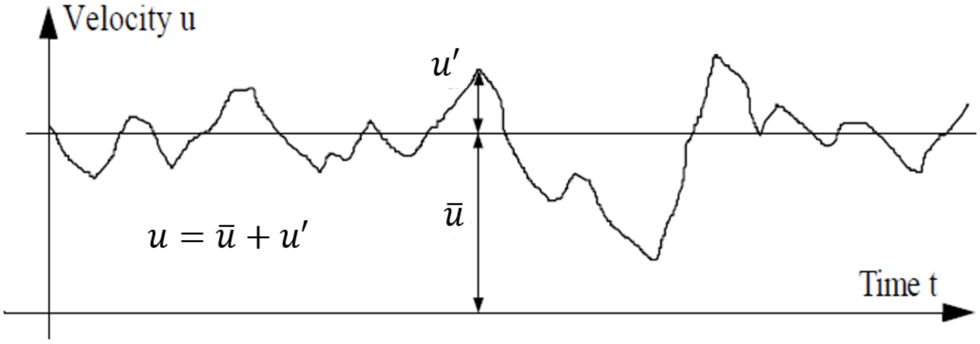

Figure 2.2.: Consideration of the velocity as the sume of a time averaged and a fluctational component (adapted from Klassen 2017).

Under this consideration, the continuity and the Navier-Stokes equations are averaged over time, presenting the following form:

$$\frac{\partial \bar{u}}{\partial x} + \frac{\partial \bar{v}}{\partial y} + \frac{\partial \bar{w}}{\partial z} = 0 \tag{2.18}$$

$$\rho\frac{\partial\bar{u}}{\partial t}+\rho\bar{u}\frac{\partial\bar{u}}{\partial x}+\rho\bar{v}\frac{\partial\bar{u}}{\partial y}+\rho\bar{w}\frac{\partial\bar{u}}{\partial z}=-\frac{\partial\bar{p}}{\partial x}+\frac{\partial}{\partial x}\left(\mu\frac{\partial\bar{u}}{\partial x}-\overline{u'u'}\right)+\frac{\partial}{\partial y}\left(\mu\frac{\partial\bar{u}}{\partial y}-\overline{u'v'}\right)+\frac{\partial}{\partial z}\left(\mu\frac{\partial\bar{u}}{\partial z}-\overline{u'w'}\right)+\rho g_x \quad (2.19)$$

$$\rho\frac{\partial\bar{v}}{\partial t}+\rho\bar{u}\frac{\partial\bar{v}}{\partial x}+\rho\bar{v}\frac{\partial\bar{v}}{\partial y}+\rho\bar{w}\frac{\partial\bar{v}}{\partial z}=-\frac{\partial\bar{p}}{\partial y}+\frac{\partial}{\partial x}\left(\mu\frac{\partial\bar{v}}{\partial x}-\overline{v'u'}\right)+\frac{\partial}{\partial y}\left(\mu\frac{\partial\bar{v}}{\partial y}-\overline{v'v'}\right)+\frac{\partial}{\partial z}\left(\mu\frac{\partial\bar{v}}{\partial z}-\overline{v'w'}\right)+\rho g_y \quad (2.20)$$

$$\rho\frac{\partial\bar{w}}{\partial t}+\rho\bar{u}\frac{\partial\bar{w}}{\partial x}+\rho\bar{v}\frac{\partial\bar{w}}{\partial y}+\rho\bar{w}\frac{\partial\bar{w}}{\partial z}=-\frac{\partial\bar{p}}{\partial z}+\frac{\partial}{\partial x}\left(\mu\frac{\partial\bar{w}}{\partial x}-\overline{w'u'}\right)+\frac{\partial}{\partial y}\left(\mu\frac{\partial\bar{w}}{\partial y}-\overline{w'v'}\right)+\frac{\partial}{\partial z}\left(\mu\frac{\partial\bar{w}}{\partial z}-\overline{w'w'}\right)+\rho g_z \quad (2.21)$$

Time averaging of these equations results in additional terms in the Navier-Sotkes equations, the so-called Reynolds stresses. The equations 2.18 to 2.21 are refered as the Reynolds-Averaged Navier-Stokes equations abbreviated RANS. The Reynolds stresses represent the prouduct between the fluctuations of the velocity components.

The RANS contain six further unknown variables, which can be determined using different approaches. In general most turbulence models can be classified into two groups Reynolds-Stress models and eddy-viscosity models. The former determines the Reynolds-stresses based on transport equations in which they appear as dependant variables. The transport equations can be algebraic or differential type. The algebraic transport equations are of emprical origin, however, two additional diferential equations usually have to be solved to determine two further variables appearing in the transport equations: the turbulent kinetic energy k and ist dissipation rate ϵ (Musall, 2011). The differential approaches make use of seven further differential equations: six to determine the Reynolds-stresses and one for the calculation of a siutable length measure based on the energy dissipation (Musall, 2011). For the implementation of Reynolds-stress models, a number of numerical assumptions have to be made, furthermore the CFD-codes for their solution are computational expensive and lack of numerical stability. As a result those type of models are not widespreaded in the engineering praxis.

The second kind of statistical turbulence models, the eddy viscosity approaches, consider the reynolds-stresses to be porportional to the spatial gradients of the velocity and are described through the equations 2.22 to 2.27:

$$\overline{-u'u'} = 2\nu_t \frac{\partial u}{\partial x} - \frac{2}{3} k \delta_{ij} \tag{2.22}$$

$$\overline{-v'v'} = 2\nu_t \frac{\partial v}{\partial y} - \frac{2}{3} k \delta_{ij} \tag{2.23}$$

$$\overline{-w'w'} = 2\nu_t \frac{\partial w}{\partial z} - \frac{2}{3} k \delta_{ij} \tag{2.24}$$

$$\overline{-u'v'} = \nu_t \left(\frac{\partial u}{\partial y} + \frac{\partial v}{\partial x} \right) \tag{2.25}$$

$$\overline{-u'w'} = \nu_t \left(\frac{\partial u}{\partial z} + \frac{\partial w}{\partial x} \right) \tag{2.26}$$

$$\overline{-v'w'} = \nu_t \left(\frac{\partial v}{\partial z} + \frac{\partial w}{\partial y} \right) \tag{2.27}$$

$$k = \frac{1}{2} \left(\overline{u'u'} + \overline{v'v'} + \overline{w'w'} \right) \tag{2.28}$$

where:

ν_t	eddy viscosity	$[m^2/s]$
δ_{ij}	kroneckar delta	$[-]$

The proportionaly factor ν_t is a measure of the degree of turbulence as a function of the shear of the mean flow field. The higher the eddy viscosity, the higher the turbulence generated by the fluctuations of the mean velocity field (Malcherek, 2001). From the equations 2.22 to 2.27 can be oserved, that the eddy viscosity is not constant, but dependent on the flow condition, i.e. it varies in time and space. With this approach the determination of the reynolds stresses is reduced to finding the eddy viscosity. To find this variable diverses approaches have been proposed and they are clasified based on the number of differential equations they use for this aim. There exist from zero to four equations models. Zero-equation models employ algebraic equations based on the mean flow variables to calculate the eddy viscosity. On the other hand, two equation models use two differential equations, usually to determine two variables: the kinetic energy k and its dissipation rate ϵ, in order to calculate the ν_t. One of the most widespreaded turbulence closure models is the $k - \epsilon$ model and it was first presented by Launder and Spalding in 1974 (Malcherek, 2001). This model is implemented in Delft3D and is used within the framework of the present work. The use of the $k - \epsilon$ model implies that the horizontal length scales are larger than the vertical scale (Deltares, 2014). Some of the advantages of this approach are its low computational cost, simple implementation in a CFD-code and the intensive validation due to its spread use. Disadvantages of the $k - \epsilon$ model are known to be quality issues with the simulation of secondary currents, flow separation and curved streamlines. The mentioned disadvantagesare mainly due to the assumption of isothropy of the turbulece. The suitability of this model for the simulating ambients with stratified flow conditions has been confirmed through numerous scientific publications (see Postma and Boon 1999; Burchard and Baumert 1995)

The RANS and the advection-diffusion equation represent a system of partial differential equations which describe the flow dynamics and the transport of heat and/or suspended sediments. In order to get a unique solution to the specific flow problem being studied, a set of initial and boundary conditions are required.

Any model includes closed and opend boundaries. Closed and open boundaries represent respectively the interface water/water body's margins and the water/water interface, they both delimit the model area (see Figure 2.3). The initials conditions should describe the values of the dependent variables i.e., velocity, pressure/water depth, temperature and suspended sediment concentrations at the beginning of the simulation period. The influence of the initial conditions on the simulation's results should decrease over the simulation time, while the boundary conditions have a direct impact on the distributions of the calculated variables at every time step of the simulation. Initial conditions should be specified as realistic as possible, this will reduce the computational effort invested for the model getting away from the otherwise unrealistic intial boundary conditions.

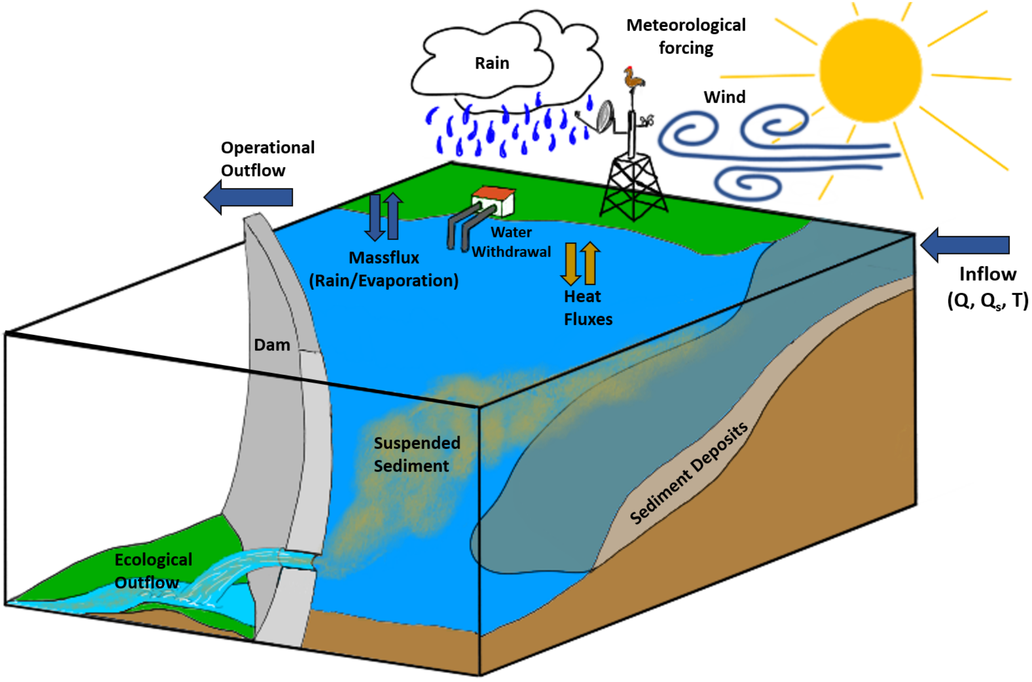

Figure 2.3.: Location of the boundaries in a numerical model of reservoir with multiple tributaries.

On a theoretical basis, boundary conditions are of the following types (Musall, 2011; Malcherek, 2001):

- Dirichlet-boundary conditions: in this case the magnitude of the unknonw variable has to be available at the open boundary.
- Neumann-boundary conditions: this condition specifies the spatial variation or gradients of the unknown variables at the open boundary.
- Cauchy-boundary conditions: representes a linear combination of the both previously mentioned boundary conditions.

- Periodic boundary conditions: for this type of boundary condition, the values of the variables repeat peridiocially.

The RANS are second order partial differential equations, for which the open boundary condition have to be specified as a Neumann or a Dirichlet type of condition. The physical interpretation of the Neuman boundary condition is the specification of the the energy grade line, the normal or shear stresses (Bergen, 1999). For a Dirichlet boundary condition the velocity or the water level (pressure) are required.

In Delft3D the component of the flow velocity normal to the closed boundaries is set to be zero (Deltares, 2014). It is assumed that the flow is in the subcritical regime, so upstream and downstream or inflows and outflows boundary conditions are required. Boundary conditions describe the value of the searched variables or they spatial gradients for every time step. In general for the inflows the amount of water entering the model through each tributary and its flow direction has to be prescribed. For the outflow, the water level at the location of the open boundary is required. For some situations as is the case of reservoirs, discharges can also be introduced as outflow boundary conditions. Nevertheless, for that case if no water level information for each time step is used, the modeled situation will indeed depend on the initial conditions.

The model also has to be forced in the vertical direction: at the bottom of the water body through the bed shear stress and at the water-air interface through the wind shear stress.

The impermeability of the air-water interface and of the bottom of the water body is included by taking the vertical component of the velocity vector as zero for these two layers. At the bottom of the water body the gradients of the horizontal velocities components along the horizontal directions (i.e. Neumann-type of boundary condition) are given by the components of the bed shear stress, which will be calculated based on the flow characteristics just above the bed as follows:

$$\vec{\tau_b} = \frac{g\rho_0 \vec{u_b}|\vec{u_b}|}{C^2} \tag{2.29}$$

where:

$\vec{\tau_b}$	Bed-shear stress vector	$[N/m^2]$
$\vec{u_b}$	Horizontal velocity vector at the bottom	$[m/s]$
C	Chezy coefficient	$[m^{0.5}/s]$

For three-dimensional numerical simulations, the Chezy-coefficient is user defined and can be calculated using the following expression:

$$C = \frac{\sqrt{g}}{\kappa} ln\left(1 + \frac{\Delta z_b}{2z_0}\right) \tag{2.30}$$

where:

κ	von Karman-constant	$[-]$
Δz_b	Distance bottom to closest computational point	$[m]$
z_0	roughness height of the bed	$[m]$

The parameter z_0 represents the geometric roughness of the bed and can be linked to the

Nikuradse roughness length k_s. The bottom roughness can also be expressed through the White-Colebrook's formulation or the Manning coefficient. The Chezy coeffcient will be calculated using the formula:

$$C = \frac{\sqrt[6]{H}}{n} \tag{2.31}$$

where:

H	total water depth	$[m]$
n	Manning coefficient	$[m^{\frac{1}{3}}/s]$

Table 2.1 displays a compilation of typical Manning coefficients as a function of the morphology of the channel. This compilation is give just as a guide, since the hydraulic roughness of water body is in no way a simple phenomenon to generalize.

Table 2.1.: Manning coefficients for different types of channels (adapted from Chow 1959)

Channel's characteristics	Manning coefficient$(s/m^{1/3})$		
	Minimum	Normal	Maximum
a. clean, straigh, full stage no rifts or deep pools	0.025	0.030	0.033
b. same as above, but more stones ad weeds	0.030	0.035	0.040
c. clean, winding, some pools and shoals	0.033	0.040	0.045
d. same as above, but some weeds and stones	0.035	0.045	0.050
e. same as above, lower stages, more ineffective slopes and sections	0.040	0.048	0.055
f. same as d. with more stones	0.045	0.050	0.060
g. sluggish reaches, weedy, deep pools	0.050	0.070	0.080
h. very weedy reaches, deep pools, or floodways with heavy stand of timber and underbrush	0.075	0.100	0.150

As already mentioned in the previous paragraphs, wind heavily affects the flow dynamics at the surface boundary layer. The direct effect of wind on the time averaged momemtum equations is expressed through the shear stress at the boundary water-air. The wind shear stress magnitude is calculated through equation 2.32 as a function of the wind speed at $10m$ above the free surface.

$$\tau_s = \rho_a C_{10} U_{10}^2 \tag{2.32}$$

where:

ρ_a	Air's density	$[kg/m^3]$
C_{10}	Wind drag coefficient	$[-]$
U_{10}	Wind speed at 10 m above the free surface	$[m/s]$

The values of the wind drag coefficient are subject for discussion, since they should not be constant but depend on the wind velocity and also on the wave development state at the water surface. In Delft3D the wind drag coeffcient is user defined and can be introduced as a piecewise function of the wind speed as described in equation 2.33). where:

$$C_{10}\left(U_{10}\right) = \begin{cases} C^A_{10} & U_{10} \leqslant U^A_{10} \\ C^A_{10} + \left(C^B_{10} - C^A_{10}\right) \frac{U_{10}-U^A_{10}}{U^B_{10}-U^A_{10}} & U^A_{10} \leqslant U_{10} \leqslant U^B_{10} \\ C^B_{10} + \left(C^C_{10} - C^B_{10}\right) \frac{U_{10}-U^B_{10}}{U^C_{10}-U^B_{10}} & U^B_{10} \leqslant U_{10} \leqslant U^C_{10} \\ C^C_{10} & U^C_{10} \leqslant U_{10} \end{cases} \tag{2.33}$$

U^i_{10}	Wind speed for i= A, B and C	$[m/s]$
C^i_{10}	Wind drag coefficients for the corresponding wind speeds A, B and C	$[-]$

The function 2.33 offers the possibility to define three threshold velocities for the drag coefficient will take the prescribed value, but is also possible to define just two ranges for its variation or even assign it a constant value by respectively dessignating equals values for U^B_{10} and U^C_{10} or setting all U^i_{10} to be the same. For a typical value's range of the drag coefficient it is referred to Figure 2.4.

At the defined open boundaries the water level (pressure), the velocity component perpendicular to the boundary line or both of them have to be provided to the model. In Delft3D is supposed that the velocity vectors at the inflows is perpendicular to the boundary (i.e. tangential velocity component is assumed to be zero). The type of data that can be applied as boundary condition dependson its availability and on the specific problem to study. In the case of Delft3D boundary conditions at the open boundaries can be introduced in the form of water level, velocity magnitudes, discharge (total and per cell), Neumann (water level gradient along the boundary) and/or Riemann (weakly reflective boundaries). The variation of the boundary condition over time can be expressed as time series, astronomic conditions (for modelling of tides), harmonic conditions (wave related problems) and in the case of the water level as a QH-relation.

The advection-diffusion equation has to be additionally forced through the temperature of the water at the open boundaries for the case of heat transport and the concentration of suspended solids carried by the water entering the model through the inflows.

In the vertical direction, the forcings for the case of heat transport are the **heat fluxes** at the bottom (interface sediment-water) and at the free surface (interface air-water). In Delft3D it is assumed that no heat flux at the bottom of the reservoir occurs. At the water-air interface the source/sink term for the advection-diffusion equation is calculated through the heat flux models. Those models are simply a balance of the radiation entering and leaving the water column. The incoming radiation comprehends the solar radiation (short wave radiation) and the atmospheric radiation (long wave radiation). The energy losses through radiation refers to back radiation, convection and evaporation. In Delft3D there are five approaches to model this heat balance. Within the framework of the present work the **Ocean Heat Flux Model** was applied (Gill and Adrian, 1982; Lane, 1989). A further source of heat can be the rain, which temperature should be indicated by the modeler as a time series and it will be considered in the advection-diffusion equation via the heat balance at the water-air interface. The software can calculate the evaporation heat flux and include it in the heat balance. The effect of rain an evaporation in the mass balance of the system are considered in the continuity equation.

A further phenomenon taking place in water reservoir is the **density stratification**, which is determinant for the mixing patterns in lakes and reservoirs. It slows down vertical mixing by concentrating the mechanical energy along horizontal layers (Imboden and Wuest, 1995). Isopycnals are the surfaces of constant density, which are rarely still and can be distorted by internal waves and external forces (Imboden and Wuest, 1995). At the boundaries location aditional terms have to be added to the Equations 2.2 to 2.4 in order to include the effect of external forces e.g. wind (Imboden and Wuest, 1995).

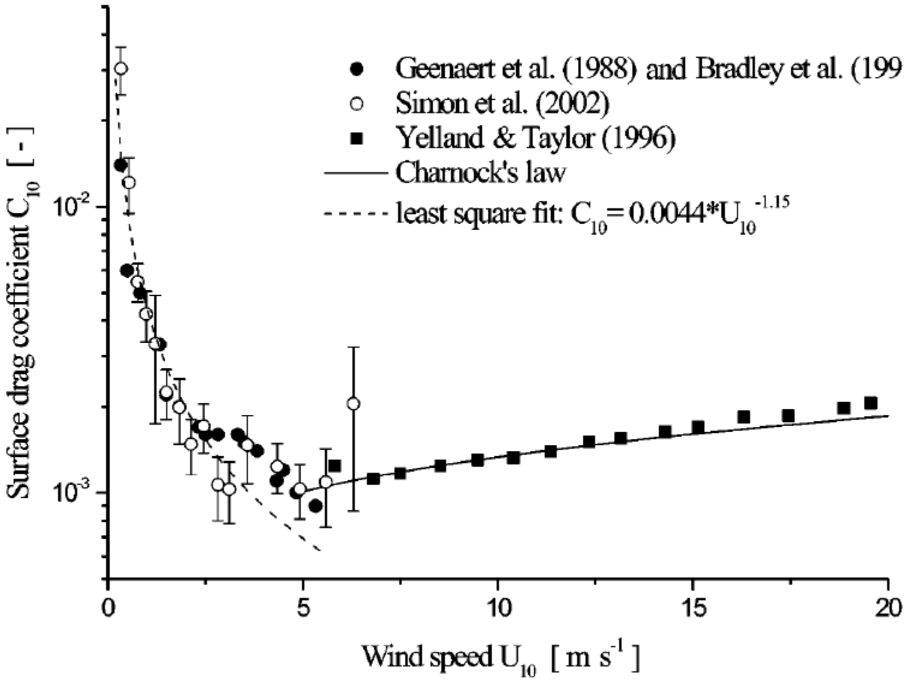

Figure 2.4.: Measured wind drag coefficients as a function of the wind speed at 10 m above the free surface (Wuest and Lorke, 2003). Original data source depicted on the diagramm: Geernaert et al. 1988, Simon et al. 2002 and Yelland et al. 1998

.

In order to quantify the local stability of the vertical temperature stratification the buoyancy frequency N, also called Brunt-Väisälä frequency was stablished and is defined as presented in Equation 2.34 Wuest and Lorke (2009). According to N, the stability of the water column becomes stronger with higher density gradients. The typical values for the buoyancy frequency in lakes and reservoirs vary between 10^{-10} and $10^{-1}s^{-2}$ (Wuest and Lorke, 2003).

$$N^2 = -\frac{g}{\rho}\frac{\partial \rho}{\partial z} \quad [s{-}2] \tag{2.34}$$

Due to strong vertical gradients of the horizontal currents the water column can become unstable. The most important factor imposing shear stress to the water column is the wind.

Depending on the ratio between the stabilizing forces and the velocity shear developed between the layers of the fluid, stratified flows may become unstable and the horizontal currents will turn into turbulence (Wuest and Lorke, 2009). The gradient Richardson number Ri_g is a measure of the tendecy of a flow towards instability (equation 2.35). For values of $Ri_g < 0.25$ the shear generated by the vertical velocity gradients overcome the stabilizing force of stratification and as a turbulent mixing will occur. For large Ri_g values the buoyancy dominates over the velocity shear and the stratified flow remains stable.

$$Ri_g = -\frac{N^2}{{}^{\partial u}\!/_{\partial z}} = \frac{Buoyancy}{Shear} \quad [-] \tag{2.35}$$

A significant number of physical indices have been developed to quantify or characterize the dynamics of stratification processes in embeded water bodies. Three parameters are used within the framework of the present study in order to analyze the dynamics of the density stratified flow. The *Weddeburn number* W expresses a ratio between buoyancy and surface wind shear (Imberger and Patterson, 1989) in a two layered system and rectagular basin. For the case when $W >> 1$ the tilting of the isotherm layers in the stratified water column will be small when wind stress is applied on the water surface. This corresponds to a situation with strongly stratified water column, weak winds and and slow deepening of the mixed layer, i.e. slow mixing of the water column. If the magnitude of the Wedderburn number is much smaller than the unity ($W << 1$) the deepening of the upper mixed layer is governed by internal turbulence in a short time scale. As consequence from this upwelling may take place at upwind and sharp gradients are present at downwind. This situation is typical for water bodies wiht a weak stratification and exposed to strong wind or storms. A representation of the behaviour of the upper mixed layer under stratification and wind is ilustrated in Figure 2.5 where the section (a) represents large Wedderburn numbers and the presence of internal waves. In the same figure sections (b)and (c) indicate Wedderburns number close to unity and (d) small Wedderburn numbers, complete upwelling (Boegman, 2009). The Wedderburn number can be mathematically defined through the following expression (Read et al., 2011):

$$W = \frac{g' z_e^2}{u_*^2 L_s} = \frac{Buoyancy}{Wind \quad Shear} \quad [-] \tag{2.36}$$

Where g' stands for the reduced gravity due to the density variations between the hypolimnion and the epilimnion, z_e is the depth to the top of the metalimnion, L_s is the lake fetch length and u_*^2 is the water friction velocity originited at the surface due to wind stress.

The Wedderburn Number considers the embedded water body as an approximation to a two layered system, for cases in which this is not a feasible assumption, a generalization of this parameter has been created, i.e. the *Lake Number* L_N (Boegman, 2009). The Lake number L_N , describes the response of the entire lake or reservoir to wind including the effects of an arbitrary reservoir's shape and several stratified layers (Robertson and Imberger, 1994). This index can be written as (Read et al., 2011):

$$L_N = \frac{S_T\,(z_e - z_h)}{2\rho_h u_*^2 A_s^{0.5} z_V} \tag{2.37}$$

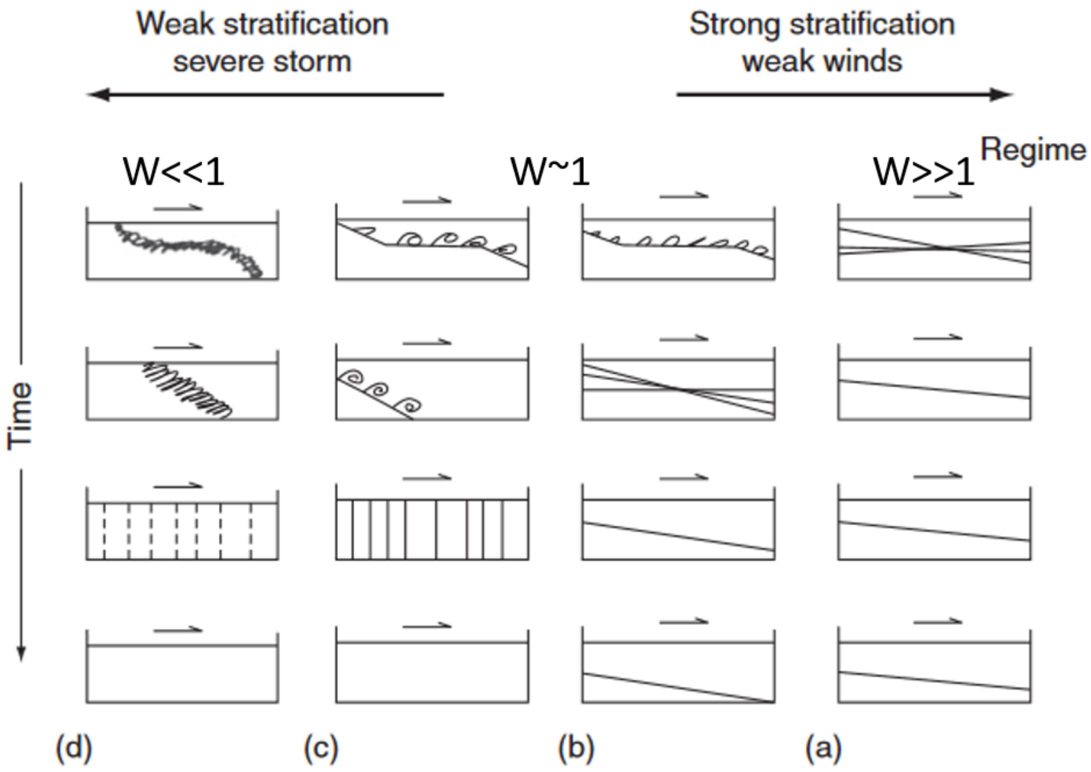

Figure 2.5.: Deepening of the upper mixed layer in presence of wind and according to the strength of stratification in the water column (adapted from Boegman 2009).

Where z_h is the depth to the bottom of the metalimnion, ρ_h is the water density at the hypolimnion, A_s is the surface area of the lake, z_v is the depth to the centre of volume of the water body and S_T is the Schmidt stability, defined as (Read et al., 2011):

$$S_T = \frac{g}{A_s} \int_0^{z_D} (z - z_V)\, \rho_z A_z \, dz \quad , [J/m^2] \tag{2.38}$$

Where z_D is the maximum depth of the lake, A_Z and ρ_Z are the area and density of the lake at a depth z. The Stability S_T can be defined as the amount of energy per unit area necessary to fully mix a lake or reservoir, which displays an arbitrary vertical density stratification, under consideration of the water body's volume development (Kirillin and Shatwell, 2016).
For $L_N >> 1$ the stratification of the water body is strong and will remain stable under the presence of wind. The Buoyancy Frequency, the Weddeburn number W and the Lake number L_N will be determined for both the measured data and the simulations results, using the software Lake Analyzer (Read et al., 2011).

A further phenomenon taking place in lakes and reservoirs are the **density driven currents**. Those are formed when the water inflowing into a reservoir has a different density to the one of the impounded water body. The incoming fluid will enter the water column at the depth of the layer whose density is more similar to its own (Wetzel, 2001).

Depending on the density of the inflow in comparison to the water in the reservoir, three different types of flows can be identified (see Figure 2.6). An underflow exists when the inflow density is larger than the density of the reservoir, the water then travels along the bottom of the reservoir. Overflow occurs when the water entering the reservoir is warmer (lower density) than the water column, in this case the water will travel at the water surface of the impounded body. If the temperature of the incoming water is higher than the water at the bottom of the reservoir but colder than the water at the surface, it will travel as an interflow in an intermediate layer of similar density. The importance of the different types of density driven flows is highlighted well by Ishikawa et al. (2021): the nutrients and orgnic mater laden water entering the reservoir as underflows can become a source of pollutants for the bottom sediments or if the water enter the reservoir as an overflow, the inflow would deliver those nutrients to the photic zone, increasing the growth of phytoplankton. The renewal of the water at deep layers of the water body would be suppressed by underflows, triggering anoxic conditions at these locations and thus the formation/release of compounds such as methane, hydrogen sulfide and phosporous (Ishikawa et al., 2021).

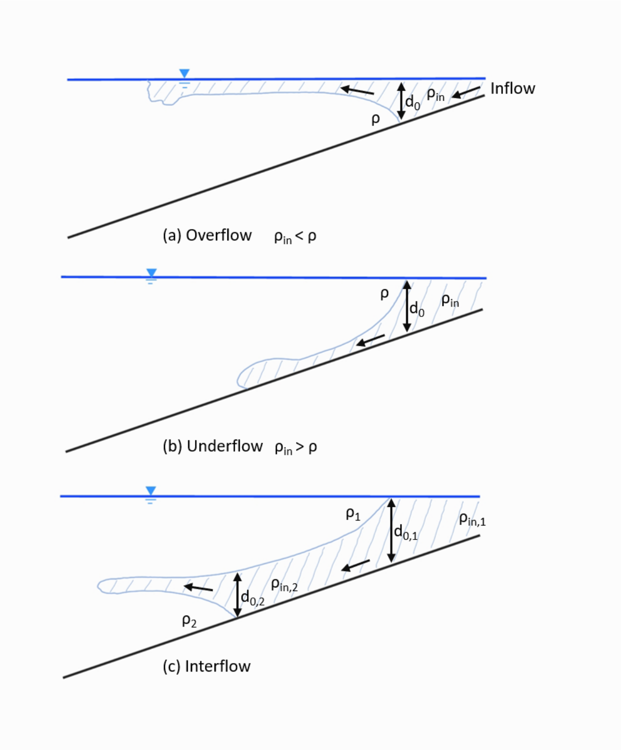

Figure 2.6.: Types of density driven currents (adapted from Wunderlich 1971).

2.2. General Description of the Sediment Transport in Reservoirs

The transport of sediments into a reservoir takes place either in form of density currents or as regular transport. Under regular transport, it can be understood the movement of the sediments caused by the advection and diffusion of the flow in the water body, transporting the sediments as suspended load or bed load. Suspended sediments are normally composed by fine particles (fine sand to clay) and are transported in suspension due to the turbulence present in the water column. Bed load refers to the transport of coarser sediments along the bed of a water body. It is important to notice, that even though the terms fine sediments and suspended sediments are often used as synonyms, they are not necessarily the same, since the transport of sediments in suspension and/or bed load depends on the capacity of the flow to transport a particle of a determined diameter. The same applies for the use of the terms bed load and coarse sediments. One example to clearly understand the distinction would be the fact that during a high discharge event in a river, the flow may be able to transport coarse sand or even gravel, in suspenion.

The advection-diffusion equation describes the transport of suspended sediment in the water column. Notice that the advection-diffusion also describes the transport of heat. When modelling heat and suspended sediments more than just one equation of this type have to be solved, i.e. one equation for the thermal processes and one further equation per each sediment grain size defined in the model. The advection-diffusion equation for the transport of suspended sediment can be written as follows:

$$\frac{\partial C}{\partial t} + \frac{\partial uC}{\partial x} + \frac{\partial vC}{\partial y} + \frac{(w - w_s)\partial C}{\partial z} = \frac{\partial}{\partial x}\left(\epsilon_{s,x}\frac{\partial C}{\partial x}\right) + \frac{\partial}{\partial y}\left(\epsilon_{s,y}\frac{\partial C}{\partial y}\right) + \frac{\partial}{\partial z}\left(\epsilon_{s,z}\frac{\partial C}{\partial z}\right) \tag{2.39}$$

where:

C	suspended sediment concentration	$[kg/m^3]$
ϵ_s	eddy diffusivities of sediment fraction	$[m^2/s]$
w_s	settling velocity of sediment fraction	$[m/s]$

In Delft3D the eddy diffusivities for suspended sediment to be used in the advection diffusion equation are calculated based on the values of the eddy viscosities derived from the turbulence closure model in the modelling of the hydrodynamics. For cohesive sediments the diffusivities have the same magnitude as the viscosities. For the case of non-cohesive sediment, the diffusivities can be calculated as a factor of the eddy viscosity as indicated by equation 2.40 and 2.41:

$$\epsilon_s = \beta_{eff}\nu_t \tag{2.40}$$

$$\beta_e ff = 1 + 2\left(\frac{w_s}{u_{*,c}}\right)^2 \frac{\tau_c}{(\tau_w + \tau_c)} \tag{2.41}$$

where:

β_{eff}	effective Van-Rijn beta factor (includes the effect of waves)	$[-]$
$u_{*,c}$	shear velocity	$[m/s]$
τ_c	shear stress due to the currents	$[N/m^2]$
τ_w	shear stress due to waves	$[N/m^2]$

Notice that the effect of waves maybe included for coastal areas. Nevertheless, it is not necessary for the case of reservoirs.

The **settling velocity** of a sediment particle falling across the water column can be determined by stating the equation for the equilibrium between the drag force that the particle experiences while settling and the gravity force under lift. In this way, it can be observed that the settling velocity w_s can be expresed as:

$$w_s = \sqrt{\frac{1}{C_D}\frac{4}{3}d_m g \rho'} \tag{2.42}$$

Where C_D is the drag coefficient, which is a function of the shape, surface texture and the shear reynolds number of the particle Re^*. For particles with $Re^* < 1$, Stokes (2009) derived an expresion for the C_D:

$$C_D = \frac{24}{Re^*} \tag{2.43}$$

Combining Equations 2.42 and 2.43 results in the well-known formula for the settling velocity of particles in the Stoke's regime:

$$w_s = \frac{d_m^2 g \rho'}{18\nu} \tag{2.44}$$

The previous expression for the settling velocity considers spherical particles, which is not close to reality since sediments can strongly differ from this shape. To overcome this, the shape factor was introduced. Numerous studies indicated that the shape factor is around of 0.7 for natural sediments in rivers (Komar and Cui, 1984). Considering these facts, Zanke (1982) derived his well-known formula for $Re^* < 2 \cdot 10^5$:

$$w_s = \frac{11\nu}{d_m}\left(\sqrt{1 + \frac{0.01\rho' g d_m^3}{\nu^2}} - 1\right) \tag{2.45}$$

A further approach for the zone $1000 < Re^* < 2 \cdot 10^5$ (also called the Newton-area) reads:

$$w_s = 1.83\sqrt{\rho' g d_m} \tag{2.46}$$

An additional process, which should be conidered when dealing with fine sediments in the silt-clay range is the flocculation. This process has its origins in the cohesive properties of the fine particles ($d < 63\mu m$), which induce electrochemical forces in the interaction of fine grained sediments. Flocculation may cause both aggregation of fine sediment (primary particles) into larger porous structures called flocs or disaggreagation of flocs due to shear stresses in the water column Klassen (2017). Flocculation causes changes in the characteritics of sediments, e.g. changes in the apparent sediment size of the particles in the water column and their density. The following example is intended to ilustrate the effects of flocculation: in a reservoir with low flow velocities regime, middle sand is found in suspension according to the diameters of the sediment in the water column measured with laser techniques. Nevertheless, in sediment samples from the bottom of the water body, only sediments in the silt-clay range are found. This situation could be explained through flocculation: the fine particles in suspension built flocs of the size of middle and fine sand and the size of the flocs were measured by the laser technique. An in the samples from the bottom taken to the laboratory, the diameter of the primary particles was detected. Just having the information from the water column, would induce to a wrong calculation of the settling velocity of the suspended sediment and the same is true when just knowing the diameter of the particles at the bottom.

In rivers and reservoirs, the flocculation is considered as complex phenomenon influenced by several factors like the properties of the particles, their concentration in the suspension, the salinity of the fluid, the pH-value, the temperature, the content of organic mattera and last but not least the turbulence intensity in the flow (Klassen, 2017). The physics of the flocculation processes is not completely understood until now and hence their application in numerical model is rather poor. Most approaches includes the modification of the settling velocity of the suspended particles, when cohesive sediments are detected. For the case of Delft3D the modified settling velocity due to flocculation can be calculated only by taking into account the salinity of water. A widely known formulation for the calculation of the settling velocities of flocs was derived by Winterwerp and Van Kesteren (2004) and reads as follows:

$$w_s = \rho' \frac{g}{18\nu} d_f^2 \left(\frac{d_p}{d_f} \right)^{(3-n_f)} \tag{2.47}$$

where:

d_f	diameter of the floc	$[m]$
d_p	diameter of primary particle	$[m]$
n_f	fractal dimension	$[-]$

The magnitude of the fractal dimension n_f ranges between 1 to 3. The highest the fractal dimension, the more compact and denser is the structure of the floc (Klassen, 2017).

A further process affecting the behaviour of particles in suspension is produced when their concentration in the water column is too high. Under this condition individual particles stop to move independently (Cuthbertson et al., 2008). With high SSC the density of the sediment-fluid mixtures increases and experiments have shown that the drag induced by the flow on the single particles in higher than for clearer water conditions (Dey, 2014). Furthermore, the upflow generated by the many settling particles contributes in some measure to the phenomenon. In fine sediment suspensions, hindered settling has been observed to onset for SSC of 3 to 15 g/l (Raudkivi, 2020).

The settling velocity for non-cohesive sediments in Delft3D is calculate according to the approach by van Rijn (1993). The formula is defined as a step function depending on the size of the sediment fraction as follows:

$$w_s = \begin{cases} \frac{\rho' g d_m^2}{18\nu}, & 65\mu m < d_m \leqslant 100\mu \\ \frac{10\nu}{d_m}\left(\sqrt{1+\frac{0.01\rho' g d_m^3}{\nu^2}} - 1\right), & 100\mu m < d_m \leqslant 1000\mu \\ 1.1\sqrt{\rho' g d_m}, & 1000\mu m < d_m \end{cases} \tag{2.48}$$

Notice that each part-function of equation 2.48 are quite similar if not the same as for the settling velocity according to stokes (equation 2.44),to Zanke (equation 2.45) and for the Newton area (equation 2.46).

The advection-diffusion equation has to be forced through the concentration of suspended sediment carried by the water entering the model through the inflows. Rating curves are employeed to quantify the amount of solids flowing through the cross section of a water body. They are constructed based on coupled measurements of the SSC and the corresponding discharge. Based on those measurements a regression is performed, in order to determine an equation to calculate the SSC for the stream based as a function of the discharge. Rating curves present different behaviours. One of the most common are the positive linear,log-linear and power function behaviours, which leads to the notion that with highest discharges, higher SSc will be measured as well (Wagner, 2020; Horowitz, 2002). This is not always the case in streams. Figure 2.7 shows several rating curves, which were derived using different forms of regression.

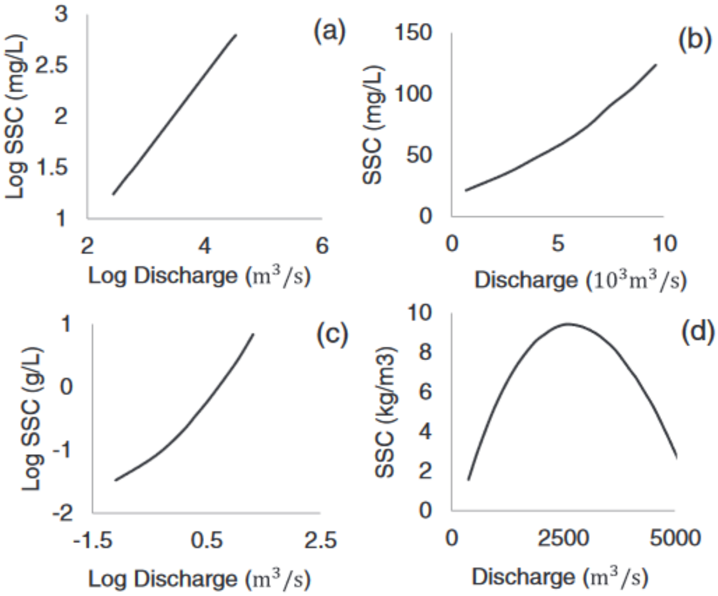

Figure 2.7.: Rating curves derivated with different forms of regression: a) Broad River, USA use of linear regression, b) Tributary to the River Rhine, Germany use of non-linear left squares regression, c) Celone River, Italy use of second order polynomial regression and d) Reach of the Yellow River in Mongolia, use of a third order polynomial regression. (Vercruysse et al., 2017)

.

In general, rating curves tend to underpredict SSCs for high flows and overpredict them for low flows (Horowitz, 2002). This is partially due to the scattering of the data around the regression line. To avoid this, several methods have been developed such as the production of seasonal rating curves, yearly/hydrological rating curves, the use of correction factors and non-linear regression equations (Horowitz, 2002). The selection of the sampling scheme (calender-based, event (storm)-based, will also have an impact on the realiability of the predicted SSC. In general, the measuring campaigns to produce rating curves should cover 80 to 85% of the discharges taking place during the year and as many high flow events as possible (Horowitz et al., 2015).

It is important to keep in mind, that the sediments entering a stream are originated at the catchment as a product of soil erosion. Hence further events which depends on the studied temporal scale, such as land use changes (usually decades)and agriculture (months) will have an influence on the resulting rating curve (Wagner, 2020).

Rating curves for high flow events do not always present a direct proportionality between the SSCs and the discharges. The measured SSC usually depends on the pre-existing conditions in the catchment, i.e. there is a hysteresis-pattern between the SSCs and the discharge. Figure 2.8 shows the main three forms of hysteresis to be found in rating curves of a high flow event according to Juez et al. (2018). The classification into one type of hysteresis is based on the temporal evolution of the discharge(hydrograph) in relationship to the temporal evolution of the SSCs (sedigraph). The single-valued line in figure 2.8 (i) shows no hysteresis, for this relationship the SSCs are the same for the same discharge either in the rising or falling limbs of the hydrograph. A clockwise or positive hysteresis (ii) presents higher SSCs for rising limb of a hydrograph than those measured for the same discharges on the falling limb Many rating curves describe this type of hysteresis for high flow events, often due to sediment depletion in the stream or the augmented component of the base flow during the falling limb (BAČA, 2008). An anti-clockwise hysteresis (iii) shows lower SSCs on the rising limb than on the falling one for a given discharge. This kind of hysteresis occurs probably due to further sediments coming from distant sources or due to bank erosion (BAČA, 2008).

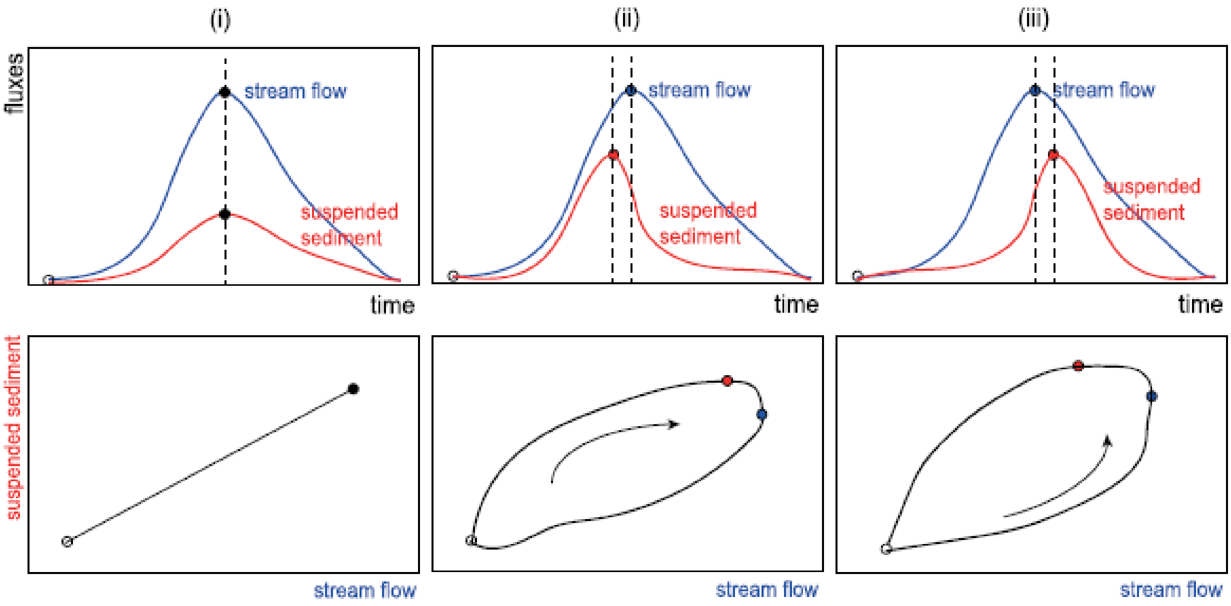

Figure 2.8.: Most common three forms of hysteresis between the SSCs and water discharge at a stream duing a high flow event (Juez et al., 2018)

.

Suspended sediment is a natural component of the water entering reservoirs. It constitutes a major agent shaping the morphological characteristics and defining the water quality of a water body. Hence is of paramount importance to understand the dynamics of these sediments in the reservoirs and also their sources from the rivers to the catchment scale (Vercruysse et al., 2017). Sediments in general, are generated in great proportion in the catchment as a product of soil erosion. After that, those sediments are transported to the rivers principally through the action of gravity. Rivers transport sediments as bed or suspended load, depending on the transport capacity of the stream and the characteristics of the sediments (e.g. size).

For the numerical cells nearest to the bottom the amount of SSC enterig the water column is calculated taking into account the deposition and erosion processes. At the free water surface it is normally considered, that neither input nor output of solids takes place. The erosion and deposition source/sink terms applied to the lowest computational cell can be calculated depending wether the sediment fraction is cohesive or not. For the cohesive case the formulations of Partheniades-Kron (Partheniades, 1965) have widely been applied:

$$E = Mf\left(\tau_0, \tau_{cr,e}\right) \tag{2.49}$$

$$D = w_s c_b f\left(\tau_0, \tau_{cr,d}\right) \tag{2.50}$$

where:

E	Erosion flux	$[kg/(m^2 s)]$
D	Deposition flux	$[kg/(m^2 s)]$
M	Erosion parameter	$[kg/(m^2 s)]$
$f\left(\tau_0, \tau_{cr,d}\right)$	Deposition function	$[-]$
$f\left(\tau_0, \tau_{cr,e}\right)$	Erosion function	$[-]$

The erosion and deposition functions are defined as:

$$f\left(\tau_0, \tau_{cr,e}\right) = \begin{cases} \left(\frac{\tau_0}{\tau_{cr,e}} - 1\right), & \tau_0 > \tau_{cr,e} \\ 0 & \tau_0 \leqslant \tau_{cr,e} \end{cases} \tag{2.51}$$

$$f\left(\tau_0, \tau_{cr,d}\right) = \begin{cases} \left(1 - \frac{\tau_0}{\tau_{cr,d}}\right), & \tau_0 < \tau_{cr,d} \\ 0 & \tau_0 \geqslant \tau_{cr,d} \end{cases} \tag{2.52}$$

where:

τ_0	Actual bed shear stress	$[N/m^2]$
$\tau_{cr,d}$	Critical bed shear stress for deposition	$[N/m^2]$
$\tau_{cr,e}$	Critical bed shear stress for erosion	$[N/m^2]$

Equations 2.51 and 2.52 state that two threshold values for the erosion and deposition exist and given the actual bed shear stress exerted by the flow on the bottom of the water body, one of both processes will take place. General agreement exist about the existence of a treshold value for the entrainment star of sediments from the bed. Table 2.2 shows some reference values for $\tau_{cr,e}$. The magnitude of $\tau_{cr,e}$ does not only depend on the grain size of the sediments at the bottom, but also on their dry bed density, consolidation grade and the mineral composition. This makes of the selection of a magnitude for this parameter, solely based on tables, a questionable decision. Nevertheless, without any in-situ measurements of the bed shear stress for erosion, there is often no further way to proceed.

On the other hand, the existence of a critical bed shear stress for deposition is still subjected to debate (Feng et al., 2020; Klassen, 2017). Authors like Winterwerp (2007) stated that there is no threshold for the depositionof sediment particles, which would mean that deposition and erosion can occur simultaneously. Opposite to this, Zhu et al. (2016) afirmed based on field measurements that the deposition and erosion are mutually exclusive. Particles will always settle under the action of gravity bt deposition will happen onlyif the bed shear stress is lower than a treshold value. A further variable included in equation 2.49 is the ersoion parameter M which is tipically found in the range of 1^{-5} to $5 \cdot 10^{-}4 kg/(m^2 s)$ (Winterwerp et al., 2012).

Table 2.2.: Magnitude of the critical bed shear for erosion as a function of the grain size adapted from DIN19661-2 (2000)

Bed Material	$\tau_{cr,e} [N/m^2]$
Fine Sand (0.063 - 0.2 mm)	1
Medium Sand (0.2 - 0.63 mm)	2
Coarse Sand (0.63 - 1 mm)	3
Coarse Sand (1 - 2 mm)	4
Sand-Gravel Mixture(0.63 - 6.3 mm)	9
Sand-Gravel Mixture Consolidated	15
Coarse Gravel (20-63 mm)	60
Rubble (63 - 100 mm)	24
1 Clayey Fine Sand	2
Clayey Mud	2.5
Clayey Gravel	15
Loose Clay	3.5
Consolidated Clay	12
Clay and Consolidated Mud	12
Grass, temporally stressed	20 - 30
Grass, stressed for the longer term	15 - 18

For the case of non-cohesive sediments the erosion and deposition fluxes are determined according to the following equations(Deltares, 2014):

$$E = \epsilon_s \frac{\partial c}{\partial z} \tag{2.53}$$

where:

ϵ_s Sediment diffusion coefficient at the bottom of the reference layer $[kg/(m^2 s)]$

$$D = w_s c_{ref} \tag{2.54}$$

In order to calculate the concentration and the concentration gradients at the reference layer a Rouse SSC-profile is assumed in Delft3D. The Rouse-Profile can be derived by setting an equilibrium situation between the gravitational force and the turbulence and obtaining the following equation for the vertical distribution of the SSC:

$$C = c_r ef \left[\frac{a(h-z)}{z(h-a)} \right]^{\xi} \tag{2.55}$$

where:

h	water depth	$[m]$
z	elevation above the bed	$[m]$
ξ	Rouse Number	$[-]$

The reference concentration c_{ref} is calculated in Delft3D it is assumed that the suspended sediment concentrations at the reference layer is equal to the mean concentration of particles in the bedload transport area, i.e. the the bed load transport approach is used to calculate this quantity. The Rouse number is calculated as shown in equation 2.56. This number shows a relationship between gravity (numerator) and turbulence (denominator). With increasing Rouse numbers the gravitational force will be domninating the distribution of the sediments in the water column and thus the SSC will be much higher towards the bed. For Rouse numbers smaller than one, turbulence will dominate the process and the SSC will be more evenly distributed over the water column (see figure 2.9).

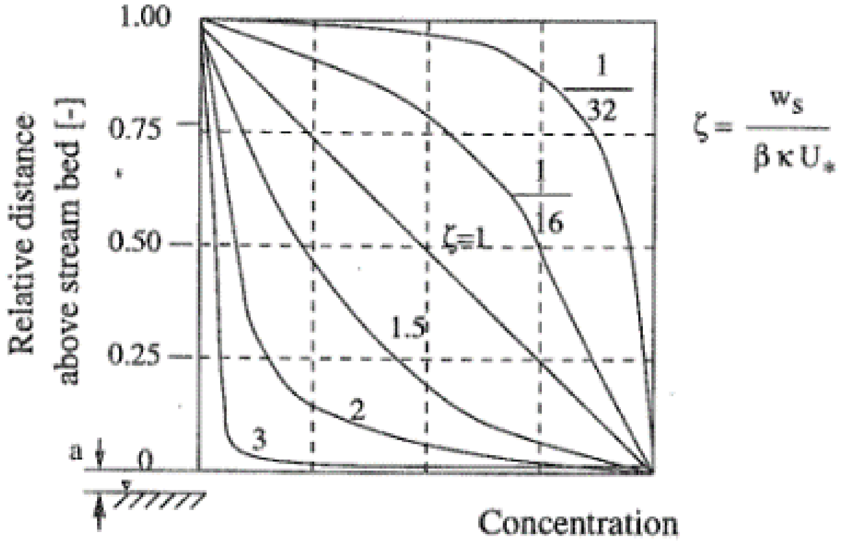

Figure 2.9.: Vertical suspended sediment concentration distribution according to a Rouse profile (Xu, 1998)

$$\zeta = \frac{w_s}{\beta \kappa u_*} \tag{2.56}$$

where:

κ	Von-Karman constant	$[-]$

The transport of sediments as density or **turbidity current** occurs when the density of the water-solids mixture entering the reservoir exceeds the density of the storaged reservoir's water by a large factor. Turbidity currents can travel large distances along the bottom of the reservoir and even reach the dam. They carry mainly fine to very fine sediments and normally are the process governing reservoir siltation. The sediment transported by these means not only contributes in great manner to the decrease of the storage volume of the reservoir, but may also block the intake structures at the dam (Jenzer Althaus et al., 2015).

Figure 2.10 shows the structure of a turbidity current moving through a reservoir. The water depth at the location of the plunge point can be approximated using the densimetric Froude number (see equation 2.57) and also knowing the fact, that measurements in the field and laboratory indicate that the magnitude of the F_p at the plunge point is of ca. 0.78 (Morris and Fan, 1998).

$$F_p = \frac{V}{\sqrt{\frac{\Delta\rho}{\rho_w} g h_0}} \tag{2.57}$$

where:

$\Delta\rho$	density difference between inflow and ambient water	$[kg/m^3]$
V	mean velocity	$[m/s]$
h_0	water depth at the plunge point	$[m]$

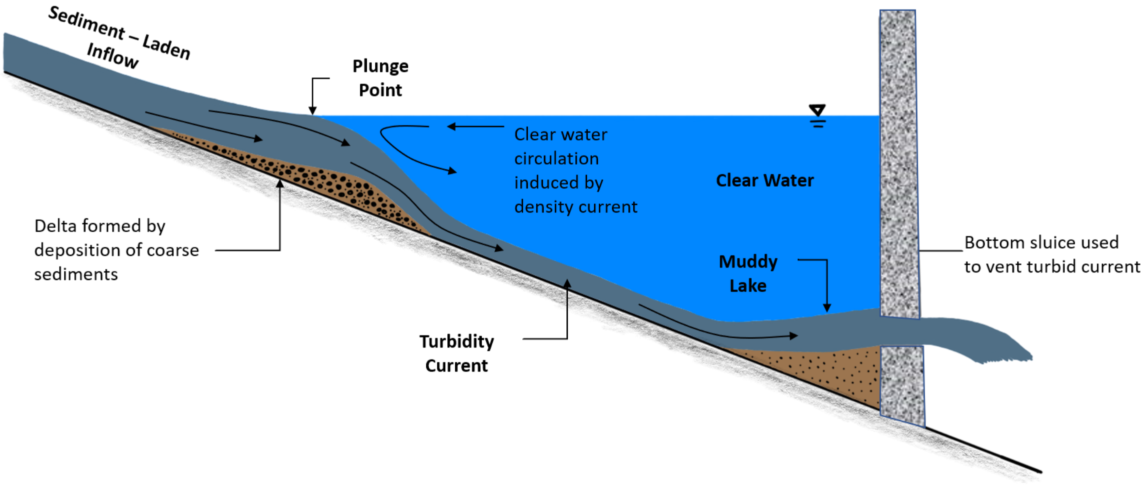

Figure 2.10.: Structure of turbidity current moving through a reservoir (adapted from Morris and Fan 1998)

.

As explained by Morris and Fan (1998) several phenomenon in the reservoir may indicate the presence of turbidity currents. For example, when turbid water leaving the impounded body through a bottom outlet at the dam is observed, while the water at the surface is clear, may be an indicator for a turbidity current. A turbid flow entering and dissapearing at the upstream area of the reservoir would also be a clear indicator for a plunging flow. This phenomenon can be observed from the air. Nevertheless, the best way to confirm the presence o turbidity currents is via field measurements. Continuos monitoring of the SSC at the Inflow of the reservoir and at various locations along the longitudinal axis until reaching the dam, would provide a clear picture of the phenomenon.

When both coarse and fine sediments enter a reservoir under conventional conditions, i.e. no flood event, coarse sediments deposit at the topset reach of the reservoir, forming a delta (see Figure 2.11). This is due to the reduction of flow velocities in comparison to the inflowing river, which induces a reduction in the transport capacity of the flow. Depending on the geometry of the reservoir, the flow conditions and the characteristics of the incoming sediments, further coarse sediments may deposit in the foreset reach. The fine sediments will deposit before the dam and if turbidity currents are present in the water body, muddy lake deposits may be observed. It is of importance to keep in mind, that the sedimentation pattern showed in this figure is a generalization and an attempt to give an idea from a descriptive point of view. Sedimentation patterns can and will differ from the one presented in the figure 2.11, since they depend on the flow regime of the reservoir and on the sediments entering the water body.

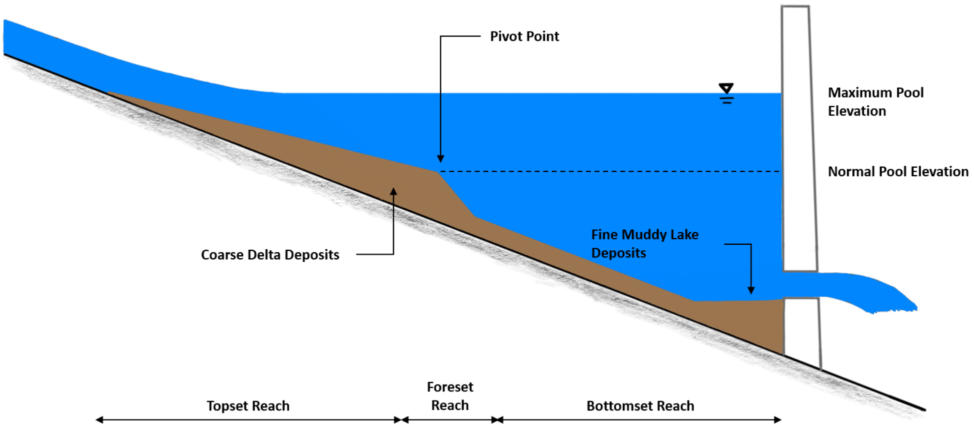

Figure 2.11.: Typical sedimentation pattern in reservoirs (adapted from Annandale et al. 2016)

.

Further common siltation patterns are illustrated by the figure 2.12 and they can be described as follows (Morris and Fan, 1998):

- The **Delta pattern** is a result of the sedimentation of coarse sediments, as already explained.
- **Wedge-like deposits** usually occur as a consecuence of the fine sediment transport by turbidity currents. Nevertheless, it also may take place in small reservoirs, receiving a large amount of fine sediments.
- **Tappering patterns** are the result of the progressive thiner sediment layer, which is common for long reservoirs maintained at a high pool level.
- The **uniform pattern** can happen in narrow reservoirs, for which the suspeded sediment load is low and the fluctuations on the water level are considerable.

The discussed patterns also tend to occur simultaneously. For example, a reservoir exposed to turbidity currents and otherwise receiving rather coarse sediment, may present a combination of the wedge-shaped and delta patterns.

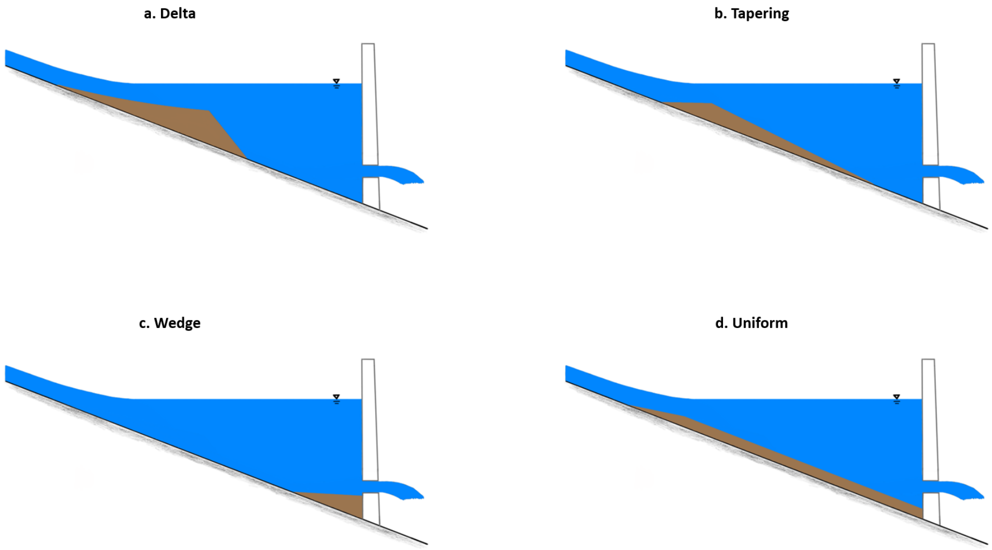

Figure 2.12.: Sedimentation patterns in reservoirs (adapted from Annandale et al. 2016)

.

2.3. Conclusions

Complex processes have to be considered while modelling the suspended sediment transport in Reservoirs. The results of the hydrodynamics will directly affect the final picture of the sedimentation patterns and amounts of sediments deposited in the reservoir, since the velocity field resulting from the numerical solution of the Navier-Stokes-Equations and the diffusivities from the turbulence closure model directly affect the Advection-Diffusion-Equation for the transport of suspended sediments. Moreover, the velocity gradients will also determine the shear stress acting on the bed and thus influencing the deposition and erosion processes.

When modelling the hydrodynamics of a reservoir processes like thermal stratification have to be considered. This has as consequence a larger number of input data (wind forcing, meteorological data and temperature of the inflows) for the numerical model when compared to the situation in e.g. rivers. Notice that when having a large amount of user input variables the model will have more error sources. Stratification and mixing processes caused by temperature play an important role in lakes and reservoirs. Nevertheless, variations in suspended sediment concentrations will also contribute to vertical stratification in reservoirs. Those two parameters (suspended sediment and temperature) directly affect the density of the water and hence may induce density-driven currents. The density of water can be calculated as a function of the temperature, the total dissolved solids and the SSC as follows:

$$\rho = \rho_T + \Delta\rho_{TDS} + \Delta\rho_{SS} \tag{2.58}$$

where:

$\Delta\rho_T$	density as function of temperature	$[kg/m^3]$
$\Delta\rho_{TDS}$	density variation due to total dissolved solids	$[kg/m^3]$
$\Delta\rho_{SS}$	density variation due to total suspended solids	$[kg/m^3]$

Temperature gradients will be the paramount mechanism for the existence of density difference and hence density currents, if the inflowing SSCs are low (Morris and Fan, 1998). For example, at 25 $\circ C$ in order to get the difference in density induced by 1 $\circ C$ temperature gradient , one would have to have SSCs of around 420 mg/l with a specific density of 2.65 (Morris and Fan, 1998).

For the morphological modelling is also of paramount importance to define the sediment-related data based on field measurements and avoid standard values. Along this chapter could have been observed how the hydrodynamics completey affect the suspended sediment transport. The linkage between the hydrodynamics and sediment transport modelling is aimed to be illustrated in the diagram 2.13, which is valid for any water body. Due to the additional forcing/phenomena (wind, meteorological forcing and thermal stratification) that affect the hydrodynamics of reservoirs, it should be further investigated if those processes have or not an influence in the transport of suspended sediment.

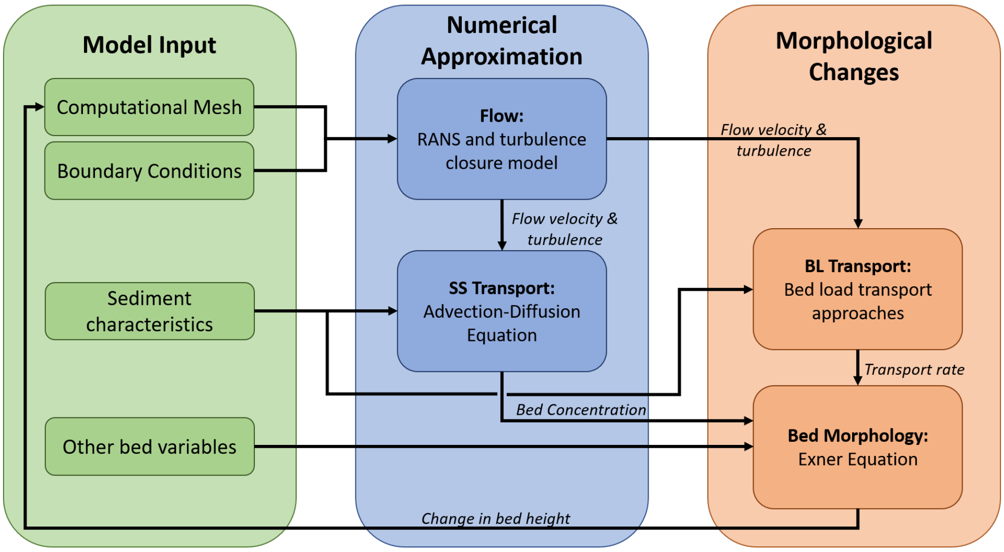

Figure 2.13.: Flow diagram for the numerical modelling of rivers and reservoirs (adapted from Murali et al. (2020)).

3. Hydrodynamics and Sedimentation: Field Measurements

[1] Field campaigns are key to construct numerical models. Without high quality data sets to feed and calibrate/validate them, models will have low capacity to predict variables for further scenarios. Within the framework of the MuDaK-Project two reservoirs were investigated. The first one was the Big Pre-Dam of the Größe Dhünn-Talsperre in Germany. The second water body was the Passaúna Reservoir in Brazil. Most of the field campaigns took place in the last one, making of this a well monitored water body. The present chapter presents and analyzes the measurements performed in the brazilian reservoir, which is the study object of the present work. The chapter is divided in two major sections. First, all data related to the hydrodynamics including thermal mixing and stratification will be discussed. The aim of the second part is to analyze the available data regarding the sediment transport in the same water body. Most data presented within this chapter were gathered by the scientists participating in the field campaigns during the MuDaK-Project (MuDak-WRM, 2019) and not by the author of the present dissertation.

3.1. Study Area

Passaúna Reservoir is located at the west margin of the City of Curitiba in the federal state of Paraná, Brazil. Passaúna is located at coordinates 25°31'44"S, 49°23'37"W, in the transition from the tropical to the subtropical zone. The reservoir was commisioned in 1989 and supplies with drinking water to about 22% of the population of the metropolitan region of Curitiba (Xavier et al., 2017). It has a storage capacity of approximately 69.3 x 10^6 m^3. Passaúna is a canyon-shaped narrow reservoir, 11 km large and 0.7 km width and a surface area of approximately 8.5 km^2. The maximum depth of the reservoir is approx. 16.5 m (Sotiri et al., 2019) at the vicinity of the dam. The mean depth of the water body amounts to 8.2 m. The Passaúna River flows into a shallow pre-bay called the Buffer. The Buffer includes a mean depth of approximately 1 m and was constructed in order to trap the sediments entering the reservoir. A narrow channel connects the Buffer with the main reservoir. This location will be called the Ferraria Bridge, since a small transitable bridge was constructed over the channel. The reservoir is managed by the state-owned company SANEPAR (Companhia do Saneamento do Paraná). The Environmental Institute of Paraná State classified the water quality of the reservoir as moderately degraded (Xavier et al., 2017).

---

[1] This section is based on the measurement campaigns performed within the framework of the MuDak Project (MuDak-WRM, 2021), based on those data, the author of the present dissertation carried out the analysis presented in this chapter.

Figure 3.1.: Overview Passaúna Reservoir (created with cartographical elements from ESRI).

3.2. Characterization of the Hydrodynamics and Thermal Stratification

To fully describe the hydrodynamics of the reservoir, variables in the fields of hydrology and meteorology are requiered. Moreover, the elements determining the thermal stratification, such as temperatures along the water column are necessary. In the present section, the measurements gathered within the framework of the MuDak-Project regarding the hydrodynamics of the reservoir are presented.

3.2.1. Inflows and Outflows

The main inflow of the reservoir; the Passaúna River, enters the water body at the northern part of the reservoir with an average discharge of 2.0 m^3/s (Carneiro et al., 2016). The second largest inflow is the Ferraria River located at the northwest area of the reservoir with an average discharge of ca. 0.15 m^3/s. Within the framework of the MuDak-Project, discharges and water temperatures of the 64 tributaries for the period August 2017 to February 2019 were simulated making use of the Large Area Runoff Simulation Model LARSIM-WT (Haag and Luce, 2008). The model LARSIM-WT was calibrated with measurements of the discharge and water temperature of four gauging station upstream of the Passaúna Reservoir for the periods 2010-2013 (Ishikawa et al., 2022). The location of all 64 inflows and the mean discharge for the ten highest of them are shown in Figure 3.2, each inflow is identified with a number for clarity purposes. The inflow 154 corresponds to the Passaúna River and the inflow 195 to the Ferraria River. Furthermore, within the framework of this work the number of each inflow will be preceded by the pre-fix TGB, short for "sub-catchment" in german: Teileinzugsgebiet.

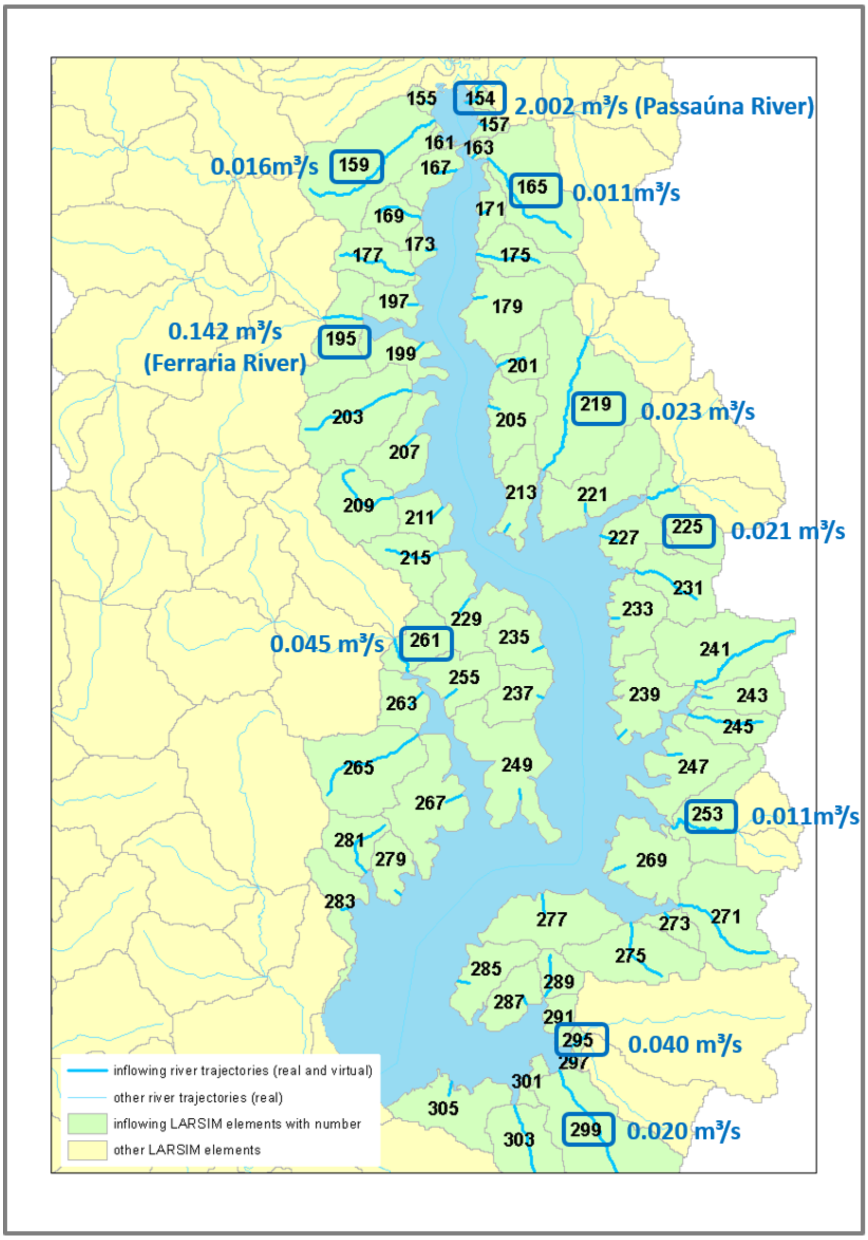

Figure 3.2.: Tributaries with the ten highest mean discharges for the period August 2017 - February 2019 (adapted from MuDak-WRM 2019).

The modeled discharges for the main inflow TGB154 for the period August 2017 to February 2019 are shown in Figure 3.3. Using LARSIM-WT it was possible to simulate the discharge of the Passaúna River with a temporal resolution of one day, a higher temporal resolution was not possible to achieve with the model, due to the temporal resolution of the input data for LARSIM-WT. According to LARSIM-WT, the discharge varies between 0.6 and 10.9 m^3/s with a mean discharge of 2 m^3/s. The highest discharge was modeled for January 21 of 2018. 25% of the discharges were higher than 2.4 m^3/s and lower than 1.1 m^3/s.

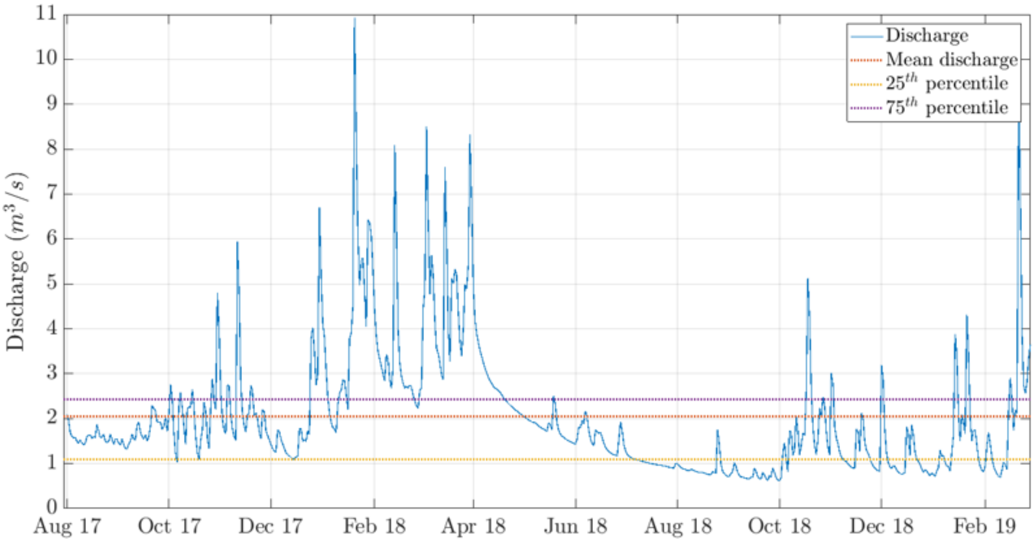

Figure 3.3.: Discharges for the main inflow to the Passaúna Reservoir TGB154 for the period August 2017 - February 2019.

A historical series of the discharges gathered at a monitoring station officially identified as 65021800, which is located approximately 2.3 km upstream the main inflow of the reservoir (see Figure 3.4) at the bridge over the Passaúna River at the highway BR277. From now on, this location will be called BR277.

The measurements were peformed between the years 1985 and 2015 and are part of the data base of the Brazilian National Water Agency (ANA) and AGUASPARANA (Rauen et al., 2017). This data set comprehends the longest period recorded for discharges of the Passaúna River and according to it, the river carries a mean flow of 1.7 m^3/s, which is lower in comparision to the mean discharge modeled by LARSIM-WT. Actually, the inflows at the BR277 and the TGB154 should be similar, since there are no further confluences or bifurcations to/of the river after the station BR277. The difference between discharges may be due to further factors like the fact that even though the temporal resolution for both data series is one day, the measurements at the BR277 could have been performed repeatedly not at the peak discharge of the day. Furthermore the studied periods are different and the hydrological conditions at the catchment could have been different. 75 % of the time the discharges were respectively higher than and lower than 0.98 and 2.02 m^3/s. The median of the time series amounts to 1.5 m^3/s. In general the highest and lowest discharges registered at the main inflow were 27 and 0.12 m^3/s in the years 1988 and 1993 respectively.

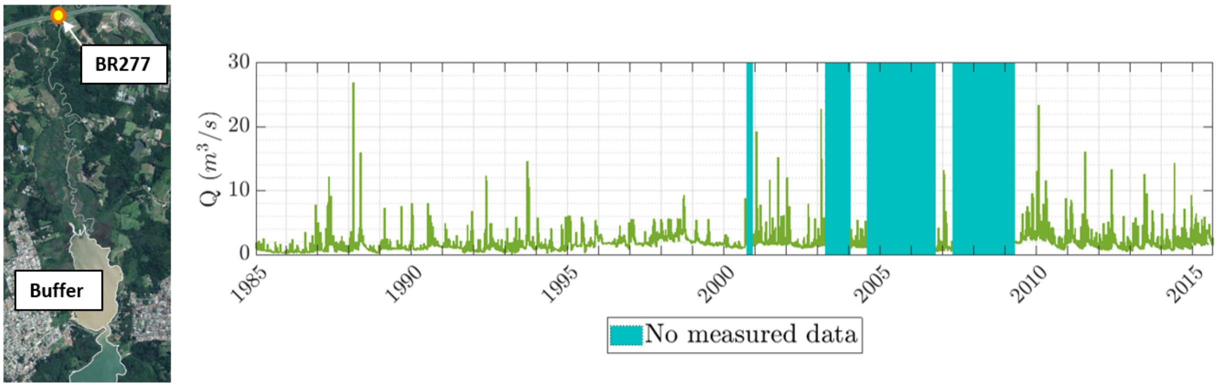

Figure 3.4.: Historical discharges for the main Inflow. Discharges measured at the station BR277.

Higher resolution measurements of the discharge at the BR277 were available for the period July 2016 to August 2018 where one measurement was performed every 15 minutes, with some time slots where no data was gathered. The lowest and the highest discharges measured were respectively 0.59 and 24.1 m^3/s. The mean discharge for this data serie amounts to 2.1 m^3/s, meanwhile the median was 1.6 m^3/s. The first and third quartiles were calculated as 1.11 and 2.1 m^3/s.

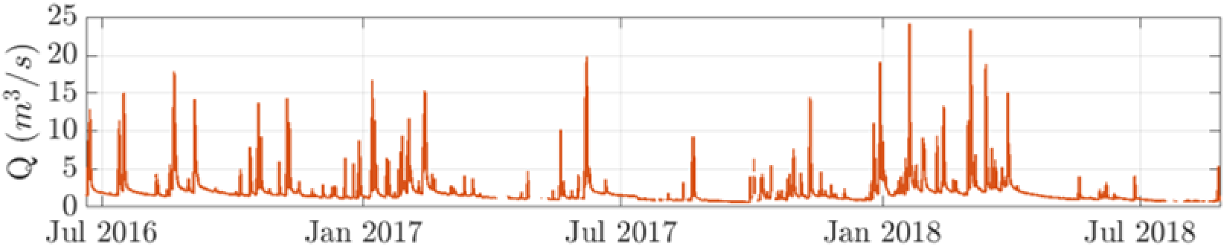

Figure 3.5.: Historical discharges for the main Inflow. Discharges measured at the station BR277 with 15-minutes resolution for the period July 2016 to August 2018.

Further measurements of the discharge of the Passaúna River at the BR277 were available for a high flow event which took place in October 2018. The first measurement was performed six hours before the event's peak being this of 5.4 m^3/s. The registered peak discharge was 15 m^3/s and after 18 hours the discharge returned to approximately the same first measured value. Notice that the mentioned high flow event is not well described in the simulated discharges by LARSIM-WT (see Figure 3.3), for this case the peak discharge was 5 m^3/s. The high flow event of January 2018 depicted in Figure 3.5, which exhibits a peak discharge of approx. 24 m^3/s is also suggested in the LARSIM-WT discharges but with a much lower magnitude of approx. 10.9 m^3/s. This should be entirely due to the daily temporal resolution of the latter.

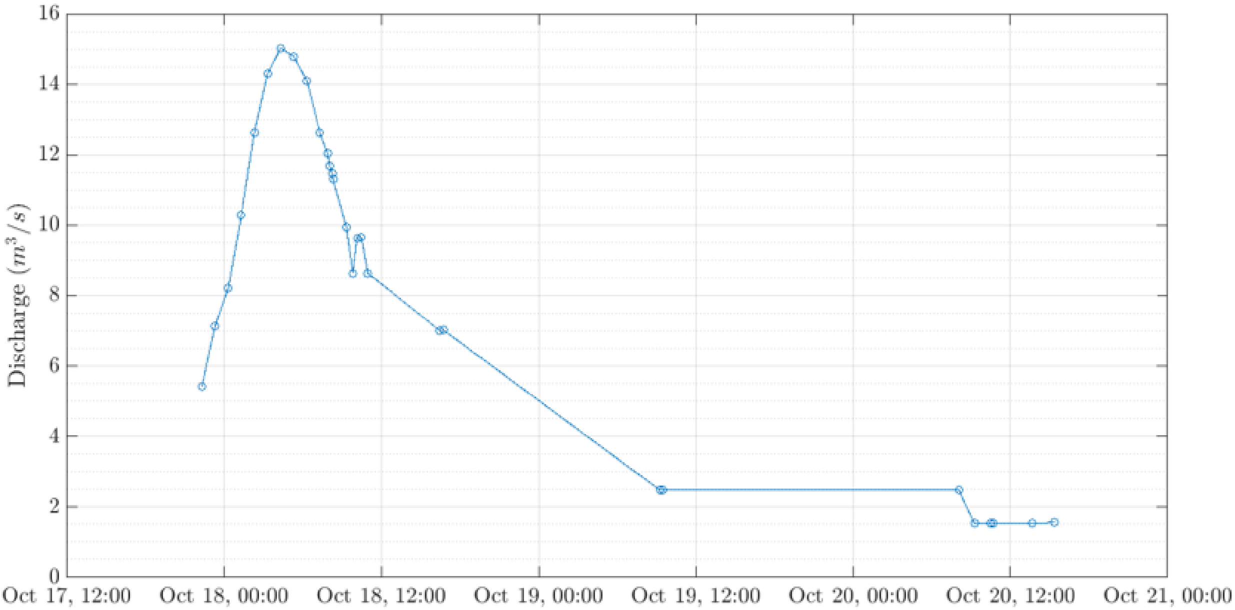

Figure 3.6.: Hydrograph of the high flow event on October 2018.

The storaged water leaves the reservoir through three outflows: the water Intake, the spillway or/and the bottom outlet (see Figure 3.1). The water Intake is located in the central part of the reservoir and allows for a mean withdrawal of 1.7 m^3/s (SANEPAR Companhia de Saneamento do Paraná, 2013) which are then conducted to the water treatment plant.

The bottom outlet guarantees a minimum discharge of around 0.4 m^3/s for the Passaúna River downstream of the dam, this minimal inflow is necessary to maintain the ecological equilibrium for the ecosystem downstream the reservoir. Figure 3.7 shows how the discharge of the withdrawal was under 2 m^3/s for the largest part of the studied period with two exceptions in June and November 2018, probably due to moments of high demand in the supplied population. Figure 3.7 also depicts the precipitation in mm/h at the meteorological station located at the dam. The highest precipitation registered was 2.3 mm/h with a representative mean value of 0.18 mm/h. The resolution of the precipitation and the outlet discharge is daily, meanwhile the data for the water withdrawal were available in a resolution of one hour.

Figure 3.8 describes the variation of the water level measured at the water Intake of the reservoir with a 30 minutes resolution. The dashed red line represents the position of the crest of the spillway, which is taken as a reference for the water level in the reservoir. In this sense, a negative value for this quantity means that the water level is below the spillway crest and a positive value means, that water is leaving the reservoir through the spillway. During the studied period the water level was most of the time below the spillway crest i.e. 76% of the time, for the 26th of December 2017 until the 13th of May 2018 was over the spillway crest. Before and during this period the magnitude of the precipitation was continuously higher than the mean value, which would cause the rise in the water level over the spillway, added to the fact that during the mentioned period the inflow discharges through the main inflow were mostly above the mean discharge (see Figure 3.3).

At the beginning of April 2018 the precipitation decreases and a larger discharge leaves the reservoir through the bottom outlet, this is reflected in the decreasing water level in the reservoir. Later in october the water level increases but the water entering the reservoir is not enough to fill the system and in consecuence the water level remains below the spillway crest.

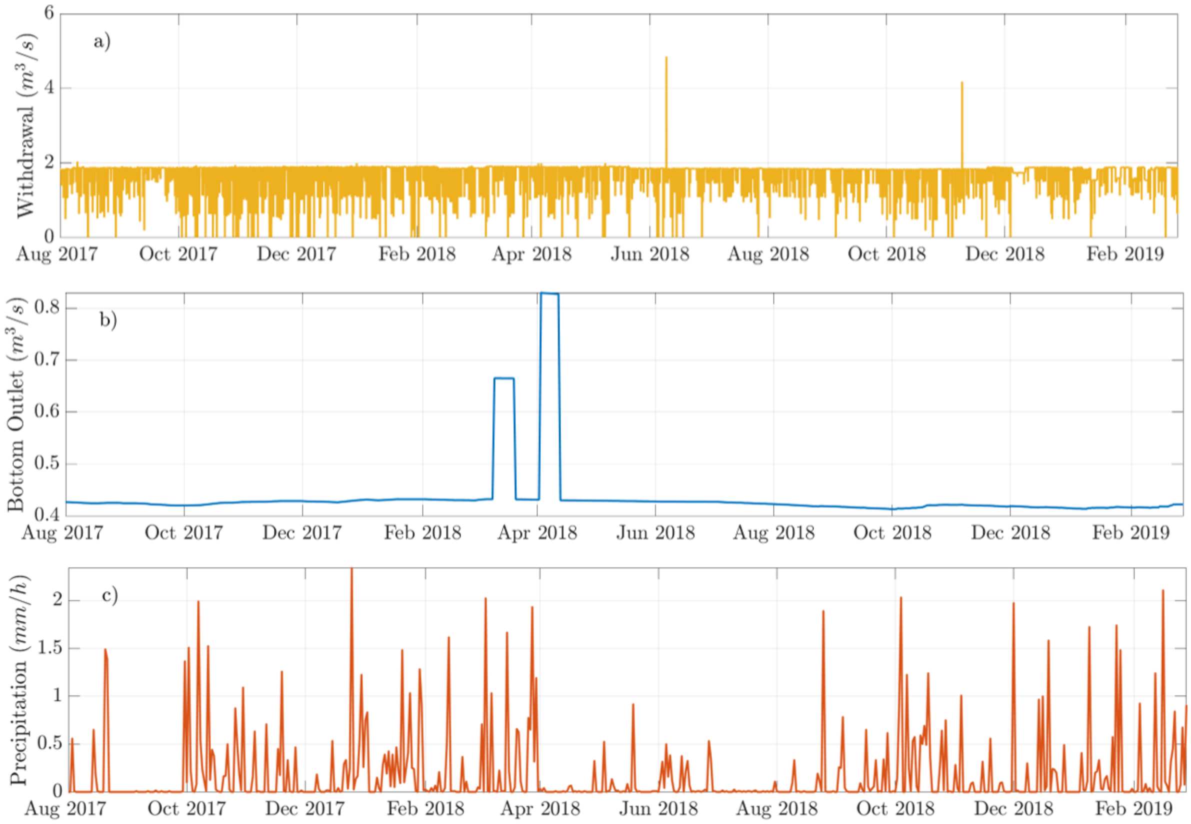

Figure 3.7.: Further Inflows and Outflows to the Passaúna Reservoir. Top: outflow through the water withdrawal. Middle: outflow through the bottom outlet. Bottom: precipitation at the meteorological station located at the dam.

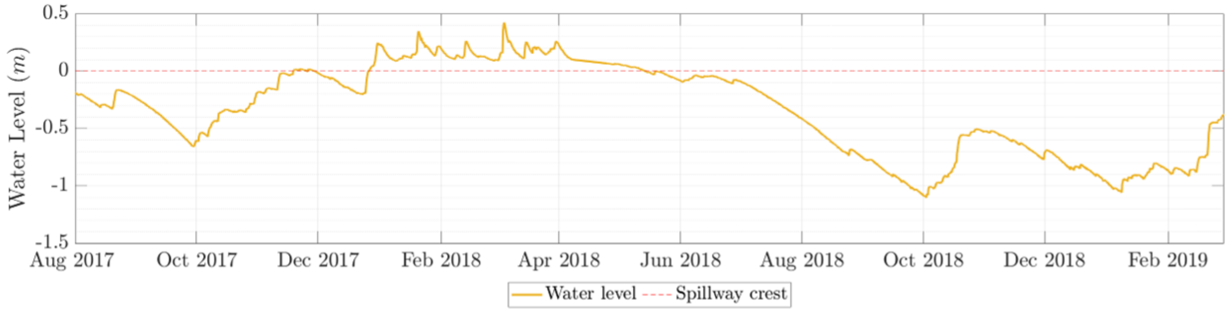

Figure 3.8.: Measured water level at the Passaúna Reservoir for the period August 2017 to February 2019.

3.2.2. Wind and Meteorological Data

Wind and meteorological factors can be an important boundary conditions for lakes and reservoirs. In contranst to rivers, reservoirs and lakes are low flow velocity systems, where the wind can exert shear stress at the water surface, which can enhance processes like internal mixing of the fluid. On the other hand, the meteorological conditions like humidity, air temperature and solar radiation are determinant factors in the heat exchange between the water column and the air, and hence conditioning the thermal stratification processes.

Figure 3.9 shows the wind direction, relative humidity, air temperature, cloud coverage and solar radiation for the period March 2018 to February 2019. Likewise, Figure 3.10 ilustrates the wind roses for the study area in order to complete the information about the wind parametrization, i.e. speed and direction. Notice that the analyzed period is shorter than the usual (August 2017-February 2019) this is not due to data availability. The reason for this is that the measurements of the water column stratification (see section 3.2.3) are restricted to the shorter period March 2018 to February 2019 and the analysis of the latter should be performed together with the meteorological data. For interested readers, Figures A.1 and A.2 in the Appendix section A show the meteorological parameters for the larger time period.

The wind velocity at the Passaúna Reservoir does not overpass the limit of 9 m/s with an average of 2 m/s. With the highest mean velocities during spring (2.2 m/s) and the lowest during fall (1.7 m/s). The prevailing seasonal wind directions are: northeast for fall, north for winter, east for spring and summer. The relative humidity presents a mean value of 78% with large variations even within the same meteorological season. The air temperature ranges between 2 and 35 $°C$. The average temperature varies between 16 and 24 $°C$ for the winter and summer respectively. The cloud coverage for the region presents a large variation with mean values between 25 and 75 % for fall and spring respectively. For summer the mean cloud coverage was of 65 % and hence higher than in winter (35%). The solar radiation reaches the value of 1630 W/m^2 in summer and shows as expected, the lowest magnitudes during winter. The temporal resolution of the data was as high as one minute for all the variables except for the cloud coverage, which resolution was of one day. For the present work, the resolution of the original meteorological data was reduced to 15 minutes in order to be used for the numerical model. In the mentioned Figures, the data are depicted with a 15-minutes resolution.

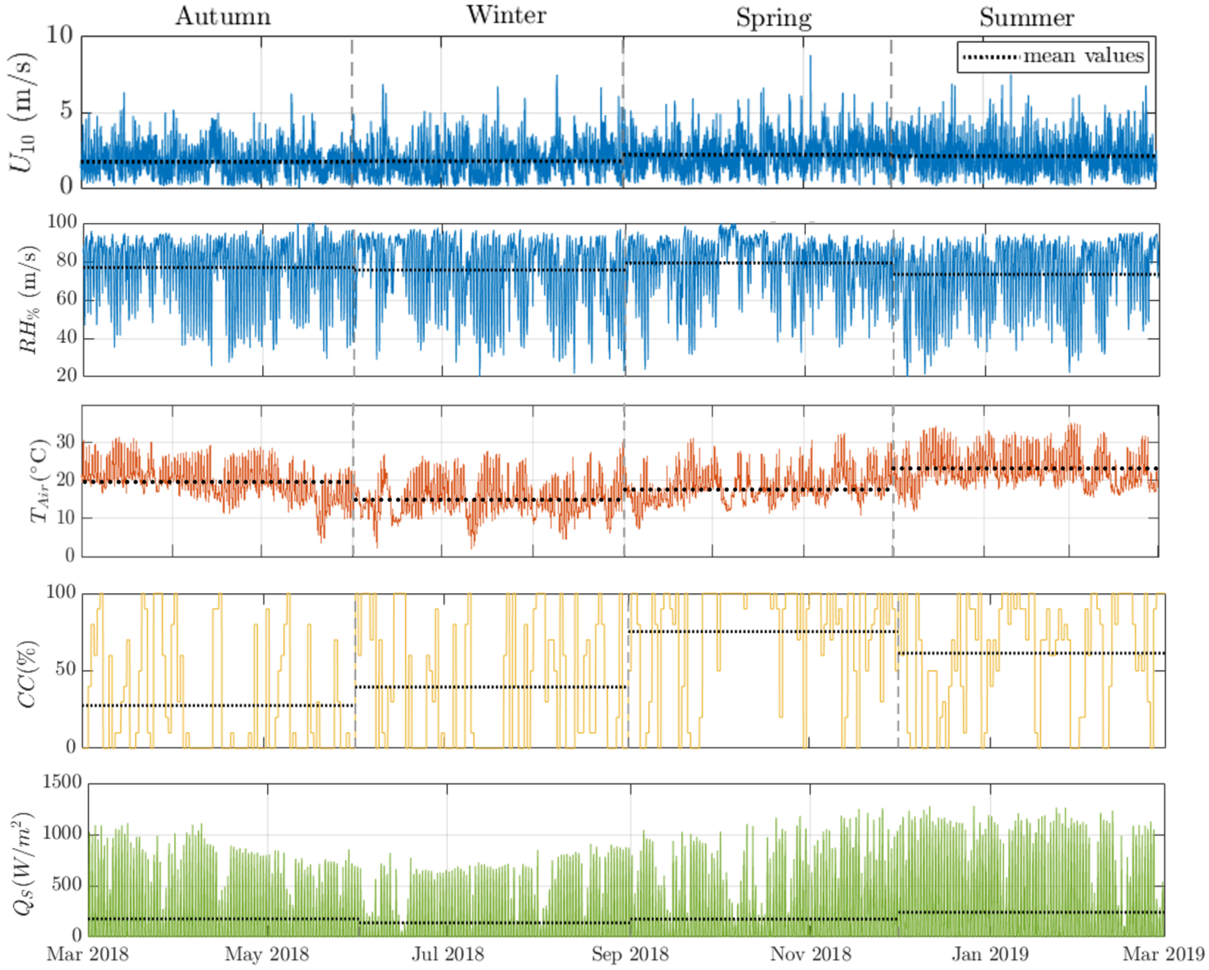

Figure 3.9.: Meteorological parameters for the period of interest March 2018 - February 2019.

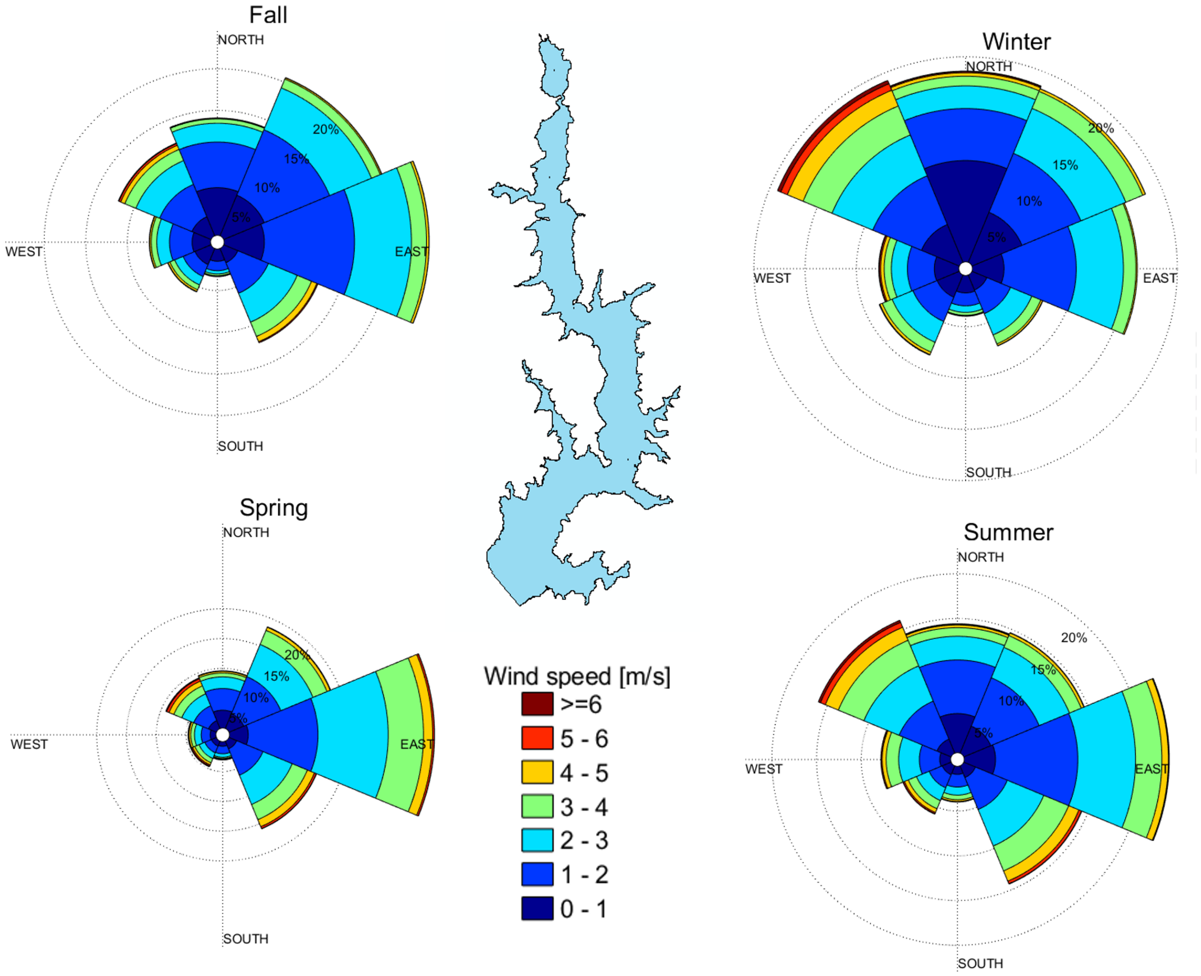

Figure 3.10.: Wind roses for the period of interest March 2018 - February 2019.

3.2.3. Temperature and Stratification Processes

In order to characterize the stratification of the reservoir is necessary to measure the temperature along the water column. In Passsaúna the water temperature was measured at eleven positions over the water column near the water Intake. Those measurements were available for the period March 2018 to February 2019 in an one minute resolution and were performed with a thermistor chain (Minilog-II-T, Vemco, ± 0.1 °C accuracy and 0.01 °C resolution). The result is the variation of the temperatures over a year as shown in the middle diagram of Figure 3.11. The logger 1 measured the temperature at one meter from the bottom of the water body and the logger 11 at the surface.

While analyzing the temperatures over the water column the reservoir was stratified at the end of summer and begin of autumn. In the middle of April the first overturn could be observed, followed by a new stratified phase. A second overturn started in the middle of May this time the reservoir remained mixed until mid-June where the reservoir stratified again, this time the water column presented a weaker stratification than during the first month of

Fall. This dynamic of mixing events followed by stratification periods was reapeated four further times during winter. Mid-August the reservoir stratified again and remained in this state with increasing temperature gradients (surface-bottom) towards spring and summer. This kind of behaviour is typical for polymictic lakes (Wetzel, 2001). Since the temperature in the water column in Pasaúna remains above 4 °C, the reservoir can be classified as warm polymictic (Wetzel, 2001). It can also be observed that the spring-summer stratification was accompanied by the highest wind speeds of the observed period, nevertheless the water column remained stable and no mixing was registered at the Intake position.

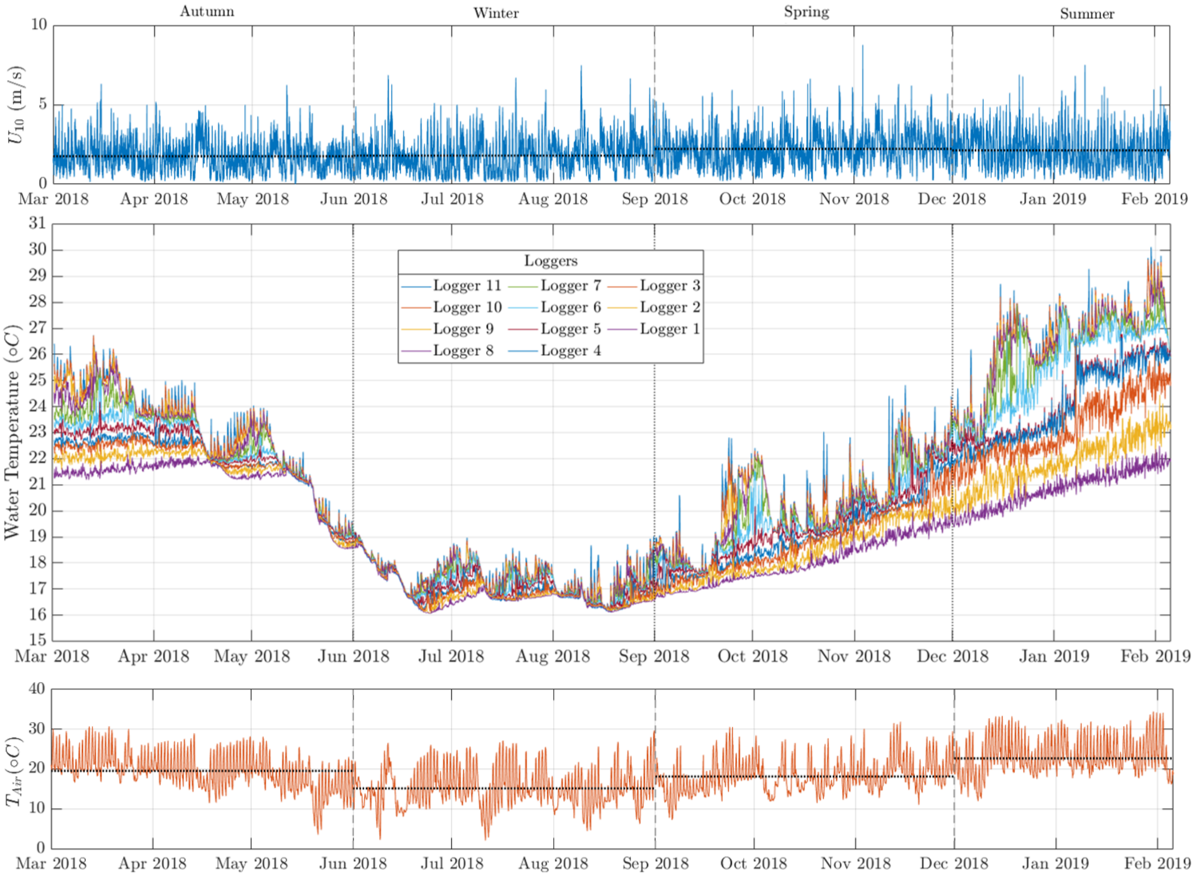

Figure 3.11.: Stratification at the Intake position for the period of interest March 2018 - February 2019. Top: wind speed. Center: water temperatures measured at the loggers of the thermistor chain. Bottom: air temperature.

Several variables can be calculated with the aim to characterize the vertical mixing and stratification processes in reservoirs. Within the framework of the present study the characteristic parameters buoyancy frequency N^2, Wedderburn Number W, Lake Number L_N and Schmidt stability S_t, were calculated employing the software Lake Analyzer (Read et al., 2011).

Through the analysis of the mentioned parameters, some conclusions about their meaning for the hydrodynamics of the reservoir can be made. In Figure 3.12 the temporal variation of the mentioned parameters can be observed for the same period as the measurements with the thermistor chain. This figure will be analyzed together with Figure 3.11. The loss of stratification which took place mid-april, is clearly reflected in the decrease of the Schmidt stability, the buoyancy frequency and the Weddeburn and Lake Number going both below one. All the analysed parameters again increased during May when the water body stratified again. Nevertheless, the stratification was not as strong as at the beginning of Autumn, as indicated by the Schimdt Stability. As it was already notice, during winter several stratification/mixing events occured. This is also described with the Lake and Weddeburn's Number droping below the unity. The stratification events were not as stable as at the beginning of Fall. The strenght of the stratification increases towards summer as evidenced by the Schmidt Stability. During the spring and summer the Lake and Weddeburn's Numbers also remained about their threshold value of one.

The first turnover in Fall is probably induced by periods of low air temperature (starting on April 13 to April 15 2017) and wind action. The increasing in the Schmidt stability, the Wedderburn and Lake Numbers after the first turnover is probabbly due to calm winds and an increasng air temperature.

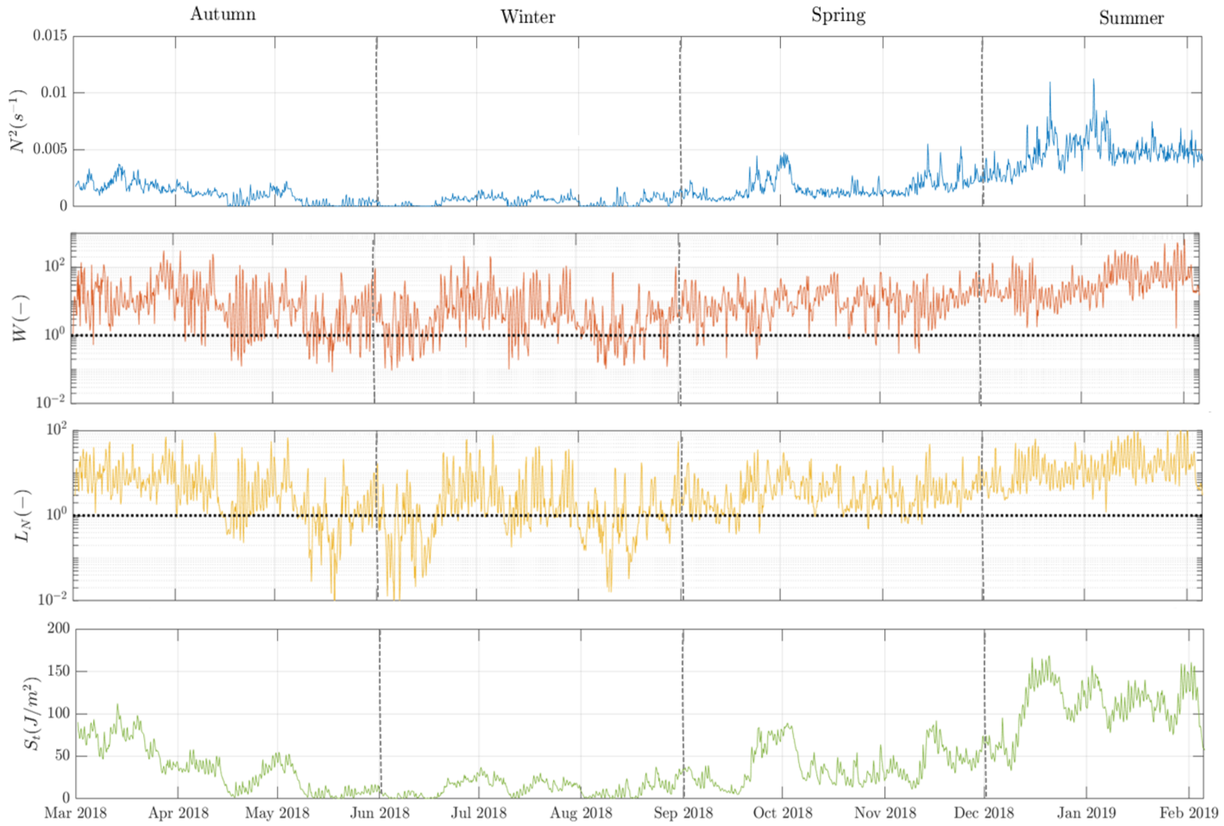

Figure 3.12.: Characteristic numbers for the stratification at the Intake position for the period of interest March 2018 - February 2019. From top to bottom: Buoyancy Frequency, Wedderburn's Number, Lake Number and Schmidt's Stability.

Another phenomenon which is partially conditioned by the temperature of water are the density currents. In this section the development of possible density currents due to temperature gradients is analysed. Figure 3.13 illustrates the magnitude of the water temperature at the main inflow of the reservoir, at the Ferraria Bridge, at the thermistor closest to the surface at the Intake and at the one closest to the bottom. The period analyzed correspond to the longest one for which measurements at the respective points were available. When comparing the temperatures of the infow and the FB it is clear, that the Buffer provides the place for the cold water from the river to become warmer, with the differences between the two temperatures getting smaller as the weather advances into winter. The diagram at the bottom of Figure 3.13 reveals that if the temperature at the main inflow is considered then the incoming water would mostly travel until te Intake as underflow. On the other hand, if the water temperature at the FB is considered, then overflows would be expected to occur, as the temperature at the FB goes over the surface temperature at the Intake. Similarly as the temperature is between the ones at the surfaceand the bottom of the reservoir, then interflows will take place. Finally, for the periods where the water temperature at the FB is below the temperature at the bottom of the Intake, a underfloww would be expected. The frequency of the three types of temperature-induced density currents taking place at the Passaúna Reservoir is depicted in Figure 3.14. The frequency refers to the different flows occuring during the span of day of measurements. The top of the figure shows that when considering the temperature at the FB the interflows dominate the picture followed by underflows. Overflows are also observed, specially during March and May, when the water reaching the FB is warmer than for later months. On the other hand, if the temperature of the main inflow is considered, then mostly exclusively underflows would be observed with a few interflows ocurring. Notice that the time span of the two diagrams is different, the reason is that the temperature logger at the position FB was removed at the beginning of August (illegal activities in the zone).

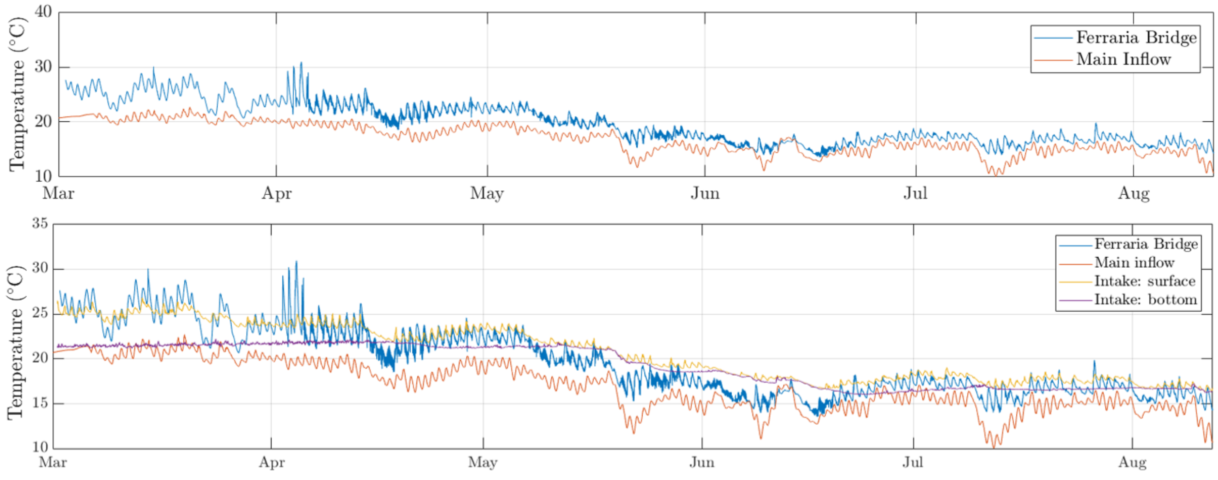

Figure 3.13.: Analysis of possible thermal induced density currents.

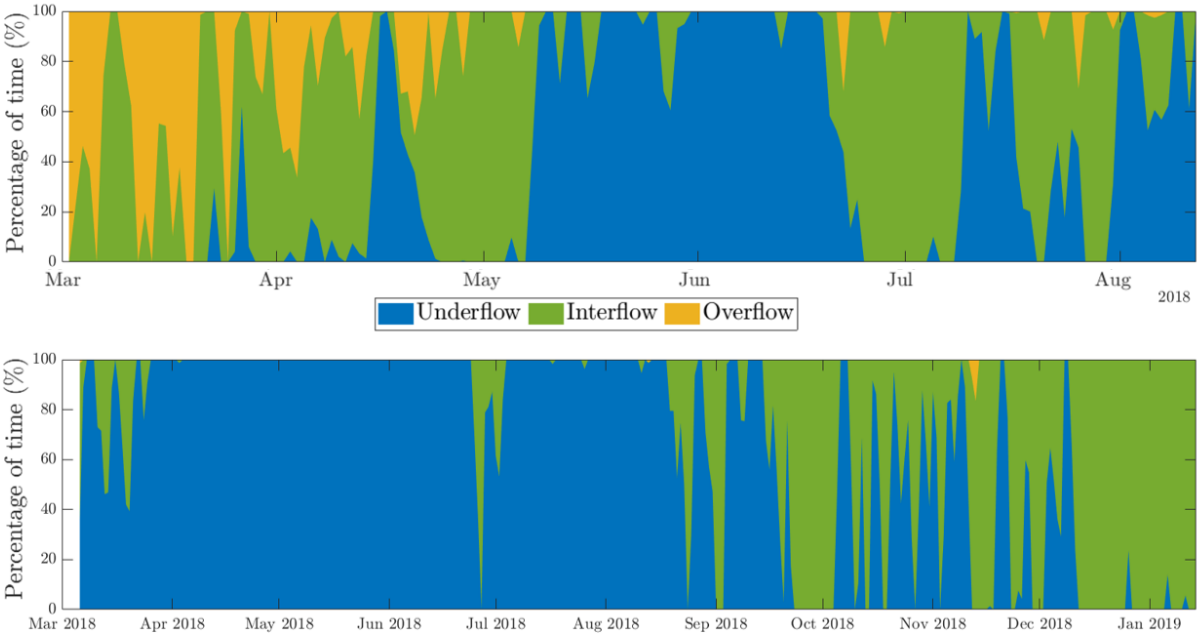

Figure 3.14.: Frequency of density currents. Top: based on the temperatures at Ferraria Bridge and the Intake. Bottom: based on the temperatures at the main inflow and at the Intake. Diagrams created by the author of the present dissertation based on Ishikawa et al. (2021).

3.2.4. Flow Velocity

Measurements of the horizontal flow velocity were carried out with an acoustic Doppler current profiler (ADCP Signature 1000, Nortek AS) deployed nearby the water Intake with a resolution of 10 minutes (for the period Feb 2018- March 2019) and 5 minutes (for the period June 2018 - February 2019) and a spatial resolution of 0.5 m in the water column.

Figure 3.15 illustrates the flow velocities at three depths. It can be observed that their magnitudes are the lowest at the bottom of the reservoir with the peaks taking place near the water surface. The highest measured velocity near the water surface was approximately 14 cm/s. Otherwise the flow velocities at the surface rarely overpassed the 10 cm/s. The most probable location for high flow velocities is near the water surface due to the action of wind, which is also observed in the figure. The velocities near the bottom sporadically overpassed the magnitude of 5 cm/s.

Figure 3.16 summarizes the information gathered by the adcp by time and depth-averaging the measurements of the horizontal flow velocity. In the left part of the figure, the time averaged velocities can be observed. Near the water surface a mean velocities of 2.7 cm/s with the lowest velocities appearing at the bottom of the water column with a mean magnitude of 1.2 cm/s. 75% of the velocities were under 3.4 cm/s and above 0.7 cm/s. Notice, that on average, the velocities are not strictly increasing towards the water surface. Between 2.7 a 9.2 m from the bottom the mean values of the velocities remained almost constant ranging from 1.9 to 2.2 cm/s. The depth averaged flow velocity over time presented a highest magnitude

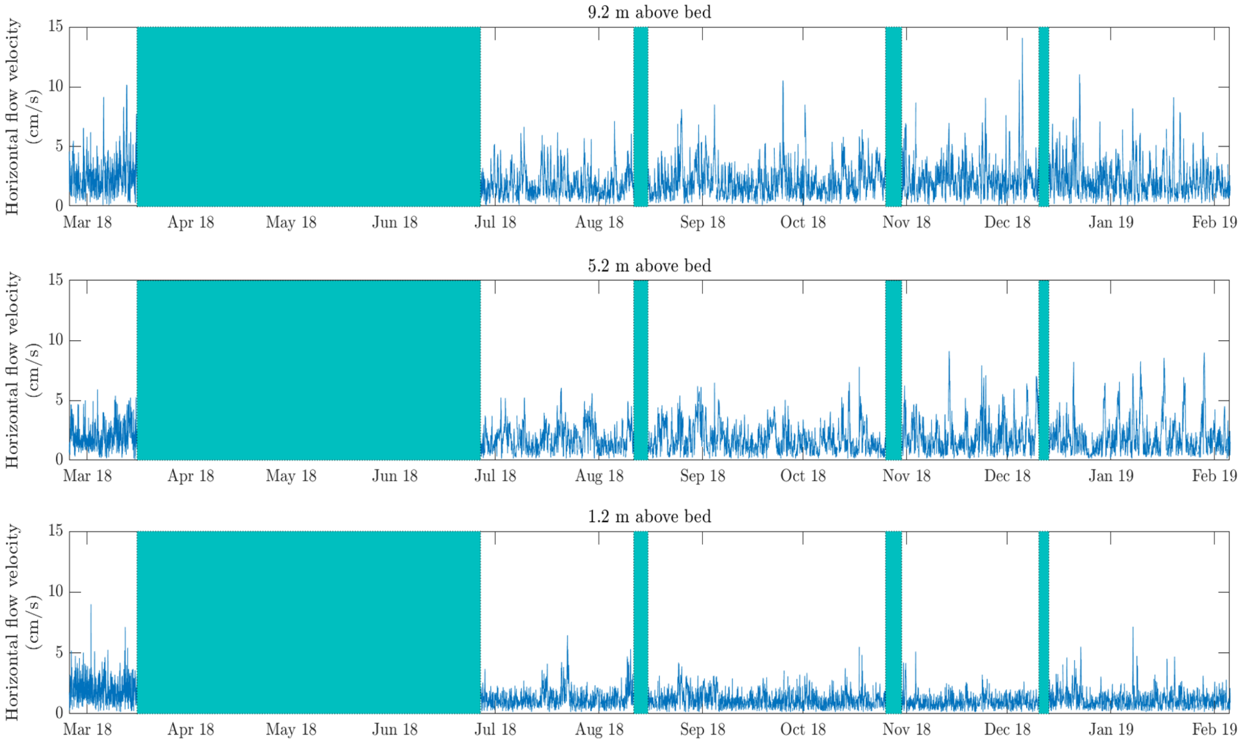

Figure 3.15.: Horizontal flow velocities registered at three diferent depths near the water Intake. The blue rectangles represent periods without data.

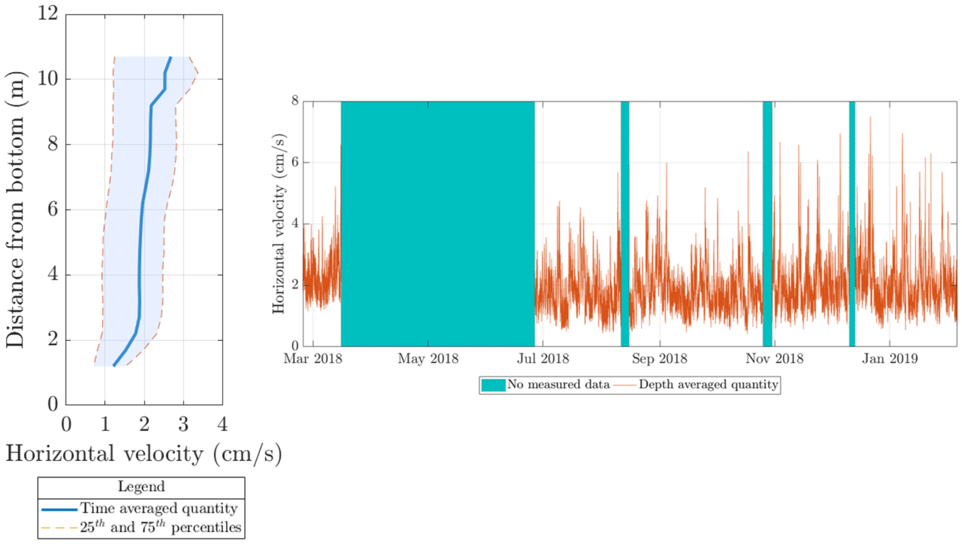

Figure 3.16.: Measured horizontal flow velocities. Left: time averaged horizontal flow velocities over depth. Right: depth averaged flow velocities over time.

of 7.8 cm/s and a lowest of 0.42 cm/s. The mean value of the depth averaged velocities for the system is of around 1.9 cm/s. This value could be taken as representative for the lacustrine zone of the Passaúna Reservoir

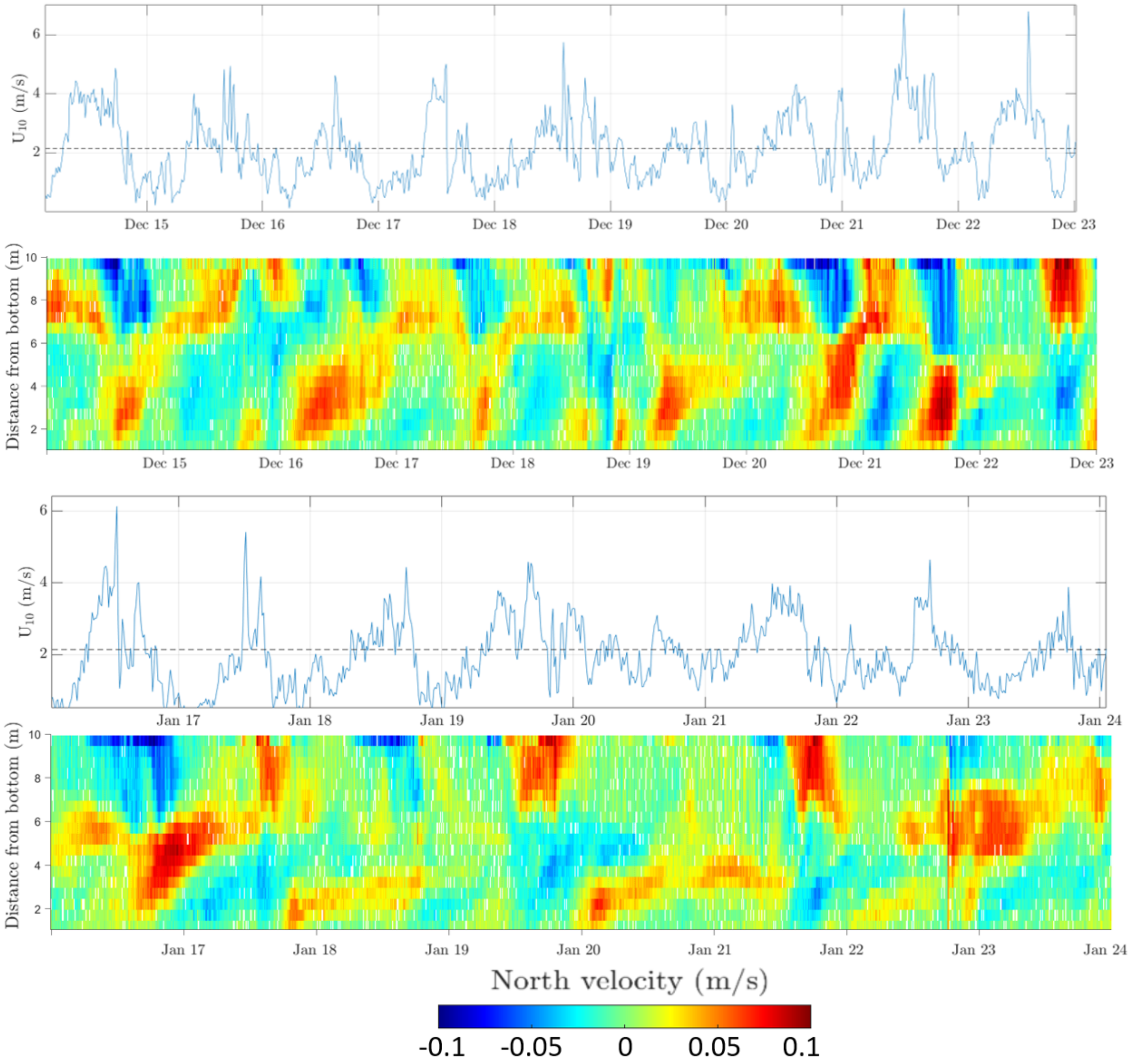

Figure 3.17.: Measured north component of the horizontal flow velocities at high resolution and relation to the wind velocity. Comment: flow velocity diagrams were created with a tool provided by Prof. Dr. Andreas Lorke within the frame of the MuDak-Project.

Until this point the velocities at the reservoir were analyzed in a rather discretized form, i.e. time and depth averaged (Figure 3.16) or over a few positions over depth (Figure 3.15). The reason for this is that when analyzing the whole time period of the measurements at all depths in one single diagram, it is difficult to extract important information. Figure 3.17 shows such a diagram, but for a shorter period of time and only for the north component of the horizontal velocity. This figure also includes the wind speed for the same periods of time. Notice, that for both periods showed, there were stratified conditions at the reservoir. It can be observed that the direction of the north component of the velocity changes along the depth for the same time instant, from flowing in the positive to the negative direction (e.g.:before December 15, December 21, January 17 and other time instants). Furthermore, it can also be observed, that peaks in the wind velocity happen simultaneously or immediately preceeding peak in the north velocity component (negative or positive direction).

In summary, the Passaúna Reservoir presented low flow velocities of around 2 cm/s at the water Intake. Velocity peaks at the water surface can be induced by wind. unfortunately, very little can be said about the flow velocity at other locations of the reservoir such as the Buffer, since no further measurements were performed.

Figure 3.18 shows the time averaged flow velocities for the mixed and stratified periods. In general for stratified conditions higher flow velocities were registered. It can also be noticed that the velocities for the mixed condition were more uniform over the depth in comparison to the stratified one. For the latter the horizontal velocities show a pronounced gradient towards the surface between 9 a 10 m above the bottom.

Unfortunately for the water body under study no measurements of the flow velocities at further positions were gathered, this means it will not be possible to analyse the velocites of shallower zones like the Buffer or the constriction at the Ferraria Bridge. The velocities at those shallow zones are presumably higher that at a position in the lacustrine zone like the Intake. Higher velocities than the measured at the Intake and their correspondig high bed shear stresses can generate erosion of the previously deposited material e.g. at the Buffer and account for deposition downstream of the bridge.

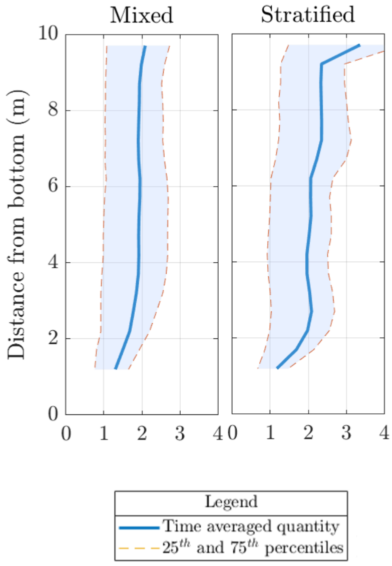

Figure 3.18.: Horizontal flow velocities for mixed and stratified period.

3.2.5. Secchi Depths

The secchi depth is a parameter necessary to represent the extinction of the sun radiation along the water column. Indirectly, is also a measure of the turbidity of water, since the clearer the water the further the light can penetrate the water column. Figure 3.19 illustrates the secchi depths measured at eight points in the reservoir for eight different dates. The highest registered value was 3.1 m on August 2018 the dam. This coincides with the fact that at the dam the lowest concentrations of suspended sediments should be expected due to the low flow velocities. It can be observed that for dates with measurements at different points in the reservoir, the secchi depths increase in the downstream direction. This is not the case for August and December 2018, where this variable increased suddenly at the position Ferraria Bridge. At this location the flow velocities are expected to be higher than at the Buffer, since it represents a constriction in the flow path. One possible explanation,

is the sedimentation of deposits during low flow periods and their later resuspension in the water column during higher discharges.
The light can penetrate further into the water column at the dam than at points upstream. A mean value of 2 m will be used within this work as a representative Secchi depth for the Passaúna Reservoir.

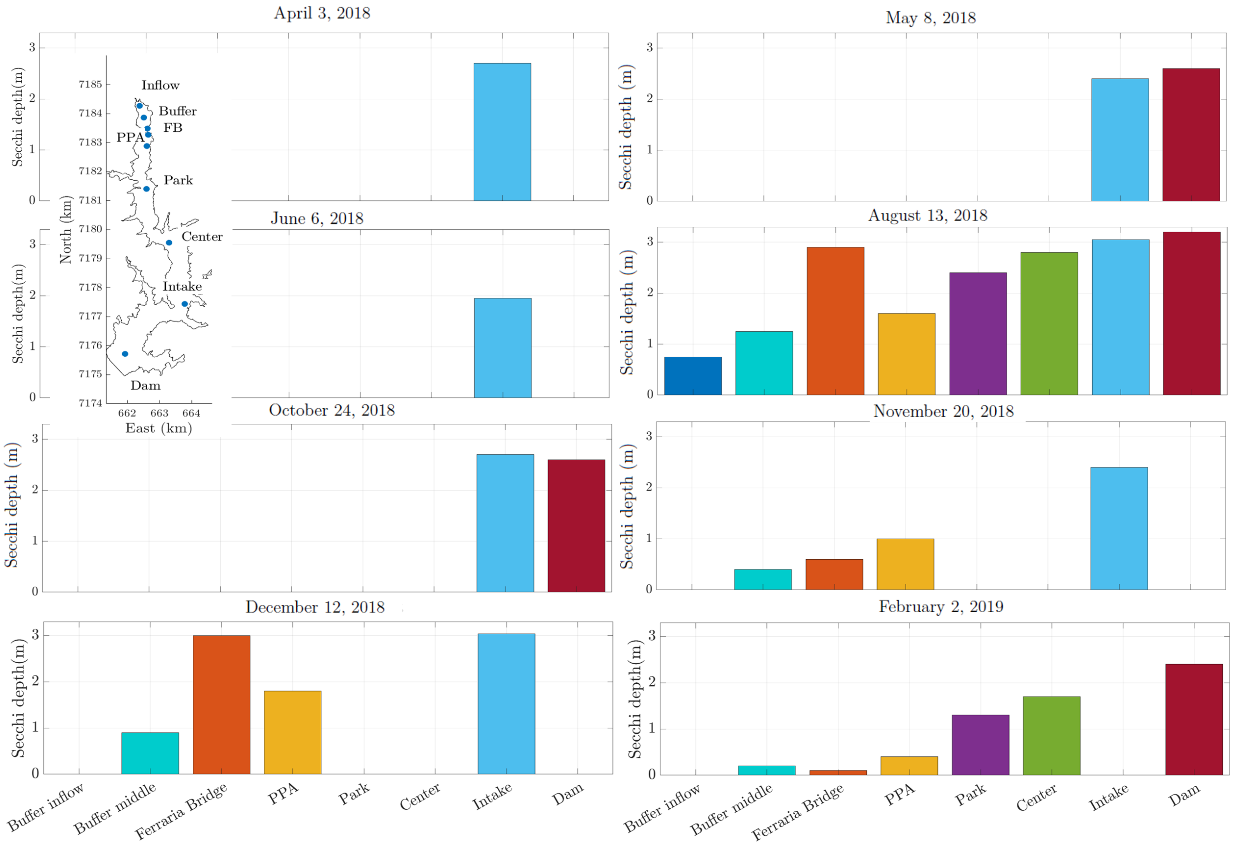

Figure 3.19.: Measured secchi depths along the longitudinal axis of the reservoir for several dates.

3.3. Characterization of the Suspended Sediment Transport

The description of the sediment transport in a water body requieres a large amount of data. From the incoming sediment loads to the grain diameter of the sediment are needed to have an idea of the morphological processes taking place in the reservoir. In the present section, the sediment-related data gathered within the field campaigns of the MuDak-Project are analysed.

3.3.1. Suspended Sediment Rating Curves

For the Passaúna Reservoir three different rating curves were available for analysis and implementation as input data for the numerical model. Rauen et al. 2017 built a rating curve based on data gathered at a monitoring station officially identified as 65021800, which is located approximately 2.3 km upstream of the main inflow of the reservoir (see Figure 3.20a) at the bridge over the Passaúna River at the highway BR277. In total 115 measurements of the SSC at the monitored cross section and the corresponding discharges were analyzed. The measurements were peformed between the years 1985 and 2015 and are a part of the data base of the Brazilian National Water Agency (ANA) and AGUASPARANA. Figure 3.20b displays the resulting rating curve as suspended sediment load, including the equation of the expoential relationship for the calculation of the load based on the discharge. This exponential-type of rating curve was adjusted based on the measured data set. In order to calculate the sediment loads, Rauen et al. 2017 multiplied the measured SSC by the measured discharges, taking into account the unit's consistency and considering an uniform distribution of the sediments over the cross section.

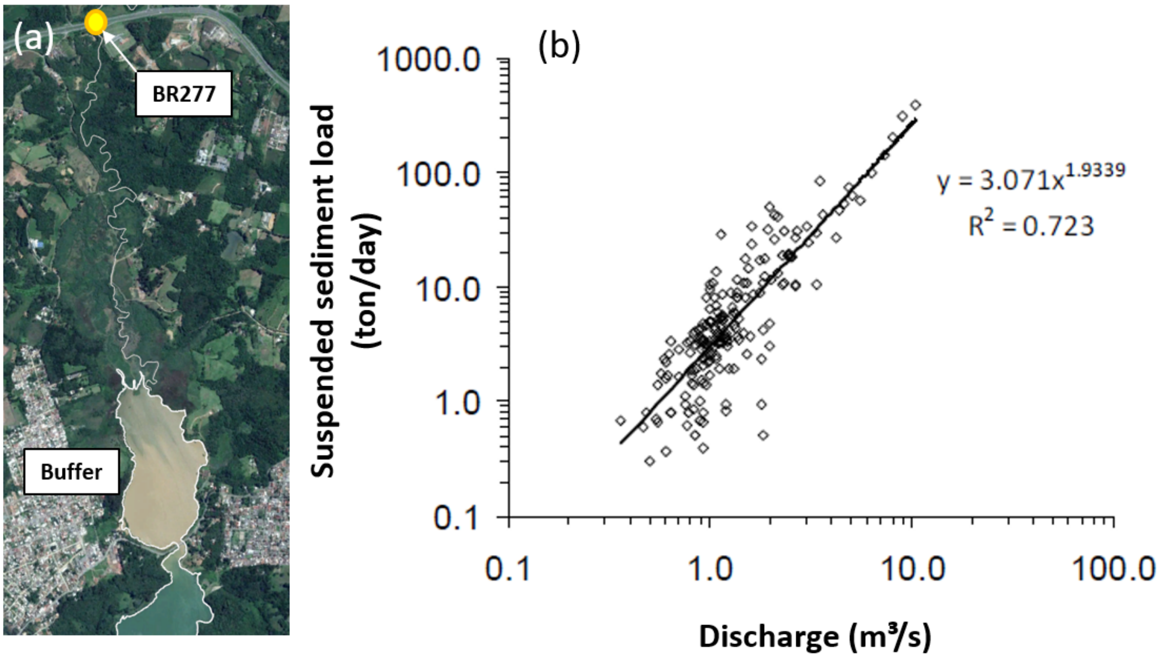

Figure 3.20.: Suspended sediment load at the monitoring station BR277 (a) as a function of the measured discharge and fitted rating curve equation (b) (adapted from Rauen et al. 2017).

In the analyzed data set composed by 115 measurements of SSC for 115 days in the previously mentioned period Rauen et al. 2017 found that the lowest and highest registered SSC were of ca. 5 mg/l and 294 mg/l. Also 50% of the concentrations were higher than 45 mg/l (50th percentile for the data set). The first and third quartiles for the measured SSC were respectively 26 mg/l and 75 mg/l.From this point on, the rating curve derived by

Rauen et al. 2017 will be named **RC1**. Using the adjusted equation for the suspended load by Rauen et al. 2017, which reads:

$$Q_{suspended} = 3.071 Q_{TGB154}^{1.9339} \tag{3.1}$$

where:

$Q_{suspended}$	Suspended sediment load	$[ton/day]$
Q_{TGB154}	Discharge at the main Inflow	$[m^3/s]$

and applying it to the discharges for the main inflow (see time series presented in the Figure 3.3), the SSC-time series for the modelling period presented in Figure 3.21 can be obtained. During this period the SSC varied between 22 and 332 mg/l with a mean value of 70 mg/l when applying the RC1.

The second rating curve available for the Reservoir will be denominated **RC2** and was derivated within the framework of studies of the MuDak-Project (MuDak-WRM, 2019). The data correspondig to the RC2 were gathered during a high-flow event in the Passaúna Catchment during October 2018. The SSC were measured at one point in the cross section at the station BR277 at different intervals during four consecutive days. Figure 3.23 displays the data gathered during the mentioned event and the equations for the RC2 derived by Wagner 2020.

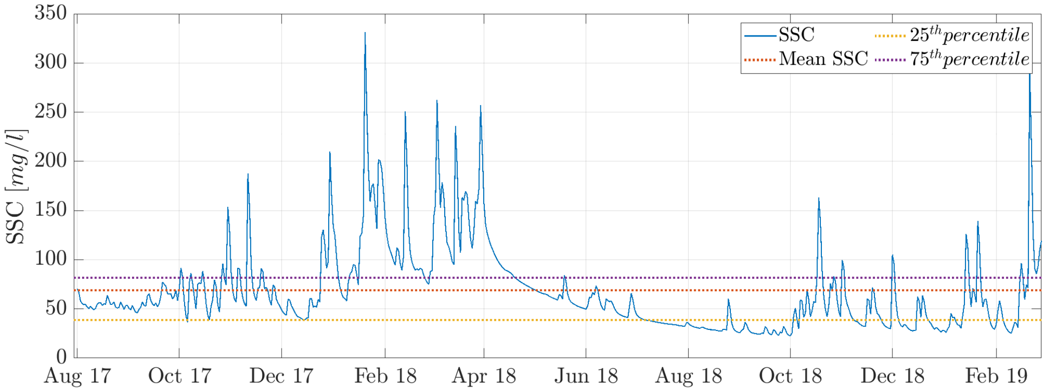

Figure 3.21.: Suspended sediment concentrations for the main inflow to the Passaúna Reservoir; TGB 154 for the period October 2017 - February 2019 according to the rating curve after Rauen et al. 2017.

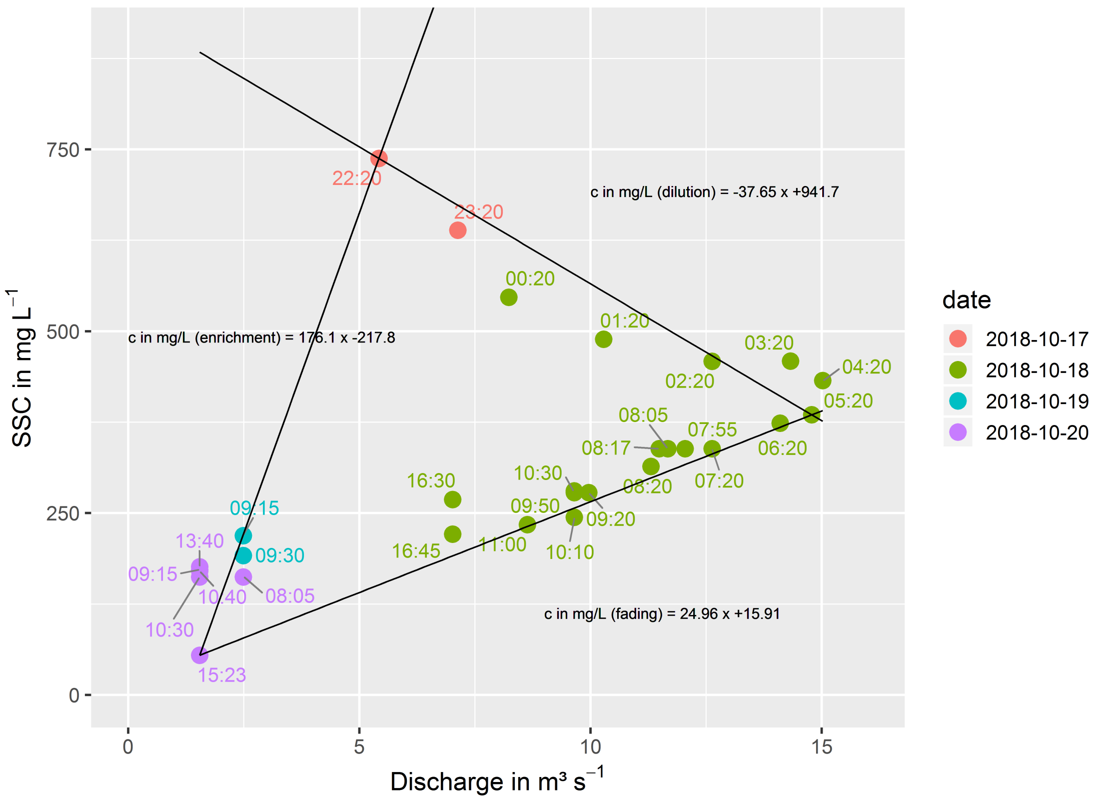

Figure 3.22.: Suspended sediment concentrations for the main inflow to the Passaúna Reservoir; TGB 154 as a function of the incoming water discharge during the high-flow event of October 2018 (Wagner, 2020).

The RC2 was described within the framework of the MuDak-Project (MuDak-WRM, 2019) through the following mathematical relations:

$$SSC\left(Q_{TGB154}\right) = \begin{cases} -37.65Q_{TGB154} + 941.7 & Dilution \\ 24.96Q_{TGB154} + 15.91 & Fading \\ 176.1Q_{TGB154} - 217.8 & Enrichment \end{cases} \tag{3.2}$$

The choice of which equation to use for a given case, depends on the magnitude of the Q_{TGB154} as follows:

- if $Q_{i-1} < Q_i < 5.4m^3/s$ then apply **enrichment curve-equation**.
- if $Q_{i-1} < Q_i > 5.4m^3/s$ then apply **dilution curve-equation** .
- if $Q_i > 15.2m^3/s$ then assume $SSC = 385mg/l$.
- otherwise apply **fading curve-equation**.

The application of equation 3.2 to the discharges of the main inflow during the simuation period delivers the following incoming concentrations into the reservoir:

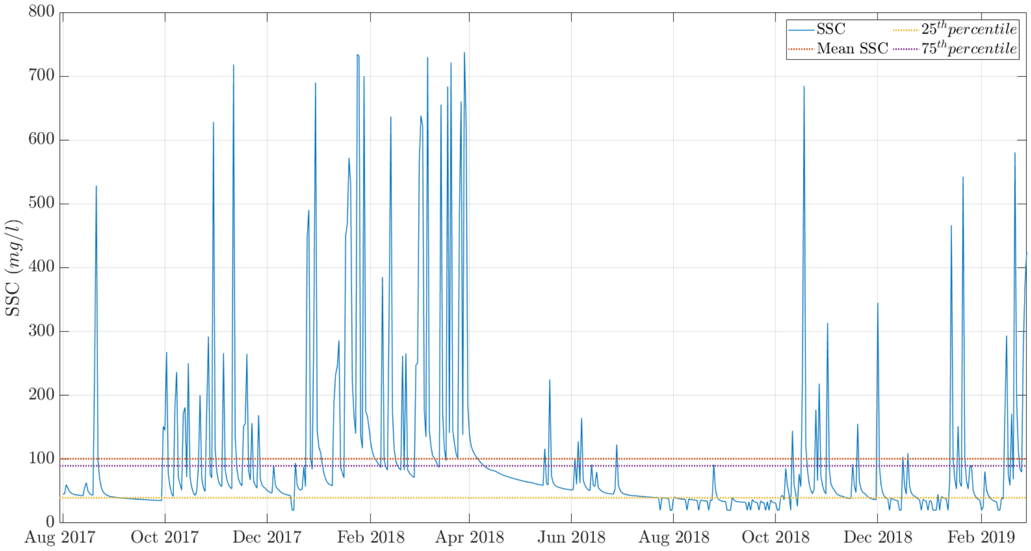

Figure 3.23.: Suspended sediment concentrations for the main inflow to the Passaúna Reservoir; TGB 154 for the period October 2017 - February 2019 according to the rating curve of the high-flow event of October 2018 after MuDak-WRM 2019.

The data showed in Figure 3.23 can be presented in a more traditional way (hydrograph and sedigraph) in order to better appreciate the development of the magnitudes of the water discharge and the suspended sediment concentrations as the high flow event starts and ends (see Figure 3.24). This rating curve shows clearly a clockwise hysteresis, since the SSCs are higher on the positive limb of the hydrograph than those on the falling limb for the same discharges (see section 2.2).

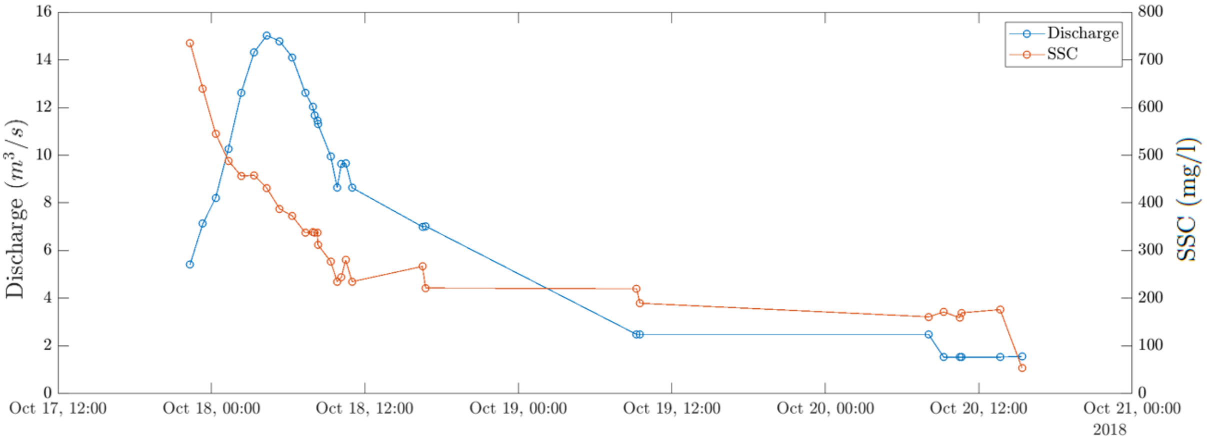

Figure 3.24.: Temporal variation of the suspended sediment concentrations and the water discharges for the main inflow to the Passaúna Reservoir during the high flow event of October 2018 after MuDak-WRM 2019.

The third description of the amount of suspended solids entering the reservoir as a function of the liquid discharge. **RC3** is based on the work of Sotiri 2020. Sotiri 2020 studied the sedimet input to the Passaúna Reservoir from the catchment via modelling based on the Revised Universal Soil Loss Equation (RUSLE)- method. The sediment loads are available in monthly time steps for the period May 2017 to July 2018. The sediment loads after Sotiri 2020 correspond to 99% fine sediments (i.e. $d \leq 64.3\mu\text{m}$). Through this approach the sediment loads are not calculated as a function of the discharge of the inflows. Nevertheless, in order to define the boundary conditions for the numerical model, the suspended sediment loads will be considered as a function of the temporal variation of the discharge at each inflow.

Figure 3.25 shows the sediment loads for the mentioned period at Inflow Passaúna River. The sediment loads for all the creeks and virtual inflows entering the reservoir were also calculated. The tributary apporting the highest sediment load is the Passaúna River as expected, with a total of 73.6% of the total sediment input to the reservoir, followed by the Ferraria River contributing with a 13.0% of the total sediment budget. Further important tributaries were TGB261 and TGB219 represeting 2.11% and 0.84% of the total sediment load entering the reservoir.

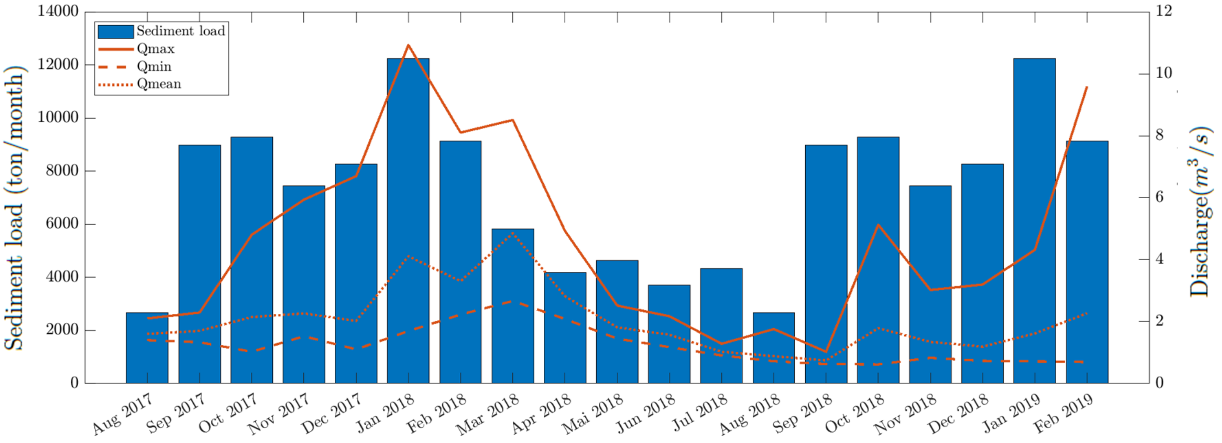

Figure 3.25.: Fine sediment loads calculated by Sotiri 2020 for the main inflow to the Passaúna Reservoir; TGB 154 using the RUSLE method and representative liquid discharge values for each month of the period October 2017 - February 2019.

For the calculation of the incoming SSC an non-uniform daily load distribution was adopted in function of the discharge. It was considered, that the mass of sediments entering the reservoir during one day was proportional to the volume of water entering the reservoir during the same day with respect to the volume of water flowing into the reservoir through one specific tributary for the whole month. Applying the expression 3.3, it is possible to find the constant SSC for each month based on the monthly load and the sum of the daily water discharges. Thus, the incoming SSC for every day of the month is constant, but the mass of solids entering the reservoir depends on the discharge.

$$SSC = \frac{Load * 10^6}{24 * 3600 * \sum Q_i} \tag{3.3}$$

where:

SSC	incoming suspended sediment concentration	$[mg/l]$
$Load$	Load for a determined month	$[ton/month]$
$\sum Q_i$	Sum of the discharges of each day of the month	$[m^3/s]$

Another way to perform this analysis would be to consider the sediment load to be equally distributed on each day of the month independently of the discharge. The first option seemed the most appropiate way to perform this analysis, since the others rating curves also showed a dependency of the SSC on the water discharge. When applying the **RC** to the modelling period, the monthly SSC depicted in Figure 3.26 are obtained.

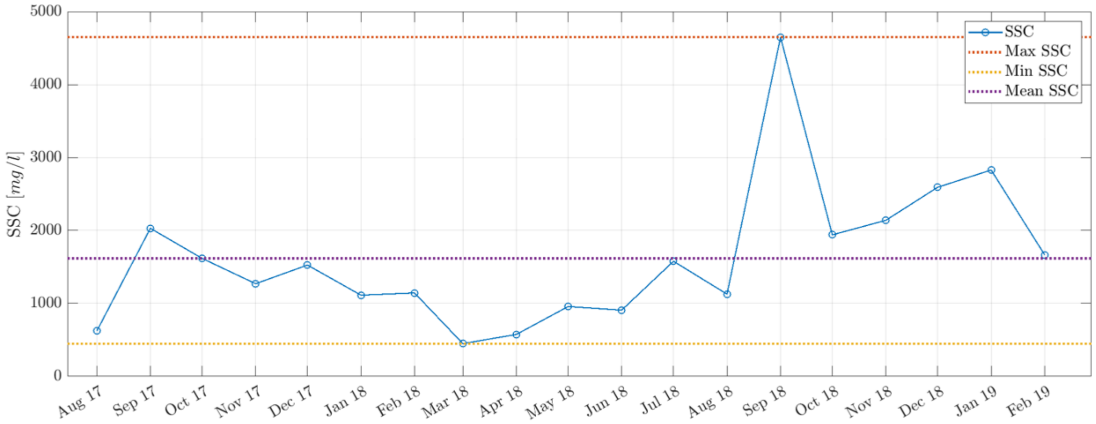

Figure 3.26.: Suspended sediment concentrations for the main inflow to the Passaúna Reservoir; TGB 154 for the period October 2017 - February 2019 according to the sediment loads modeled by Sotiri 2020.

Taking into account the SSC entering the reservoir through all 64 inflows and their respective daily water discharges, the sediment load mass transported by each rating curve during the 19 months of the simulation period can be calculated. Making use of the measurements of the dry bulk density found in the sediment cores (refer to section 3.3.4), the corresponding sediment volumes can be determined as: 11607, 20268 and 153425 m^3 for the curves RC1, RC2 and RC3 respectively.

The totally different SSCs and hence sediment load entering the reservoir when comparing the three rating curves reflect the relevance of the method used for the construction of them. The rating curve RC1 is based on daily values captured over a wide time period, this curve will probably not capture the high sediment amounts entering the reservoir during a high flow event. Hence is not surpirsing that the RC2 presented higher SSC, since it was constructed with data based on such an event. Also the measuring technique for the collection of samples maybe different for those rating curves, e.g. the location of the sample point in the cross section of the river. The SSC from the RC3 was developed with data from the catchment and further sources as satelite data, which represent further sources of uncertainty. The RC3 on the other hand, is based on erosive processes in the sub-catchments around the Passaúna Reservoir. Even though this is the main source of sediments for a stream (Vercruysse et al., 2017), all of the sediments eroded in the catchment may not even reach the water body due to lack of connectivity to the latter (Wagner, 2020; Vercruysse et al., 2017). The variability of the human activities in the catchment on different time scales are also to be taken as a further factor, which may cause discrepancies among rating curves predictions.

At this point it is important to keep in mind, that the RC1 and RC2 were derived based on measurements perfomed at the location BR277, which is 2.5 km away from the reservoir's main inflow. It is difficult to predict wether erosion or sedimentation processes do take place along this reach, since no measurements of the bed composition are available. Nevertheless, it is possible to affirm that no further tributaries are contributing to the sediment load being carried by the river until reaching the inflow. Another reasonable assumption is that sedimentation may occur caused by the reduction in the flow velocities due to the presence of the reservoir. Therefore, it can be hypothesized that the suspended sediment load reaching the reservoir will not be larger than the one measured at BR277.

3.3.2. Suspended Sediment Concentrations at the Passaúna Reservoir

Figures 3.27 to 3.30 present the SSC profiles along the depth, which were measured in the reservoir for time instants at 11 days in at least one location. Water samples were taken at specific depths and analyzed in the laboratory. The suspended solids correspond to the solid fraction retained after filtrating the sample using a filter with a pore size of $0.6 \mu m$.

For the 21th of february 2018 (Figure 3.27) the SSC pattern along the longitudinal axis of the reservoir can be observed. The highest concentration is found at the inflow ($19 mg/l$) from this point to the middle of the Buffer some of the suspended sediment settle reducing the measured SSC at the latter location. The SSC keep decreasing along the longitudinal axis until reaching the point park. Interesting to notice are the similar SSCs for the points PPA, PPB and Park even though the distance between PPA/PPB and Park is considerable. This would mean that either the the variations of the vertical velocity (turbulence) are large enough to keep the sediment in suspension or tributaries downstream of PPB and upstream of Park (e.g. the Ferraria River) deliver further sediment to the reservoir. At a depth of 3 m the SSCs in the profile at Park are the highest, not matching the clasical Rouse profile. A similar situation is presented at the point Center, but the SSC in the middle of the water column is eigth times higher than at the bottom. A possible explanation for this would be the transport of solids as interflow due to a temperature induced density current. Nevertheless, the CTD data (see Figure A.6)do not show any kind of interflow. The SSCs at the Intake and at the Dam are similar or even higher than the measured at Park, again suggesting possible further sources of suspended sediments after the point Park (e.g. the SAL).

On August 13, 2018 (see Figure 3.28) a further measurement campaign was carried out, the SSC along the longitudinal axis are in general lower (from 1 mg/l at the dam to max. 8 mg/l at the inflow) than the ones measured on February 21 of the same year. The liquid discharges through the main inflow are also higher for the latter day ($2.7 m^3/s$) than for the former ($0.8 m^3/s$). The SSCs are as expected increasing towards the reservoir bottom and decreasing along the longitudinal axis of the water body. The only unexpected profile is the one at PPA, which presents higher SSCs than at the Buffer.

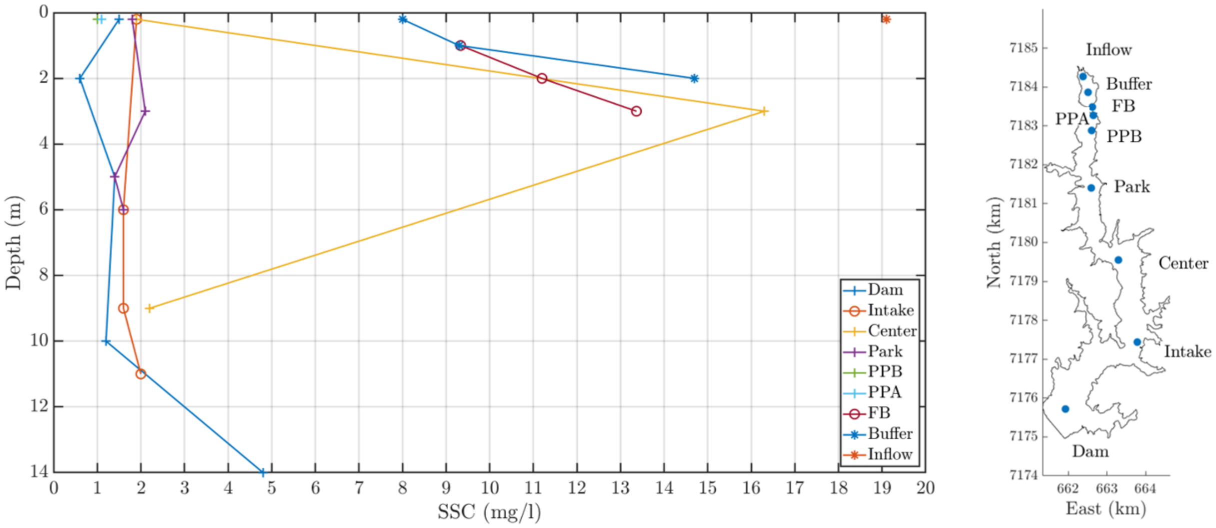

Figure 3.27.: Measured SSC-profiles at the Passaúna Reservoir on February 21, 2018.

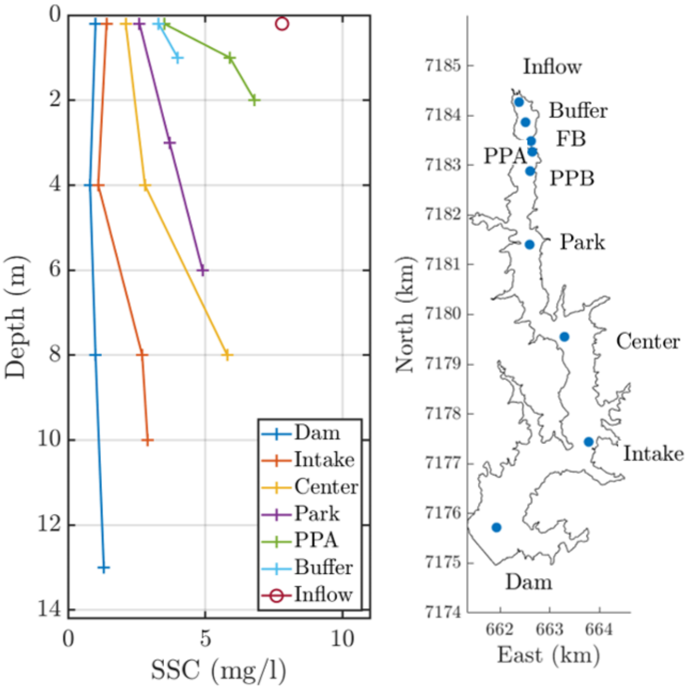

Figure 3.28.: Measured SSC-profiles at the Passaúna Reservoir on August 13, 2018.

On November 20, 2018 (see Fig 3.29) the measured SSCs decrease in the downstream direction until the point PPA. At the bottom of the Intake the registered concentration were 4.5 times larger than at the Buffer. This could be the result of a high amount of further sediments entering the reservoir through other inflow(s) different from the main one. It would imply that a further tributary can temporaly assume the role of main sediment source for the reservoir. An additional explanation would be the resuspension of previously deposited fine sediments and the consequent high SSCs.

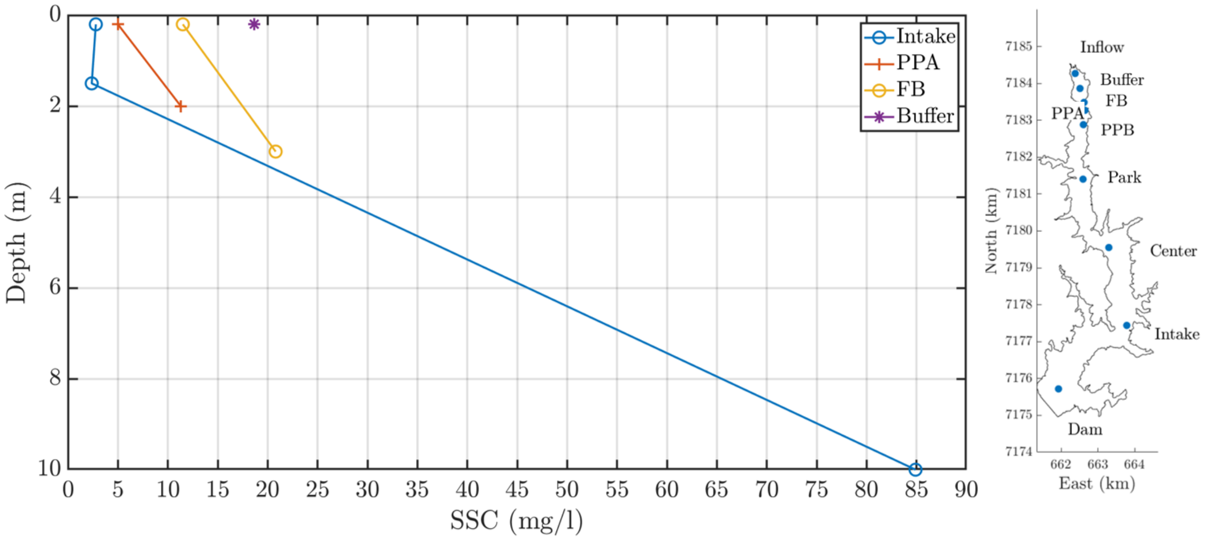

Figure 3.29.: Measured SSC-profiles at the Passaúna Reservoir on November 20, 2018.

On the 5th of February 2019 (see Figure 3.30) the highest SSC at the reservoir's inflow were registered ($52mg/l$) regarding all the measurements campaigns. Even though the discharge at the TGB154 ($1.12m^3/s$) is not the highest among the different dates studied. The SSC profiles for this date show several peculiarities. The concentrations at the Ferraria Bridge (FB) are higher than at the Buffer and even higher than at the inflow. This could be explained by erosion of previously deposited materials in the Buffer region. After the Ferraria Bridge the SSCs decrease in comparison with the northern region of the reservoir. Interestingly, the concentrations for the positions Park, Center and Intake are on the same range (between 3.9 and 8 mg/l) without an obvious tendency. Similar to the measurements of February of the previous year, at the position Center the highest SCSs are not to be found at the bottom but again at around $3m$ depth. A comparable trend is observed at the point Intake, but it is not further observed downstream,i.e. at the position Dam. It seems that the suspended solids are being trasported in this reach by an interflow plume. Interesting to notice, the SSC at the bottom of the dam are higher than at the last three upstream positions, which could be caused by sources of suspended sediments downstream of the Intake e.g. the SAL or source provenient from bank erosion.

Figure A.4 in the appendix section shows the SSCs for seven dates for which measurements were only performed at the positions Ferraria Bridge (FB)or at the Intake, this measurements unfortunately do not allow to make any deductions for the SSCs along the reservoir.

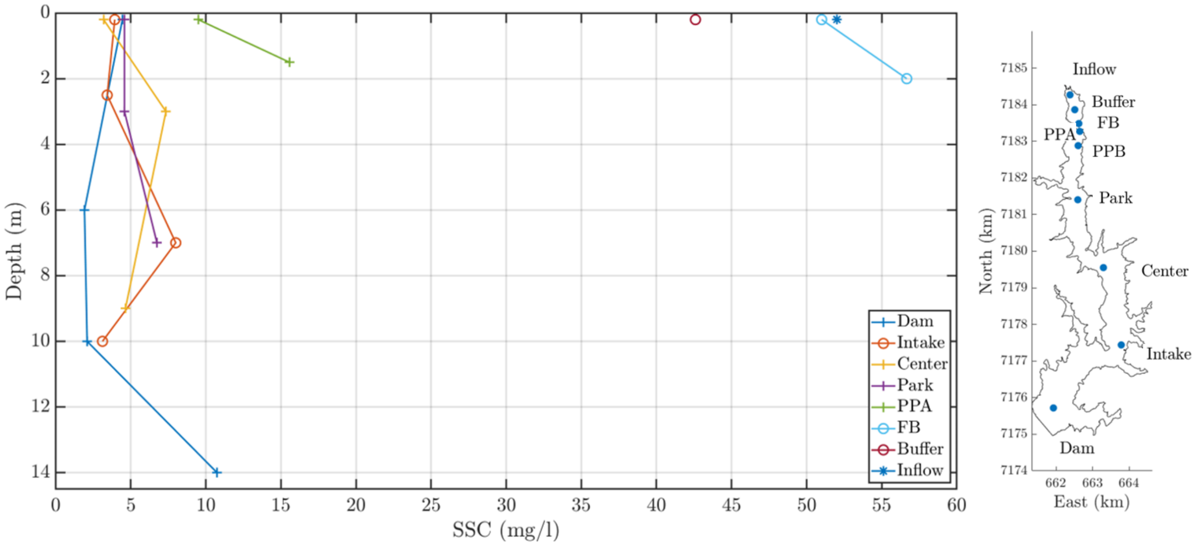

Figure 3.30.: Measured SSC-profiles at the Passaúna Reservoir on February 5, 2019.

Table 3.1 shows a comparison of the measured SSC at the inflow of the reservoir and the concentrations predicted by the three sediment rating curves studied in section 3.3.1. The predictions of the RC1 and RC2 were similar for all three dates and they approximate the measured value the most on the 5th of February, 2019. The predictions' quality of both rating curves for the first two dates is rather poor and is more than 4 times higher as the measured value. Important to keep in mind, is the fact that the rating curves RC1 and RC2 were developed with data coming from BR277 and not the inflow of the water body. Hence, some divergences between the SSCs at these two locations should not be surprising.

Table 3.1.: Comparison of the measured SSC at the reservoir's inflow and the predicted concentrations by the rating curves.

Date	SSC measured (mg/l)	RC1 (mg/l)	RC2 (mg/l)	RC3 (mg/l)	Q_{TGB154} (m^3/s)
21.02.2018	19.1	82.9	89.3	1142	2.7
20.11.2018	18.7	36.2	29.3	1126	0.8
05.02.2019	52	44	39.7	1665	1.1

Within the framework of the MuDak-Project, further measurements of the SSCs were performed making use of an Acoustic Doppler Current Profiler or ADCP (ADP-M9 Sontek-Xylem) calibrated through the actual SSCs determined in the laboratory from water samples (MuDak-WRM, 2019; Wosiacki, 2020). Measurements of the SSCs at the cross section of the Ferraria Bridge and at the longitudinal axis of the reservoir (from the Buffer until approximately 600 m downstream of the PPA) were performed. For further information on the calibration procedure of the ADCP-device as a surrigate technology for measuring SSCs it is advised to consult Wosiacki 2020. Figure 3.31 ilustrates the SSCs over the cross section at the Ferraria Bridge and over a longitudinal transect covering from the Buffer position to

500 m downstream of the PPA. These measurements were performed on the 21th of February 2018. The numbers in the profiles refer to SSCs at the indicated points. The position Ferraria Bridge presented a rather uniform SSCs distribution with a slight increase of the concentrations over the depth. After the Ferraria Bridge the longitudinal profile shows a sediment plume traveling along the bottom of the reservoir until it reaches a position of around 400 m downstream of the FB and the SSCs get more uniform over the water column. This sediment plume would remind the reader of a turbidity current, nevertheless the SSCs are very low (max. 50 mg/l) in order to talk about such a process. Besides these high concentrations are not observed at the cross-section of the FB. Notice, that the longitudinal transects did not follow the thalweg in the Buffer. It is important to remember that density currents being a gravity-driven flow, they follow the deepest part of the cross section, i.e. the thalweg (Morris and Fan, 1998). This could be the reason why the SSCs in the Buffer are shown to be lower than after the FB in the Figure 3.31. A further explanation would be the existence of a temperature induced density current, underflow in this case, which also induced the water-laden sediment to move along the bottom of the reservoir. Indeed, Figure A.6 in the Appendix section shows the existence of an underflow between the FB and the PPA positions. The observed sediment plume could also simply means that the vertical turbulence in the reservoir was low enough for the settling processes to be dominant over it, i.e. the Rouse number for the vertical profiles would be larger than the unity. The resuspension of previously deposited fine sediments could be also responsible for the high SSC measured at the bottom of the reservoir. A similar situation is showed in the Figure 3.34, but in this case the SSCs reached higher magnitudes up to 100 mg/l.

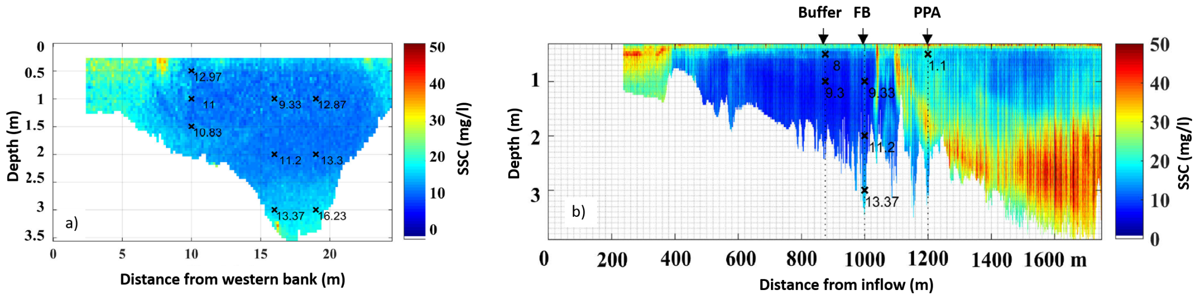

Figure 3.31.: Measured SSC-cross sectional at the Ferraria Bridge(a) and longitudinal profile (b) between the Buffer and 500 m downstream of PPA on February 21, 2018 (adapted from Wosiacki 2020).

Figue 3.32 ilustrates the SSCs at the cross sections of the BR277 and the FB measured during the peak of the high flow event of October 2018 (see Figure 3.24). For both cross sections, the SSCs are higher towards the bed of the river and reservoir respectively. For a high flow event, it would be expected, at least at the river cross-section, that the suspended sediments would be equally distributed over the depht. This is clearly not the case for the situation presented in the mentioned Figures. The cross seciton at the FB seems to depict a typical turbidity current travelling at the bottom of the reservoir, unfortunately no longitudinal profiles were measured during this event. The magnitude of the SSCs during these day are the highest measured in the Passáuna reservoir, reaching the 200 mg/l in the lower part of the water column at the FB. Two days after the peak of the event, the SSCs were measured again (see Figure 3.33). The SSCs were much lower than during the peak of the event, reflecting the behaviour of the sedigraph depicted in Figure 3.24.

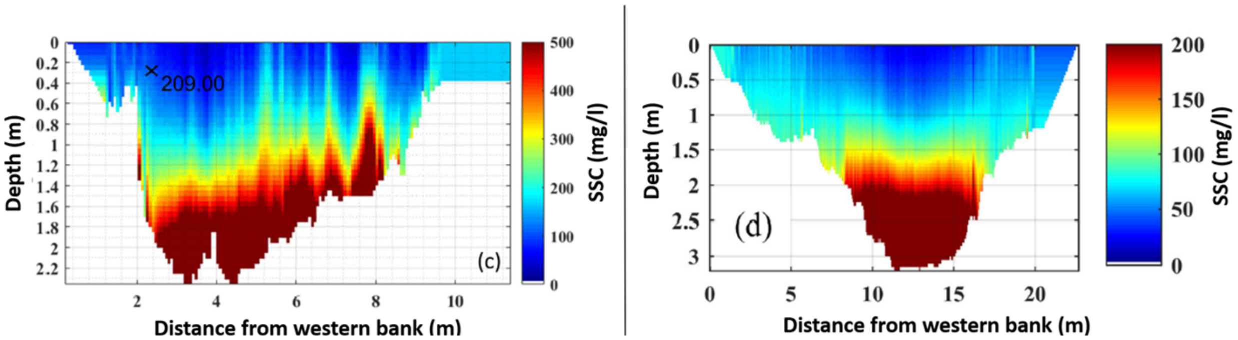

Figure 3.32.: Measured SSC-cross sectional profiles in the Passaúna catchment at the positions BR277 (a) and Ferraria Bridge (b) on October 18, 2018 (adapted from Wosiacki 2020).

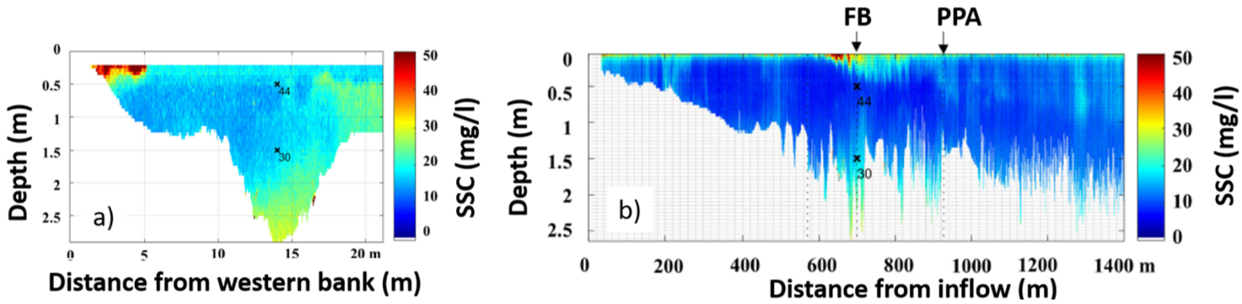

Figure 3.33.: Measured SSC-cross sectional at the Ferraria Bridge (a) and longitudinal profile (b) between the Buffer and 500 m downstream of PPA on October 20, 2018 (adapted from Wosiacki 2020).

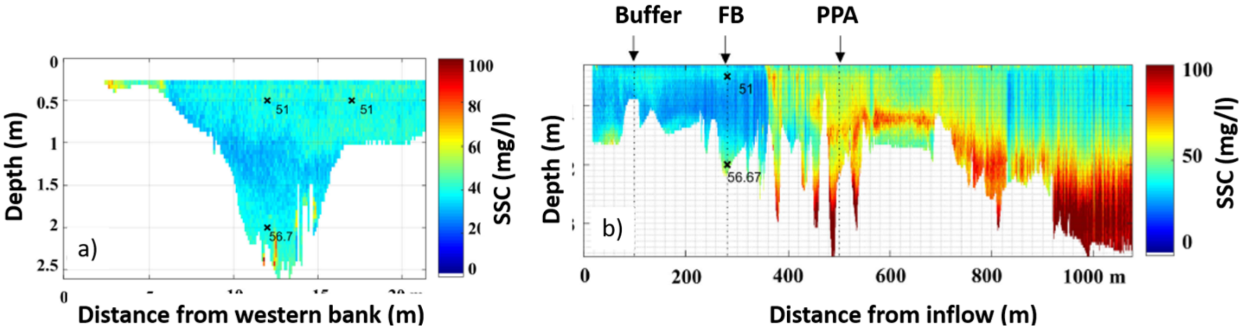

Figure 3.34.: Measured SSC-cross sectional at the Ferraria Bridge(a) and longitudinal profile between the Buffer and 500m downstream of PPA on February 5, 2019 (adapted from Wosiacki 2020).

3.3.3. Particle Size Distribution of the Sediments

Measurements of the particle size distribution (PSD) of the suspended sediment were performed at BR277 and at the Buffer (Wosiacki, 2020). At each cross section up to three verticals were selected and along them, several water probes were sampled and studied in the laboratory in order to obtain the PSDs. The results are depicted in the Figures 3.35 to 3.37 for the Buffer and 3.38 to 3.39 for the BR277. The circles in the cross sections represent the approximate location from where the probes were taken. The numbers nearby the circles represent the D50s of each suspended sediment sample.

All the samples reflect a common fact: the sediments found in suspension both in the river and in the reservoir had diameters between 1 μm and 0.5 mm i.e. in the range of clay to fine sand. Nevertheless, it is possible that some of the sediments in the range of sand are actually flocs built by finer grains, since the sediments found at the bottom of the reservoir are rather fine and muddy (refer to section 3.3.4 for details).

For the measurements performed at the FB the mean D_{50} for the cross section were 49.8, 22.2 and 18.7 μm with standard deviations of 8.3, 11.8 and 6.8 μm for August 14 2018, October 20 2018 and February 2 2019 respectively. For these dates the mean discharges through the main inflow were 0.8, 3 and 1.1 m^3/s respectively. The highest variability is presented by the measurements in October 2018 two days after the peak of the high flow event and the highest D_{50} was obtained during the day with the lowest discharge. Again, this could be a product of flocculation processes, since during events with low discharges the shear stresses trying to destroy the flocs are lower in comparison to turbulent conditions which are often given during high flow events. After the high flow event (see Figure 3.36) coarser sediments were found in the upper part of the water column, meanwhile for the other two measurement campaigns at the FB the size of the sediments across the section were rather uniform.

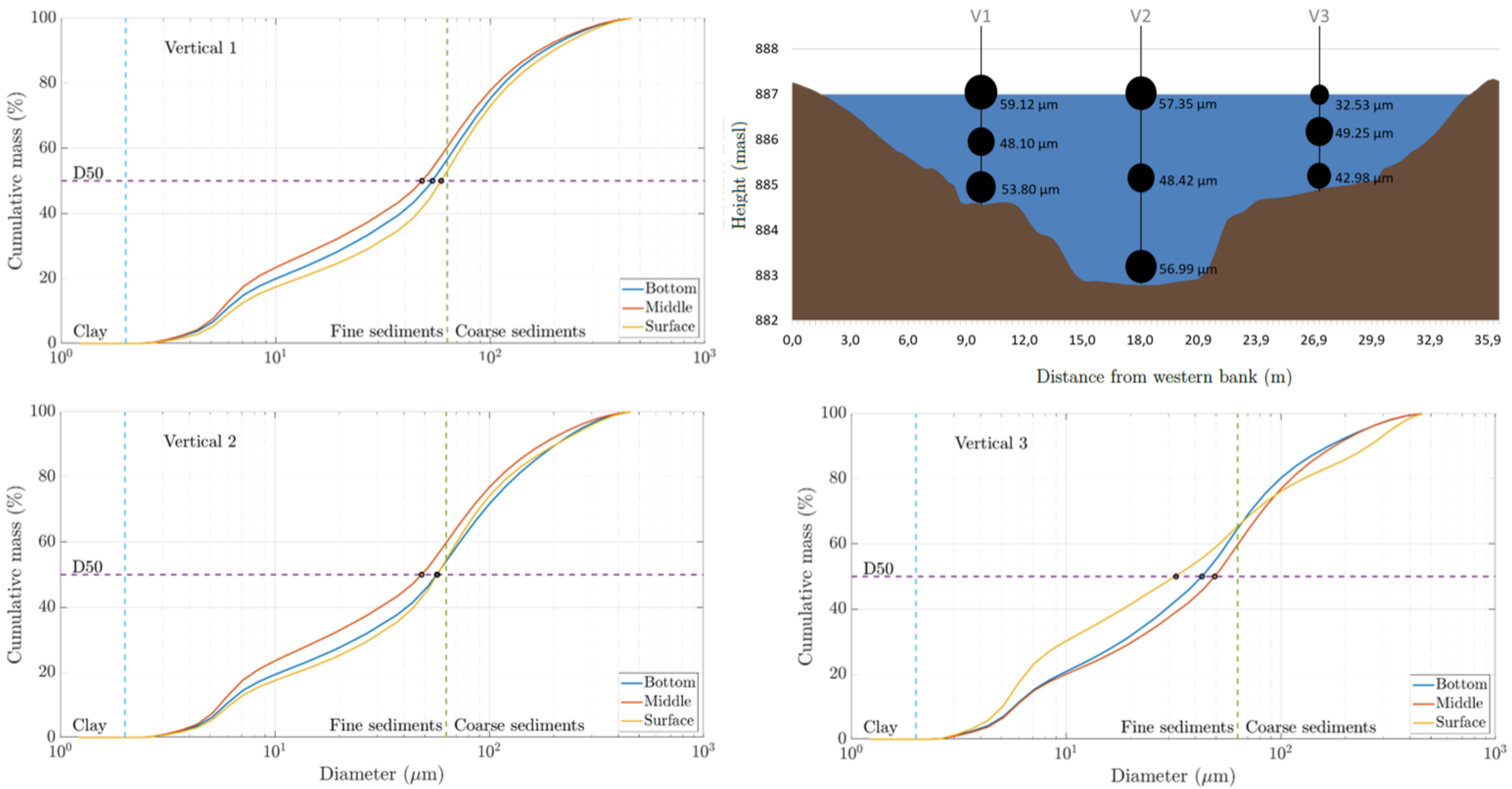

Figure 3.35.: Particle size distribution (PSD) at the Buffer on August 14, 2018.

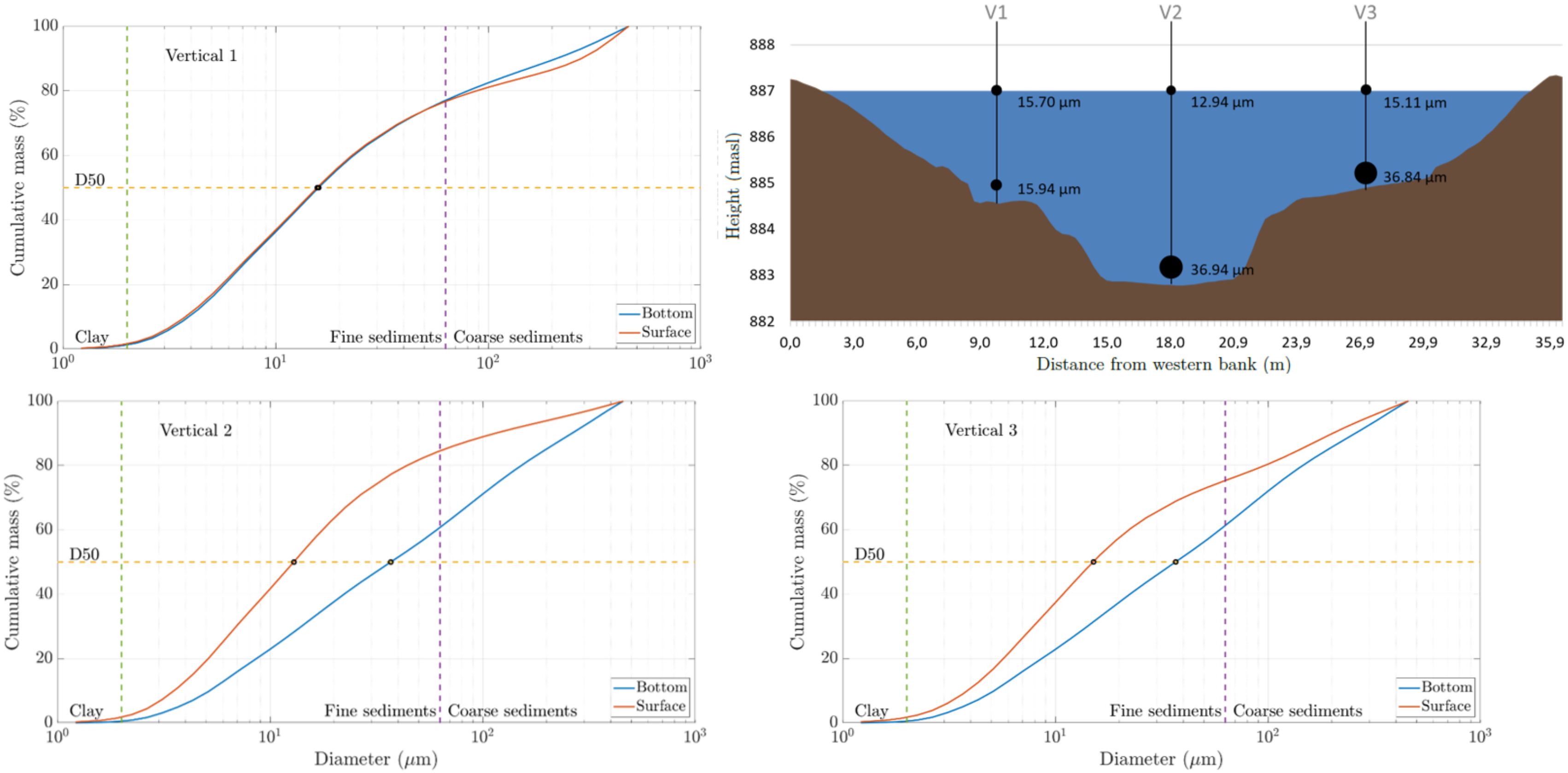

Figure 3.36.: Particle size distribution (PSD) at the Buffer on October 20, 2018.

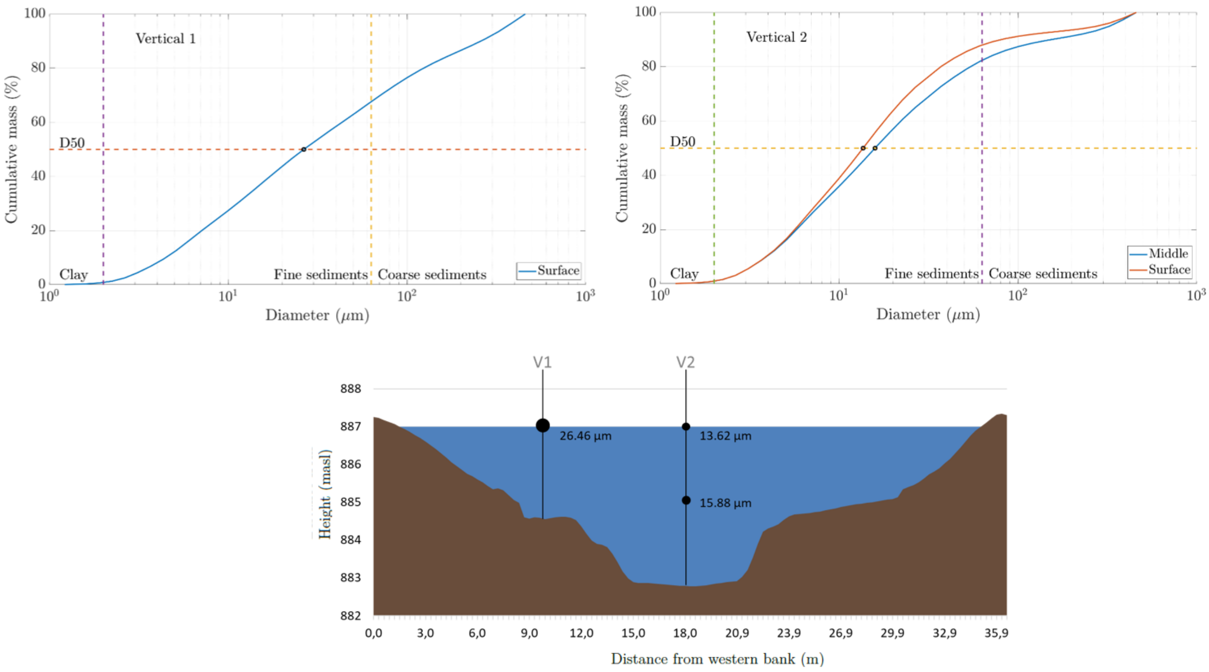

Figure 3.37.: Particle size distribution (PSD) at the Buffer on February 5, 2019.

In general, for all samples gathered at the FB the D_{50} could always be classified as fine sediment. When comparing the measurements at the FB and the BR277 is also evident that the sediments in suspension at the latter position where coarser than at the former for similar dates. Just as expected, since the closer we are to the reservoir, the less turbulent the flow is and consequently the less capacity the flow has to keep the coarser sediments in suspension.

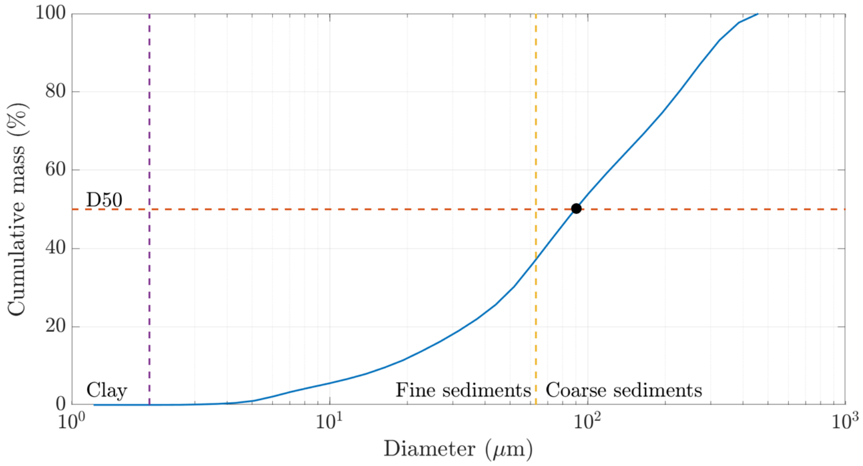

Figure 3.38.: Particle size distribution (PSD) at the Bridge BR277 on August 13, 2018.

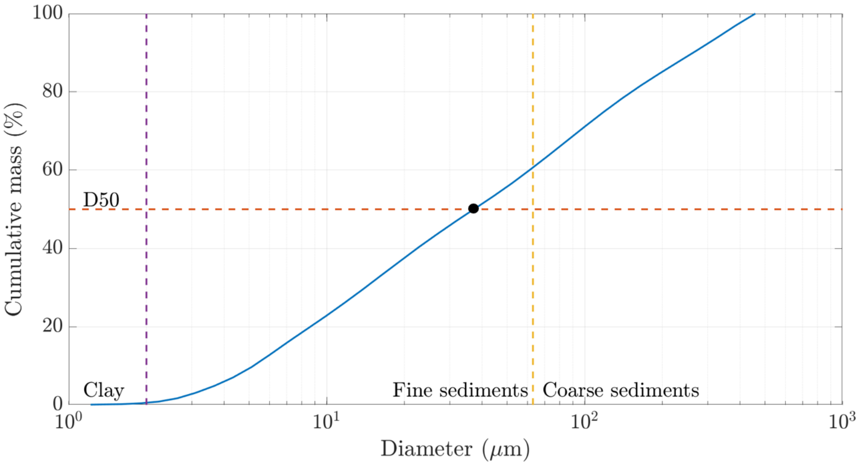

Figure 3.39.: Particle size distribution (PSD) at the Bridge BR277 on October 20, 2018.

3.3.4. Quantifying Sedimentation at the Passaúna Reservoir

Measurements of the sedimentation rates and sediment characteristics at the bottom of the reservoir were performed wihtin the framework of the MuDak project (MuDak-WRM, 2019; Ono, 2020; Sotiri, 2020). The findings from the corresponding measurement campaigns are of paramount importance to understand the sedimentation processes in the Passaúna Reservoir and they are summarized in the following.

Four different methods were employed to determine sedimentation rates: sediment cores sampling, application of the dynamic free fall penetrometer (DFFP), sediment traps and hydroacustic measurements.

Sediment Cores Sampling

In total 30 sediment samples were collected through sediment cores (23 units) and grabs (7 units). The location of the sediment samples are distributed all over the reservoir to characterize the totality of its extension. The thickness of the cores and the thickness of three sediment layers were measured. Furthermore, the dry bed density (DBD) and the content of fines (% of mass of the sample with a sediment size smaller than 63.4 μ m) were also recorded. The mentioned parameteres and the position of the samples are shown and summarized in figure 3.40.The thickness of the sediment cores ranges from 12 to 92 cm, which translates in a sedimentation rate varying from 0.4 to 3.1 cm/year. The mean sedimentation rate for the reservoir amounts to 1.5 cm/year. Using the information provided by the sediment samples, in 19 samples the granulometric distribution indicated a minimum fine sediment content of 95% (d_m < 63.4 µm). In total 25 out of 30 sediment samples displayed a fine sediment fraction higher than 85% of the sample composition.

The dry bed density (**DBD**) is employed to calculate the thickness of the deposited or eroded layer, based on the mass available at the bottom layer. The DBD of a sediment sample depends mainly on its grain size distribution, mineral composition and consolidation grade. A relevant role is also played by the reservoir operation strategies, since those can affect the degree of consolidation of fine sediments (Verstraeten and Poesen, 2001). Sandy sediments will settle with a DBD, which will remain approximately constant over the course of time, whereas fine sediments will deposit with a low initial DBD due to the presence of water in their pores and after around 15 years half of the final consolidation degree will be reached (Annandale et al., 2016). The fact that the DBD of fine sediment deposits increases over time should be considered when analyzing the measured rate of volume loss from bathymetrical surveys over the years. The latter will be declining due to consolidation processes and not due to a decrease in the sediment yield from the catchment (Annandale et al., 2016). The weight of overlying sediments will also promote the consolidation of older sediment layers by compressing single sediment particles closer together and diminishing the pore volume between them and thus increasing their DBD (Verstraeten and Poesen, 2001). An analysis of 1129 sediment samples in 101 reservoirs in the United States resulted in DBD variating between 300 and 1880 kg/m^3 (Lara and Pemberton, 1963). The variation range of the DBD is notorious not only between reservoirs but also within the same water body, for example in the coarse delta deposits the DBD will be higher than in the fine deposits nearby a dam. The DBD of the sediment samples in Passaúna varied between 0.71 and 1.58 g/cm^3 with an average value of 1.12 g/cm^3 (Sotiri, 2020). The range of typical values for the bulk density of fine sediment deposits in reservoirs varies between 0.3 to 1.88 g/cm3 (Verstraeten and Poesen, 2001; Lara and Pemberton, 1963). Hence, the measured data gathered in the reservoir matches the literature values. The correlation between content of fines and bulk density can be observed in the collected data as well: the cores with the finest materials also presented a low DBD.

According to Sotiri (2020) the materials with similar characteristics within one core were designated as a layer. Figure 3.40 shows the thickness of three sediment layers L1,L2 and L3 found in the materials of the cores.

The sediments at the Buffer (C1) present almost just fine materials and a low DBD, suggesting the abscence of a coarse delta deposit in the reservoir. The presence of just one layer of sediments and this core being the second largest of the sampling campaign, maybe an indicator of the temporal uniformity of the sediments entering the reservoir through the main inflow. A further hypothesis, which would not contradict the former one, is that this large sediment amount at the Buffer was deposited during a few recent events and the lack of layers would indicate the erosion of previously deposited materials. In contrast to the core C1, the shortest core (C2) was collected at the position Ferraria Bridge. Due to the relatively high flow velocities caused by the constriction of the bridge the bed shear stress at this area probably constantly exceeds the bed shear stress for sedimentation, causing the further transport of the fine suspended sediments in the water column southward the Buffer. Both this core and the grab sample G7 collected directly downstream to it, displayed a higher content of sand than most of the samples. The sand fraction does not seem to reach the reservoir through the main inflow, since no such a coarse fraction was found in the core collected from the Buffer. Given the low flow velocities in the Buffer and the high settling velocity of sand, if a high sand content was being brought by the main tributaries located before FB, some of this should be present at the core C1. It is possible that this sand fraction reached the FB positions as part of side bank erosion's material. Another possibility is the presence of sandy pre-impoundment materials given the low thickness of the core.

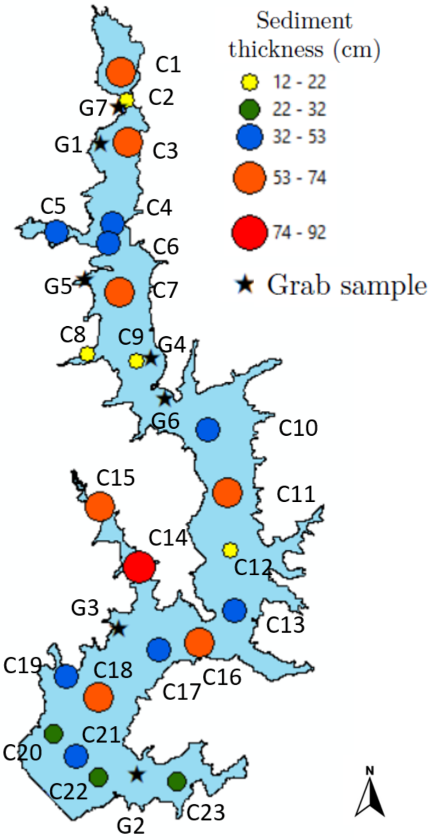

Sample	Sediment thickness (cm)	L1 (cm)	L2 (cm)	L3 (cm)	DBD (g/cm^3)	Content of fines (%)
C1	74	74	-	-	0.98	99.6
C2	12	5	7	-	1.26	79.6
C3	65	65	-	-	1.07	97.7
C4	42	28	14	-	1	97.7
C5	38	38	-	-	1.23	85.0
C6	45	15	30	-	1.47	98.6
C7	55	20	35	-	1.25	93.1
C8	19	7	12	-	1.58	67.9
C9	22	14	8	-	-	99.2
C10	50	10	40	-	1.18	96.8
C11	60	29	21	10	0.94	86.3
C12	20	20	-	-	1.14	92.2
C13	44	20	24	-	0.81	96.9
C14	92	39	23	-	0.96	97.9
C15	69	30	25	14	0.98	97.8
C16	65	25	40	-	-	89.7
C17	40	40	-	-	-	96.0
C18	61	61	-	-	-	95.8
C19	53	22	16	15	0.71	98.7
C20	32	12	20	-	-	97.3
C21	51	28	23	-	-	88.6
C22	24	24	-	-	1.06	38.2
C23	26	6	20	-	1.48	76.2
G1	-	-	-	-	-	99.9
G2	-	-	-	-	-	99.0
G3	-	-	-	-	-	98.7
G4	-	-	-	-	-	99.7
G5	-	-	-	-	-	95.4
G6	-	-	-	-	-	99.4
G7	-	-	-	-	-	34.2

Figure 3.40.: Sediment cores and samples collected at the Passaúna Reservoir. Figure created based on data gathered by MuDak-WRM (2019) and Sotiri (2020).

The core C3 at the PPB region shows high sedimentation rates in one layer of fine materials, suggesting that the materials of the main inflow can reach until this position.

According to the information collected from the core C5, the Ferraria river carried a coarser material (85% content of fines)into the side arm, which have low temporal variability (one-layered core). On the other hand, the cores C4 and C6 show more than one layer, which could represent the reception of sediments coming from the main inflow and the Ferraria river.

The longest core (C14) was obtained at the SAL (TGB261), which may indicate a high sediment input entering the reservoir through this inflow. The third longest core (C15) was extracted from this side arm as well. According to Sotiri (2020) and his investigation on sediment input to the Passaúna Reservoir, the catchment contributing to the inflow TGB261 was characterized by intense agriculture and potential erosion, which would be a reason for the high sedimentation rate (3.1 cm/year) at this location. According to the LARSIM simulation, this tributary does not present high discharges in comparison to the Passaúna River. It was nevertheless the third highest mean discharge over the period (August 2017 until February 2019, see Figure 3.2). According to the cores information the stream of this tributary is capable of transporting the sediments from this inflow at least 1.3 km until the position of C15. The presence of layers in the cores extracted in the SAL would point out to the temporal heterogeneity of the incoming sediments through this tributary and to the sedimentation process taking place during different events.

The presence of high sedimentation rates in the dam region (e.g. C18 and C21)could be the transport of sediments through turbidity currents, which would be able to carry the sediments long distances until the dam. The turbidity currents would not necessarily be generated at the main inflow, but at other tributaries.

For example turbidity currents could generate at the SAL, which already showed high sedimentation rates, and trasnport sediments until the dam region. The same could be hypothesized for the southernmost side arm where the tributaries TGB287 to TGB305 flow into the reservoir (see Figure 3.2). Another simpler explaination for the high sedimentaton rates at the dam is the underprediction of the modelled sediment loads and water disharges entering the reservoir through the side arms different from the main inflow.

Dynamic Free Fall Penetrometer

Further measurements of the sediment layers at the reservoir were performed making use of a dynamic freefall penetrometer by Sotiri (2020). This device travels across the water column in free fall and at the bottom of the water body, intrudes the sediment layers. The dynamical behaviour of the penetrometer will depend on the strength conditions of the sediments, which are indirectly measured using integrated accelerometers and pressure sensors (GP, 2022). Then the collected data can be translated into a sediment layer thickness by using a dynamical model. For the present case, the device was deployed at 134 locations(see Figure 3.41). The thickness of the sediment layers variated between 0 to 1.8 m. The thickest sediment layers (between 1.51 and 1.81 m) are concentrated in both the north (from the Buffer until Park) and the south (from the height of SAL until the dam) of the reservoir.

The fact that the SAL showed larger sediment layers than the core, confirms a high sediment input through this tributary. Figure 3.42 shows a satellite image corresponding to January 22, 2018 two days after a storm event we are certain of ($Q_{peak} = 24.1$). The same figure also ilustrates the recorded hydrograph with a 15-minutes resolution. The change in the turbidity of the water can be observed between the inflow of the tributary TGB261 and the downstream portion of the SAL. It can be hypothesized that we are in the presence of a turbidity current,which sediment load can be transported further into the main body of the reservoir in the dam region.

Similarly, Figure 3.42 also shows the satellite image for the same day for the Buffer area. The change in the turbity of the water between the Buffer and the zone downstream of the Ferraria Bridge can be observed. An explanation for this phenomena would be this being caused by the resuspension of already fine deposited material, caused by high flow velocities and the inherent high bead shear stress. Nevertheless, for both cases, the coloration of the water surface changes suddenly, which could indicate that the fine sediment-laden water goes into deeper layers after reaching a plunge point. This could be an hint for the presence of turbidity currents in the Pasaúna Reservoir. Otherwise, it is difficult to explain how all of the suspended sediments just deposited suddenly right before the cross section A in Figure 3.42. It is also relevant to mention, that the SAL has a Buffer-like structure: a shallow forebay separated from a deeper water region by a constriction.

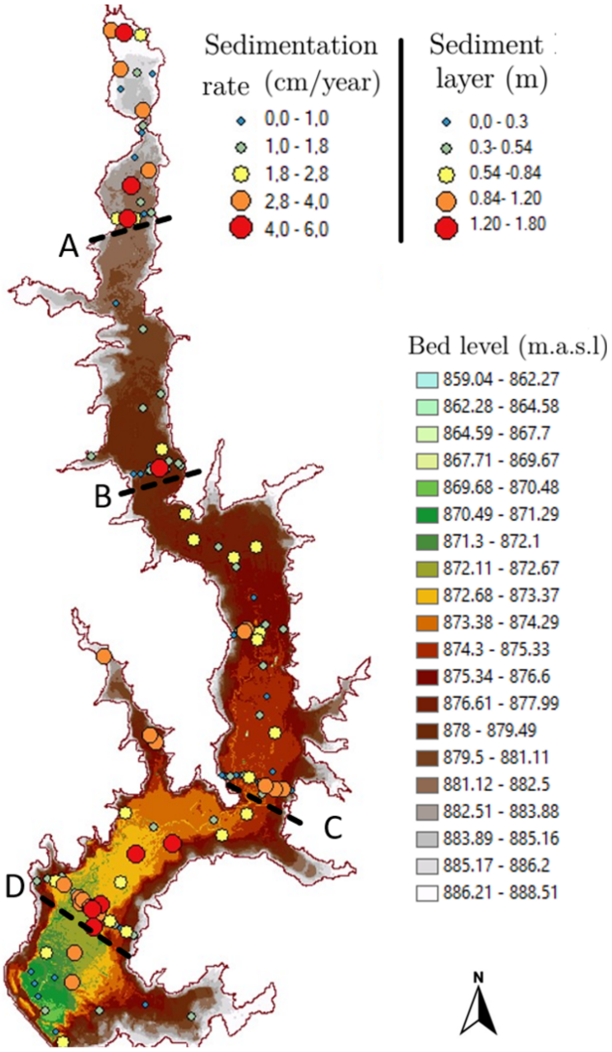

Figure 3.41.: Measurements of the sediment layer performed with the free fall penetrometer within the framework of the Mudak-project (MuDak-WRM, 2019).

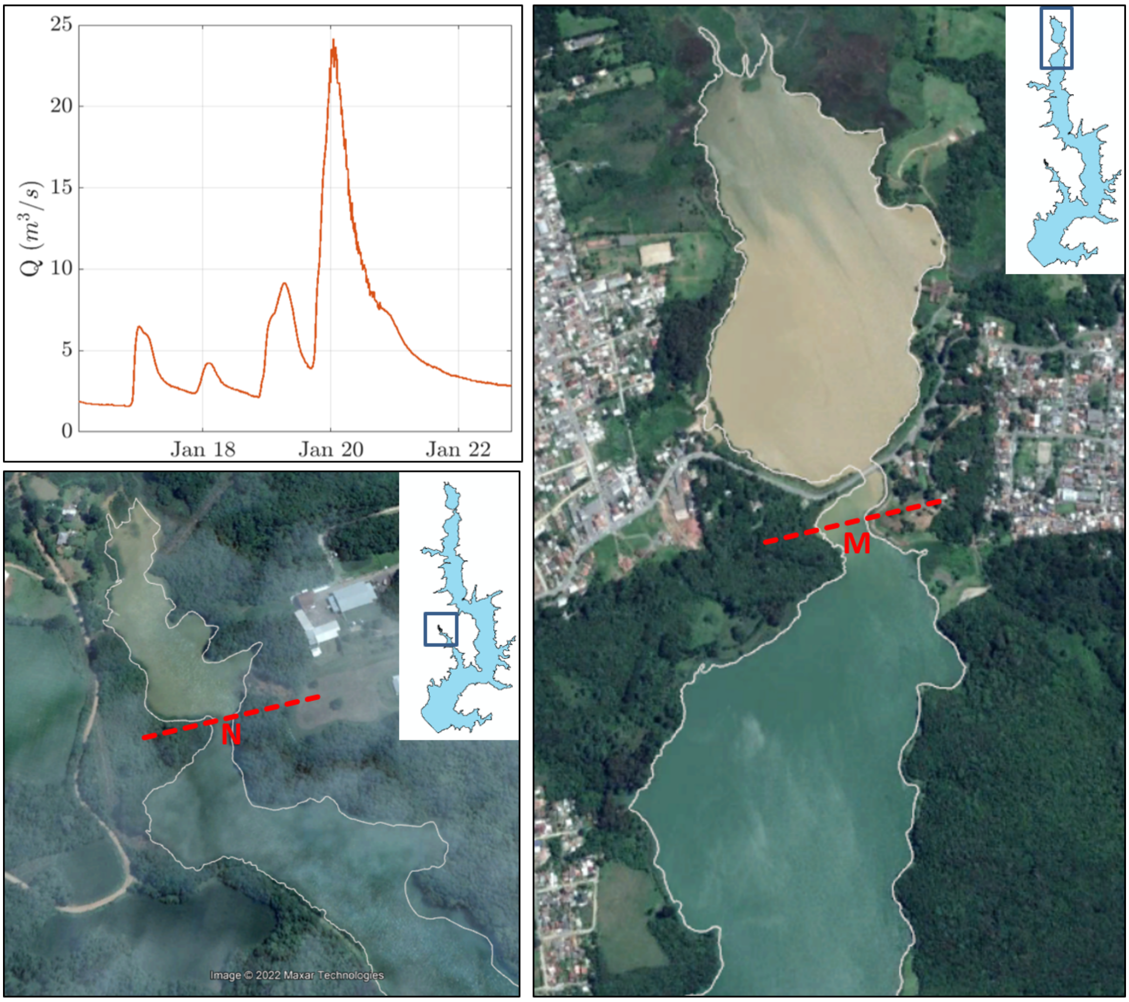

Figure 3.42.: Possible turbidity current at Passaúna Reservoir. Top left: hydrograph of the event with peak on January 20, 2018 at the BR277. Bottom left: satellite image of the SAL on January 22, 2018. Right: satellite image of the Buffer on January 22, 2018. Source of the satellite imagery: Google Earth.

The high sedimentation rates at the northern part of the reservoir coincide with the well-known delta deposition pattern. This delta pattern is observed in all measurements: sediment samples, DFFP and on the sediment traps (see following section). This pattern can be well explained through the regular or "every day" hydrodynamics, where the transport capacity of the flow ligated to the low flow velocities of the reservoir are not able to transport the suspended sediment until the dam but only until the end of the delta region (Point Park).

The high deposition rates at the southern area (downstream from the SAL, see Figure 3.41) could be explained through turbidity currents, produced during extreme events, transporting high SS-amounts all the way through the thalweg of the reservoir and depositing them at the dam region. Another hypothesis is the underestimation of the sediment input through tributaries like the one of SAL and/or their transport capacity (via underestimation of the liquid discharge). A hint for the underestimation of the role of TGB261 on the sedimentation process is the fact that several of the thickes sediment samples with both methods (penetrometer and core sampling) were obtained within this side arm.

In general, the sediment cores and the penetrometer offer similar information about the irregular sedimentation pattern of the reservoir in a qualitative manner. Nevertheless, the penetrometer indicated a higher sedimentation rate than the cores. According to Sotiri (2020), some of the sediment cores were not able to reach the pre-impoundment soil (C14, C15, C17, C18, C21). This could explain the large discrepance between the results of the penetrometer and the cores for those positions in the resevoir.

A further interesting aspect observed through the measurements with the penetrometer is the fact that the highest sedimentation across the cross sections A to D (see figure 3.41) does not always take place along the thalweg. Figure 3.43 shows the sediment layer thickness along the mentioned sections and the bed levels of the reservoir. Section A does present the highest sedimentation at the thalweg and towards the side banks the sedimentation decreases, as expected. This fact is not surprising, considering that this section is the nearest to the main inflow and the sedimentation there will be controled by the sediment load and the transport capacity of it. For the further sections the thickest sediment layers are not found at the thalweg.

The old river bed can be observed and the sedimentation in its vecinity is not the highest along the cross section. One possible reason for this situation could be the inflow from tributaries different from the main inflow control the sedimentation processes at the mentioned sections. A second hypothesis is the relocation of materials coming from the bank erosion inside the reservoir itself.

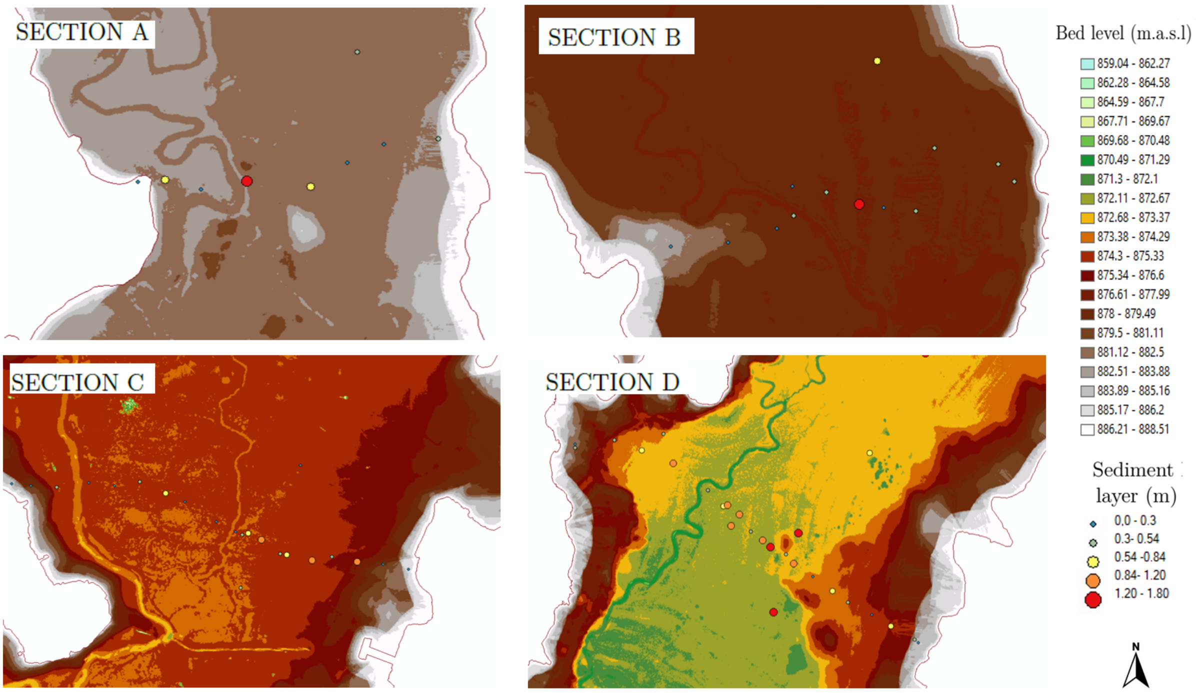

Figure 3.43.: Thickness of the sediment layers found at the sections A, B, C and D with the DFFP.

Sediment Traps

Sediment traps have been widely applied in limnological studies (Schillereff, 2015b). They are not only applied for the determination of sedimentation rates but also for the investigation of nutrients and pollutants present in the sediments, like in the cases of the investigations at the Great Lakes in North America (Eadie, 1997; Urban et al., 2004). They are simple cylindrical instruments with a removable container at the base for trapping the settling sediments and provide a time averaged signal for the sedimentation rates (Schillereff, 2015a). At the Passaúna Reservoir five sediment traps were deployed by Ono (2020) at one meter from the bottom in the locations indicated in Figure 3.44.

Position	Campaign- sedimentation rates (g/m^2day)								μ	CV (%)
	1	2	3	4	5	6	7	8		
PPA	-	-	-	-	-	186.65	175.57	184.70	182.31	3
Center	-	-	2.89	9.27	16.63	14.06	-	-	10.71	56
SAL	-	-	-	-	5.61	8.19	6.72	3.12	5.91	36
Intake	-	4.29	3.04	3.79	4.67	6.85	5.31	2.71	14.38	32
Dam	2.73	3.75	2.68	2.22	2.18	6.11	3.88	1.79	3.17	44
$Q_{Inflow}(m^3/s)$	2.3	1.2	1.5	1.3	-	-	-	-	-	-
Cum. Precip.(mm)	57	498	138	347	345	399	197	264	-	-

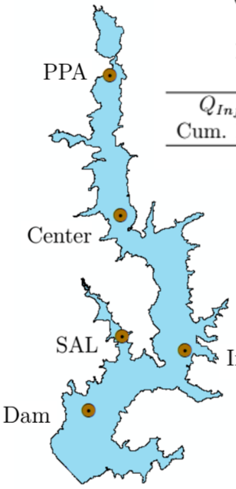

Campaign	Period	Number of days
1	06.04.2018-21.05.2018	45
2	21.05.2018-25.10.2018	157
3	25.10.2018-10.12.2018	46
4	10.12.2018-12.02.2019	64
5	12.02.2019-25.04.2019	72
6	25.04.2019-16.07.2019	82
7	16.07.2019-24.09.2019	71
8	24.09.2019-14.12.2019	80

Figure 3.44.: Sedimentation rates measured with sediment traps. Left: position of the traps. Top right: measured periods. Bottom right: measured sedimentation rates after Ono 2020.

Figure 3.44 also shows the time periods for the deployment of the traps. The coefficient of variation (CV) is applied to analyze the dispersion of the measured sedimentation rates for each point and it can be calculated trough equation 3.4:

$$CV = \frac{\sigma}{\mu} \tag{3.4}$$

where:

σ	standard deviation of the data	$[g/m^2day]$
μ	mean of the data	$[g/m^2day]$

Furthermore, the mean incoming discharges trough the main inflow are presented, considering a positive relation between this parameter and the amount of solids entering the reservoir. For periods, for wich the discharge for TGB154 was not available, the cumulative precipitation at the dam weather station was used as a proxy parameter for it.

In general the sedimentation rates strictly decreased along the longitudinal axis of the reservoir with increasing distance from the main inflow. The rates measured during the campaign three built an exception, They indicated that for that period, the sedimentation rate at the center of the reservoir was slightly lower than at the Intake. This could be an indication for further sediments sources downstream of the former point. From the campaign number six, it can be observed than the sedimentation rate at PPA reahes a value ten times larger than at the center of the reservoir. The differences between the sedimentation rates at the further points SAL, Intake and Dam is not as notorious as between the points PPA and Center. Observing the mean sedimentation rate at each point, the traps registered sedimentation rates corresponding to a clear delta deposition pattern. Due to the variability of the sedimentation rates along the longitudinal axis of the reservoir, a general value or mean value should not be deifined and applied for the whole water body. In other words, the mean value of all measured rates is 25.7 g/m^2day, but this values would not be representative at all for the dam region at any time period.

The calculated CVs identify the points Center and PPA, respectively as the positions with the largest and the lowest variabiality among the campaigns. The comparison of the discharges at the main inflow and the cumulated precipitation shows no positive correlation between those variables. A possible explanation for it would be the seasonal variation of the vegetation cover, which would affect the amount of surface runoff reaching the reservoir.

Table 3.2 presents the sedimentation rates calculated in cm/year. For the conversion of mass into volume, the mean DBD found in the sediment cores was used (sedimentation rate (1)). In addition, the DBD measured in the core nearest to each trap was used as a second value to observe the influence of this parameter on the sedimentation rates (sedimentation rate (2)). A Wilcoxon signed-rank test suggested that the difference between each pair of resulting sedimentation rates (cm/year) were not statistically significant. Confirming the use of the mean DBD of 1120 kg/m^3 as a good value when converting from mass to volumen and viceversa.

Table 3.2.: Registered sedimentation rates (cm/year) at the traps positions.

Position	Campaign/ sedimentation rates (1)/(2) (cm/year)							
	1	2	3	4	5	6	7	8
PPA	-	-	-	-	-	6.08	5.72	6.02
						6.37	5.99	6.30
Center	-	-	0.09	0.3	0.54	0.46	-	-
			0.08	0.27	0.49	0.41		
SAL	-	-	-	-	0.18	0.27	0.22	0.10
					0.21	0.31	0.26	0.11
Intake	-	0.14	0.10	0.12	0.15	0.22	0.17	0.09
		0.19	0.14	0.17	0.21	0.31	0.24	0.12
Dam	0.09	0.12	0.09	0.07	0.07	0.2	0.13	0.06
	0.14	0.19	0.14	0.11	0.11	0.31	0.2	0.09

Hydroacustic Measurements

Based on the measurements performed with a linear single-beam hydroacoustic system in 2019 by Sotiri (2020), a total of 3.7 mio m^3 sediment have accumulated at the bottom of the Passaúna Reservoir during an operational period of 30 years (MuDak-WRM, 2019). According to the measured storage volume (69.3 mio m^3) the reservoir has lost approx. 5.3% of its volume to siltation during the period 1989-2019. This translates into a sedimentation rate of 0.18% per year. In comparison, the average annual sedimentation rate of reservoirs around the world have been calculated to be of approximately 1% of the initial storage volume (Mahmood, 1987; ICOLD, 2009). This fact would situate the sedimentation at the Passaúana Reservoir as mild and not a pressing issue. Of course this world wide value is just a rough average and its purpose it to serve as orientation, since sedimentation rates vary for each region around the world and they are a function of the hydrology and the land use in the watershed (Haun et al., 2013). With the application of the single beam methodology, the thickness of the sediment layers all over the reservoir were determined as no larger than one meter and the mean sediment thickness amounts to 36 cm (Sotiri, 2020). Figure 3.45 shows no obvious sedimentation pattern. The thickest sediment layers are concentrated at the southern part of the reservoir (from the point Center until the dam region). For the Buffer region the collection of data was not possible due to low water levels at the day of the measuring campaign.

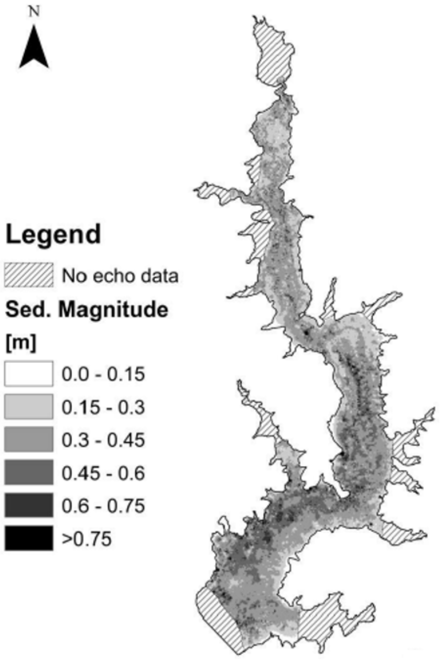

Figure 3.45.: Sediment layers thickness at the Passaúna Reservoir (Sotiri, 2020).

General Considerations

A further study on sedimentation at the present investigation area was carried on by Saunitti et al. 2004. Based on the results from 18 cores extracted all over the reservoir a sedimentation rate variating between 0.66 to 3.04 cm/year was found with a mean value of 1.2 cm/year (see Figure A.5 in the appendix section, for the core's position and their corresponding sedimentation rates). The data from this study suggest, that the highest sedimentation rates will be found at the southern part of the reservoir. Nevertheless, just one core was extracted at the northern region (at approx. PPA, showing a value over the average (1.4 cm/year).

In a general way, the sediment layers measured with the cores, the graviprobe and the hydro acustic equipment show the "picture" of the Reservoir's state after 30 years. The results of the measurements were the sediment layer thickness deposited in the period of 30 years. This hardly means that the sedimentation was uniform each year. The yearly variability of the inflowing discharges, the soil use, the vegetation cover, the single flood events all directly influence the amount of sediments reaching the reservoir, assuring that the latter won't be of the same magnitude every year. Figure 3.4 shows the temporal variation of the discharge at TGB154 for the period 1985-2015 and the annual variability of it. Consequently, the fair distribution of the sedimentation over the years since the impoundment is just a reference value for the reservoir and this fact has to kept in mind when for example calibrating a numerical model. Normally, a full 3D-numerical model will not simulate all 30 years, for sure not during the calibration process due to the high computational costs. Hence, the measured sedimentation normally cannot be proportionally transfered to the duration of the modelling period. This is very probable the case for the Passaúna Reservoir. By contranst the sedimentation rates derived from the sediment traps for every single campaign comprehend the matter of days (at the longest 157 days for the campaign 2). For the latter case a direct use of the measured values for model calibration purposes is possible.

Table 3.3 summarizes the measured sedimentation at the Passaúna Reservoir for all the presented studies. For the point data (cores and DFFP).Sotiri 2020 calculated the deposited sediment volume taking into account just the mean sediment thickness and the reservoir area. Ono 2020 calculated a mean sedimentation rate of 29.49 $g/cm^2 day$ for the reservoir taking into account the area of influence of the sediment traps. Using the DBD of the sediments, the area of the reservoir and extending this value to 30 years uniformly, one can get an approx. deposited sediment volume for the whole operation period of the water body. As Table 3.3 shows, the calculated deposited sediment volumes for the first 30 years of operation are of the same order of magnitude for all four presented methods. Nevertheless, the sediment traps presented a much lower volume (less than one third of the volume resulting from the other methods). This same method registered the highest sedimentation rate at a single location and the highest variability between all the measured date (see columns 3 and 4 in Table 3.3).

Table 3.3.: Sedimentation rates at the reservoir: summary.

Source	Period	Sed. rate span (cm/year)	Mean sed. rate± std (cm/year)	Sed. volume (mio m^3 in 30 years)
Cores	1989-2019	0.4 to 3.1	1.5± 0.68	3.9
DFFP	1989-2019	0 to 6	1.9 ± 1.2	3.36
Acoustic	1989-2019	0 to 2.5	1.2	3.7
Traps	05.2018-12.2019	0.06 to 6.08	0.84±1.88	1.14
Saunitti et al. 2004	1989-2019	0.66 to 3.04	1.17±0.62	-

To translate the calculated sediment volumes to the period of interest studied within the numerical modelling chapter (01.08.2017 till 28.02.2019)an analysis of the historical and LARSIM data (1989-2019) for the discharge through the main inflow. The volume of water through TGB154 and all further tributaries for the 30 years of operation was calculated. Since no data was available for the further tributaries, some simplifications have to be made: a mean discharge for each tributary over the period of interested was calculated, since for this period there is LARSIM data which can be used. Then it was supposed that for those tributaries the mean discharge remained constant over the years and the water volume entering the reservoir through them during 30 years was calculated. In the following the total volume of water entering the reservoir during the period of interest was calculated and the amount of sediment deposited during this period was proportionally distributed according to this water volume in comparison with the volume for the whole operation period. The described process indicated that 5.2% of the sediment volume deposited during the period of interest. Table 3.4 shows the calculated sediment input in section 3.3.1 using the different available rating curves in direct comparison with the measured deposited sediment volume for the period of interest. Considering a trap efficiency of 100%, is evident that all three examined rating curves do not "deliver" enough sediments to reach the deposition volumes measured in the reservoir with the in table 3.4 three first listed mehtods.

RC3 delivers the highest sediment loads of the studied curves and is in the order of magnitude of the measurements with cores, DFFP and acoustic methods. Nevertheless, the rating curve RC3 showed high daily SSC at the inflow, which were never measured with the ground true techniques (compare 3.3.2), not even during a high discharge event. The fact that the mentioned methods to evaluate sedimentation volumes in a reservoir include the events taking place all along the reservoir lifetime and that the rating curves were constructed based on time discrete measurements of the SSC indicates that the comparision of those measurements in order to validate one or another is not appropiate. This is a important point for the calibration of a numerical model. The best option for this would be the selection of the sedimentation results from the sediment traps, which enclose a known and limited time period. Another possibility is that some sediment measured at the bottom of the reservoir is not being accounted through the presented rating curves. This could happen if for example, catastrophic events were not covered with the measurement campaigns or if just one sample was taken at a not representative location over the cross section of the river. The contribution of the bank erosion caused by the constant water level change and the waves to the sediment budet of the reservoir have not been quantified. Nevertheless, this factor will not be the only responsible for the missing incoming sediments.

Table 3.4.: Deposited sediment volume at the reservoir for the period August 2017 til February 2019: summary.

Source	Sed. volume ($10^5 m^3$)
Cores	2.03
DFFP	1.75
Acoustic	1.92
Traps	0.59
RC1	0.12
RC2	0.20
RC3	1.53

3.4. Conclusions

Passaúna is a canyon-shaped reservoir located in the metropolitan region of the city of Curitiba in Brazil. The water body has its major tributary inflowing through the northern region of the reservoir: the Passaúna River. According to the hydrological modelling carried outwith LARSIM-WT, the mean discharge of this tributary is of around 2 m^3/s. The highest ever registered discharge at the Passaúna River was 27 m^3/s. The water withdrawal extracts fluid from the reservoir with a mean discharge of around 1.7 m^3/s. The highest registered wind speed at the reservoir's region was 9 m/s and the mean value of this parameter was found to be 2 m/s. Measured air temperatures ranged from 2 to 35 $°C$. The reservoir presented several mixing events during the observed period, being this the main reason to clasify it as a warm polymictic water body. Measurements of the flow velocity were available only for one position near the water Intake, where an ADCP-measuring device was deployed. The time and depth averaged flow velocity was around 2 cm/s. It is important to mantain present, that this value is representative only for the lacustrine zone of the reservoir. The highest flow velocity was registered at the water surface and its magnitude was 14 cm/s. The averaged Secchi depth for the Passaúna Reservoir was calculated to be 2 m, with the highest penetration of light measured to be 3.1 m.

The pronounced difference between the prediciton of the RC1/RC2 and the RC3 is a clear indicator of the importance of the method for the construction of such mathematical relation. Since during the field campaigns within the framework of the MuDak-Project, no such high SSC as predicted by the RC3 were measured, in the next chapters of the present work, the RC1 or RC2 will be used to feed the numerical model. RC1 and RC2 deliver SSCs at the inflow of the reservoir which are in the order of magnitude of the measured concentrations.

The sediment found at the bottom of the Passaúna Reservoir are mostly of fine nature. According to the ground truth survey, on average 94% of the mass of the bottom sediments have a size lower than 63.4 µm, i.e. the sediments are below the silt range. The sediments presented a low bulk density, corresponding to fine materials. The bulk density of the extracted sediment cores varied between 500 and 1580 kg/m^3, with an average of 1120 kg/m^3. The sedimentation pattern encountered in the Passaúna Reservoir through the sediment cores sampling does not correspond to only one of the schemes presented in section 2.2 in chapter 2, but to a combination of several patterns. The "image" resulting from the field sampling is the product of 30 years of sedimentation marked by low and high discharge events, events that for the latter case were probably not recorded with the proper temporal resolution.

Passaúna Reservoir is a complex water body, which does not only have one inflow but 64 tributaries. The SSC entering the reservoir were only measured for the main inflow for limited time periods, the information of the sediments entering the reservoir relies on the results of modelling the sediment input of the several catchments, which feed the water body. The same situation occurs in the case of the water discharges. The information extracted from the modelling, is of course subjected to some degree of accuracy. Models in their nature are just a mathematical representation of reality.

The deposition pattern registered through the penetrometer clearly states that the thickest sediment layers are found at the northern and southern regions of the reservoir. On the other hand, the sedimentation rates derived from the sediment traps show a clear delta deposition pattern with rates (time averaged quantity) variating from 3.17 g/m^2day at the dam up to 182.3 g/m^2day at the PPA. For the calibration of a numerical modelling on sediment transport, the most recomended measurements of the deposited volume are the sediment traps, since they comprehend a known time period, which at the same time is computationally feasible to simulate.

4. Numerical Modelling of the Hydrodynamics including Wind and Heat Transport

Abstract
The simulation of the water quality in reservoirs has increasingly become an invaluable tool to scientists and practicioners in the management of those water bodies. The hydrodynamics including the thermal structure of the reservoir have to be calibrated in order to have a reliable model to later simulate the transport of substances. In the present study, the hydrodynamics of a subtropical reservoir in the southeast of Brazil is simulated using the software Delft3D. The influence of numerical and physical parameters like the wind drag coefficient, the number of layers, the background mixing coefficients and additional variables related to the heat fluxes on the thermal structure and flow velocities are investigated and compared with field measurements. In the studied ranges of the parameters, the Dalton number affected the most the calculated temperatures. The horizontal flow velocity was most influenced by the change in the user defined background vertical viscosity. Moreover, the existence of density driven currents and their simulation with the model are evaluated. The performances of Z-and Sigma-layered systems are studied as well. The Z-model better simulated the stratification of the water column and the Sigma-model offered a more realistic prediction of the density currents. The inclusion or exclusion of wind in the numerical model showed to have an effect on both the thermal structure and the flow velocities in the reservoir.

Keywords: subtropical reservoir, hydrodynamics, numerical modelling, thermal stratification.

4.1. Introduction

Reservoirs are designed to achieve a wide range of tasks such as water supply, flood protection, hydropower generation and/or recreation. The construction of reservoirs around the world is constantly rising due to the increasing water scarcity and energy demand. Nowadays, their construction is concentrated in developing countries and emerging economies, including South America (Zarfl et al., 2015). 2010 approximately 60% of the reservoirs worldwide were situated in the tropical and subtropical zones (Selge and Gunkel, 2013). Brazil possesses around 12% of the world fresh water sources (OECD, 2015), nevertheless the distribution of it is highly uneven in the territory: the major portion of the population (>50%) concentrates in the regions near to the Atlantic coast, whereas 70% of the fresh water is available in low populated regions such as the Amazon basin (OECD, 2015; Milano et al., 2018). This makes the construction of reservoirs necessary to cover the water demand of the population. Ensuring the water quantity and quality in storage reservoirs is the most important management goal to be achieved by public water companies.

One relevant factor influencing the quality of the water is the temperature since it directly limits the chemical reactions in the water body, the amount of dissolved oxygen and hence the flora and fauna grow rates (Wang et al., 2020b). The water temperature and thus the water quality in reservoirs are strongly influenced by the hydrodynamics. At the same time, the hydrodynamics of a reservoir or a lake is strongly ligated to the dynamics of the stratified water column induced by external forcing, the stability of stratification itself, the dynamics of turbulence and the interactions of those factors in a stratified water body (Monismith and MacIntyre, 2009).

For the case of a stratified water column, three different layers have been defined in the literature: the epilimnion, the metalimnion and the hypolimnion. The metalimnion is the region of high temperature gradients over the depth. Above the metalimnion an upper well-mixed layer (epilimnion) is found. Below the metalimnion a less strongly stratified layer is located (hypolimnion). The hypolimnion may include another isothermal layer at the bottom of the water body. (Monismith and MacIntyre, 2009). Temperature and hence density stratification in lakes and reservoirs have a strong influence in the vertical fluxes of matter over the water column. Stratification diminishes the exchange of nutrients between the hypolimnion and the upper mixed layer. As a result of it, the hypolimnion becomes rich in nutrients and light limited while quite the opposite is true for the epilimnion. Furthermore, due to its separation from the surface, the hypolimnion usually becomes oxygen depleted (Wetzel, 2001).

The processes of mixing and transport in reservoirs are in general, induced by mass fluxes and the input of mechanical or thermal energy either directly to the water surface through wind and solar radiation or through the reservoir's margins (Peeters et al., 1996). One of the main factors causing stratification in lakes and reservoirs is the input of solar radiation at the water surface. In general, with increasing solar radiation, the stratification of the water column will become more stable. Further determinant factors influencing thermal stratification are wind, tributaries' inflows and outflows (e.g. through water withdrawal). Even though vertical fluxes in the water column are inhibited by stratification, there are certain mechanisms in the water body which promote the horizontal particle's fluxes and are even intensified with increasing stratification (Monismith and MacIntyre, 2009). The duration of stratified periods in a lake or reservoir may vary in the scale range of hours to decades (Read et al., 2011). The main forces triggering mixing of the water column are wind and convective cooling.

The numerical simulation of the hydrodynamics and thermal stratification of storage reservoirs has become a valuable tool in the decision making of the companies managing these water bodies. The better understanding and prediction of the reservoir behaviour under the change of defined boundary conditions are of paramount relevance. The correct simulation of the hydrodynamics of a reservoir not only demands data about the inflowing water discharges and their temperature but also a good coupling between the lake surface and the wind forcing and the vertical turbulent mixing (Xavier et al., 2017), quality information about the meteorological data, the tributaries discharges and temperatures and outflows are equally important.

Chanudet et al. (2012b) simulated the hydrodynamics of the Nam Theun 2 Reservoir in Lao PDR including temperature, while studying the sensitivity of the simulation results specifically the water temperature and flow velocity to several physical and numerical parameters. Soulignac et al. (2017) successfully simulated the stratification, mixing periods and the internal wave dynamics in an urban shallow lake in making use of Delft3D. Additionally, they compared the sensitivity of the results to several numerical input parameters with the findings of several authors studying the same aspects in different reservoirs. Polli and Bleninger (2019b) applied the software Delft3D to simulate the stratification processes at the Vossoroca Reservoir in Brazil. They further studied the effect of temperature on the transport of a conservative tracer and on the flow velocities. Finding that the inclusion of temperature in the numerical model showed to have an effect on both aspects. Zhang et al. (2020) modeled the temperate monomictic Tarago Reservoir in Australia by using the software MIKE 3 Flow. This investigation focused on the influence of the inflow temperature, wind and rain on the thermal structure of the water body at the riverine, transition and lacustrine zones. Zamani and Koch (2020) modeled the Maroon Reservoir in Iran making use of the two diferent 3D CFD programs: MIKE3 and AEM3D. They studied the power of both models to simulate stratification, mixing and propagation of cold density currents and compared the result to existing measurements. Ishikawa et al. (2022) studied the impact of different model dimensionalities on the hydrodynamics and thermal stratification in the Passaúna Reservoir. This study aimed to define the requiered model dimensionality to adequately describe the hydrodynamics of the water body in concordance with field measurements.

The aim of the present study is to investigate the hydrodynamics, mixing and stratification processes in the reservoir not only at the Intake position but also in further regions. Also, the identification of the relevant factors/processes driving the hydrodynamics on the reservoir is a key issue to be studied. This study also includes the analysis of the effect of wind and vertical discretization system on the simulation results. The conclusions of the present analyses should serve as a guide for modelers when studying and setting up models for similar systems.

4.2. Materials and Methods

[2] This section describes the main characteristics of the CFD software used for the modelling of the hydrodynamics. Moreover the numerical grid, the main model input data, the field measurements for model calibration and the statistical parameters to quantify the quality of the model results are briefly explained.

---

[2] This section partly consists of excerpts of the peer-reviewed conference paper (Gonzalez et al., 2022) written by the author of the present dissertation and published in the proceedings of the 39th IAHR World Congress.

4.2.1. Hydrodynamic Model Delft3D

The hydrodynamic software Delft3D developed by Deltares (Deltares, 2014), solves the Reynolds-averaged Navier-Stokes equations (RANS) for incompressible free surface flow. For the solution of the RANS, the software reduces the vertical momentum equation to the hydrostatic pressure distribution. The density differences in the fluid are considered according to the Boussinesq approximation. The numerical solution is performed using a finite differences approach on a staggered grid, i.e. velocity vectors are defined on the cell faces and scalar quantities at the cells centers (Deltares, 2014). Horizontal advection is approached with a multidirectional upwind scheme and vertical advection is estimated using a second order central difference scheme (Chanudet et al., 2012b). Time discretization is implicit making use of an alternate direction implicit scheme (ADI). For the vertical spatial discretization, the software offers two layering schemes; the terrain following σ-model and the strictly horizontal Z-model. For the former the number of the vertical layers remains constant over time and space and their thickness is defined by the user as a percentage of the water depth. For the latter the number of active cells in the vertical direction depends on the local water level and hence can variate with time.

To resolve the sub-grid scale turbulence the eddy viscosity concept is employed. In the present study the $k-\epsilon$ closure model was applied to determine the eddy viscosities and diffusivities. The applied vertical (v_V) and horizontal (v_H) viscosities are defined as follows (Deltares, 2014):

$$\nu_V = \nu_{mol} + max\left(\nu_{3D}, \nu_V^{Back}\right) \tag{4.1}$$

$$\nu_H = \nu_V + \nu_H^{Back} \tag{4.2}$$

Where v_{mol} is the kinematic viscosity of water, v_{3D} is the vertical viscosity calculated by the $k-\epsilon$ closure model, v_V^{Back} and v_H^{Back} are respectively the vertical and horizontal user-specified ambient viscosities.

At the free-surface the model is forced through the wind shear stress, which in Delft3D is assumed to be a function of the wind speed and is calculated using the approach proposed by Smith and Banke (1975). In Delft3D there is the possibility to introduce a piecewise variating wind shear stress to reflect the variation of the wind drag coefficient C_{10} with the wind velocity at 10 m above the water surface as follows (Deltares, 2014):

$$C_{10}\left(U_{10}\right) = \begin{cases} C_{10}^A & \text{if} \quad , U_{10} \leq U_{10}^A \\ C_{10}^A + \left(C_{10}^B - C_{10}^A\right)\dfrac{\left(U_{10} - U_{10}^A\right)}{\left(U_{10}^B - U_{10}^A\right)} & \text{if} \quad , U_{10}^A \leq U_{10} \leq U_{10}^B \\ C_{10}^B + \left(C_{10}^C - C_{10}^B\right)\dfrac{\left(U_{10} - U_{10}^B\right)}{\left(U_{10}^C - U_{10}^B\right)} & \text{if} \quad , U_{10}^B \leq U_{10} \leq U_{10}^C \\ C_{10}^A & \text{if} \quad , U_{10}^C \leq U_{10} \end{cases} \tag{4.3}$$

Where C_{10}^{A}, C_{10}^{B} and C_{10}^{C} are the wind drag coefficients at the wind velocities U_{10}^{A}, U_{10}^{B} and U_{10}^{C}, respectively. At the bottom of the water body the forcing takes place via the bed shear stress by means of the Manning's, Chézy's or Colebrook-White's formulations. The transport of heat is simulated using the advection-diffusion equation. The solution to this equation is approximated with the Van-Leer 2 scheme. The vertical (D_V) and horizontal (D_H) diffusivities are calculated as follows (Deltares, 2014):

$$D_V = \frac{\nu_{mol}}{\sigma_{mol}} + max\left(D_{3D}, D_V^{Back}\right) \tag{4.4}$$

$$D_H = D_V + D_H^{Back} \tag{4.5}$$

Where σ_{mol} is the Prandtl number for diffusion of heat (0.7), D_{3D} is the vertical diffusivity calculated by the $k-\epsilon$ closure model, D_V^{Back} and D_H^{Back} are respectively the vertical and horizontal user-specified ambient diffusivities.

The exchange of heat at the interface air-water interface can be calculated through five different approaches. In the present study two of the most used heat flux models were employed: the Murakami heat flux model (Murakami et al., 1985) and the Ocean model (Gill and Adrian, 1982). In Delft3D no heat flux between the water column and the bottom is considered. The density of water can be calculated by using one of two different formulations of the equation of state: the Eckart's (Eckart, 1958b) and the UNESCO formulations (Unesco, Ices and SCOR, IAPSO, 1981). In the present study the latter was applied.

4.2.2. Model Set-Up: Computational Grid

The numerical grid used for this study was constructed using the data obtained during a bathymetrical survey with multibeam echo-sounding in 2019. The grid is curvilinear with cell resolution varying between 9 and 150 m. The grid cell resolution is at highest at the Buffer and at the Ferraria Bridge.

A Z-layer configuration with maximum 15 layers of maximum 1 m thickness was used for the calibration of the model. The number of active layers over time is dependent on the water depth of the reservoir, e.g., when the water level in the model reaches the spillway crest, the number of active layers ranges from 1 (at shallow locations) to 15 (near the dam) hence also dependent on the location of a point in the reservoir. The thickness of the bottom and surface layers varies with time and the spatial location within the study area. The thickness of intermediate layers remains constant over time and all over the model. An overview of the numerical grid in the horizontal and the vertical planes and the bathymetry of the Passaúna Reservoir are shown in the Figures 4.1 and 4.2 .

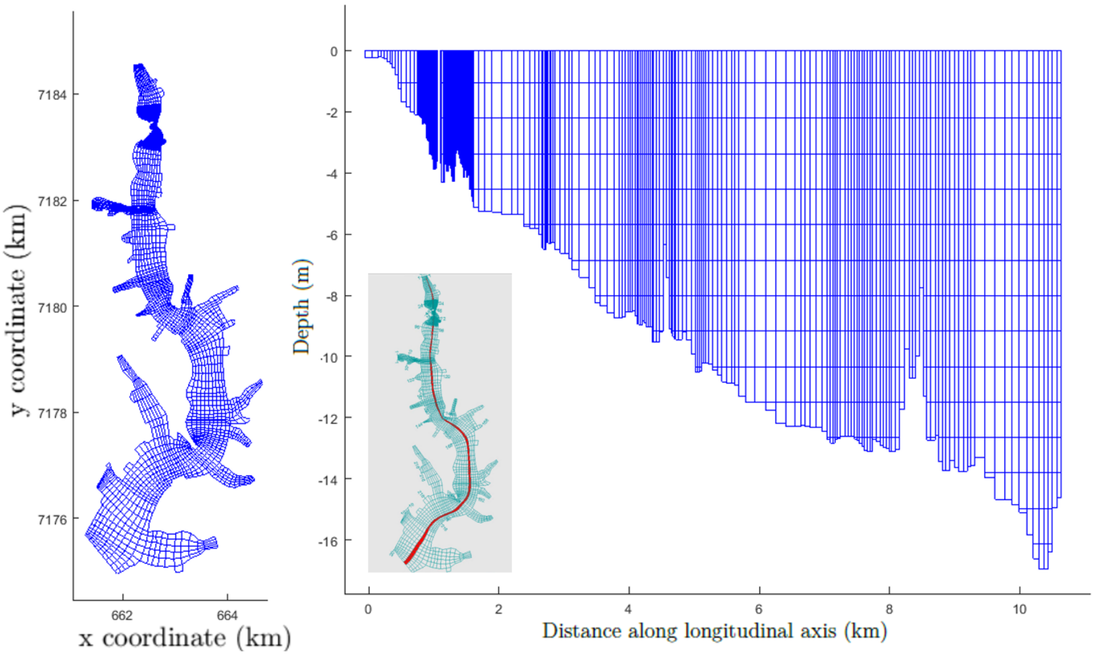

Figure 4.1.: Numerical grid. Left: view of the horizontal plane. Right: View along central longitudinal axis.

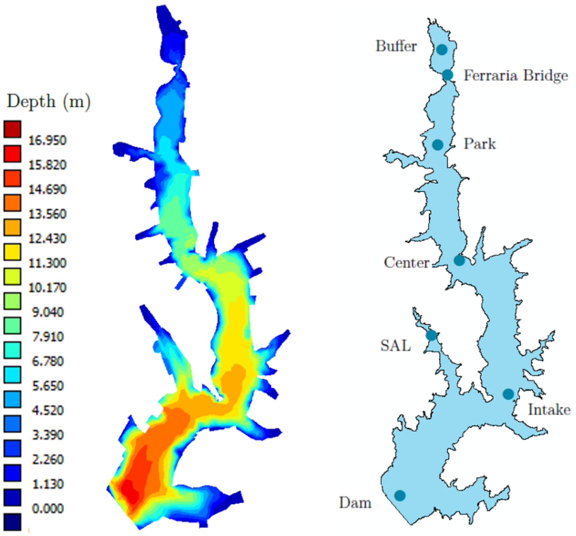

Figure 4.2.: Passaúna Reservoir. Left: Bathymetry of the water body with depth below the spillway crest (reference point). Right: relevant locations for the field measurements

4.2.3. Input and Monitoring Data

The simulations comprehended a period of 19 months, starting on August 2017 and going until the end of February 2019, selected according to the availability of monitoring data. The 7 first months were used as spin up for the model and the remaining months were considering as the time period for validation. As initial condition a uniform water temperature of 17 °C was applied, since according to measurements, in the month of August 2017 the Passaúna Reservoir was well mixed.

The model was calibrated using the measurements of the water temperature in eleven different depths at a location in the vicinity of the water Intake (point Intake showed in Figure 4.2). Those measurements were available for the period March 2018 to February 2019 in a 1-minute resolution and were performed with a thermistor chain (Minilog-II-T, Vemco, ± 0.1°C accuracy and 0.01 °C resolution). The measurements resulting from the thermistor chain were analyzed in section 3.2.3. Using loggers of the same type, water temperature was recorded at the locations Ferraria Bridge (abbreviated FB), Park and Side Arm Laggus (abbreviated SAL, see locations of the points in Figure 4.2) at one depth for different durations but all beneath the simulation period.

Measurements of the horizontal flow velocity were carried out with an Acoustic Doppler Current Profiler deployed (ADCP Signature 1000, Nortek AS) nearby the water Intake (position I1) with a resolution of 10 minutes (for the period Feb 2018- March 2019) and 5 minutes (for the period June 2018 - February 2019) (Ishikawa et al., 2021).

The incoming discharges through the main river and through the multiple tributaries and their respective temperatures were available in daily resolution. They are the result of a water balance and temperature model for the catchment, calibrated model in the software LARSIM-WT (Large area Runoff Simulation Model-Water Temperature) (Haag and Luce, 2008). In total 64 inflows were considered for the simulations and their location and denomination are shown in chapter 3 Figure 3.2. For the Passaúna River, measurements of the temperature of the incoming water were performed with a temperature-oxygen logger in an interval of 15-minutes and were prefered for the Delft3D-model set up over the results from the water balance model LARSIM, since the former were ground-truth data. A comparision of the values subministred by the two sources is shown in chapte 6 Figure 6.1. The discharge being extracted through the water Intake was available in hourly resolution with an average withdrawal rate of around 1.72 m^3/s for the studied period (see Figure 3.7 in chapter 3). The amount of water leaving the reservoir through the ground outlet was available in daily resolution with an average discharge of 0.44 m^3/s (see Figure 3.7 in chapter 3). The model was forced using the recorded water levels in a 30-minutes interval, the variation of the water level during the studied period was of about 1.5 m (see Figure 3.8 in chapter 3). Rainfall was measured in a pluviometric station situated at the dam of the reservoir with a daily time step and included in the model (see Figure 3.7 in chapter 3) . Evaporation is calculated by the model and included in the mass balance of the reservoir.

For the applied heat flux model, the meteorological parameters: air temperature, air humidity and solar radiation in a 15-minutes interval, as well as an average of the measured Secchi depth were used as input data (see Figure 3.9 in chapter 3). They were collected at a weather station located 4 km east from the study site. The cloud coverage data was gathered from the web-application InMeteo (2019) in a daily resolution. The measured wind velocity and direction were also used to force the model at the air-water interface in 15-minutes resolution. Due to the high resolution of the data, wind roses are presented for the wind related parameters (i.e. wind velocity and direction) and not just time series of them (see Figure 3.10 in chapter 3). The impact of the magnitude of the time step on the simulation's results was studied in preliminary investigations through sensitivity analyses and a time step of 2 minutes was selected for the calibration and further simulations. For all simulation a computer with the following specifications was used Intel ® Xeon® W-2145 CPU @ 3.70 GHz 3.70 GHz.

4.2.4. Statistical Model Quality Parameters

In order to evaluate the performance of the simulation results with respect to the measured data, different statistical metrics such as the mean absolute error (MAE), the root mean square error (RMSE) and the mean bias error (MBE) were used. The MAE (see equation 4.6) is a measure of the average magnitude of the errors of the simulation results. It is calculated as follows:

$$\mathrm{MAE} = \frac{1}{n} \sum_{j=1}^{n} |M_j - S_j| \tag{4.6}$$

Where n is the number of samples, M is the observed/measured value and S is the corresponding simulated value. The MAE does not consider the sub- or overestimation of the predicted values in relation to the observed ones. This metric considers high and low errors as equally important. The RMSE is the squared root of the average of the squared errors. The RMSE gives more weight to errors with larger absolute values than to errors with smaller absolute values, i.e. this statistical metric penalizes the variance (Chai and Draxler, 2014). Similar to the MAE, the RMSE does not consider the direction of the errors. By definition the RMSE is always larger than the MAE. The RMSE is calculated through the following equation:

$$\mathrm{RMSE} = \sqrt{\frac{1}{n} \sum_{i=1}^{n} (M_i - S_i)^2} \tag{4.7}$$

If the absolute value of the equation 4.6 is not considered, then the resulting metric corresponds to the MBE. The expression reads as follows:

$$\mathrm{MBE} = \frac{1}{n} \sum_{k=1}^{n} (M_k - S_k) \tag{4.8}$$

The MBE is not commonly used in model performance evaluation because positive and negative errors may cancel each other resulting in a low error which should not be interpreted as good performance of the model, instead the MAE is used. In the present study the MBE was used in some sensitivity analyses to evaluate if the model underestimates or overestimates the studied variable. All three mentioned statistical metrics express the error of the simulation's results in the same units as the studied variable and are negatively-oriented scores, i.e. the lower their values, the better the performance of the model.

4.3. Results and Discussion

This section is divided in four parts. In the first one (4.3.1), the calibration process of the model is explained and the effect of the variation of the parameters listed in Table 4.1 on the water temperature and velocities at the water Intake is analyzed. In the same part, further aspects of the hydrodynamics of the reservoir will be studied through the model's results at the Intake. In the second part 4.3.2, the hydrodynamics at further locations in the reservoir will be studied, the impact of the parameters listed in Table 4.1 wil also be investigated for positions different to the Intake . The third part 4.3.3 comprehends investigations regarding density currents and their role on the stratification and mixing processes in the reservoir. In this section the effects of the application of a sigma-layer model on the simulation's results are discussed as well. Closing the section (4.3.4), the influence of wind on the reservoir's hydrodynamics are presented and discussed.

4.3.1. Validation of Simulated Water Temperature and Flow Velocities

For the calibration of the model a reference simulation was defined. The input parameters for this simulation are summarized in Table 4.1. If not indicated the parameters are uniform in the whole model area and constant over time. The calibration of the model was carried out through sensitivity analyses of the reference simulation's parameters, variating one parameter at the time. Table 4.2. Shows the range of variation, which was defined according to the relevant literature (Deltares, 2014; Dissanayake et al., 2019; Polli and Bleninger,

Table 4.1.: Parameters used for the reference simulation. A, B, and C describe a piecewise selection of the wind drag coefficients in function of U_{10} wich is the wind velocity at 10 m above the ground.

Paramater	Magnitude	Units
Number of layers[1]	15	-
Manning's coefficient	0.035	$s/m^{-1/3}$
Wind drag coefficient	$C_{10}^{A} = 0.003 \quad U_{10}^{A} = 0 \quad m/s$ $C_{10}^{B} = 0.0025 \quad U_{10}^{B} = 1.25 \quad m/s$ $C_{10}^{C} = 0.0018 \quad U_{10}^{C} = 3 \quad m/s$	-
Background horizontal viscosity	0	m^2/s
Background horizontal diffusivity	0	m^2/s
Background vertical viscosity	0	m^2/s
Background vertical diffusivity	0	m^2/s
Ozmidov length scale	0	m
Dalton number	0.0013	-
Stanton number	0.0013	-
Secchi depth	2	m

[1] Maximum number of active layers. For a given position the number of active layers might vary depending on the local water depth, which is also a function of time.

2019b; Chanudet et al., 2012b; Wüest and Lorke, 2003; Wu, 1982; Smith and Banke, 1975; Chow, 1959) . Each simulation was assigned an abbreviation or denomination, which is also mentioned in Table 4.2 and will be used throughout the present chapter.

Table 4.2.: Summary of the simulations performed to evaluate the influence of the parameters listed in Table 4.1 on the simulated temperatures and velocities in the reservoir.

Parameter	Abbreviation	Magnitude	Units
Number of layers	L10	10	-
	L20	20	
Manning's coefficient	M1	0.01	$s/m^{(-1)/3}$
	M2	0.025	
	M3	0.15	
Wind drag coefficient	W1	0.0018	-
	W2	0.003	
Background horizontal viscosity	BHV1	0.625	m^2/s
	BHV2	1.25	
Background horizontal diffusivity	BHD1	0.625	m^2/s
	BHD2	1.25	
Background vertical viscosity	BVV1	0.0001	m^2/s
	BVV2	0.001	
Background vertical diffusivity	BVD1	0.0001	m^2/s
	BVD2	0.001	
Ozmidov length scale	OL1	0.05	m
	OL2	0.1	
Dalton number	DN1	0.0031	-
	DN2	0.006	
Stanton number	SN1	0.0031	-
	SN2	0.006	
Secchi depth	SD1	1	m
	SD2	2.6	

Table 4.3 shows the MAEs, RMSEs and MBEs for each simulation with respect to the measured temperatures and horizontal velocities at the Intake position. The variation of the number of layers affected the model's results and also the computational time needed to run the simulation. As expected, better results for the water temperature were obtained with increasing number of layers, which is reflected on both the MAE and the RMSE for the simulations L10, Reference and L20. In general, all three simulations overestimated the measured water temperatures, as can be observed in the MBEs. Figure 4.3 a displays the time averaged temperature over the water column of each simulation compared to the measured data. In this figure, it can be observed that the farther away from the bottom of the reservoir the more similar the predictions of the models become independently on the number of layers. Regarding the horizontal flow velocities, the resulting RMSEs and the MAEs are in the same range of magnitude (see Table 4.3, columns 5 to 7), suggesting little influence of the number of layers on the calculated horizontal flow velocities. Figure 4.4

a also indicates the similarity of the three simulations while predicting the time averaged horizontal velocities over depth. The computational times of the simulations were of 53, 77 and 100 hours for the 10, 15 and 20 layered models respectively. The resulting MAEs and the RMSEs of the simulations with 15 and 20 layers for the whole water column are similar in magnitude and according to these results, the employment of the 20 layered model would not deliver much better predictions than the 15 layered one, neither for the water temperatures nor the horizontal velocities. Due to the lower computational time, the model with a 15 layers setting was selected over the one with 20 layers for the following sensitivity analyses.

The studied range of the Manning's coefficient comprehended values between 0.01 and 0.15 $^{s}/_{m^{-1/3}}$ corresponding to a smooth artificial channel and to a rough natural channel with weedy reaches, heavy stand of timber and underbrush (Chow, 1959). According to the MBEs all four simulations (M1, M2, M3 and Reference) overestimate, in average, the measured temperatures (see Table 4.3). Figure 4.3 b evidences discrepancies of the time averaged temperatures of less than 0.5 °C, those being highest at the bottom layers. For the horizontal velocities, the largest error was obtained with the highest Manning's coefficient (see Table 4.3). Figure 4.4 b shows the time averaged simulated horizontal velocities along the water depth for the simulations M1, M2, reference and M3. It evidences how the change in the roughness' coefficient affected the magnitude of the calculated horizontal velocities through the water depth in some measure. Nevertheless, the major changes were found at the bottom layer. Given that the bottom resistance to the flow affects the cells near itself more than the cells close to the water surface.

At the interface water-air the boundary conditions for the momentum equation are related to the wind-shear stress which at the same time presents a linear dependency on the wind drag coefficient C_{10}, i.e. the higher thhe drag-coefficient, the higher the wind shear stress. In general, the wind drag coefficient depends on both the wind speed at 10 m above the water surface and the wave development state (Wüest and Lorke, 2003). In classical approximations such as the one from Wu (1982), the wind drag coefficient strictly increases with augmenting wind speed, which reflects a higher roughness of the water surface (Deltares, 2014). Further studies have identified an increase in the wind drag coefficient with decreasing wind velocity when the latter is lower than 3 m/s (Wüest and Lorke, 2003).

For the reference simulation a piecewise expression for the drag coefficient was defined according to the field data analysed and compiled by Wüest and Lorke (2003). The investigated values for the simulations W1 and W2 represent a constant wind shear stress, in which the shear stress for the simulation W1 ($C_{10} = 0.0018$) is lower than for the simulation W2 ($C_{10} = 0.003$) (Zhu et al., 2009; Wahl and Peeters, 2014; Soulignac et al., 2017; Dissanayake et al., 2019). Figure 4.3 c displays the time averaged horizontal water temperatures over the depth in function of the wind drag coefficient's studied values. The variation of the calculated temperature with respect to the reference simulation increase towards the reservoir's bottom for W1 and W2 as well. Observing the result of W2, the selection of a higher or lower wind drag coefficient than in the reference simulation, induces more and less mixing into the water column respectively. Due to the fact that the measured wind speeds are on average 2 m/s, the C_{10} adopts a value of 0.0018 for around 20% of the simulated period. Also to notice is the small difference in the time averaged water temperatures between the reference simulation and the simulation W1. The same is valid for the calculated time averaged horizontal flow velocities (see Figure4.4 c). It can be observed that the horizontal flow velocities changed all over the depth in some measure with respect to the reference simulation. A time-constant and high wind drag coefficient of 0.003 resulted in the highest time averaged flow velocities over the depth for all three explored wind drag coefficients.

Despite of the choice of C_{10}, the horizontal flow velocities are underestimated by the model, as can be seen in the sign of the MBE (see Table 4.3, column 7). Even though the resulting velocities from the simulation W2 are higher than the ones of the other two studied cases, they don't result in a lower error since the velocity peaks of the simulations do not coincide in time of occurrence with the peaks of the measurements. The lowest MAE and RMSE are obtained for the wind drag coefficients of the reference simulation (see Table 4.3).

In medium to large reservoirs the horizontal eddy viscosity is larger than the vertical eddy viscosity, since in those systems horizontal mixing is fast when compared to vertical mixing, as a result of this the most pronounced concentrations gradients develop along the vertical direction (Peeters et al., 1996). The background horizontal viscosities are used to account for the turbulent motions that are not resolved by the RANS (Deltares, 2014).

The magnitude of background horizontal diffusivity depends on great measure of the grid size and can be considered as a calibration parameter, since it offers the option of changing the diffusivity coefficients independent of the calculated vertical viscosity coefficient by the turbulence closure model. Both coefficients (vertical and horizontal), similar to the viscosities, account for forms of unresolved mixing. For the vertical background coefficients of the simulations, values of 1×10^{-4} m^2/s and 1×10^{-3} m^2/s were applied, which was selected based on the experience with simulation in high stratified flows with Delft3D (Deltares, 2014). For the horizontal ambient diffusivity and viscosity, the magnitudes of 6.25×10^{-1} m^2/s to 1.25 were used m^2/s (Chanudet et al., 2012b; Bogucki et al., 2005; Wahl and Peeters, 2014; Soulignac et al., 2017). The background values for the reference simulations represent a situation, where no additional mixing is necessary to that calculated by the $k-\epsilon$ turbulence closure model. Figure 4.3 d shows a decrease in the predicted time averaged water temperature with increasing background horizontal viscosity. Meanwhile, Figure 4.3 e. Presents the increase of the bottom temperature with increasing magnitude of the background horizontal diffusivity. A similar behavior is observed for the influence of the vertical background viscosity and diffusivity on the calculated temperature (see Figure 4.3 f and g). The evident increase in the water temperature, when augmenting the horizontal and vertical diffusivities is due to the inclusion of further mixing into the model. In all cases, the changes in the time averaged temperature took place at the bottom layers of the model. Figure 4.4 d and Figure 4.4 e display respectively, the decrease of the simulated time averaged flow velocities over the depth with increasing horizontal background viscosity and diffusivity. Nevertheless, this tendency in the horizontal velocities is further accentuated in the case of the horizontal background viscosities. The same trend is observed in Figure 4.4f and g, when studying the effect of the vertical background coefficients on the simulated time-averaged horizontal velocities. According to the calculated MAEs and RMSEs, no additional mixing to the one calculated by the turbulence closure model is necessary (see Table 4.3).

The Ozmidov length scale (Loz) represents mixing through the water column induced by the breaking of internal waves in strongly stratified flows (Chanudet et al., 2012b). Since, the current turbulence closure models available in Delft3d, are not able to simulate this, the introduction of a Loz may be necessary. This variable typically ranges from centimeters to several meters (Wüest and Lorke, 2003). For the reference simulation a value of 0 m was selected, indicating a situation where no additional mixing caused by the breaking of internal waves was lacking. For the simulations OL1 and OL2 additional mixing was introduced (Chanudet et al., 2012b) (see Table 4.2). The increment in the Loz has as consequence the increase of the simulated time averaged temperatures and the decrease of the horizontal velocities in comparison to the case with no additional mixing (see Figure 4.3 h and Figure 4.3 h). For the time averaged velocities, the major changes were found at middle layers (5 to 8 m above the reservoir bottom), meanwhile for the temperatures the variations were concentrated towards the bottom layers. While comparing the measurements to the simulations Reference, OL1 and OL2 was found that a Loz of zero was the best fit for the model (see Table 4.3).

The Ocean model (Gill and Adrian, 1982; Lane, 1989) was calibrated for the North Sea and it has been applied with success to numerous lakes and reservoirs (Zhu et al., 2009; Chanudet et al., 2012b; Wahl and Peeters, 2014; Soulignac et al., 2017). The use of the ocean model, implies the calculation of the heat losses of the water body due to evaporation and convection. In order to calculate the evaporative and convective heat fluxes at the water surface, the Dalton number and the Stanton number are required. The reference values for these two numbers were selected based on the studies developed at a reservoir in the vicinity of Passaúna Reservoir (Polli and Bleninger, 2019b). Similar values were obtained at the North See (Dalton number $c_e = 0.0015$ and Stanton number$C_H = 0.00145$) (Lane, 1989) and within the framework of additional studies performed with Delft3D in different lakes or reservoirs around the world (Chanudet et al., 2012b; Soulignac et al., 2017). The decrease on the water temperature with the increase of the magnitude of the Stanton number is mostly uniform all over the water column, as can be observed in the Figure 4.3 i. Figure 4.3 j. displays the same behavior for the Dalton number. Nevertheless, the changes of the water temperature over the depth with respect to the reference simulation were more pronounced with the variation of the evaporative heat flux than with the convective heat flux. The major changes on the time averaged horizontal flows velocities took place in layers between 6 and 9 m above the reservoir's bottom (see Figure 4.4 j and Figure 4.4 h). For those layers, the increase on the Dalton number produced a decrease on the horizontal flow velocities. The variation of the Stanton number caused an opposite effect on the time averaged horizontal flow velocities when compared to the variation of the Dalton number. Also, the magnitude of the variations of the horizontal flow velocities for the former were much lower than for the latter. The use of a Stanton number of 0.031 and a Dalton number of 0.0013, delivered the lowest errors (see Table 4.3) when compared to the measured water temperatures and horizontal flow velocities.

For the applied heat flux model, the portion of the incoming solar radiation absorbed at the surface and the part absorbed at deeper layers can be determined in function of the extinction coefficient of the water for a specific case. This coefficient is inversely proportional to the Secchi depth, which is a measure for the clarity of the water. During the field campaigns for the present study, several measurements of the Secchi depth at different dates were performed. The reference value corresponds to an average value (see Table 4.1) and the values in Table 4.2 are the lowest and highest measured Secchi depths. The increase of the water clarity produced the obtention of increase water temperatures towards the reservoir bottom (see Figure 4.3 i), since the incoming solar radiation could be distributed and adsorbed further into the water column with increasing Secchi depth. Figure 4.4i shows how the increase on the Secchi depth, produced a decrease on the time averaged horizontal flow velocities, with the variations being more pronounced towards the water surface.

As can be appreciated in Table 4.3, all simulations underestimated the horizontal velocities at the Intake position. The lowest errors (Table 4.3) were obtained for the simulation SN1 (0.38 °C), whose configuration will be considered as the calibrated simulation for the further analyses. Figure 4.5 displays a comparison of the measured and simulated water temperatures over the depth for the Intake position. The model reproduced well the sequence of measured stratified and mixed periods for the Passaúna Reservoir. The highest underestimation of the water temperature was of about 2 °C (see Figure 4.5 c) and it occurred mainly at the bottom of the reservoir (2 to 4 m above the ground). Around the end of November 2018, the model overestimated the temperatures at the most by 2 °C (see Figure 4.5 c). In average, the highest MAEs were observed at the bottom layers of the reservoir and the lowest ones at around 4 m above the reservoir bottom (Figure 4.5 a).

Table 4.3.: Statistical metrics for the simulated water temperatures and horizontal flow velocities at the Intake position regarding the measured temperatures for the period March 2018 until February 2019. Columns (2) to (4) show the MAEs, RMSEs and MBEs for the simulated temperatures over the depth for the whole water column for each simulation. Similarly, columns (5) to (7) show the MAEs, RMSEs and MBEs of the simulated horizontal flow velocities over the depth for the whole water column.

Simulation (1)	MAE ($°C$) (2)	RMSE ($°C$) (3)	MBE ($°C$) (4)	MAE (cm/s) (5)	RMSE (cm/s) (6)	MBE (cm/s) (7)
L10	0.77	1.05	0.73	1.03	1.42	-0.57
Reference	0.55	0.71	0.49	1.01	1.39	-0.58
L20	0.54	0.69	0.35	1.03	1.41	-0.6
M1	0.61	0.79	0.57	1.04	1.42	-0.48
M2	0.56	0.73	0.51	1.02	1.4	-0.54
M3	0.6	0.75	0.55	1.1	1.49	-0.75
W1	0.53	0.68	0.44	1.02	1.4	-0.61
W2	0.9	1.21	0.88	1.07	1.45	-0.41
BHV1	0.54	0.68	0.31	1.08	1.47	-0.8
BHV2	0.58	0.74	0.21	1.14	1.54	-0.93
BHD1	0.73	0.92	0.7	1.07	1.45	-0.68
BHD2	0.8	1.02	0.77	1.1	1.48	-0.73
BVV1	0.57	0.74	0.14	1.19	1.61	-1.02
BVV2	0.82	1.2	-0.3	1.58	2.04	-1.56
BVD1	1.25	1.77	1.21	1.13	1.53	-0.74
BVD2	1.43	1.95	1.38	1.3	1.74	-1.01
OL1	1	1.45	0.97	1.07	1.46	-0.63
OL2	1.16	1.67	1.13	1.13	1.53	-0.7
DN1	1.19	1.25	-1.18	1.04	1.43	-0.63
DN2	2.83	2.87	-2.83	1.07	1.47	-0.67
SN1	0.38	0.48	0.12	1.01	1.38	-0.57
SN2	0.49	0.59	-0.36	1	1.37	-0.55
SD1	0.48	0.64	0.09	1.01	1.38	-0.43
SD2	0.75	0.96	0.71	1.01	1.38	-0.69

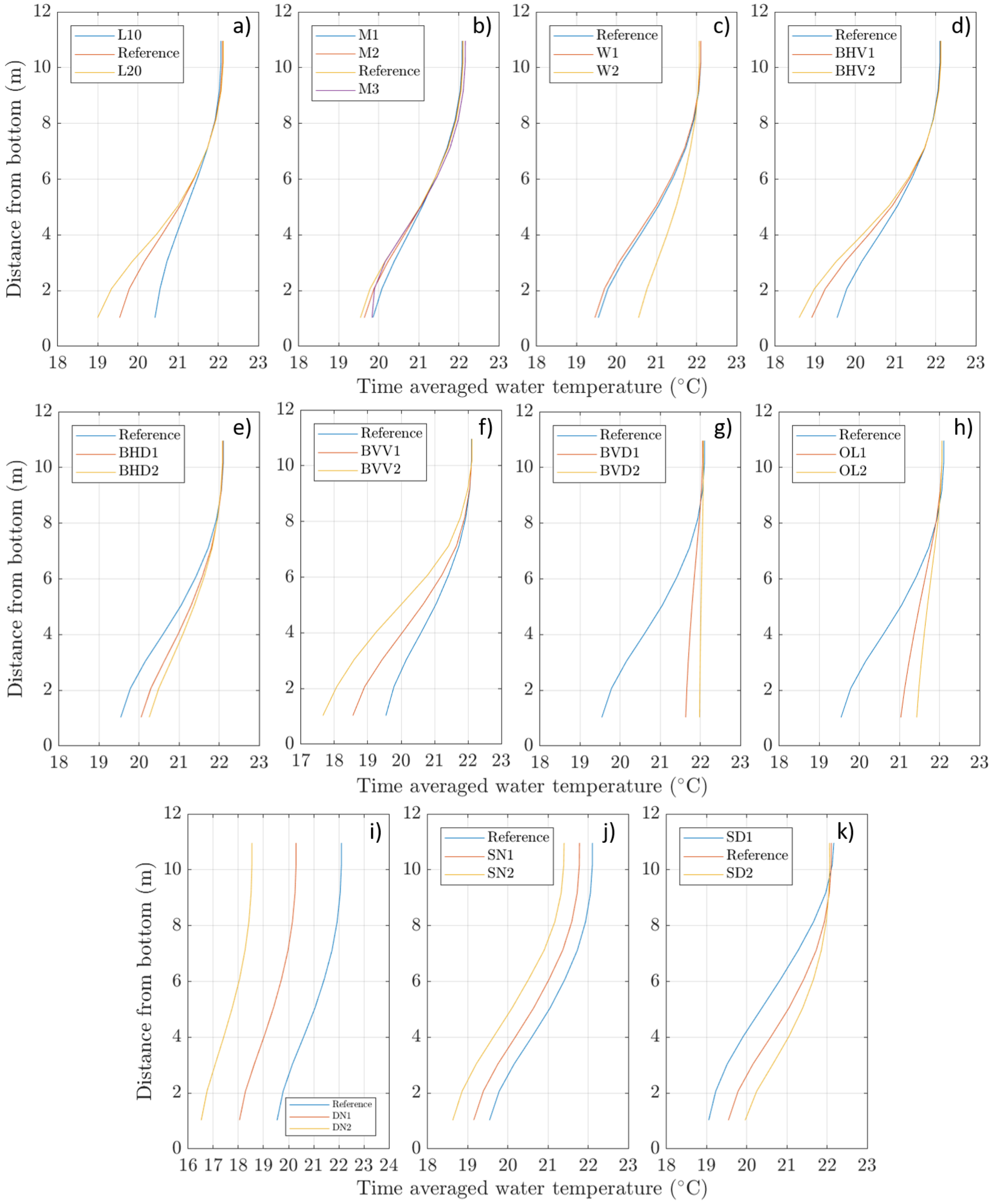

Figure 4.3.: Time averaged temperatures over the water column for the variation of the parameters listed in Table 2 at the Intake position. Each figure represents the variation of one parameter, namely: a) number of layers, b) Manning's coefficient, c) wind drag coefficient, d) background horizontal viscosity, e) background horizontal diffusivity, f) background vertical viscosity, g) background vertical diffusivity, h) Ozmidov length scale, i) Dalton number, j) Stanton number and k) Secchi depth.

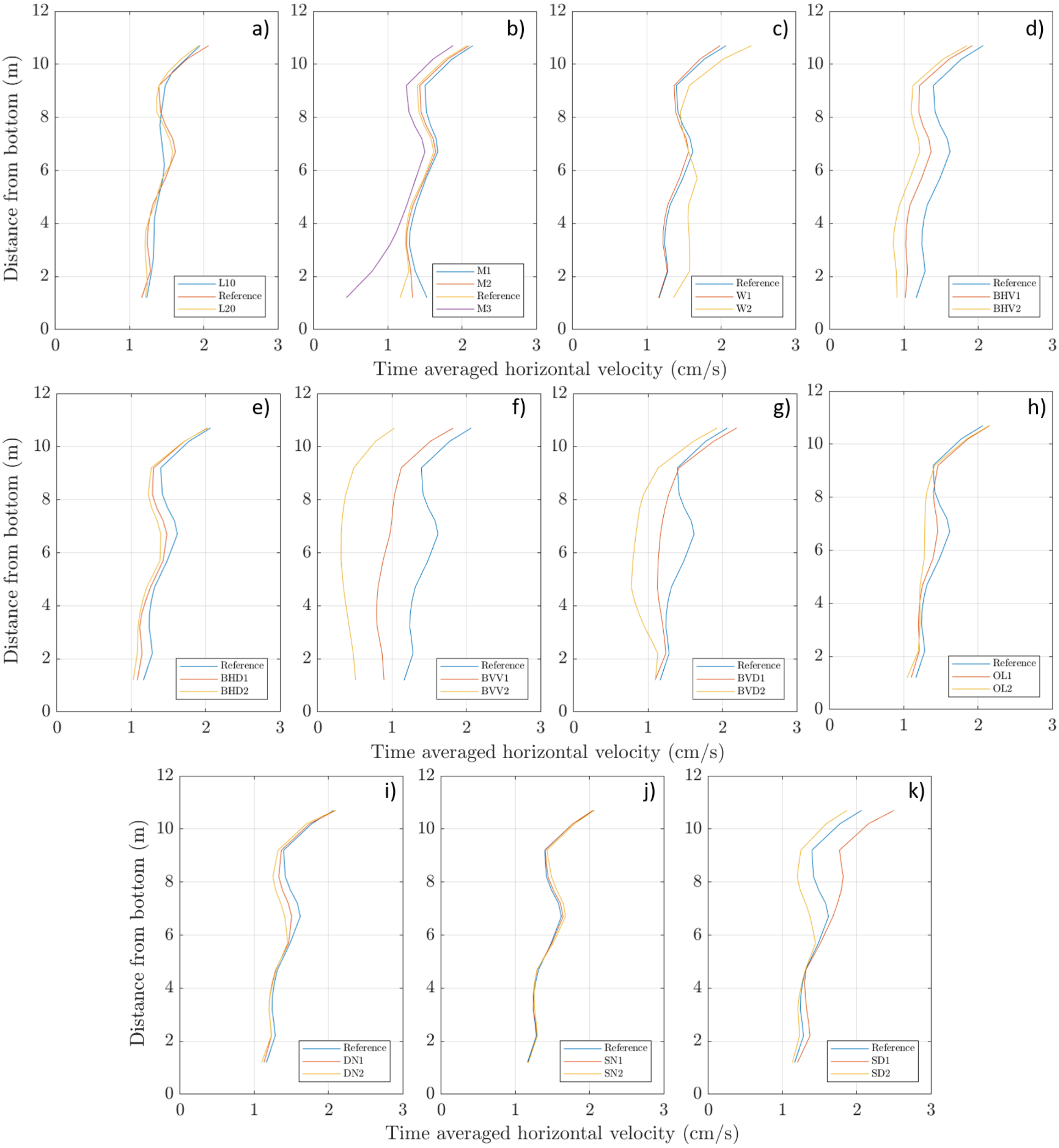

Figure 4.4.: Time averaged horizontal flow velocities over the water column for the variation of the parameters listed in Table 2 at the Intake position. Each figure represents the variation of one parameter, namely: a) number of layers, b) Manning's coefficient, c) wind drag coefficient, d) background horizontal viscosity, e) background horizontal diffusivity, f) background vertical viscosity, g) background vertical diffusivity, h) Ozmidov length scale, i) Dalton number, j) Stanton number and k) Secchi depth.

For the further analysis and modelling the simulation SN1 was selected as the calibrated version of the model. This simulation presented the lowest MAE for the temperature and the second lowest for the flow velocities. The range of the MAE/RMSE for the temperature were similar in order of magnitude to further studies of hydrodynamics in reservoirs (Mi et al., 2020; Dissanayake et al., 2019; Soulignac et al., 2017; Chanudet et al., 2012b; Marti et al., 2011).

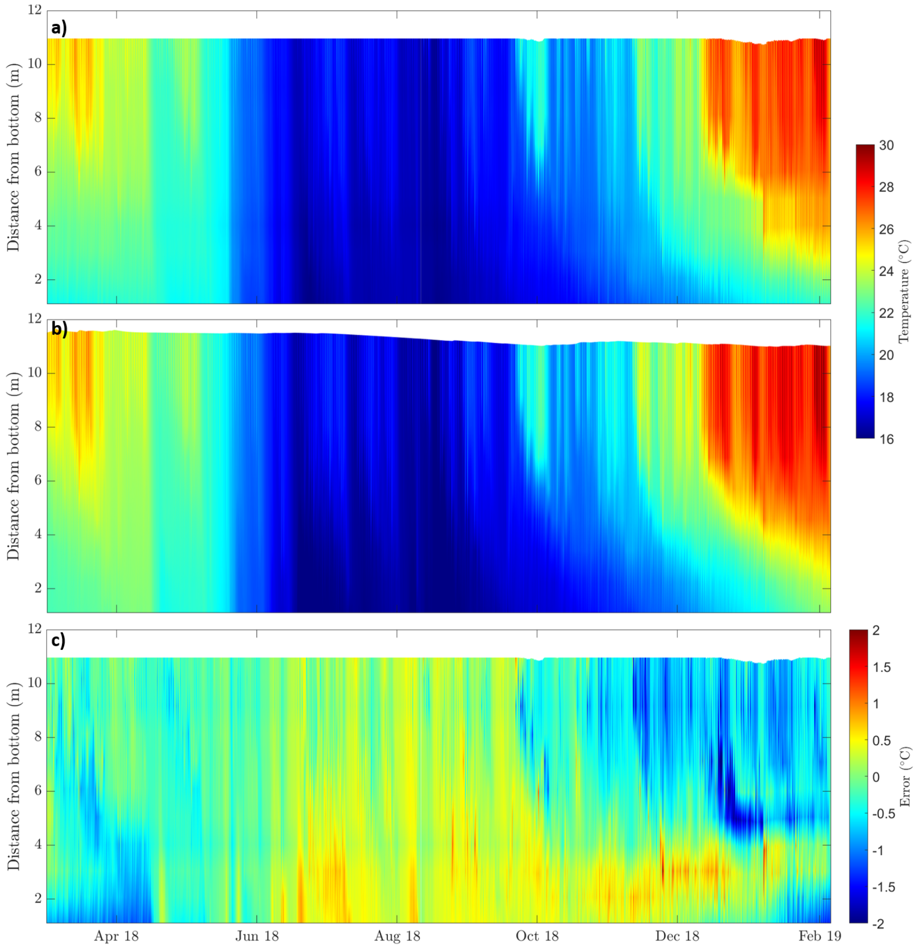

Figure 4.5.: Comparison of the modeling results to the measured water temperatures at the Intake position for the period March 2018 until February 2019: a) measured water temperatures, b) simulated water temperatures and c) error for the calibration period. The magnitude of the error corresponds to the expression: measured temperature - simulated temperature.

Even though the MAE/RMSE for the velocities were over 1 and 1.38 cm/s respectively, they were also in a similar order of magnitude than existing investigations for similar reservoirs (Dissanayake et al., 2019; Chanudet et al., 2012b). Figure 4.5 shows the thermal stratification at the Intake position for the studied period. Visually, the measured and simulated temperatures are in the same range also represeting temporal synchronization. Mid-March, at the beginning of October and during January the model calculated higher temperatures than the actually presented in the reservoir. On the other hand, for the bottom of the reservoir for the period October - January the model presented lower temperatures than the field measurements. The errors also show this information. They are positive and had higher absolute value (highest underestimation of the temperature) mostly for the bottom of the water column. The highest overestimation of the temperature according to errors, took place during January.

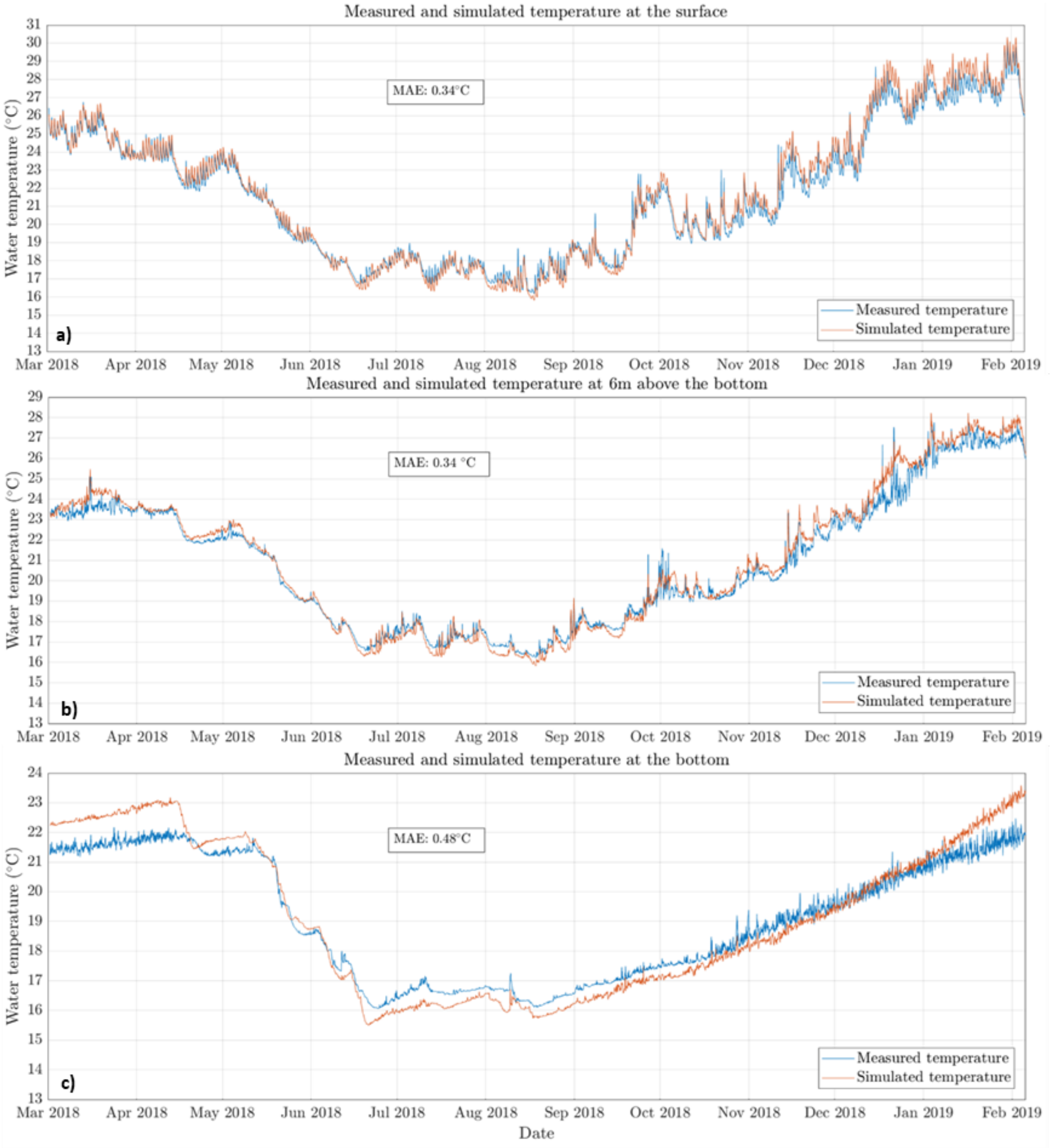

Figure 4.6.: Simulated and measured water temperature at the Intake position at three depths: a) surface (approx. 11 m above the ground), b) middle i.e. about 6 m above the reservoir's bottom and c) at the bottom of the reservoir (i.e. ca. 1 m above ground).

Figure 4.6 compares the simulated and measured water temperatures at the surface, middle and bottom of the water column. The MAE for the illustrated vertical positions indicates the poorest agreement for the bottom of the reservoir and the predictions for the middle and surface being similarly good. This may be due to the fact that the temperatures at the surface and near it are stronger ligated to the surface boundary conditions than deeper layers and if the quality of the meteorological forcing is high, the predictions of the model will be also of good quality. The disagreements at the bottom are evident specially for the stratified periods (March to Mid-April 2018 and January 2019). The time averaged MAE along the water column (see Figure 4.7 a) are indeed higher at the bottom of the reservoir. Nevertheless, the MAE is not the lowest at the surface of the reservoir but at a deeper layer at approx. 4 m above the bottom. For layers deeper than this, the MAE consistently increases. On the other hand, the MAEs remain between approx. 0.3 and 0.4 °C but not consistently decreasing towards the surface. The temporal development of the depth averaged MAEs (see Figure 4.7 b) indicates that the model performed the poorest during the summer and the best agreement was achieved during winter.

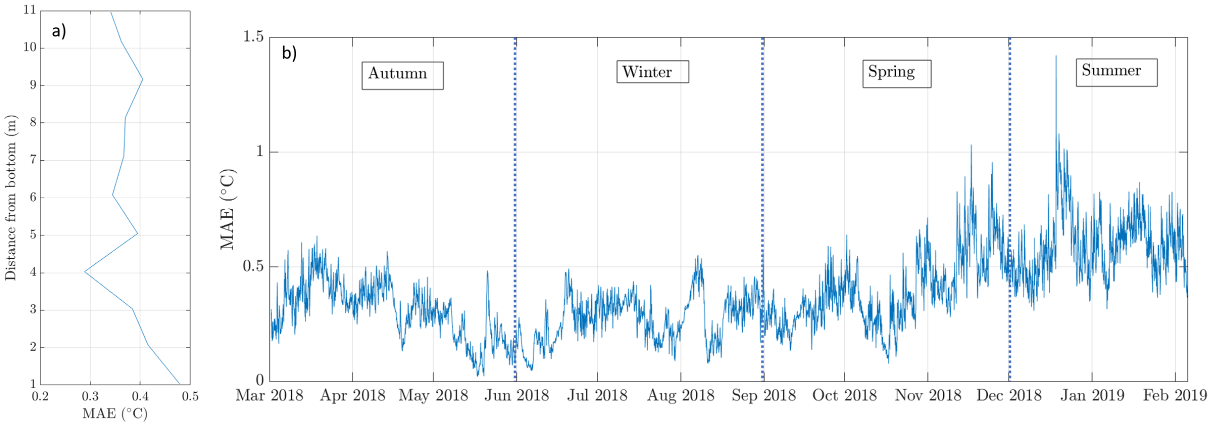

Figure 4.7.: Development of the MAE for the simulated water temperatures at the Intake position: a) time averaged MAE over the water column and b) temporal variation of the depth averaged MAE.

Figure 4.8 compares the simulated and measured horizontal velocities for three depths. The model made better predictions for the bottom of the water column than for the shallower locations. Which is the oppossite case than for the simulated temperatures. The velocity peaks at the water surface are not reached in the simulation. Also some peaks in the simulation are not found in the measurements. A possible explanation for this is the source of the input data related to the wind: the meteorological station is located 4 km away from the Reservoir. This could lead to different not only wind speed and direction but also to different moments for the occuring of velocity peaks at the study area in comparison with a location 4 km away in the city of Curitiba. The time-averaged MAEs for the horizontal velocity along depth show the quality of the mode predictions increases towards the bottom, describing a constant quality of the model performance 2 and 9 m above the bottom. The depth-averaged MAEs for the velocities over time does not show remarkable tendencies for a specific season to have higher or lower model performance.

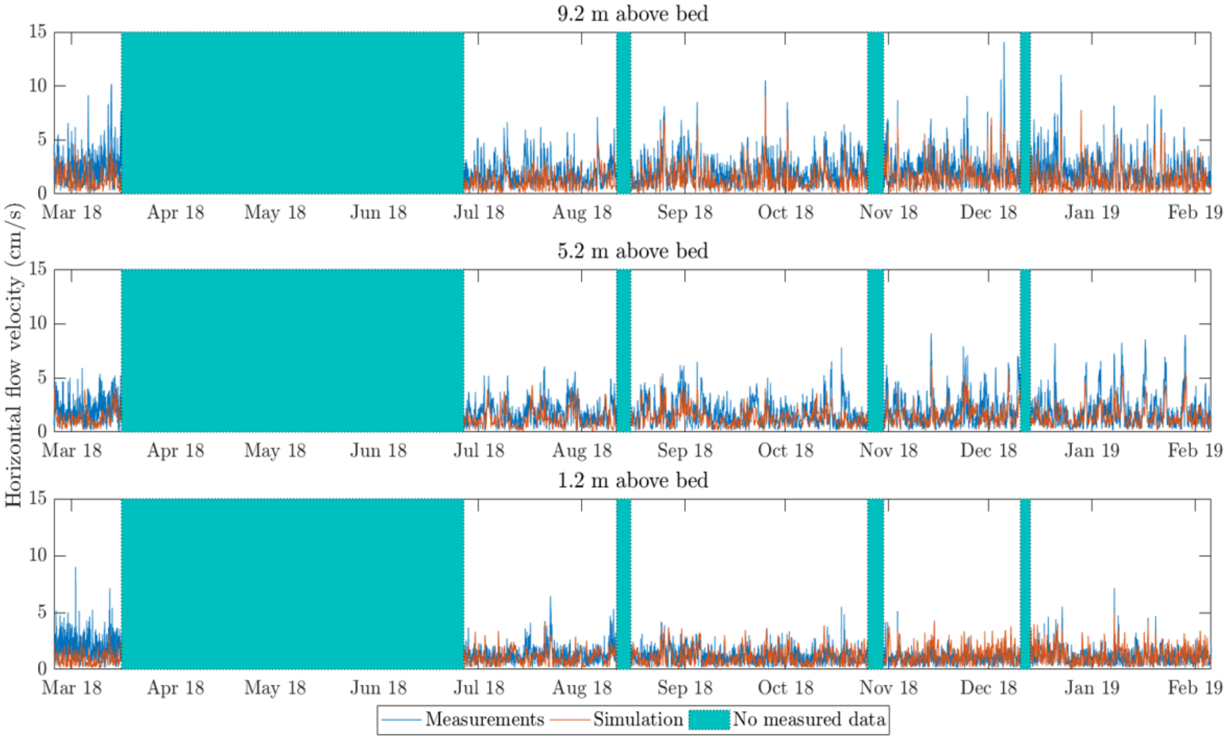

Figure 4.8.: Simulated and measured horizontal flow velocities at the Intake position at three different depths: a) 9.2 m b) 52 and c) 1.2 m above the reservoir bed for the period March 2018 until February 2019.

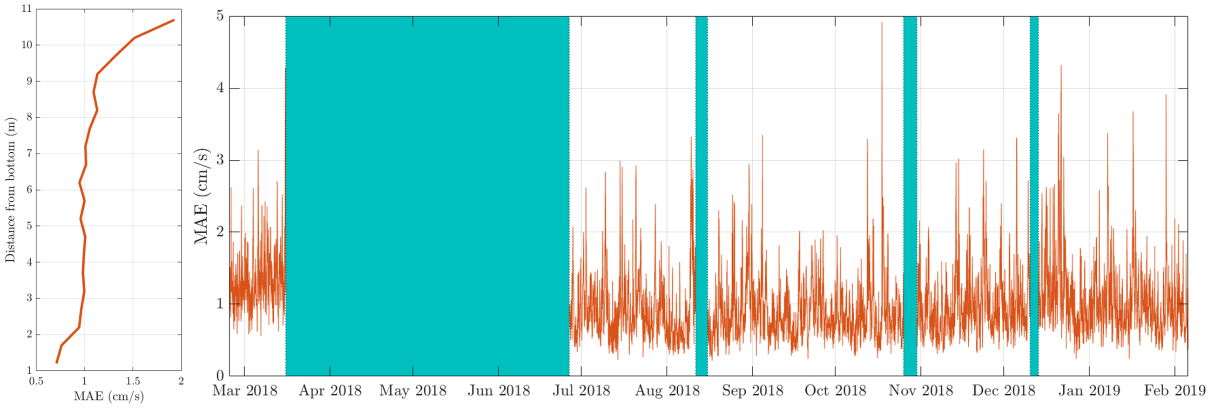

Figure 4.9.: Development of the MAE for the simulated horizontal flow velocities at the Intake position: a) time averaged MAE over the water column and b) temporal variation of the depth averaged MAE. The cyan colored rectangles represent periods, in which no measurements of the flow velocities were performed.

Figure 4.10 shows some characteristic parameters to evaluate the stratification of the water body. For the reservoir those indexes were calculated based on the measurements in chapter 3. The buoyancy frequency has it highest magnitude during summer, for this period the disagreement between the simulated and measured buoyancy are the highest. Not being this the case for the Weddeburn and Lake Numbers. For those indexes, the highest discrepancies occured during fall. The simulation partially showing lower values of both parameters during this period. The model suggest that the stratification is not as strong as in the measurements for the Fall, as the Schmidt stability is lower fofr the simulation than for the measurements during Fall. Meanwhile, the strength of stratification seems to be overpredicted by the model during the spring and the summer.

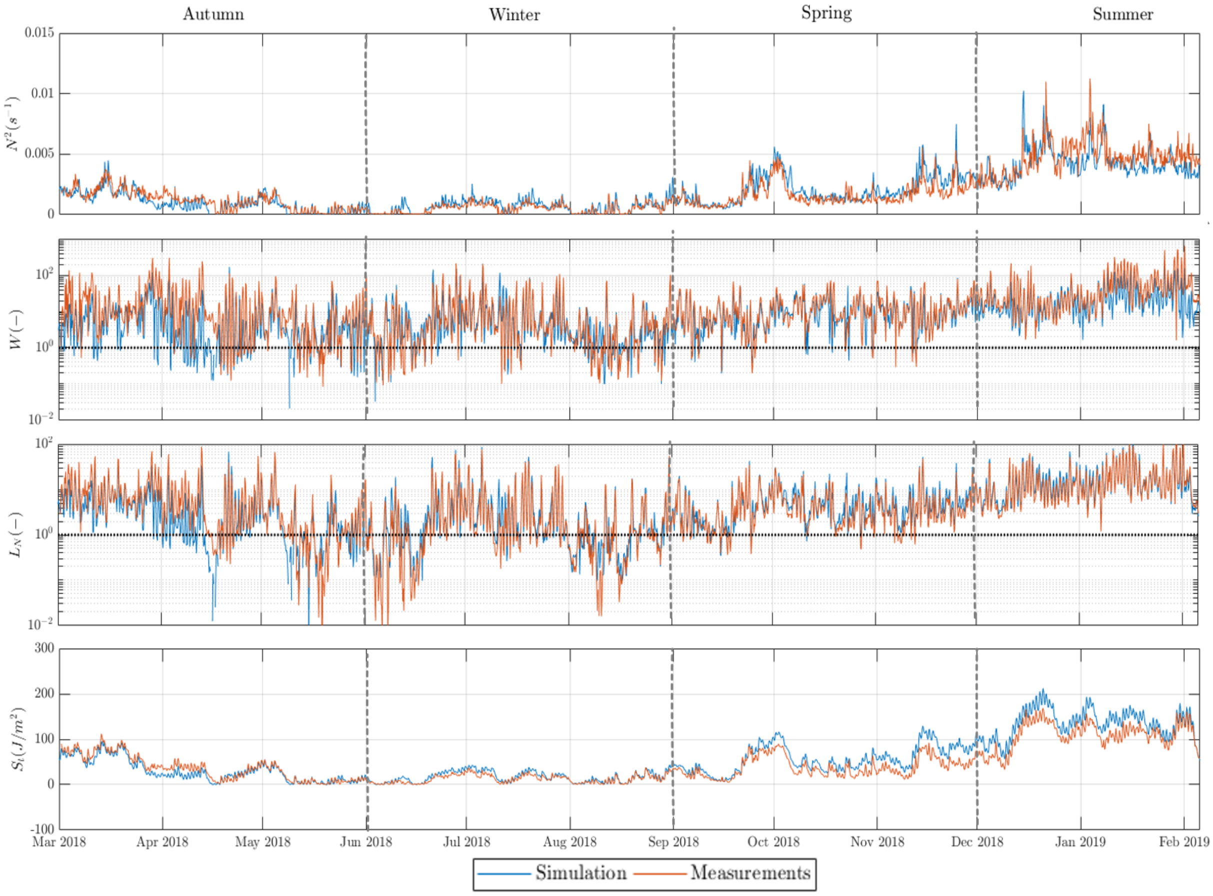

Figure 4.10.: Measured and calculated characteristic parameters for stratification. From top to bottom: buoyancy frequency, Weddeburn's number, Lake number and Schmidt stability.

4.3.2. Analysis of Hydrodynamics of the entire Reservoir

Measurements of the temperature were also available at the points Ferraria Bridge, Park and SAL (Side Arm Laggus). For those positions just one single point at one depth was measured. Figure 4.11 illustrates the course of the simulated temperatures at each of those positions in comparison with the measurements. The best agreement occurs at SAL and the poorest at the Ferraria Bridge. The course of the simulation results is the same as in the measurements. At the Ferraria Bridge the highest discrepancies are found during March 2018, where the thermistor at the reservoir registered higher temperatures than the modeled ones, with peaks reaching up to 32 °C.

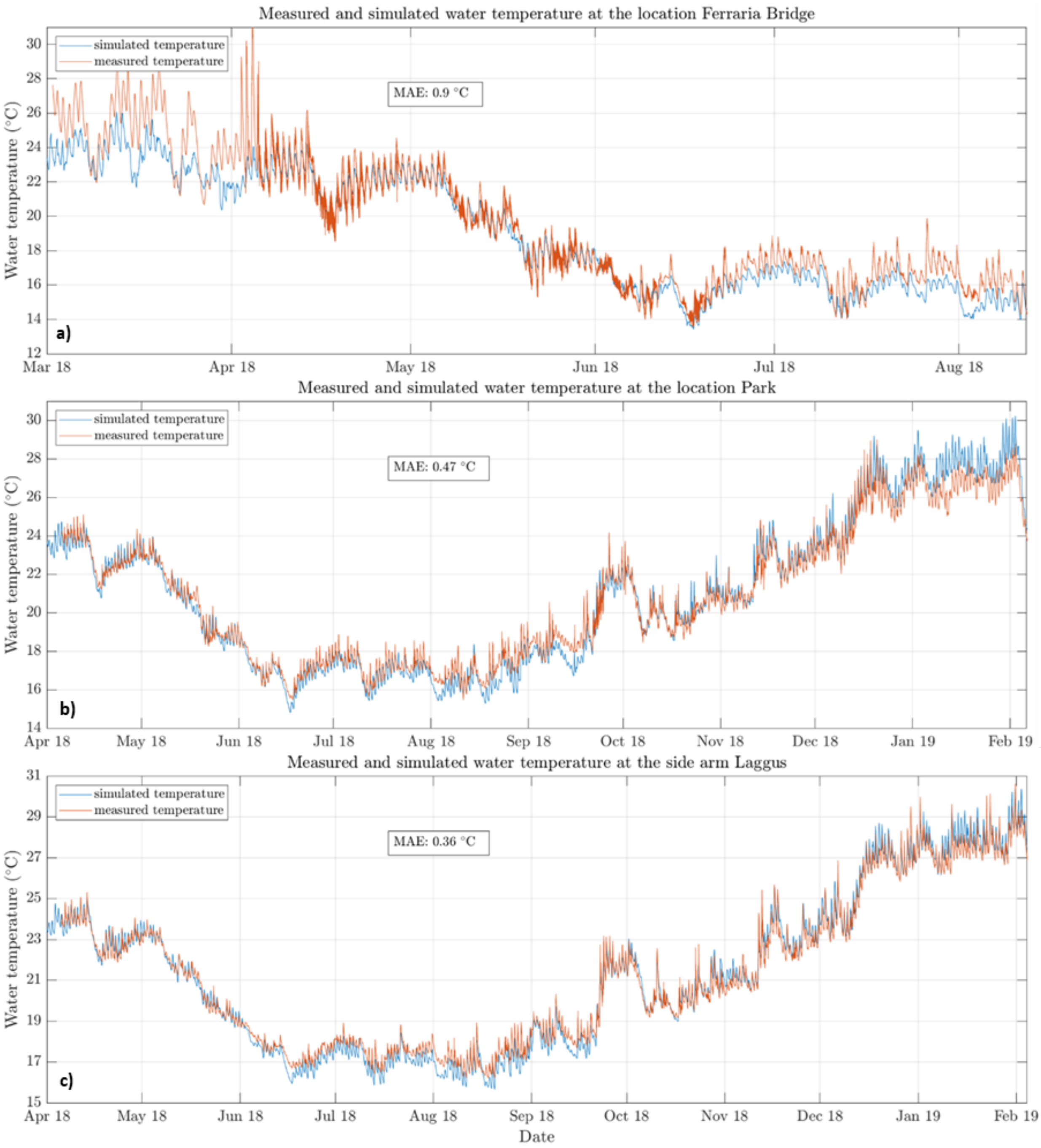

Figure 4.11.: Simulated and measured water temperatures at the positions a) Ferraria Bridge (1 m below the water surface), b) Park (2 m below the water surface) and c) Side Arm Laggus (2.8 m below the water surface).

In contrast, the model did not calculated temperature higher than 26 °C for this position. One could say that the shallowness of the location could be responsible for this disagreement, but after April 2018 the match with the measurements improves substantially. One possibility is that the meteorological data for the month of March are not accurate enough. The position Ferraria Bridge is also directly after the Buffer and the dynamics at this prebay may also have a negative influence on the simulation results if they are not well captured by the model. Nevertheless, the simulations results captured well the dynamics at the SAL and notice that this side arm has a similar morphology to the Buffer. In general, the model was able to reproduce well the behaviour of the temperature also at locations different than the Intake, with time averaged MAEs variating between 0.36 and 0.9 $°C$.

The simulated temperature gradients at several points over the reservoir are shown in Figure 4.12. The location Dam registered the highest temperature gradients of the studied positions. It is important to mention that this position is also the deepest and hence the solar radiation or mixing processes may not be able to rise the temperature of bottom layers in comparison to shallower locations. The temperature gradient at the Dam reaches magnitudes up to 9.2 $°C$ during the summer and with gradients mantained under 3 $°C$ for most part of fall and summer. For middle depths positions like SAL and Park the temperature gradients remained under 3 $°C$, with the position Park showing higher temperature gradients than SAL. This maybe due to the fact, that SAL is situated nearby a secondary inflow, wich delivers much less discharge to the reservoir than the main inflow. The position Ferraria Bridge shows somewhat higher temperature gradients than the deeper positions Park and SAL, which may be due its position right after the Buffer. At the position Center, the gradients reached the 6.4 $°C$ with peaks both in spring 2017 and summer 2019. In general, the simulation results showed the temperature gradients to be the highest for the positions with the highest water depths. It is interesting to observe than the course of the temperature gradients is not same for all positions, suggesting an influence of the water depth and also the vicinity to the model inflows on the thermal dynamics of the several points studied.

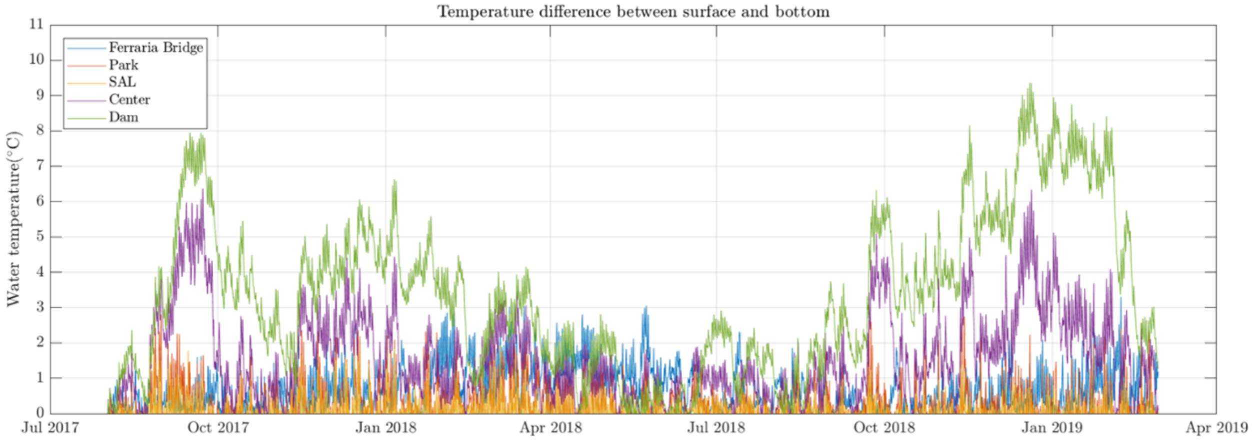

Figure 4.12.: Temperature gradients (difference between simulated temperature at the surface and at the bottom layer) at the positions Ferraria Bridge, Park, Side Arm Laggus, Center and Dam for the whole simulation period.

Table 4.4 presents the percentage of time regarding the whole simulation period for which a specific temprature gradient is present at all points indicated in Figure 4.2. Temperature gradients higher than 5 $°C$ were dominant at the Dam. Meanwhile for shallower locations like the Ferraria Bridge, Park and the SAL, temperature gradients of less than 1 $°C$ were

Table 4.4.: Percentage of time with a determinate temperature gradient for the positions Ferraria Bridge, Park, Side arm Laggus, Center, Intake and Dam.

Position	$\Delta T \leq 1°C$	$1°C < \Delta T \leq 2°C$	$2°C < \Delta T \leq 3°C$	$3°C < \Delta T \leq 4°C$	$4°C < \Delta T \leq 5°C$	$\Delta T > 5°C$
FB	73	23.6	3.3	0.1	0	0
Park	91.2	8	0.8	0	0	0
SAL	98.6	1.4	0	0	0	0
Center	39.3	30.6	16.6	8	4.8	1.5
Intake	21.8	20.9	18	15.1	8.9	15.3
Dam	15.5	17.1	15.1	18.2	11.3	22.8

dominant. It calls the attention that at the Ferraria Bridge gradients higher than 1 $°C$ were present for a significant amount of time (27% of the time) when compared to the deeper positions Park and SAL. Low temperature gradients were also present at the Intake and even at the dam (lower than 1 $°C$) for 21.8 % and 15.5 % of the time respectively. A generalization of the percentage of time that a specific temperature gradient is exceeded all over the study area is shown in Figure 4.13. In general temperature gradients higher than 6 $°C$ are not common and the take place in the southern deepest region of the reservoir. These illustrations clearly show that horizontal temperature gradients are present in the reservoir and hence the measurement of vertical temperature profiles at just one position of the water body will no be enough to understand the stratification/mixing taking place all over the reservoir. This is an evident advantage for 3D-numerical models, which once calibrated can offer an insight in the dynamics of the water body for fictional scenarios or non-measured conditions for all the reservoir area. Similar illustration were presented by Polli and Bleninger (2019b) for a different reservoir in Brazil.

Even though measurements of the flow velocities at positions different from the Intake were not performed, analysing the simulation results of the calibrated model gives an insight in the hydrodynamics at other location or regions. Figure 4.14 presents the time averaged horizontal velocities at six positions going from the shallow zones at the Buffer or the SAL, to the transition zone like Park and at the lacustrine zone. The 75^{th} and 25^{th} percentiles at each diagram allow to identify the magnitude range in which 50% of the horizontal flow velocities are to be found along the depth. In general, the simulated time averaged velocities range between 0.4 and 2.7 cm/s. Meanwhile the highest 75^{th} percentile reaches the 3.5 cm/s at the surface of the point Center and the lowest 25^{th} percentile accounting for 0.25 cm/s at the bottom of the SAL. The time averaged velocities of most positions show a lower value at the bottom in comparison to the water surface. Nevertheless, the velocities do not consistently decrease from the top to the bottom of the water column, as may be expected in classical river hydrodynamics.

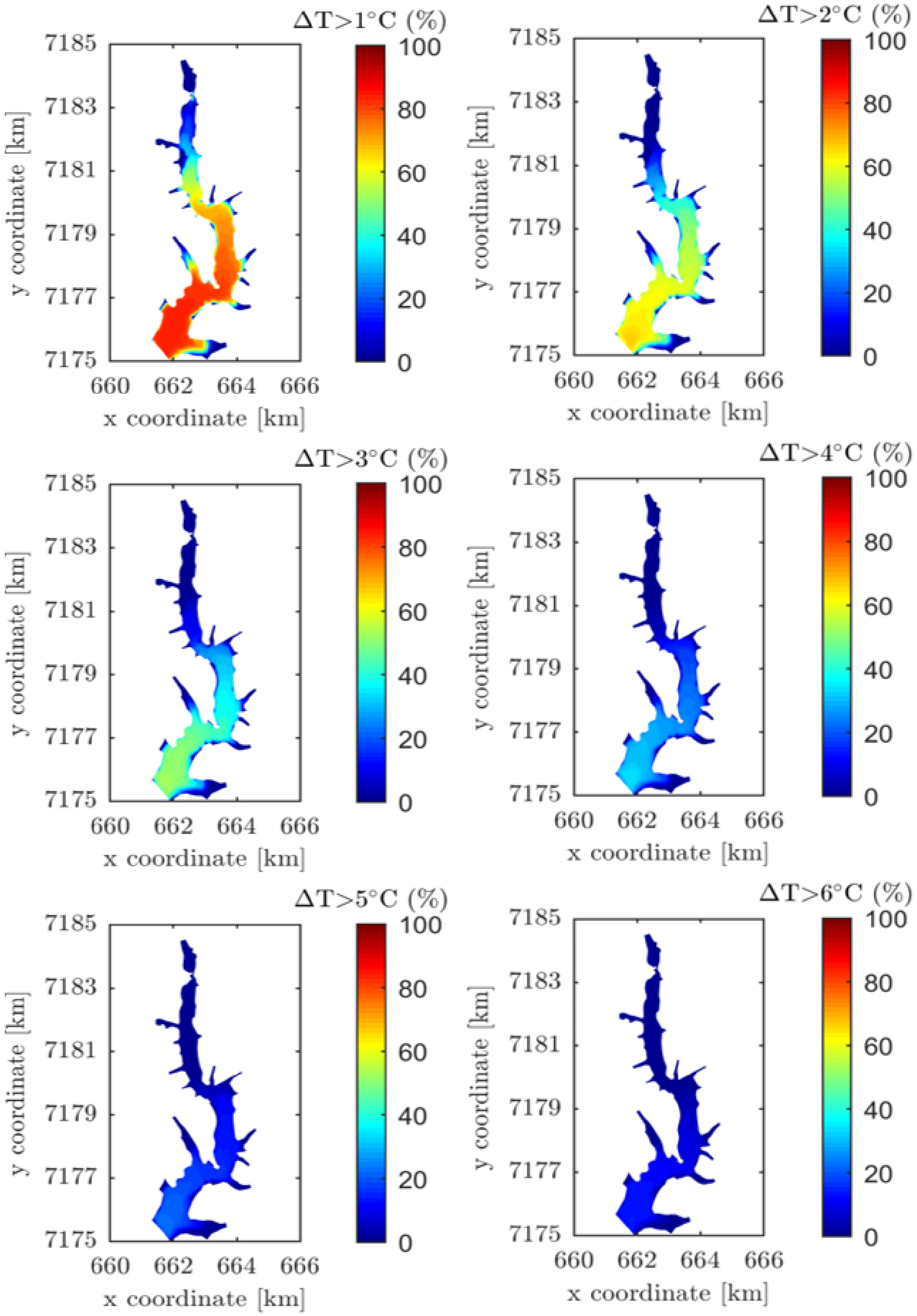

Figure 4.13.: Percentage of time for which a temperature gradient of a) 1 °C, b) 2 °C, c) 3 °C, d) 4°C, e) 5 °C and f) 6 °C is exceed on the Passaúna reservoir for the modeled period between Aug 2017 until Feb 2019.

At the Buffer the averaged velocity was quite uniform along the depth and over the whole simulation period the highest horizontal velocities were found at the bottom of the water column. It is noteworthy that in average the horizontal velocities at the Buffer are not the highest all over the reservoir despite the vicinity of this position to the main inflow. The Ferraria Bridge shows higher time averaged velocities than the Buffer probably due to its reduced cross sectional area. Advancing to Park, lower flow velocities were calculated by the model in comparison to the Ferraria Bridge. For Park, the the flow velocities go towards zero near the bottom and in this way they are clearly lower than at the surface, which is not the case for the two previously mentioned positions. The same behaviour is valid for the further studied points at deeper locations in the reservoir. SAL shows again a similar behaviour to the Buffer and Ferraria Bridge, where the velocites at the bottom and the water surface are similar. Analysing the whole simulation period, for the positions Center, Intake, SAL and Dam the highest velocity magnitudes were more often found at the water surface. Adding Park to the previous list, the lowest velocities were present at the bottom of the water column.

The seasonal variation of the time averaged horizontal flow velocities, turbulent kinetic energy and energy dissipation rate are illustrated in Figure A.7 for three points along the longitudinal axis of the reservoir also showing the variation of the mentioned parameters with increasing water depths. At the Buffer, the flow velocities profiles for spring and summer present decreasing magnitudes towards the bottom, the opposite is valid for the fall. Meanwhile for the winter the velocities are almost uniform over the depth. The highest velocities were present during fall at the bottom of the reservoir. The turbulent kinetic energy presents for all seasons an increasing trend towards the bottom the same is true for the energy dissipation rate. For summer the highest levels of turbulent kinetic energy were calculated, meanwhile the lowest ones were present during the winter. The dissipation of energy exhibits a similar behaviour. It calls the atention, that the gradients of the disspation rates between the surface and bottom for the position Buffer are similar over the seasons. At the point Center the time averaged horizontal velocities were the highest for the summer for the major portion of the water column. All seasons showed a decreasing trend towards the bottom, the trend was however not strictly decreasing presentig increasing velocities from 5 to 3 m above the bottom and again decreasing until the bottom. The highest magnitude for the turbulent kinetice energy was found for the top portion of the water colum for all seasons.On the other hand, the lowest values were calculated at an intermediate layer at 3 m above the bottom. Notice that the magnitude anc course of this variable was virtually the same for winter and fall. The last affirmation is also valid for the dissipation rate. At the Dam, the velocity profiles along the depth are higher at the surface and decrease towards te bottom. The seasonal velocity profiles differ the most at the top portion of the water column, becoming more uniform towards the bottom. The turbulent kinetic energy and the dissipation rates exhibit similar behaviours to the one for the position Center. However, the lowest magnitudes of those parameters are quite different for winter/fall and spring/summer.In general the turbulent kinetic energy and the dissipation rate reached the lowest values at the Dam of all three observed positions. For all three points the velocity at the water surface was the highest during summer. The calculated dissipation rates and TKE had similar profile's shape and were in the same range as found in inverstigations regarding measurements in lakes (Lin et al., 2021; Wuest et al., 1388).

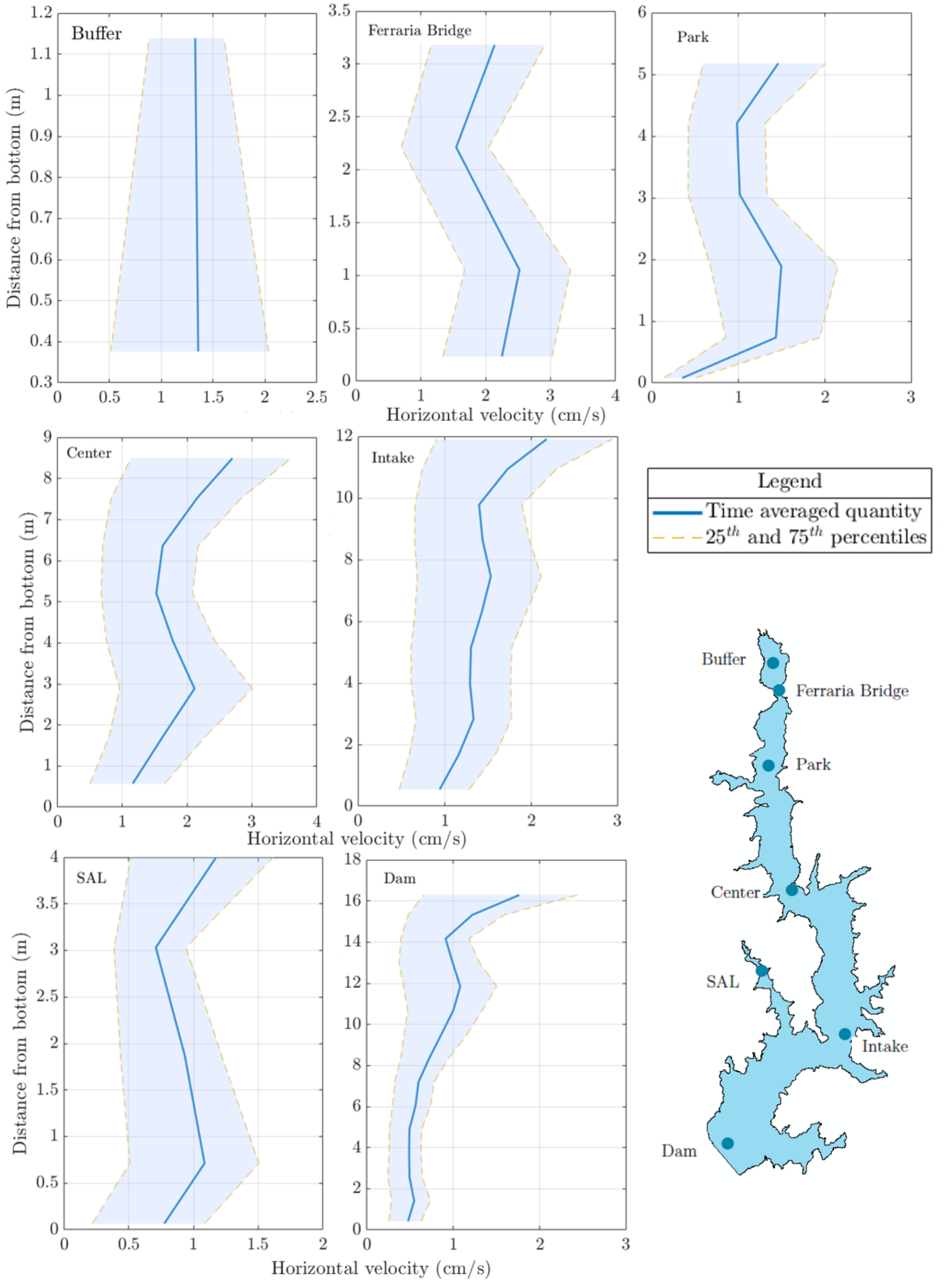

Figure 4.14.: Simulated time averaged horizontal velocity profiles along the depth (blue lines) and its range of variation during the simulation period(blue shaded area: its limits correspond to the $25th^{th}$ and $75th^{th}$ percentiles) for the indicated positions at the reservoir.

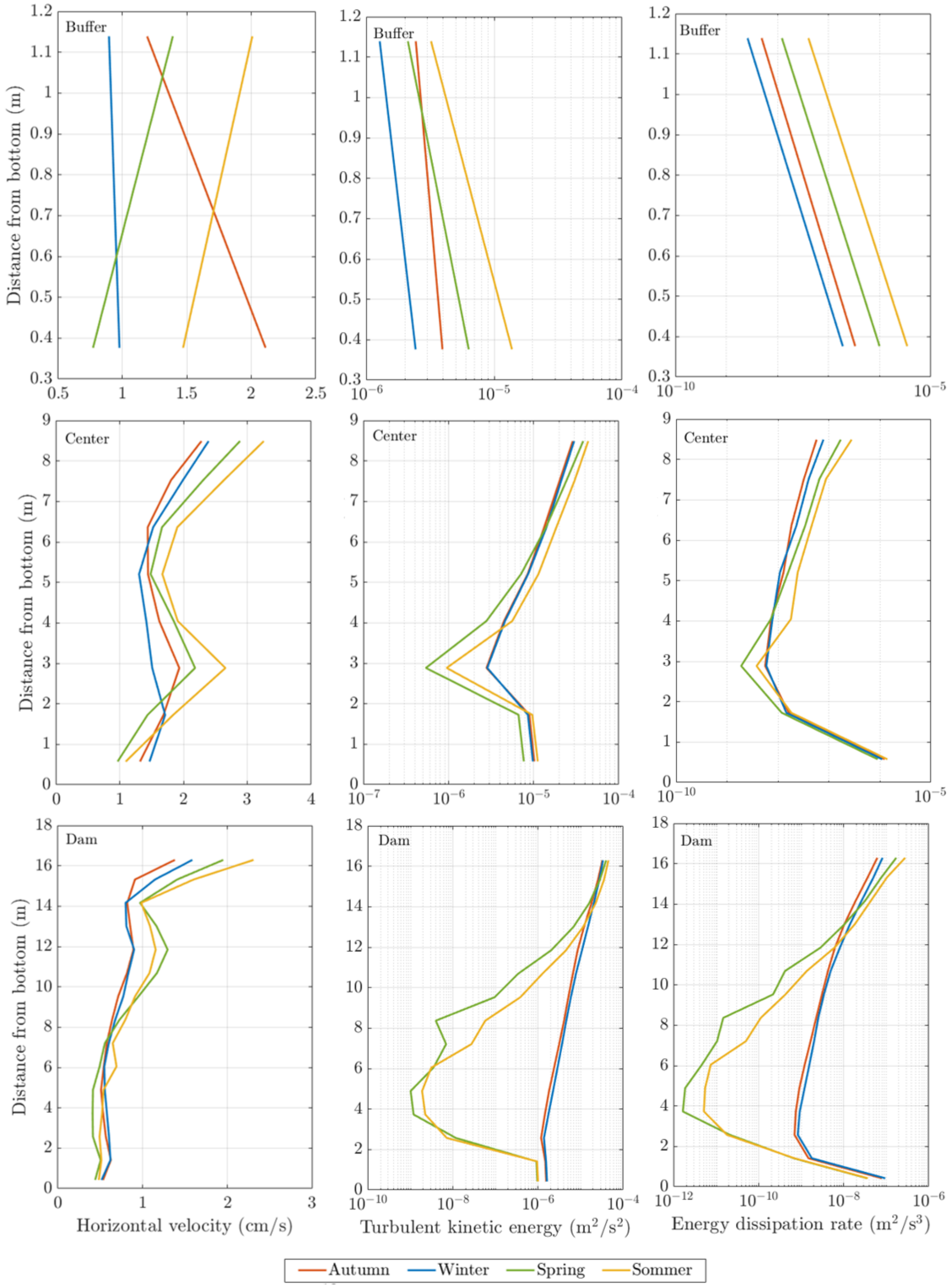

Figure 4.15.: Seasonal variation of the vertical profiles of the simulated time averaged horizontal velocity (first column), turbulent kinetic energy (second column) and energy dissipation rates (third column) for the positions Buffer, Center and Dam.

The impact of the variation of the parameters listed in Table 4.2 on the temperature and velocities at the Intake was already investigated in section 4.3.1. In the following the effect of the same parameters is studied for three positions in the reservoir namely Buffer, Center and Dam. For the following comparisons the same simulations listed in Table 4.2 are used. In those simulations just one parameter was changed at the time. The analysis is performed by calculating the average water temperature at the bottom and at the surface of each position and also taking into account the seasons for the period March 2018 to February 2019. The column number one (1) of each table shows the average of the quantity, either temperature ($^\circ C$) or horizontal flow velocity (cm/s) at the bottom of the water column for the whole analyzed period, column two (2) shows the similar quantity but for the surface. Columns three (3) and four (4) show the average quantities for the bottom and the surface during Autumn. Columns five (5) and six (6) present this information for winter, seven (7) and eight (8) for spring and columns nine (9) and ten (10) for summer.

Table 4.5 presents the time averaged velocities for the reference simulation. In general, the temperatures at the bottom of the reservoir were similar (column 1) and at the surface of the shallowest positon the water was colder than at deeper ones. On average the temperatures at the bottom and surface of the Buffer were on 0.1 $^\circ C$ different, i.e. exhibiting low gradients and weak stratification. On average, the highest temperature gradients were found at the Dam. Through all seasons the Buffer showed mostly no stratification. Meanwhile the positions Center and Dam along the meteorological seasons consistently presented some degree of stratification with the highest gradients been observed in summer, reaching the 2.8 and 5.7 $^\circ C$ for the Center and Dam respectively.

Table 4.5.: Time averaged temperatures for the reference simulation.

Location	(1)	(2)	(3)	(4)	(5)	(6)	(7)	(8)	(9)	(10)
Buffer	19.4	19.5	19.3	19.6	14.6	14.6	19.2	19.2	24.0	24.0
Center	20.6	22.4	22.5	23.5	16.8	17.4	19.2	21.2	24.4	27.2
Dam	19.4	22.6	22.3	23.7	16.8	17.7	17.6	21.4	21.5	27.2

Similarly, Table 4.6 sumarizes the results for the time averaged horizontal velocities. Observing the whole studied period, on averaged the highest velocities were obtained at the surface of the position center and the lowest at the bottom of the position Dam. This pattern was also consistent all over the seasons, with the velocities being on average as high as 2.9 cm/s during the summer at the Center and as low as 0.41 cm/s during the spring at the Dam. On average, the velocities at the bottom of the Buffer were not consistently lower than at the surface of the same position. For every position, the highest velocities were registered at the water surface duing summer.

Table 4.6.: Time averaged velocities for the reference simulation.

Location	(1)	(2)	(3)	(4)	(5)	(6)	(7)	(8)	(9)	(10)
Buffer	1.39	1.34	2.20	1.20	0.98	0.90	0.79	1.44	1.51	2.01
Center	1.68	2.30	1.55	2.07	1.50	1.95	1.66	2.47	2.00	2.92
Dam	0.49	1.80	0.53	1.37	0.60	1.57	0.41	1.97	0.53	2.57

Changing the magnitude of the Manning value does have an effect on the simulated temperatures (see Tables 4.7 and 4.5). Nevertheless, the effect is minimal for the positions Center and Dam, where the temperatures at the bottom and at surface while observing the whole period (colums 1 and 2)were at the most 0.5 $°C$ (Differece between M1 and M3). For the position Buffer the highest difference was of ca. 1.2 $°C$ when considering the whole analyzed period. Over the seasons the highest differences were observed during summer. In general the change of Manning value had some degree of influence on the simulated temperature specially on the shallow regions in the reservoir.

Table 4.7.: Effect of the change of the Manning value on the temperature.

Location	Simulation	(1)	(2)	(3)	(4)	(5)	(6)	(7)	(8)	(9)	(10)
Buffer	M1	19.8	19.8	20.1	20.2	15.0	15.0	19.4	19.3	24.3	24.3
	M2	19.5	19.6	19.5	19.8	14.7	14.8	19.3	19.3	24.2	24.2
	M3	18.6	18.8	18.9	19.2	14.1	14.2	18.2	18.2	22.4	22.4
Center	M1	20.8	22.3	22.7	23.5	16.9	17.4	19.3	21.1	24.7	27.2
	M2	20.7	22.4	22.6	23.5	16.8	17.4	19.2	21.2	24.4	27.2
	M3	20.9	22.4	22.7	23.6	16.9	17.5	19.6	21.2	24.8	27.2
Dam	M1	19.7	22.5	22.5	23.7	16.7	17.7	17.8	21.4	22.2	27.2
	M2	19.4	22.6	22.3	23.7	16.7	17.7	17.5	21.4	21.5	27.2
	M3	19.2	22.6	22.4	23.8	17.1	17.9	17.5	21.4	20.4	27.3

The effect of change in the Manning value on the velocities is more pronounced than for the temperatures as depicted in Table 4.8. When observing the averaged velocities for the analyzed period (columns 1 and 2) higher magnitudes of the Manning value result in lower flow velocities, as expected from the act of increasing roughness. The increase in the velocity with decreasing coefficcient is more pronounced for the bottom than for the surface. this pattern extends to all seasons and it is noteworthy for all three positions and not only for the shallow region as it resulted to be for the temperature.

Table 4.8.: Effect of the change of the Manning value on the horizontal velocity.

Location	Simulation	(1)	(2)	(3)	(4)	(5)	(6)	(7)	(8)	(9)	(10)
Buffer	M1	2.01	2.03	1.93	1.33	1.57	1.42	2.07	2.55	2.92	3.39
	M2	1.56	1.40	2.34	1.17	1.15	0.95	0.90	1.51	1.81	2.25
	M3	0.64	0.93	0.76	0.82	0.38	0.65	0.52	0.92	0.88	1.23
Center	M1	2.07	2.87	2.59	2.48	2.56	2.50	1.62	3.03	1.83	3.52
	M2	1.49	2.75	1.83	2.36	1.91	2.37	1.17	2.93	1.32	3.45
	M3	0.21	2.33	0.22	1.91	0.20	1.87	0.20	2.53	0.25	3.00
Dam	M1	0.83	1.82	1.00	1.48	0.98	1.59	0.72	1.97	0.79	2.49
	M2	0.60	1.80	0.67	1.40	0.67	1.57	0.55	1.97	0.62	2.56
	M3	0.01	1.70	0.01	1.33	0.01	1.49	0.01	1.87	0.01	2.33

Table 4.9 presents the effect of the change in the wind drag coefficient in the temperatures. Difference between the simulated temperatures with variating drag coefficients are indeed observed. For the Buffer the differences in the temperatures were the smallest among the studied positions with the highest difference being 0.2 $°C$. Considering the whole period (columns 1 and 2), the differences among simulations (also taking into account the reference simulation Table 4.5)were more pronounced at the bottom of the three studied locations. This pattern holds along the seasons, where the most significant changes in the temperatures are present at the bottom.

Table 4.9.: Effect of the wind drag coefficient value on the temperature.

Location	Simulation	(1)	(2)	(3)	(4)	(5)	(6)	(7)	(8)	(9)	(10)
Buffer	W1	19.3	19.5	19.4	19.8	14.5	14.7	19.1	19.2	23.8	23.9
	W2	19.4	19.5	19.4	19.6	14.6	14.7	19.2	19.2	23.8	23.8
Center	W1	19.5	22.4	21.8	23.4	16.6	17.5	17.8	21.3	22.0	27.2
	W2	21.4	22.3	22.8	23.6	16.9	17.4	20.0	21.1	26.0	27.2
Dam	W1	18.0	22.5	20.9	23.6	16.5	17.7	16.4	21.5	18.6	27.2
	W2	20.3	22.5	22.6	23.8	16.9	17.7	18.5	21.3	23.8	27.3

The resulting time averaged velocities for the studied drag coefficients are presented in Table 4.10. The variation of this parameter indeed had an influence in the simulated horizontal flow velocities at the positions studied which showed to be more marked with increasing depth of the position in question. This pattern is observed not only for the averaged hole periodbut also along the seasons. In general, with lower drag coefficients, higher velocities are obtained in the model. On averaged the highest velocities were obtained during summer at the surface of the position center, the calculated value reached the 3.92 cm/s.

Table 4.10.: Effect of the change of the wind drag coefficient value on the horizontal velocity.

Location	Simulation	(1)	(2)	(3)	(4)	(5)	(6)	(7)	(8)	(9)	(10)
Buffer	W1	1.61	1.33	2.43	1.15	1.03	0.83	0.96	1.39	1.76	2.04
	W2	1.35	1.43	2.01	1.24	1.03	0.98	0.80	1.58	1.48	2.10
Center	W1	0.81	1.98	0.96	1.72	1.12	1.96	0.65	1.97	0.70	2.17
	W2	1.55	2.92	1.67	2.45	1.59	2.37	1.38	3.14	1.61	3.92
Dam	W1	0.37	1.13	0.43	0.88	0.42	1.07	0.32	1.20	0.38	1.43
	W2	0.59	2.23	0.62	1.69	0.66	1.85	0.53	2.48	0.63	3.21

Table 4.11 summarizes the effect of the change in the background horizontal viscosity on the averaged temperature. Increasing the magnitude of this parameter (also considering the results for the reference simulation), causes a reduction on the simulated temperatures. The change of this parameter induced almost no difference during the winter, when the reservoir is mixed. While the highest differences were observed during summer, which represents a consistently stratified period for the water body. The variation of this background coefficient was able to produce a difference of 3.2 °C during the summer at the bottom of the position Dam (Reference simulation-BHV2).

Table 4.11.: Effect of the background horizontal viscosity on the temperature.

Location	Simulation	(1)	(2)	(3)	(4)	(5)	(6)	(7)	(8)	(9)	(10)
Buffer	BHV1	19.1	19.2	19.2	19.5	14.3	14.5	18.8	18.9	23.3	23.4
	BHV2	18.9	19.0	19.1	19.4	14.2	14.3	18.6	18.7	22.8	22.8
Center	BHV1	20.3	22.4	22.2	23.5	16.7	17.5	18.7	21.2	23.6	27.2
	BHV2	20.0	22.4	22.1	23.5	16.7	17.5	18.5	21.3	23.2	27.2
Dam	BHV1	18.4	22.6	21.4	23.7	16.6	17.8	16.7	21.5	19.2	27.3
	BHV2	17.9	22.6	20.8	23.7	16.5	17.8	16.4	21.5	18.3	27.3

The effect of the background coefficient for the horizontal viscosity (compare Tables 4.12 and 4.6) did not show a general tendency for the three studied positions. Nevertheless, an increase in this coefficient consistently caused a reduction in the flow velocities at the position Dam for all seasons. This was not the case for the Center and the Buffer. It calls the attention, that at the bottom of the posisiton center for all seasons, the horizontal velocities changed the most with the variation in the mentioned coefficient. This parameter should not be disgarded while performing sensitivity analysis since it can change the velocity in unpredicted directions.

Table 4.12.: Effect of the change of the background horizontal viscosity on the horizontal velocity.

Location	Simulation	(1)	(2)	(3)	(4)	(5)	(6)	(7)	(8)	(9)	(10)
Buffer	BHV1	1.45	1.17	2.11	0.88	1.08	0.76	0.88	1.37	1.42	1.89
	BHV2	1.42	1.13	1.93	0.83	1.02	0.71	0.94	1.36	1.43	1.88
Center	BHV1	0.80	2.51	0.88	2.11	1.02	2.10	0.65	2.69	0.72	3.29
	BHV2	0.65	2.38	0.70	1.96	0.84	1.98	0.53	2.58	0.60	3.16
Dam	BHV1	0.34	1.69	0.38	1.28	0.38	1.48	0.30	1.85	0.35	2.48
	BHV2	0.25	1.66	0.29	1.24	0.29	1.43	0.21	1.82	0.25	2.49

The change of the background horizontal diffusivity was proved to have a mild effect in the water temperature (compare Tables 4.13 and 4.5). The changes in this coefficient affects more the bottom than the surface layers. For the Intake position the time averaged temperatures showed a similar effect (see Figure 4.3). This pattern propagates through the seasons as well. Autumn and Winter presented the lowest seasonal variations with differences reaching only the 0.2 $°C$. Analyzing the values for the whole period (Column 1)at the bottom of the water column, the highest differences were showed to be at the position Dam.

Table 4.13.: Effect of the background horizontal diffusivity on the temperature.

Location	Simulation	(1)	(2)	(3)	(4)	(5)	(6)	(7)	(8)	(9)	(10)
Buffer	BHD1	19.3	19.3	19.5	19.6	14.6	14.6	18.9	18.8	23.4	23.4
	BHD2	19.5	19.5	19.7	19.7	14.9	14.9	19.0	19.0	23.7	23.7
Center	BHD1	21.0	22.3	22.7	23.5	16.9	17.4	19.6	21.1	25.1	27.2
	BHD2	21.1	22.3	22.8	23.5	17.0	17.4	19.7	21.0	25.3	27.2
Dam	BHD1	19.9	22.5	22.5	23.7	16.9	17.7	18.0	21.3	22.4	27.2
	BHD2	20.1	22.5	22.7	23.7	17.0	17.7	18.2	21.3	22.8	27.2

The change in the horizontal velocities induced by the background horizontal velocity is documented in Table 4.14. While considering the whole period at the bottom of the three studied positions, a decreasing trend for the velocities with increase in the parameter in question is observed. In general , the changes in the velocities did not present a trend than applies to all positions and seasons with the decreas or increase of the parameter. The changes between the velocities calculated with a value of zero (Reference) and a value of 1.25 m^2/s (BHD2) are notorious and they should be considered when calibrating models, specially low flow system like Passaúna.

Table 4.14.: Effect of the change of the background horizontal diffusivity on the horizontal velocity.

Location	Simulation	(1)	(2)	(3)	(4)	(5)	(6)	(7)	(8)	(9)	(10)
Buffer	BHD1	1.12	1.23	1.48	1.12	0.69	0.78	0.85	1.35	1.55	1.84
	BHD2	1.04	1.17	1.24	1.04	0.65	0.73	0.87	1.31	1.58	1.85
Center	BHD1	1.06	2.54	1.33	2.14	1.33	2.22	0.82	2.69	0.88	3.26
	BHD2	1.06	2.47	1.34	2.07	1.30	2.14	0.84	2.63	0.88	3.21
Dam	BHD1	0.41	1.82	0.48	1.41	0.47	1.57	0.37	1.98	0.43	2.56
	BHD2	0.38	1.85	0.43	1.44	0.44	1.59	0.34	2.02	0.42	2.57

The effect of the change in the background vertical viscosity on the temperatures is showed in Table 4.15. Observing the results for the analyzed period (columns 1 and 2) it is evident, that the major changes were present at the bottom of the water column. The changes in the temperature increase for deeper located layers: for the Dam the difference between the simulation with highest (BVV2) and lowest (Reference) reached the 2.5 $°C$. For shallower areas like the Buffer the effect (even though small) can be observed in both the surface and the bottom. The same patterns is observed thought out the seasons, with notably effects for the winter at the bottom of the Dam.

Table 4.15.: Effect of the background vertical viscosity on the temperature.

Location	Simulation	(1)	(2)	(3)	(4)	(5)	(6)	(7)	(8)	(9)	(10)
Buffer	BVV1	19.3	19.4	19.3	19.6	14.5	14.6	19.2	19.2	23.6	23.7
	BVV2	19.4	19.5	19.3	19.6	14.4	14.5	19.2	19.2	24.0	24.0
Center	BVV1	20.0	22.4	22.0	23.5	16.7	17.5	18.4	21.3	23.1	27.1
	BVV2	19.2	22.4	21.5	23.5	16.3	17.5	17.5	21.4	21.6	27.1
Dam	BVV1	17.9	22.6	20.8	23.7	16.5	17.7	16.5	21.5	18.2	27.2
	BVV2	16.9	22.6	18.7	23.6	16.3	17.8	16.1	21.6	16.5	27.2

Changes in the background vertical velocity also affected in some measure the calculated velocities (see Table 4.16). Analyzing columns 1 and 2, the changes are more evident for deeper regions. For this coefficient the changes were observed at the water surface and also at the bottom. Nevertheless, there is no an evident trend in the increase or decrease in the parameter and the subsequent increase/decreasein the simulated velocities. The highest time averaged velocities were calculated for the position Center during winter making use of a magnitude of 0.625 m^2/s for the coefficient in consideration. Neverteless, the use of this value did not produced the highest velocities for the further seasons at this position.

Table 4.16.: Effect of the change of the background vertical viscosity on the horizontal velocity.

Location	Simulation	(1)	(2)	(3)	(4)	(5)	(6)	(7)	(8)	(9)	(10)
Buffer	BVV1	1.35	1.35	2.04	1.24	0.93	0.88	0.81	1.46	1.64	2.07
	BVV2	0.93	1.09	0.98	1.05	0.56	0.63	0.90	1.15	1.61	1.84
Center	BVV1	0.95	2.45	1.06	2.05	1.39	2.14	0.74	2.58	0.73	3.13
	BVV2	0.78	1.38	0.82	1.10	1.04	1.37	0.66	1.53	0.65	1.59
Dam	BVV1	0.30	1.63	0.36	1.25	0.45	1.48	0.26	1.78	0.22	2.38
	BVV2	0.19	1.00	0.16	0.74	0.36	1.03	0.15	1.16	0.11	1.24

Changes in the magnitude of the background vertical diffusivity generated differences in the calculated temperatures,they are more evident at the bottom of deeper regions than at shallower areas. For the points Center and Dam the increase in the coefficient in consideration produced higher temperatures at the bottom. As observed in Table 4.17, the temperatures over the seasons at the surface of the studied point remain fairly constant, meanwhile the temperatures at the bottom are change higher with respect to the reference simulation, i.e. the time averaged temperatures gradients are less pronounced for the simulations with background vertical diffusivities higher than zero.

Table 4.17.: Effect of the background vertical diffusivity on the temperature.

Location	Simulation	(1)	(2)	(3)	(4)	(5)	(6)	(7)	(8)	(9)	(10)
Buffer	BVD1	19.3	19.4	19.2	19.4	14.5	14.5	19.2	19.2	23.9	23.9
	BVD2	19.4	19.4	19.4	19.5	14.5	14.5	19.2	19.2	24.1	24.1
Center	BVD1	21.9	22.3	23.2	23.6	17.1	17.4	20.6	21.0	26.8	27.2
	BVD2	22.2	22.3	23.4	23.5	17.2	17.3	20.9	21.0	27.1	27.2
Dam	BVD1	21.9	22.5	23.5	23.8	17.4	17.7	20.4	21.1	26.7	27.3
	BVD2	22.3	22.4	23.8	23.9	17.7	17.8	20.8	20.9	27.1	27.2

The modifications in the background vertical diffusivity and their repercusion on the time averaged velocities is summarized in Table 4.18. For the whole analized period (columns 1 and 2) the major changes are observed at the top of the water column. There is no general trend that can be applied to all periods and positions. The highest velocities for the Buffer and for the Dam positions were reached during winter at the water surface with the lowest value for the studied coefficient. Meanwhile for the position Center this was achieved also for winter but with a coefficient of 0.625 m^2/s, which was at the same time the highest time averaged velocity of all periods and positions.

Table 4.18.: Effect of the change of the background vertical diffusivity on the horizontal velocity.

Location	Simulation	(1)	(2)	(3)	(4)	(5)	(6)	(7)	(8)	(9)	(10)
Buffer	BVD1	1.31	1.34	1.90	1.22	0.90	0.88	0.75	1.37	1.57	2.07
	BVD2	1.12	1.27	1.42	1.14	0.79	0.87	0.81	1.41	1.39	1.85
Center	BVD1	1.60	2.65	2.04	2.27	1.54	2.30	1.27	2.71	1.62	3.47
	BVD2	1.75	2.44	2.39	2.30	1.67	2.07	1.39	2.40	1.74	3.18
Dam	BVD1	0.62	2.02	0.61	1.55	0.66	1.73	0.56	2.30	0.66	2.70
	BVD2	0.94	2.02	0.88	1.49	0.96	1.74	0.91	2.34	0.99	2.62

The effect of the changes in the magnitude of the Ozmidov length are summarized in Table 4.19. For the position Buffer there were minor changes in the calculated temperatures over the seasons and over the whoe period, with the highest difference being just 0.2 °C. For the positions Center and Dam, the changes are more notorious, specially at the bottom of the reservoir. For the positions Center and Dam there were practically no changes in the calculated temperature at the surface; the differences were at the most 0.2 °C. At the bottom an increase in the OL consistently produced higher temperatures in comparison with the reference simulation. The highest difference were of 4.9 °C and were reached during winter.

Table 4.19.: Effect of the Ozmidov length scale on the temperature.

Location	Simulation	(1)	(2)	(3)	(4)	(5)	(6)	(7)	(8)	(9)	(10)
Buffer	OL1	19.4	19.4	19.3	19.5	14.6	14.6	19.2	19.2	23.9	24.0
	OL2	19.3	19.4	19.3	19.4	14.5	14.5	19.2	19.2	23.9	23.9
Center	OL1	21.5	22.3	22.9	23.6	16.9	17.4	20.1	21.0	26.4	27.2
	OL2	21.8	22.3	23.1	23.6	17.0	17.4	20.4	21.0	26.7	27.2
Dam	OL1	21.0	22.5	22.8	23.8	16.9	17.7	19.1	21.2	25.5	27.3
	OL2	21.6	22.5	23.2	23.8	17.2	17.7	20.0	21.1	26.4	27.3

Modifications in the magnitude of the Ozmidov length produced some changes in the simulated horizontal velocities and those are depicted in Table 4.20. Among the three studied positions the most notorious difference are to be found at the Center specially at the water surface. The changes between the simulations OL1 and OL2 are milder than when compared to the reference simulation, even though the tested length scales were equally distributed i.e. 0,5 and 10 cm for the reference, OL1 and OL2 respectively. However, there is no general trend applicable to all positions or all periods studied.

Table 4.20.: Effect of the change of the Ozmidov length scale on the horizontal velocity.

Location	Simulation	(1)	(2)	(3)	(4)	(5)	(6)	(7)	(8)	(9)	(10)
Buffer	OL1	1.35	1.33	2.09	1.21	0.95	0.89	0.79	1.43	1.49	1.99
	OL2	1.28	1.31	1.87	1.23	0.91	0.89	0.75	1.37	1.45	1.93
Center	OL1	1.41	2.69	1.63	2.27	1.48	2.30	1.18	2.85	1.51	3.45
	OL2	1.50	2.61	1.80	2.20	1.48	2.28	1.20	2.73	1.60	3.37
Dam	OL1	0.55	1.86	0.59	1.43	0.56	1.59	0.48	2.06	0.62	2.56
	OL2	0.58	1.92	0.61	1.46	0.60	1.63	0.49	2.19	0.62	2.62

The modifications in th Dalton number produced notorious changes in the water temperature and those are depicted in Table 4.21. Higher magnitudes for the Dalton number induced consistently lower temperatures for all the positions studied and for the bottom and the surface of the water column. The largest and lowest changes were obtained at the positions Dam at the bottom for the summer and at the Buffer for the Autumn respectively. The difference between the simulations with the lowest and highest Dalton number was of 5.7 $°C$ and the lowest one was 0.9 $°C$. The Dalton number already showed to be a sensitive parameter also for the Intake position (compare Figure 4.3).

Table 4.21.: Effect of the Dalton number on the temperature.

Location	Simulation	(1)	(2)	(3)	(4)	(5)	(6)	(7)	(8)	(9)	(10)
Buffer	DN1	18.5	18.4	18.9	19.0	13.9	13.9	18.4	18.4	22.3	22.9
	DN2	17.7	17.4	18.4	18.5	13.2	13.2	17.6	17.6	20.9	20.9
Center	DN1	19.1	20.2	20.9	21.8	15.3	15.9	17.7	19.4	22.6	24.5
	DN2	17.6	18.3	19.2	20.1	13.8	14.4	16.2	17.8	20.9	21.5
Dam	DN1	17.9	20.4	20.5	22.0	15.3	16.2	15.9	19.6	19.8	24.6
	DN2	16.4	18.5	18.8	20.2	13.7	14.7	14.4	18.0	18.4	21.6

The differences in the calculated time averaged horizontal velocities while changing the magnitude of the dalton number are presentend in Table 4.22, they are present at all positions over the studied seasonal and absolute periods. The most notorious changes were generally produced at the position Center, with the highest magnitude change being observed during summer (column 10)and reaching the 1.45 cm/s (reference simulation - DN2). In general, the highest veocities were obtained with the lowest Dalton number of 0.0013 corresponding to the reference simulation. For most of the time periods studied (autumn to summer)an increase in the Dalton number produced higher flow velocities. This behaviour was also observed for the Intake position (compare Figure 4.4).

Table 4.22.: Effect of the change of the Dalton number on the horizontal velocity.

Location	Simulation	(1)	(2)	(3)	(4)	(5)	(6)	(7)	(8)	(9)	(10)
Buffer	DN1	1.21	1.17	1.60	1.14	0.80	0.85	0.87	1.42	1.76	1.14
	DN2	1.17	1.07	1.20	1.04	0.71	0.81	0.92	1.41	2.29	0.77
Center	DN1	1.16	2.37	1.27	2.09	1.39	2.18	0.97	2.86	1.11	2.04
	DN2	1.15	2.23	1.19	1.94	1.29	2.09	0.99	2.96	1.14	1.47
Dam	DN1	0.48	1.66	0.54	1.37	0.53	1.54	0.44	2.07	0.49	1.57
	DN2	0.49	1.62	0.53	1.34	0.53	1.53	0.43	2.24	0.48	1.18

The variation in the simulated time averaged temperatures with increasing Stanton number are depicted in Table 4.25. The increase in the Stanton number produced consistently lower temperatures all over the studied positions in comparison to the reference simulation (see columns 1 and 2). This pattern also applies to each meteorological season, for the bottom and the surface of the water column A similar behaviour showed the analysis at the Intake location, where the changes were produced all over the water column as well (compare Figure 4.3). The mildest differences are observed at the position Buffer, with its highest magnitude being 0.5 $°C$. Deeper locations, i.e. the Center and The Dam showed similar differences.

Table 4.23.: Effect of the Stanton number on the temperature.

Location	Simulation	(1)	(2)	(3)	(4)	(5)	(6)	(7)	(8)	(9)	(10)
Buffer	SN1	19.3	19.4	19.3	19.6	14.6	14.7	19.0	19.1	23.5	23.6
	SN2	19.2	19.3	19.3	19.5	14.6	14.7	18.8	18.8	23.5	23.5
Center	SN1	20.3	22.0	22.1	23.2	16.5	17.2	18.8	20.8	23.9	26.8
	SN2	19.7	21.7	21.6	22.8	16.1	17.0	18.3	20.4	23.2	26.3
Dam	SN1	18.9	22.2	21.7	23.4	16.4	17.5	17.0	21.1	20.7	26.8
	SN2	18.4	21.8	21.1	22.9	15.9	17.3	16.6	20.6	20.2	26.3

The changes of the horizontal velocities with the modification in the magnitude of the Stanton number are presented in Table 4.24, as can be observed they happen for most all observed period. Nevertheless these changes are minor and amount to a variation of maximum 0.39 cm/s in the horizontal velocity, this takes place at the position Dam at the surface during summer. The variation of the same parameter also showed similar results at the Intake position (compare Figure 4.4).

Table 4.24.: Effect of the change of the Stanton number on the horizontal velocity.

Location	Simulation	(1)	(2)	(3)	(4)	(5)	(6)	(7)	(8)	(9)	(10)
Buffer	SN1	1.36	1.33	2.11	1.19	0.98	0.90	0.77	1.39	1.47	2.01
	SN2	1.29	1.29	2.01	1.19	0.99	0.89	0.77	1.35	1.26	1.87
Center	SN1	1.16	2.70	1.32	2.28	1.47	2.39	0.97	2.89	1.09	3.26
	SN2	1.14	2.75	1.24	2.31	1.42	2.54	0.97	2.94	1.08	3.18
Dam	SN1	0.48	1.76	0.54	1.38	0.52	1.59	0.44	1.95	0.49	2.31
	SN2	0.48	1.77	0.53	1.43	0.50	1.60	0.45	1.97	0.48	2.18

The change of the magnitude of the Secchi depth introduced changes in the calculated temperatures at all studied positions (compare Table 4.25). Incresing the Secchi depth, produced higher temperatures at the positions Center and Dam, specifically at the bottom (see column 1). On the other hand the surface layer showed the opposite trend, i.e. decreasing tempertures with increasing secchi depth (see column 2). The Buffer presented a different behaviour: for both the bottom and the surface ad for all studied periods, higher vales for the Secchi depth produced lower temperatures. The highest difference is to be found at the bottom of the position Center during summer and its magnitud is 2.5 $^{\circ}C$.

Table 4.25.: Effect of the Secchi depth on the temperature.

Location	Simulation	(1)	(2)	(3)	(4)	(5)	(6)	(7)	(8)	(9)	(10)
Buffer	SD1	19.9	20.0	19.8	20.2	15.2	15.3	19.7	19.7	24.1	24.2
	SD2	19.2	19.3	19.1	19.3	14.3	14.4	19.2	19.2	23.8	23.8
Center	SD1	20.0	22.4	22.1	23.6	16.7	17.5	18.5	21.3	22.9	27.2
	SD2	21.1	22.3	22.7	23.5	16.9	17.4	19.6	21.1	25.4	27.2
Dam	SD1	18.8	22.7	21.8	23.8	16.7	17.9	17.1	21.7	20.1	27.4
	SD2	19.6	22.5	22.4	23.7	16.8	17.7	17.6	21.3	22.1	27.2

The change of the magnitude of the Secchi depth introduced changes in the calculated horizontal velocities at all studied positions (compare Table 4.26). However, there is no a general trend that can be applied to all seasons and positions. An increase in the Secchi depth did not repercuted uniformly on all the positions. The highest velocities were obtained with a Secchi depth of 1 m (SD1) at the position Center during the summer and it amounted to 4.18 cm/s.

Table 4.26.: Effect of the change of the Secchi depth on the horizontal velocity.

Location	Simulation	(1)	(2)	(3)	(4)	(5)	(6)	(7)	(8)	(9)	(10)
Buffer	SD1	1.50	1.40	2.31	1.28	1.09	0.95	0.78	1.50	1.61	2.04
	SD2	1.28	1.31	1.92	1.23	0.90	0.85	0.73	1.34	1.54	2.02
Center	SD1	1.15	3.36	1.19	2.87	1.49	2.87	0.98	3.58	1.02	4.18
	SD2	1.22	2.35	1.52	2.00	1.47	2.04	0.95	2.48	1.13	3.01
Dam	SD1	0.48	2.09	0.54	1.65	0.54	1.84	0.45	2.28	0.50	2.86
	SD2	0.48	1.67	0.52	1.25	0.53	1.47	0.44	1.88	0.51	2.35

4.3.3. Analysis of Density Currents

In order to analyze the density currents induced by temperature gradients three positions are defined as key: the Inflow, the Ferraria Bridge and the Intake position (location of the thermistor chain). The same positions were considered in the analysis of density currents based on field measurements (see Figures 3.13 and 3.14). Passaúna Reservoir has a particular structure due to the presence of the Buffer, which could affect the temperature of the incoming discharge. As observed in Figure 3.13, this pre-bay in fact has an effect on the water temperature: the water gets warmer in this zone. The measurements at the Ferraria Bridge indicated a higher temperature when compared to the measurements of the Mini-Dot at the Passaúna River. The same behaviour is depicted by the model in the top of Figure 4.16. Notice that the time period illustrated in Figure 4.16 is the same that for Figure 3.13, which is the time interval with available measurements at the Ferraria Bridge. For that period the difference between the two tempertures decreases towards winter according to the simulations. For the whole simulation period, the behaviour remained similar (see Figure A.8 in the Appendix section A): the temperature difference between the main Inflow and the Ferraria Bridge increases toward the summer and decreases towards winter.

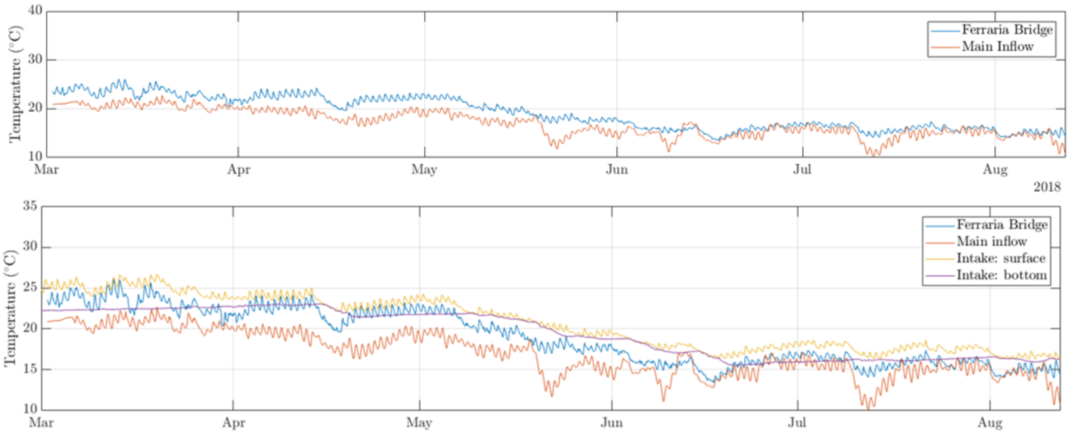

Figure 4.16.: Analysis of possible density currents based on simulated temperatures at the Inflow, Ferraria Bridge and at the Intake. Top: comparison of the temperatures at the Ferraria Bridge and the main Inflow. Bottom: comparison of the three relevant locations.

According to the simulated temperatures between March and August 2018 the Inflow temperatures is consistently lower than the temperature at the surface of the Intake, meaning that no overflow would be observed if considering those two positions. Simultaneously, the water entering the reservoir remains for most of the time colder than the water at the bottom of the the Intake position, with a few exceptions, when its temperature is to be found between the values at the bottom and the surface of the Intake. In other words, the mentioned period would be dominated by underflows with interflows rarely occuring. Analyzing the whole simulation: August 2017 to February 2018 (see Figure A.8 in the Appendix section A) the water entering through the main Inflow remains colder than the surface water at the Intake. Interflows are more often observed specially during spring and summer. A different situation is observed while considering the temperature at the Ferraria Bridge. For the time interval depicted in Figure 4.16 the temperature of the water at the Ferraria Bridge is not permanently colder than at the Intake's bottom. Indeed the water temperature is often found to be between the values at the surface and at the bottom, meaning that the presence of interflows will be significant. For the whole simulation period (see Figure A.8) the situation is similar with occasional matching or exceeding the temperature at the surface of the Intake, i.e. generating sporadic overflows.

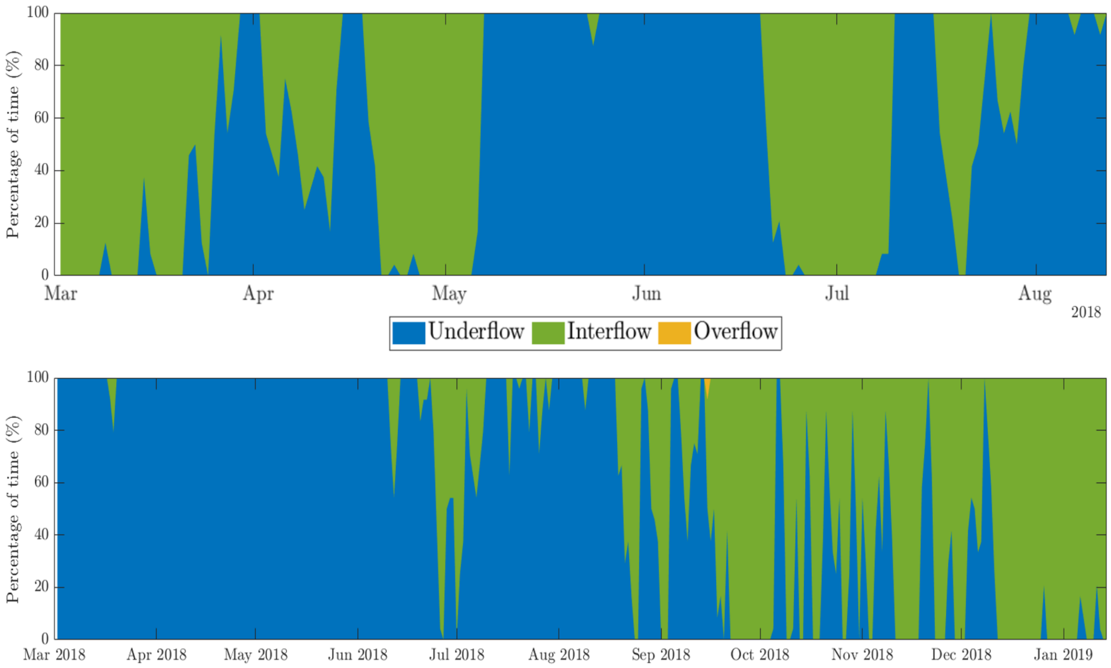

Figure 4.17.: Analysis of possible density currents based on simulated temperatures: underflow, interflow and overflow for the periods with measurements available. Top: Ferraria Bridge as inflow. Bottom: Passaúna River as Inflow. Diagrams created by the author of the dissertation based on Ishikawa et al. (2021).

Figure 4.17 shows the frequency of the different flow paths as percentage of each day of measurement. This Figure is the counterpart of Figure 3.14. According to the simulation no oveflow occurs in the reservoir while considering the temperature at the main Inflow. Towards the end of Autumn to the beginning of Winter 2018 (May to June 2018) the underflow

prevails almost the whole time. Periods controlled by overflow are also simulated e.g. March to April 2018. The measurements depict a different situation: Overflows are present and are not sporadic events. This is probably due to the mismatch between the model and the measurements when predicting the temperature at the Ferraria Bridge (compare Figure 4.11), since the simulated temperature was always lower than the measured by the thermistor at that position. From May to June 2018 the flow path is also controlled by underflows like in the simulation, similarly the period March to May 2018 was also dominated by interflows, nevertheless they were prevailing over underflows. When considering the temperature of the main Inflow and comparing it to the same parameter at the bottom and the surface of the Intake similar pictures for occurence of determined flow paths are produced by the results of the model and the field measurements (see diagrams at the top of Figures 4.17 and 3.14). Underflows are the prevailing flow path with also a strong presence of Interflow is observed in both figures. Overflows are present for a couple of days but not a the same time instants. It is not odd that the comparison between measurements and simulations while considering the main inflow temperature is more positive than the comparison while considering the temperature at the Ferraria bridge. The reason for this is that in the former case the model received as input the temperature measurements from the Mini-Dot and just predicted the temperatures at the Intake, meanwhile for the latter case a further model prediction is used, i.e. the temperature at the Ferraria Bridge.
Analyzing the whole simulation period (August 2017 to February 2019) the situations produced when considering the temperatures at the Ferraria Bridge and at the main Inflow get more similar as illustrated in Figure 4.18. For both cases underflows and interflows are present. For the case of the Ferraria Bridge (top diagram), the interflows are prevailing over the underflows, meanwhile for the case of the main inflow (bottom diagram) the opposite situation is presented: underflows prevailed. Also for the whole simulation period, overflows are not common, but they do occur for the case of the Ferraria Bridge as inflow.

Another way to analyze the flow paths is to introduce a conservative tracer at the main Inflow of the reservoir and to identify at the desired position in this case at the Intake, the layer with the highest concentration over the simulation time. The vertical position would offer an approximation of which layer used the introduced constituent to be transported until the Intake. The positions of the highest tracer concentration are presented in Figure 4.19 by the black dots. The black dots are often present at the top layer, meaning that overflows are occurring. It is noteworthy, that for the period March to Mid August 2018, the underflows (dots at the bottom layer) are dominating and the overflows are not common. This coincides with the information derived from the temperature analysis from the model results. On the other hand, for the period Mid August to February 2019 underflows are not observed and interflows are prevailing over often occuring overflows. For this case the prevailence of inerflows was also indicated by the temperature analysis but not the occurrence of overflows.

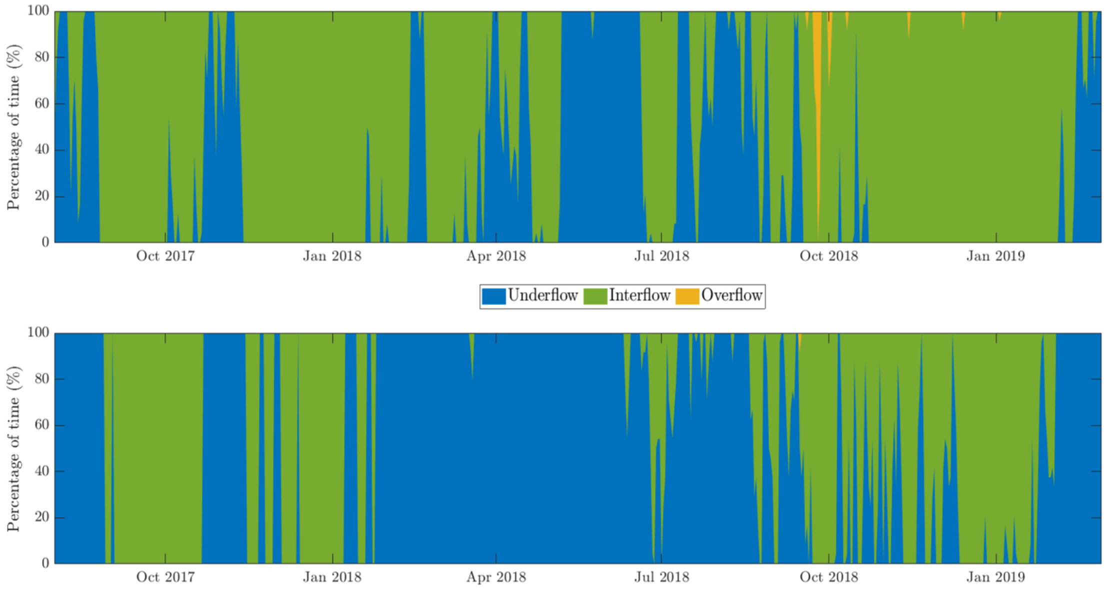

Figure 4.18.: Analysis of possible density currents based on simulated temperatures: underflow, interflow and overflow for the simulated period. Top: Ferraria Bridge as inflow. Bottom: Passaúna River as Inflow. Diagrams created by the author of the dissertation based on Ishikawa et al. (2021).

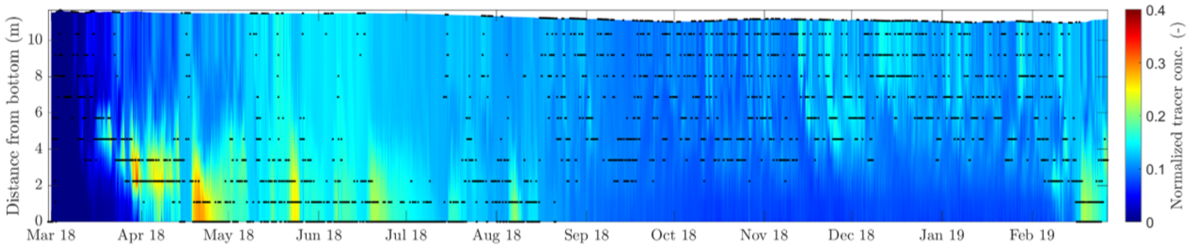

Figure 4.19.: Analysis of possible density currents based on highest tracer concetration at the Intake position with the Z-Model. Diagrams created by the author of the dissertation based on Ishikawa et al. (2022).

A further modelling aspect that could have an effect on the modelling of density currents and thermal stratification is the selection of the vertical layering model. The Z-model was introduced to Delft3d to reduce the artificial mixing caused by Sigma-layers which are in general not pararell to density interfaces in regions with steep slopes (Deltares, 2014), since they follow the terrain and are not completly horizontal like the Z-layers. On the other hand, the Sigma-model has been shown to perform better in the modelling of gravity currents than the Z-model (Lai and Wu, 2019; Harcourt-Baldwin and Diedericks, 2006). For the Passaúna Reservoir a 15-layered Sigma-model requieres 207 hours with a computer with processors Intel ® Xeon® W-2145 CPU @ 3.70 GHz 3.70 GHz. To simulate the mentioned period of 19 months in comparison to the Z-model which requieres 77 hours for the same time period on the same machine. Figure 4.20 shows the simulation results for the vertical thermal structure at the Intake position using the Z-model (mid diagram), the Sigma-model (bottom diagram) and comparing those to the field measurements. In general the Z-model depicted better the thermal stratification at the Intake producing a MAE of 0.38 $°C$ in comparison to a MAE of 0.8 $°C$ when using the Sigma-model. The many similarities between the Z-model and the measurements can also be appreciated by taking a look a the diagrams. The top of the water column got similar temperatures and structures for both models. For mixed periods the models results are very similar as well. The main discrepancies between the models are presented at the lower part of the water column where the Sigma-model artificially mixes the water and the temperatures are higher than for the Z-model. This is easily appreciable during the beginning of Autumn (March-May) and summer (December 2018 to February 2019). Specially for summer, the performance of both models at the bottom part of the water column is not the best and even contrary, i.e. the Z-model produced lower temperatures than the measured ones and the Sigma-model higher temperatures.

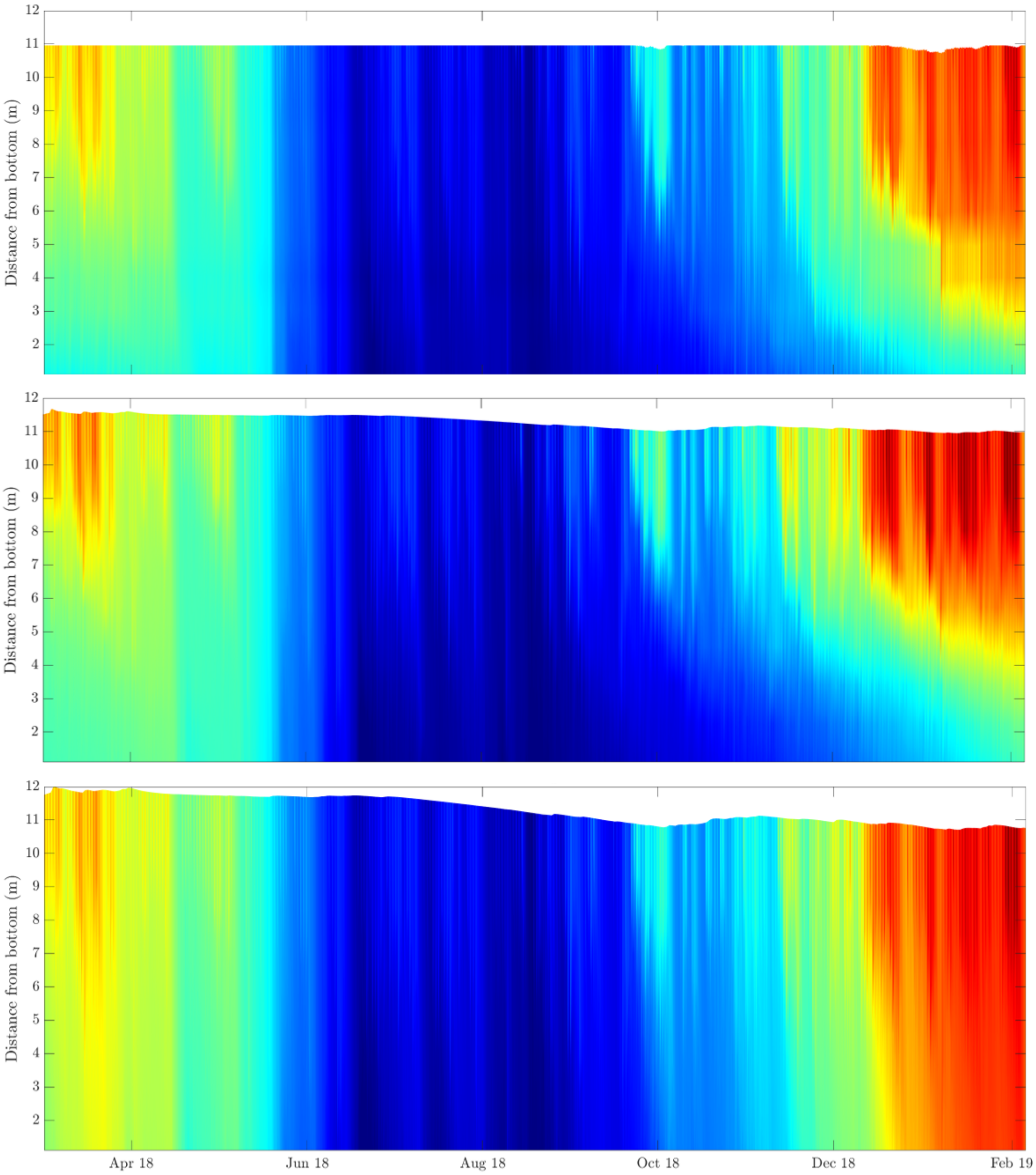

Figure 4.20.: Comparision of the measured and simulated thermal stratification at the Intake position. Top: measurements. Center: Z-Model. Bottom: Sigma-Model.

The distributions of the time averaged MAE over the depth for both models are illustrated in the diagram in the left part of Figure 4.21. For the Z-model the MAE remains fairly under 0.5 °C over the whole depth. The Sigma-model even reaches the 1.8 °C at the bottom part of the water column. For the upper 4 m, the predictions with the two layering-systems are of almost the same quality, for the lower part the performance of the Z-model remains almost constant and for the Sigma-model the performance of predictions get poorer towards the bottom, probably due to the artificial mixing introduced by this layering system. On the right section of the same figure, the temporal distributions of the depth averaged MAE are depicted for both layering systems. The quality of the prediction of both models is the poorest during the summer. Circa from mid-september when the wter column stars to stratifiy, the MAE for the Z-model consistently grows reaching values of 2.9 $°C$. Again, for the winter (mixed period), the performance of the models is comparable, with the Sigma-model delivering even better predictions than the Z-model. The course of the temperatures at the bottom, middle and surface of the Intake position is shown in Figure A.9 int he Appendix section together with the measured parameter. For all three layers the Sigma-model showed lower MAEs than the Z-model, showing a fairly constant magnitude of the errors over the depth, reflectig the behaviour just described.

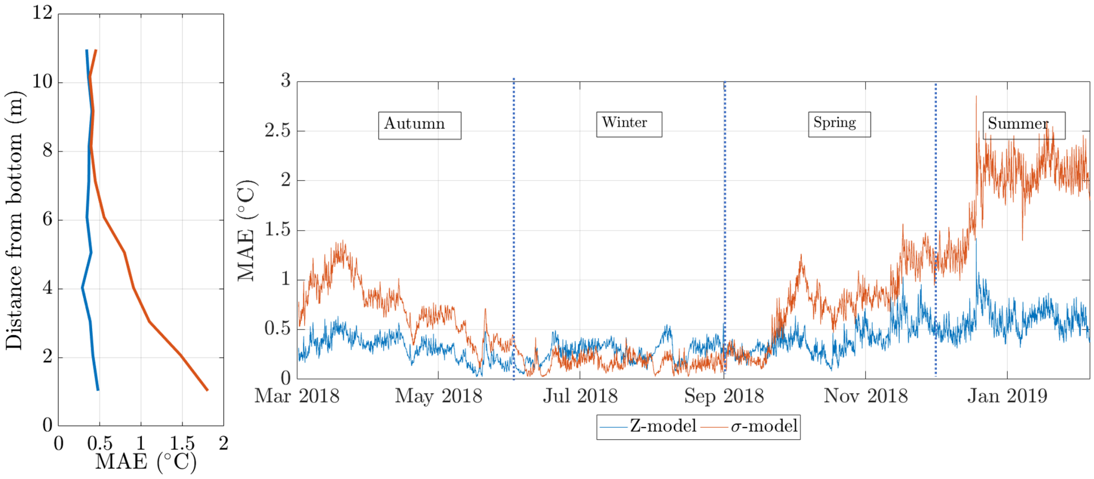

Figure 4.21.: Comparison of the performance of the Z- and Sigma models at the Intake position. Left: temporal-averaged MAE over depth. Right: Depth-averaged MAE over time.

The temperatures at the position Ferraria Bridge simulated with the Sigma-layering system are mostly higher than the same parameter calculated with the Z-model. Figure 4.22 shows that for some short periods the temperatures at this position are equal. As for the Z-model, the Buffer in the Sigma-model constituted a place for the water entering the reservoir through the main inflow to rise its temperature. The diagram at the bottom of Figure 4.22 shows an overview of the modeled temperatures with the Sigma-model. This figures aims to be the counterpart of Figure A.8 in the Appendix section A, which shows the same results for the Z-model. Considering the temperature of the main Inflow, the main flow path that would be present is underflows with a few exceptions when the temperature of the Inflow is found between the temperatures at the bottom and the surface of the Intake position, producing some interflows. When comparing the temperature at the Ferraria Bridge with the temperatures at the Intake, it is observed that often this is warmer than the water at the surface of the Intake producing overflows. The temperature at the Ferraria Bridge is also often lower than the bottom temperature at the Intake, which would send the water to travel over the bottom of the reservoir as underflow. In comparison to the Z-model (see Figure A.8), in which the water temperature at the Ferraria Bridge does not increase over the temperature at the surface of the Intake.

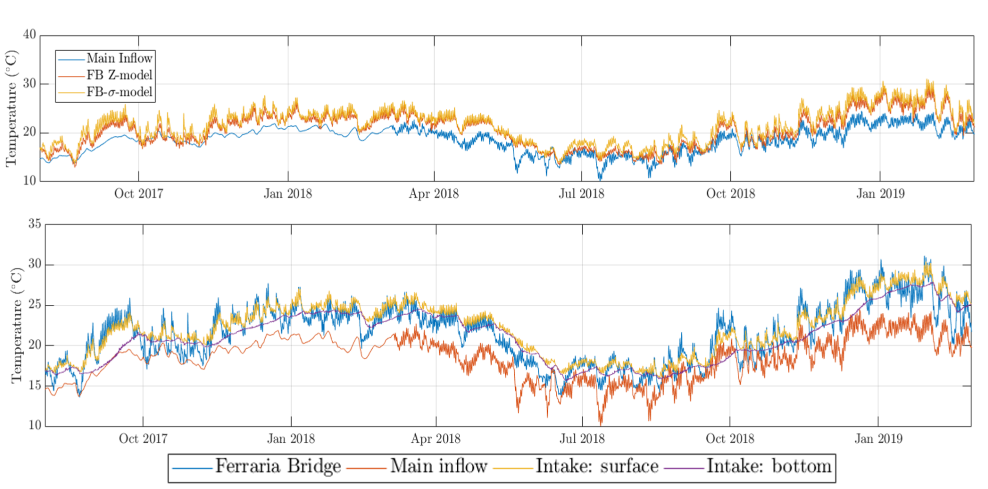

Figure 4.22.: Analysis of possible density currents with the Sigma-model. Top: comparison for the Sigma and Z-models. Bottom: simulation results for the Sigma-model temperatures at the Inflow, Ferraria Bridge and at the Intake.

Figure 4.23 shows the frequency of the different flow paths based of the results of the Sigma-model. This figure is the counterpart of Figure 4.18 with the Z-model. The Sigma-model shows a dominance of overflows specially during the periods August 2017 to January 2018 and Mid-September 2018- January 2019 which correspond to periods which are periods with strong stratification at the water Intake.

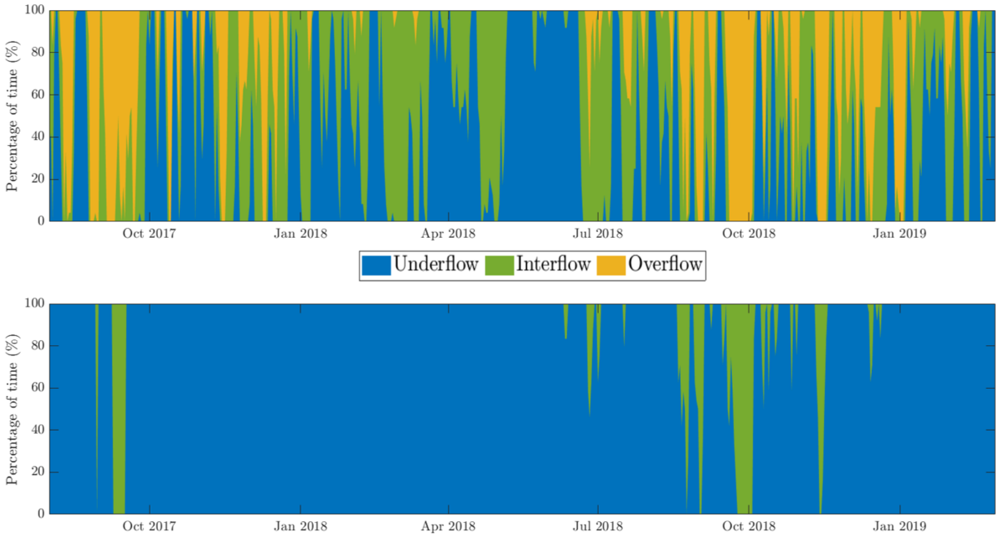

Figure 4.23.: Analysis of possible density currents based on simulated temperatures with the Sigma-Model: underflow, interflow and overflow for the simulated period. Top: Ferraria Bridge as inflow. Bottom: Passaúna River as Inflow. Diagrams created by the author of the dissertation based on Ishikawa et al. (2021).

The dominance of overflows is not to be observed in the Z-model. For the case of the Ferraria Bridge the interflows are dominating the picture in the Z-model. Considering the

temperature at the main Inflow, the Sigma-model presents a dominace of underflows with a few interflows, similarly the Z-model also shows a dominace of underflows but with more frequent interflows.
Figure 4.24 describes the position of maximum tracer concentration for the simulation with the Sigma-system, similar to Figure 4.19 for the Z-model. For the period Mid-August to February 2019 the Sigma-model showed interflows in comparison with the Z-model which, showed an absence of then for the same period. During those months, the Sigma-sytem also modelled more frequently overflows than with the Z-layering system. For the first part of the analyzed period (March to Mid-August 2018) both models showed a similar behaviour with interflows in the lower part of the water column being prevailing.

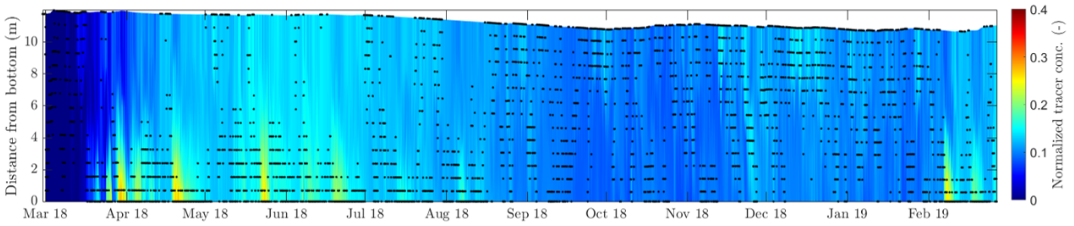

Figure 4.24.: Analysis of possible density currents based on highest tracer concetration at the Intake position with the Sigma-Model. Diagrams created by the author of the dissertation based on Ishikawa et al. (2022).

4.3.4. Role of Wind

In order to evaluate the impact of wind in the thermal structure and the flow velocities at the reservoir, a version of the calibrated model (simulation SN1) but without the inclusion of wind was started. Figure 4.25 shows the simulated water temperatures for the surface, middle and bottom layers at the Intake position. Additionally, the progress of the wind speeds over the period March 2018 to February 2019 are included. At the water surface the simulation without wind delivered higher temperatures than the scenario with its inclusion. This is probably due to the fact that the heat fluxes due to evaporation and wind driven convection at the water body surface will be diffenrent for both simulations, since those fluxes depend among other variables on the wind speed. In the heat flux Ocean model the evaporation rate used to calculate the evaporative heat flux and the forced convective heat flux are both directly proportional to the wind speed. On average the temperature without wind was 3.0 $^{\circ}C$ higher than with the inclusion of wind. The differences were fairly constant independent of seasons and wind speeds. At the middle of the water column the temperatures without wind were mostly higher than with wind with a mean difference of ca 1.2 $^{\circ}C$, but the differences were not constant over time. In fact for the time Mid-November to Mid-January the temperatures for both simulations were similar. At the bottom the temperatures without wind are lower than with it for the period March to Mid-May, which corresponds to a stratified period during autumn according to the measurements. After this, the temperatures without wind become higher until approx. Mid-November at the end of spring, this taking place during periods of relative low temperature gradients as described through the field measurements (see Figure 3.11 in chapter 3). During late spring and winter

the temperatures without wind become again lower than with it, this period corresponds to strongly stratified conditions.
In general the thermal structure with and without wind effects showed considerable differences also for the temperature gradients calculated as the difference between the surface and bottom temperature and presented in Figure 4.26. During Autumn the temperture gradients for the simulation without (mean gradient: 6.4 $°C$) wind were higher than with wind (mean gradient: 2.7 $°C$) , however the difference between the gradients gradually gets smaller until the end of the season when they are similar for the end of winter, reflecting both simulations in that way a period with low temperature gradients and hence mixed. For the spring and winter the gradients in both simulations increase, being higher for the case with no wind and the differences between the gradients gradually increasing towards late winter .

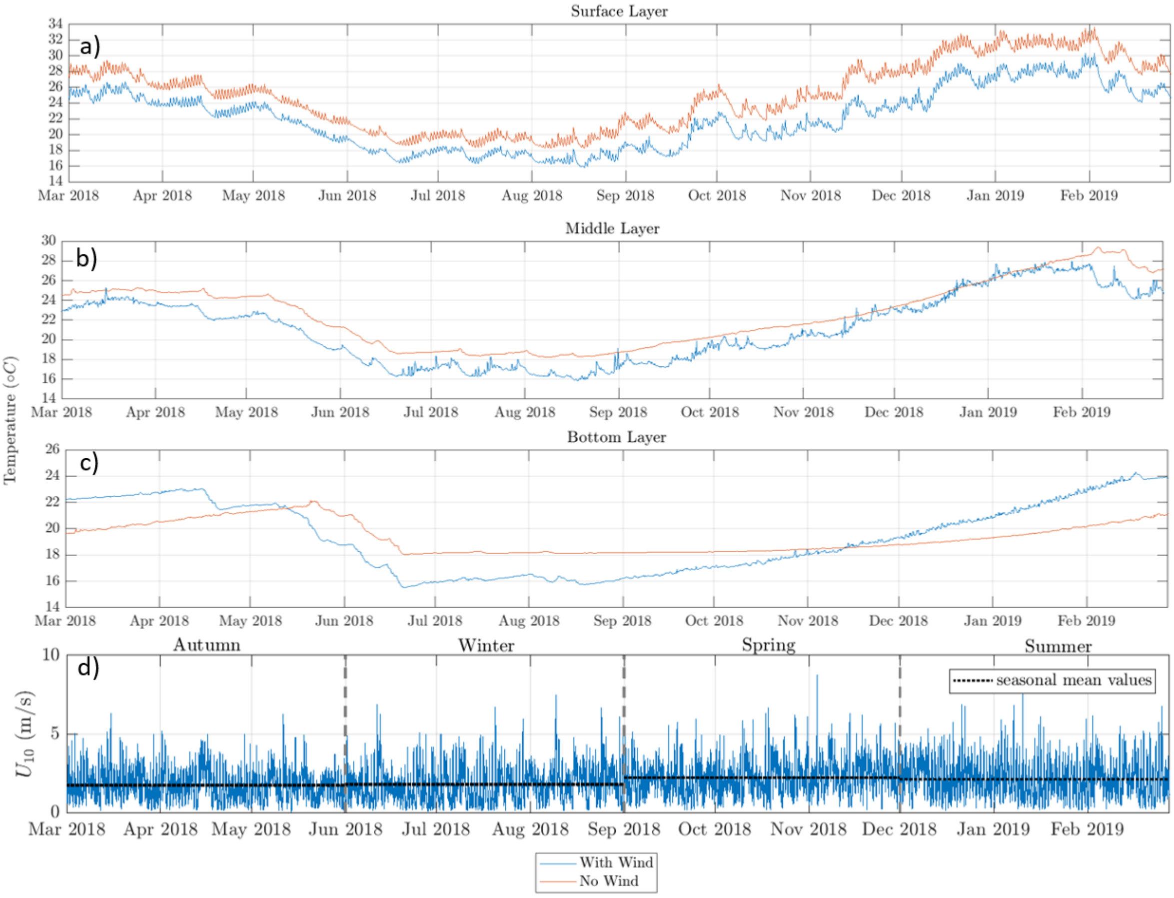

Figure 4.25.: Simulated water temperature at the water Intake with inclusion of wind (blue lines) and neglecting wind (orange lines). a) at the surface, b) at ca. 6 m above the bottom , c) at the bottom and d) wind velocity.

Figure 4.27 shows the calculated horizontal flow velocities at the surface, middle and bottom of the water column at the Intake position with the inclusion and exclusion of wind. For all three layers the velocities are considerably higher with the effect of wind. The only period when the velocities are similar is Mid-June to Mid-July when the temperature gradients are smaller and hence the stratification weakens. The mean horizontal flow velocities for the simulation with wind are 2.19, 1.39 and 0.95 cm/s at the surface, middle and bottom layers in contrast to 0.73, 0.5 and 0.38 cm/s for the same layers in the simuation without wind. It can also be observed how the fluctuations in the horizontal velocities are higher for the simulation with wind than without it. This is reflected in the standard deviations of this parameter being 1.81, 1.05 and 0.61 cm/s at the surface, middle and bottom layers for the simulation with wind in contrast to 0.6, 0.54 and 0.37 cm/s for the same layers in the simuation without wind.

At the position Buffer as indicated in Figure 4.28, the water temperature simulated with the model without wind is higher than the same parameter with the inclusion of wind, with the exception of the month of March a few individual time points. This pattern is present for both the surface and the bottom layer. On average the temperature differences were of around 1.8 and 1.4 $°C$ for the surface and bottom layers. Figure 4.29 presents the temperature gradients for this position. The case withouth wind presented higher temperature gradients than the case with wind, the average gradient being for the former ca. 0.3 $°C$ higher than the latter. In general, the simulation without wind showed gradients higher than zero more often than the case with wind.

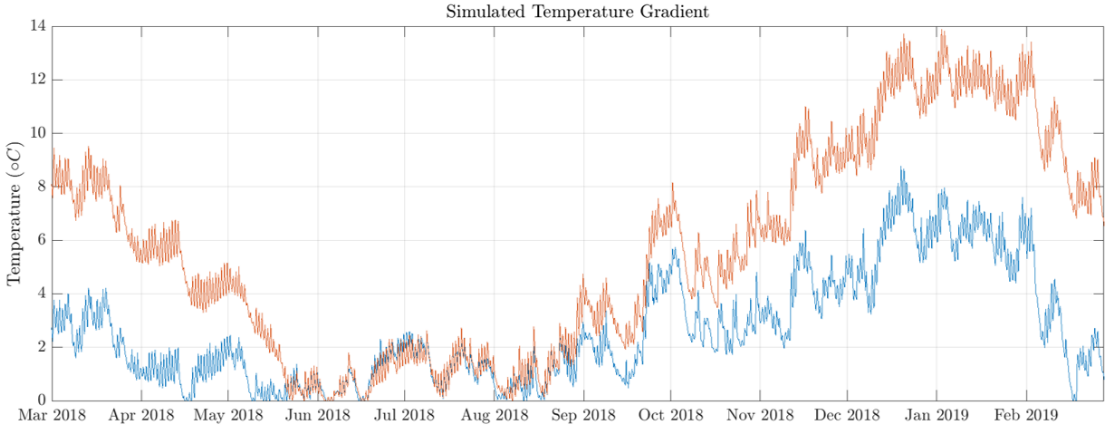

Figure 4.26.: Simulated water temperature gradient at the water Intake with inclusion of wind (blue line) and neglecting wind (orange line).

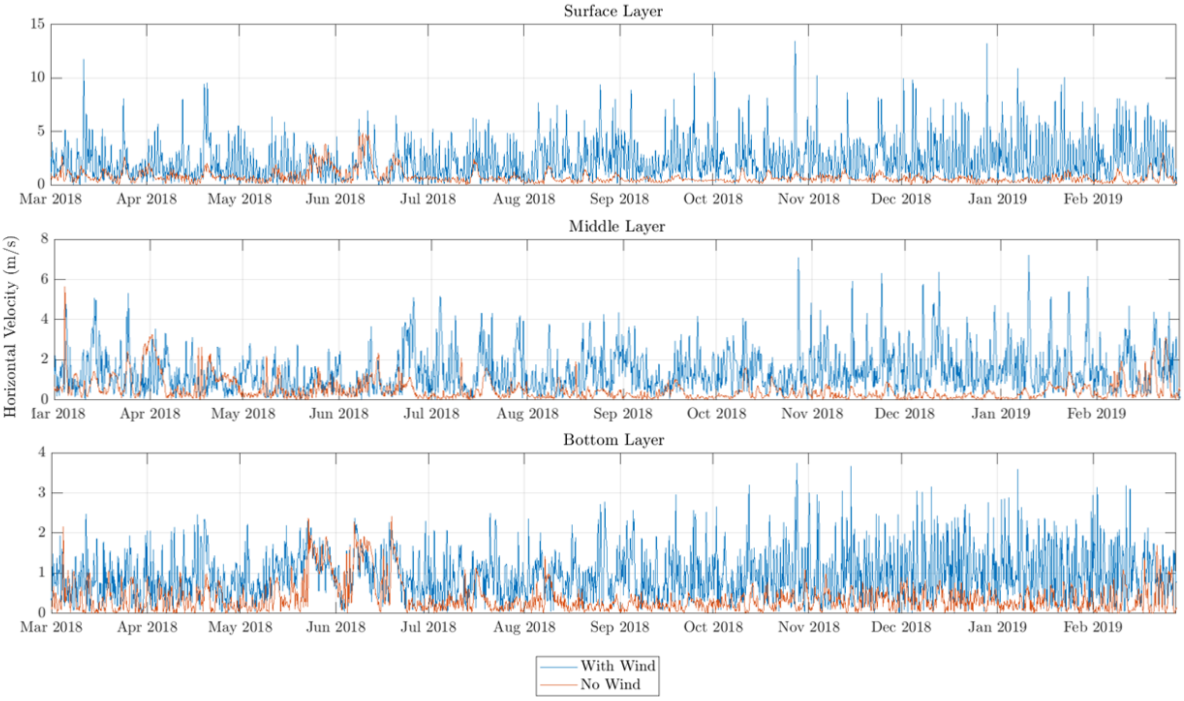

Figure 4.27.: Simulated horizontal velocities at the water Intake with inclusion of wind (blue lines) and neglecting wind (orange lines) at the surface (top diagram), at ca. 6 m above the bottom (middle diagram) and at the bottom (bottom diagram).

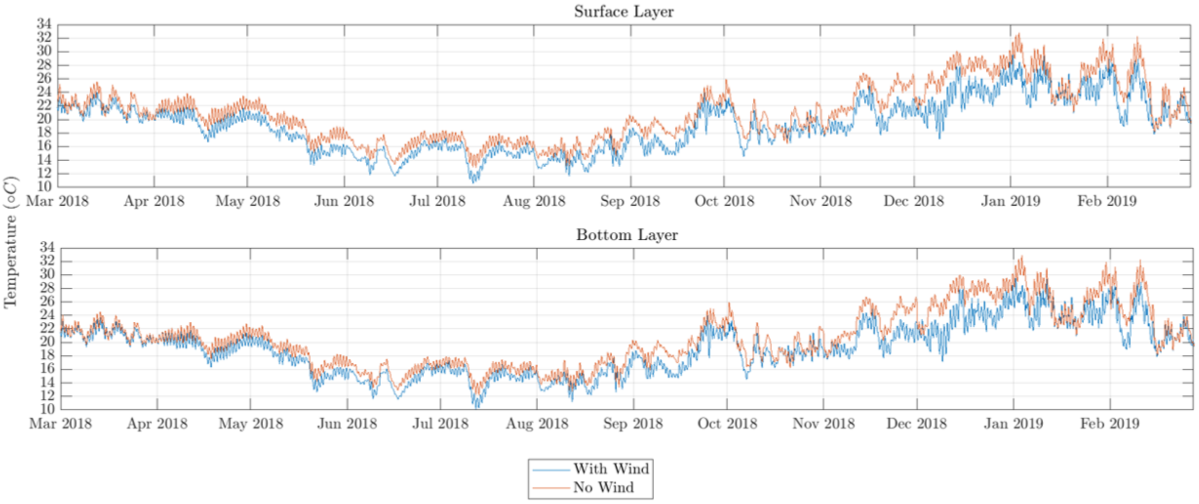

Figure 4.28.: Simulated water temperature at the Buffer with inclusion of wind (blue lines) and neglecting wind (orange lines). Bottom: at the surface. Top: at the bottom.

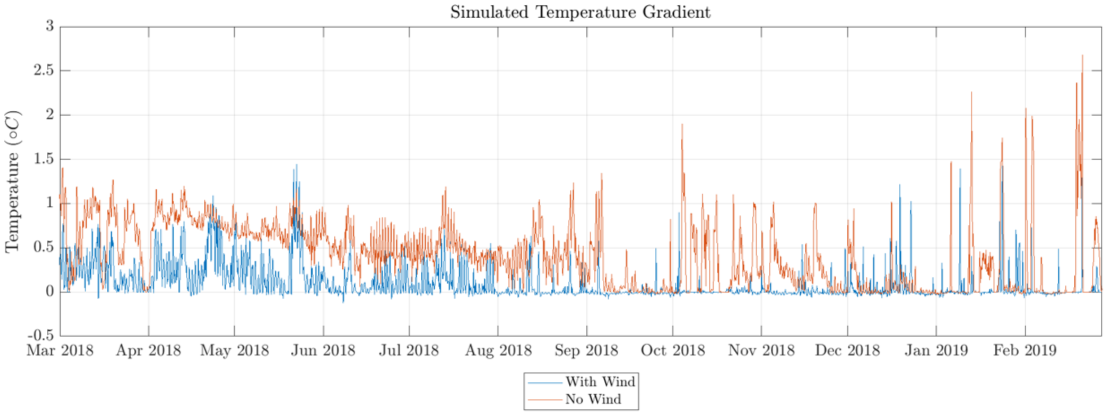

Figure 4.29.: Simulated water temperature gradient at the Buffer with inclusion of wind (blue line) and neglecting wind (orange line).

The horizontal velocities calculated by both versions of the model at the Buffer are illustrated in Figure 4.30. The velocity at the surface layer appears to be higher for the case with no wind, meanwhile the simulation with wind inclusion shows higher variations of the horizontal velocity. The average horizontal velocity is for the case with wind 1.37 cm/s and 1.63 cm/s for the case without it. For the bottom the mean horizontal velocities are 1.33 and 1.68 cm/s for the cases with and without wind respectively. For this layer the simulation without wind shows higher velocites than the simulation with wind but lower variations than the latter, similar as it was for the surface layer.

For the position Park, the simulated temperatures for the model without wind were consistently higher than for the case with wind for all three studied layers as it can be observed in Figure 4.31. The mean differences between the calculated temperatures were 3.3, 3.1 and 2.1 $°C$ for the surface, middle and bottom layers respectively. As for the horizontal velocities, they are higher for the model with wind than without the inclusion of it for the surface and middle layers. Nevertheless not through out all the simulation period: for the months March to July the results for both model are quite similar. The bottom layer exhibits a different behaviour: the velocities are on average higher for the simulation without wind (see Table 4.28) for the whole time period. Individualy, the same trend as for the surface and the middle layers can be observed for the months March to July 2018, where the velocities for the cases with and without wind are similar, even more pronounced for the bottom layer than for the other two studied layers.

Tables 4.27 and 4.28 show a summary of the time averaged temperatures and horizontal velocities for the positions in study. In general the inclusion of wind had an effect on the temperature at each one of the locations, producing higher temperatures for the case with no wind. The gradients between the bottom and surface layers at each position were higher for the case without wind. Those temperature gradients differed the most for the position Intake. As for the horizontal velocities, the simulation with wind showed in general higher magnitudes for the positions Intake and Park. The differences were more pronounced at the surface and the middle layer than at the bottom. For the position Buffer, the velocities for the case with no wind resulted to be higher than for the opposite case.

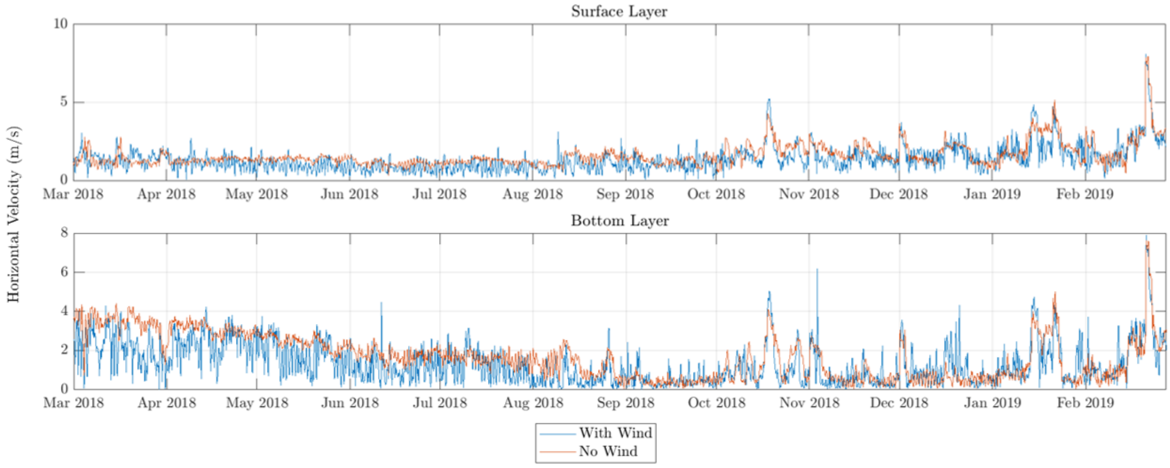

Figure 4.30.: Simulated horizontal velocities at the Buffer with inclusion of wind (blue lines) and neglecting wind (orange lines).

Figure 4.31.: Simulated water temperature at the position Park with inclusion of wind (blue lines) and neglecting wind (orange lines)

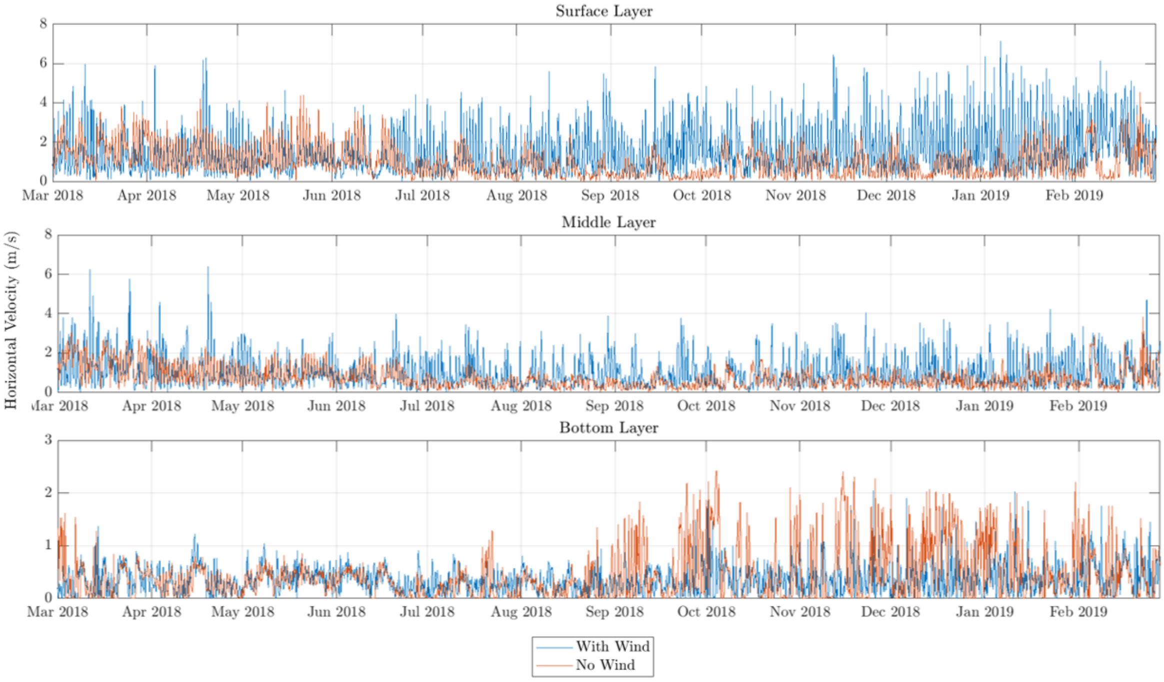

Figure 4.32.: Simulated horizontal velocities at the position Park with inclusion of wind (blue lines) and neglecting wind (orange lines).

Table 4.27.: Time averaged temperatures ($(^\circ C)$) and standard deviations ($(^\circ C)$) for the locations Buffer, Park and Intake for the simulation with and without wind.

Station	Location	Wind		No Wind	
		Mean Temperature	SD	Mean Temperature	SD
Buffer	Bottom	19.08	3.83	20.68	4.29
	Surface	19.18	3.82	21.09	4.17
Park	Bottom	21	3.72	23.34	3.83
	Middle	21.56	3.83	24.59	4.26
	Surface	21.64	3.84	24.85	4.29
Intake	Bottom	19.39	2.69	19.36	1.18
	Middle	21.18	3.47	22.66	3.23
	Surface	22.03	3.78	27.99	4.25

Table 4.28.: Time averaged horizontal velocities (cm/s) and standard deviations (cm/s) for the locations Buffer, Park and Intake for the simulation with and without wind.

Station	Location	Wind		No Wind	
		Mean Velocity	SD	Mean Velocity	SD
Buffer	Bottom	1.33	1.07	1.68	1.15
	Surface	1.37	0.82	1.63	0.76
Park	Bottom	0.36	0.28	0.44	0.48
	Middle	0.98	0.79	0.76	0.56
	Surface	1.15	1.21	0.98	0.77
Intake	Bottom	0.95	0.61	0.38	0.37
	Middle	1.39	1.05	0.5	0.54
	Surface	2.19	1.81	0.73	0.6

4.4. Conclusions

The best model results for the simulation of the temperature were obtained with the highest number of layers (20) tested. Nevertheless, the improvement of the results in comparison with the simulation with 20 layers was marginal. Also considering the computational efforts for the model with 20 layers would be larger than for 15 layers, it was decided to perform the studies regarding the hydrodynamics with the 15 layers configuration. It is interesting that the changes on the Manning's coefficient were able to generate a change in the time averaged horizontal velocities over the whole water depth and not only at the layers close to the bottom. Contrary as it would be expected for the case of reservoirs, due to their high-water levels in comparison to the roughness height at the bottom.

At the water Intake the parameters affecting the most and the least the time averaged temperature were the Dalton number and the Manning's coefficient respectively. What the horizontal flow velocity concerns, the user defined background vertical viscosity and the number of layers affected the most and the least the simulation results. It is necessary to point out, that these affirmations are valid for the studied range of the investigated parameters. Parameters included in the calculation of the heat flux (Dalton number, Stanton number and Secchi depth) at water-air interface should be kept in mind and the sensitivity of the model to their change be tested, since they have a direct influence in the thermal structure simulated with the model.

In general, for all sensitivity analysis, it was found that the flow velocity was always underestimated with respect to the measurements. No model configuration was able to reach the velocities measured at the water Intake. One possible reason for this, is the fact that important variables like the wind speed and direction were measured 4 km away from the reservoir and correspondly they could strongly differ from the ground-truth values at the water body. Polli (2017) investigated the effect of using meteorological data of two stations with an approximated distance of one kilometer between each other. One station was over the water at a floating plattform and the second one was at land. Calculating the heat fluxes in the reservoir with both data sources delivered different results and the most divergent variable was the wind velocity. Moreover, divergent heat fluxes could lead to different mixing processes and hences to different flow velocities.

The temperatures at the Intake could be modeled with a MAE of 0.38 $°C$ and the velocities with a magnitude of 1.01 cm/s for the same parameter. Those values for the errors were similar to the magnitudes found within the framework of similar studies (Mi et al., 2020; Dissanayake et al., 2019; Soulignac et al., 2017; Chanudet et al., 2012b; Marti et al., 2011). The model performed the poorest during the summer (strongly stratified conditions) and the best agreement was achieved during winter, when the reservoir was well mixed. The Schmidt stability for the measurements and the simulation showed good agreement with light underprediction of this parameter during Fall and a higher stability of the water column in the model than in the measurements for Spring and Summer. For the additional points where temperature loggers were deployed, the model showed MAE between 0.36 and 0.9 $°C$. The poorest simulation took place at the Ferraria Bridge. The highest temperature gradients were present at the Dam region were the water column also showed gradients smaller than 1 $°C$. The turbulent kinetic energy over depth at positions with high water depths like the Center and the Dam showed peaks at the water surface and at the bottom with the minimal magnitudes in intermediate layers.

Regarding the density currents it is important to select the adecuate position to compare temperatures with the bottom and the surface of the water Intake. One would be inclined to select the main Inflow temperature but due to the presence of the Buffer in the studied reservoir, the water finds the conditions to get warmer in this pre-bay. For this reason the temperature at the Ferraria Bridge should be selected for analysis, i.e. at the entrance to the main part of the reservoir. For the case of the Ferraria Bridge, the interflows are prevailing over the underflows, meanwhile for the case of the main inflow the opposite situation is presented: underflows prevailed. Also for the whole simulation period, overflows are not common, but they do occur for the case of the Ferraria Bridge as inflow. The use of the Z-model resulted in a better reproduction of the thermal stratification at the Intake than the employment of the Sigma-model. On the other hand, the density currents were better matching the measurements with the use of the Sigma-model.

The exclusion of wind in the simulations led to different thermal structures of the resevoir which were more notorious at the water surface than at the bottom. This can be explained to the changes in the evaporative and wind driven convection fluxes, since those fluxes are a function of the wind speed at 10 m above the water surface. The horizontal flow velocities were shown to be on average higher for the simulation without wind than in the simulation with wind inclusion for deep positions like the Intake. For the Buffer the velocities were slightly higher with the exclusion of wind. Nevertheless, for all over the reservoir, the oscillations in the velocities were higher for the simulation with wind inclusion.

5. Numerical Modelling of the Suspended Sediment Transport including Wind and Heat

[3]

Abstract
The transport and deposition of suspended sediments in reservoirs not only affect the life span of the storage capacity of these water bodies but also influence the quality of the water upstream of the impoundments. Hence, these processes have been object to a large number of studies, more specifically using numerical simulations. Wind and temperature influence the hydrodynamics of lakes and reservoirs affecting the shape and magnitude of the velocity profiles and also inducing mixing and stratification in the water column. The effect of those two factors on the transport of suspended sediments in reservoirs is here investigated through numerical simulations with the software Delft3D applied to the Passaúna Reservoir in Brazil. Furthermore, the sensitivity of the simulations results to two vertical grid systems implemented in Delft3D: Z- and sigma-coordinate systems was tested. The Z-layer system is usually implemented when modelling processes in which vertical exchange is relevant, e.g. thermal stratification. On the other hand, the sigma-layer configuration is the standard selection when modelling suspended sediment transport. The amount of deposited sediments, the deposition pattern and the suspended sediment concentration (SSC) profiles were investigated for the scenarios considering wind and temperature effects. It was found that the numerical results in terms of transport of suspended sediment are affected by the selection of the vertical coordinate system; furthermore, it is showed that the inclusion of temperature and wind in the numerical simulations is relevant. This work is a basis for the setup of other models in similar reservoirs, in environments where both fine sediment transport and thermal stratification processes are relevant.

Keywords: Reservoir Sedimentation, Suspended Sediments, Numerical Modelling, Wind Effects, Temperature Effects.

5.1. Introduction

Reservoirs are designed to provide water supply, flood protection, hydropower generation and/or recreation. The construction of reservoirs around the world is constantly rising due

---

[3] This chapter partly consists of excerpts of the peer-reviewed conference paper (Gonzalez et al., 2022) written by the author of the present dissertation and published in the proceedings of the 39th IAHR World Congress.

to the increasing water scarcity and energy demand. Sedimentation threatens to decrease the storage capacity of these water bodies (Schleiss et al. 2016) and therefore it is essential to understand all the processes that may have an impact on this. Water temperature and the concentration of suspended sediments are two factors directly influencing the quality of the water in reservoirs. High SSC affects the heat amount been transfered to the water column due to solar radiation and thus the temperature of water. Moreover, cohesive sediments act as a sink for chemicals and nutrients, which can be again desorbed into the water column during high flow events or due to variations in the chemical parameters of the ambient, such as the pH-value (Lee et al., 2004). Fine sediments are a well known sink and probably source of nitrogen and phosporous (Hirsch, 2012), which directly affect the growth of flora and fauna in aquatic ecosystems.

Numerous authors have successfully simulated the transport of suspended sediments in reservoirs. Hillebrand et al. (2016) studied the deposition of fine sediments at the run of river reservoir Iffezheim at the Rhine river, in Germany, using the software SSIIM3D.Omer et al. (2015) published their studies on the simulation of the hydrodynamics and the sedimentation at the Roseires Reservoir in Sudan with Delft3D in order to provide a guideline for the planning of future field campaigns for the extraction of sediment cores. Haun et al. (2013) calibrated a 3D model to simulate SSC and sediment deposition patterns at the Angostura Reservoir in Costa Rica using the software SSIIM3D.

Today's practice is to set up numerical models for the simulation of suspended sediment transport without considering wind and thermal stratification or mixing processes in the water body, this may be due to the additional computational costs ligated to the solution of the advection-diffusion equation for the heat transport. However, it is known that the hydrodynamics of reservoirs and lakes is usually influenced by these phenomena (Elci, 2008; Polli and Bleninger, 2019b; Imberger and Patterson, 1989). Due to the reduced transport capacity of the flow within a reservoir, wind can become an important forcing for the hydrodynamics and thus for the suspended sediment transport in several ways. Wind could affect the dispersion of sediments suspended in the water column, but also it may be a factor enhancing the shear stress at the bottom and inducing to sediment resuspension (Sheng and Lick, 1979). Moreover, in the case of wind of high speed and long duration, the sediment suspended in deepers layers of the water column can be influenced by the stokes drift generated by the action of wind (Constantin, 2006; Wang et al., 2020a). On the other hand, temperature gradients may affect the velocity profiles and as a consequence the mass transport in the water body.Polli and Bleninger (2019a) studied the changes in the advective and dispersive transport of a conservative tracer in the Vossoroca Reservoir with the inclusion or ommision of the water temperature. They found notorious differences in the tracer mass fluxes been transported when considering temperature in their numerical simulations. As expected, the vertical velocity profiles were also different when including temperature stratification. Hence, the inclusion of wind and thermal stratification in the numerical simulations of suspended sediment transport should be studied. In recent years, a few authors have started to investigate the influence of temperature and/or wind on suspended sediment transport in water bodies. Zhong et al. (2020) simulated the impact of cold-water masses and wind on the suspended sediment transport in the South Yellow Sea, finding that the temperature of the incoming water and the ambient water influenced the SSC-profiles, and that regular wind intensities may influence the direction of the transport of suspended sediments. (Wang et al., 2020b) studied the effect of wind on sediment transport in a 3D numerical model of the Tingalpa Reservoir in Australia, clearly identifying that it induces changes in the circulation patterns and the flow field and on the SSC-profiles all over the reservoir. Wang et al. (2020a) investigated the impact of wind on the suspended sediment transport in the largest freshwater lake in China, the Poyang Lake. They determined that the wind is an important forcing factor for the distribution of the SSC, including the effect of wind in the simulations produced results closer to the measured SSC. Zhang and Wu (2019) analysed the high suspended solid concentrations (SSC) affecting the water quality at the withdrawal location in the Deze Reservoir in China using a 3D model. They also evaluated the impact of the construction of check dams on the deposition of sediments as an water quality improvement measure. In the numerical modeling also the water temperature was taken into account; which is not the regular case while modeling sediment transport in reservoirs. GHASEMLOUNİA and KABDAŞLI (2021) investigated the effect of the temperature of the inflowing water and the reservoir's on the SSC-profiles in an fictive water body, making use of the software FLOW3D. They found that the temperature affected both the SSC-Profiles and the sedimentation patterns.

Most numerical models use a vertical Sigma-coordinate system to simulate suspended sediment transport. If temperature is going to be taken into account, then a Z-coordinate system should be considered instead, since this is the recommended option for the modelling of stratified flows, especially in combination with steep topography as the case of reservoirs (Deltares, 2014)). However, a Z-model may introduce inaccuracies in the calculation of the bottom bed shear stress (Deltares, 2014; Platzek et al., 2014). Those facts create a dilemma in the selection of a Z- or Sigma-model when the modelling of thermal stratified flows is necessary for the posterior simulation of suspended sediment transport.

In the present study, the transport of suspended sediments in a reservoir for several scenarios was simulated. First to test the sensitivity of the results to wind, temperature, and a combination of both, and secondly to test the sensitivity of the results to vertical layering schematization.

5.2. Materials and Methods

5.2.1. Hydromorphological Model Delft3D

The hydrodynamic software Delft3D (Deltares, 2014), solves the Reynolds-averaged Navier-Stokes equations (RANS) for incompressible free surface flow. For the solution of the RANS, the software reduces the vertical momentum equation to the hydrostatic pressure distribution and employs the Boussinesq approximation. The numerical solution is performed using a finite differences approach on a staggered grid, i.e. velocity vectors are defined on the cell faces and scalar quantities at the cell's center (Deltares, 2014). For the vertical spatial discretization, the software offers two layering schemes; the terrain following sigma- model and the strictly horizontal Z-model. For the former, the number of the vertical layers remains constant over time and space and their thickness is defined by the user as a percentage of the water depth. For the latter, the number of active cells in the vertical direction depends on the local water level and hence can vary with time. At the bottom of the water body, the forcing takes place via the bed shear stress by means of the Manning's formulation. At the free-surface, the model is forced through the wind shear stress, which in Delft3D is assumed to be a function of the wind speed and is calculated using the approach proposed by Smith and Banke (1975). The total heat flux at the interface air-water interface was calculated with the Ocean model (Lane, 1989; Gill and Adrian, 1982). In Delft3D no heat flux between the water column and the bottom is considered. In the present study a k-epsilon closure model was applied to the RANS simulation.

For the modelling of sediment transport with the software up to 99 grain sizes can be defined. The transport of the sediment in the water column is calculated using the advection-diffusion equation considering the particle sink rate under the action of gravity through the settling velocity in the vertical advective term. At the lowest computational cell the deposition and erosion rates are calculated for each sediment class. The formulation to calculate those rates depend on wether the sediment group is cohesive or non-cohesive. For the case of cohesive sediments, the formulations of Partheniades-Krone (Partheniades, 1965) are implemented (see section 2). Under this formulations the erosion rate can be calculated as a function of the erosion parameter and the critical bed shear stress for erosion. On the other hand, the deposition rate is calculated based on the settling velocity of the sediment group and a critical bed shear stress for deposition. Erosion and deposition rates for the case of non-cohesive sediments are calculated with a different approach. The erosion flux is considered as function of the upward diffusion at the lowest layer in the water column and the SSC gradient. On the other hand, the deposition flux depends on the settling velocity of the sediment group and the SSC at the bottom of the reference layer. The settling velocity for the case of cohesive sediments is defined as an user input, meanwhile for non-cohesive sediment, it will be calculated using the approach of Van-Rijn (van Rijn, 1993). The bed load transport rate was calculated using the formulation of van Rijn (1993), which defines a reference height a. Sediments above a are defined as in the suspended transport mode and below it as bed load. With the deposition and erosion rates and the bed load transport rate, it is possible to calculate the changes in the bed height, i.e. erosion or deposition at each bottom cell. The software also offers the option to consider the effect of high SSC in the water density.

5.2.2. Computational Grid

The numerical grid used for this study was constructed using the data obtained during a bathymetric survey with multibeam echo-sounding in 2019 (see Figure 4.2 in chapter 4). The depth increases from the north to the south with maximum depths of about 17 meters upstream of the spillway. The grid is curvilinear, the cell resolution is higher at the Buffer and at the Ferraria Bridge, in order to capture possibly density currents starting at this constriction. Both a Z- or Sigma-model configuration with maximum ten layers were used for the simulations. For the Sigma-model the number of layers remains constant during the simulation and their thickness varies with changing water depth. For the Z-model the number of active layers over time is dependent on the water depth of the reservoir. Any 2D aspect of the present grid coincides with the ones of the grid presented in section 4.2.2, which was used to perform simulations for the hydrodynamics. The vertical resolution of the grid for the modelling of sediment transport has 10 layers instead of 15, as it was for the hydrodynamical grid. This change of vertical resolution was introduced due to the high computational costs while calculating not only suspended sediment transport but also temperature stratification simultaneously. An overview of the numerical grid and the bathymetry of the Passaúna Reservoir is shown in Figure 5.1, for both layering systems employed. A computational time step of 30 seconds was employed in the simulations.

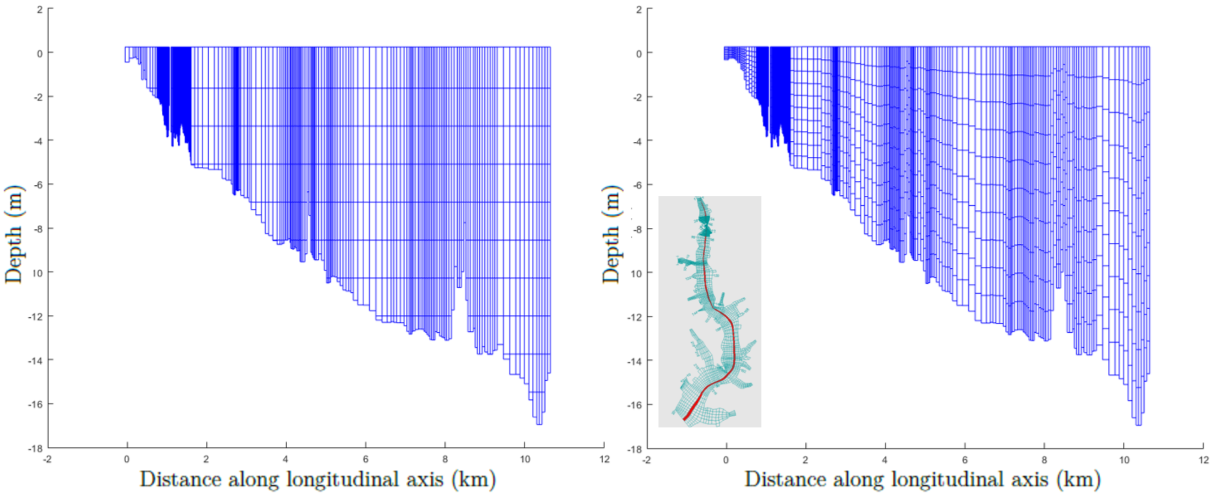

Figure 5.1.: Longitudinal view of the vertical layering for the numerical grid with the Sigma (left) and Z-model (right).

5.2.3. Input Parameters and Field Measurements

All data regarding the modelling of the hydrodynamics and thermal structure of the reservoir (when applicable) was the same applied for the calibrated hydrodynamical model (see section materials and methods in chapter 4). The hydromorphological data used as input for the model were in their majority collected in field campaigns (see chapter 3), if no measurements were available for a parameter, then either literature values were assumed or the parameter was calibrated.

The ammount of incoming sediments through the main inflow could be derived from any of the three sediment rating curves described in section 3.3.1 in chapter 3. The first rating curve RC1 was derived from historical data gathered non-continously during the years 1985 to 2015 at the station BR277 (see Figure 3.4 in chapter 3). The rating curve RC2 was created based on data from a four-days high-flow event at the same station during October 2018. Lastly the RC3 was created based on data modelled while studying the erosion processes at the catchment level. In the simulations all three rating curves were employed and their repercusions studied. The inflowing sediments through the further tributries were determined as a percentage of the concentration entering the reservoir through the main inflow. Those percentages were determined within the framework of the MuDak Project in the studies regarding river catchment erosion. Based on data availability for the calibration, the sedimentation rate for the period 10.12.2018 to 12.02.2019 of the sediment traps were employed. Considering the results of preliminary simulations, two sediment groups were defined to be present in the inflows and the model in general, according to the granulometry measurements of sediments in suspension in the reservoir. The soil composition in the reservoir was prescribed through the information provided by the sediment cores. The settling velocities of the sediments were calculated using the formulas of Zanke and Winterwerp (see sections 2). The erosion parameter was selected according to literature values for fine sediments as 0.0001 $kg/(m^2s)$ (Feng et al., 2020; Deltares, 2014; Winterwerp et al., 2012). The critical bed shear stresses for erosion and deposition were defined as calibration parameters, nevertheless guided by literature values (Wu et al., 2018; Klassen, 2017; Shi et al., 2015; Winterwerp et al., 2012).

5.3. Results and Discussion

5.3.1. Calibration of Suspended Sediment Concentrations

For the calibration of the suspended sediment concentrations, a stationary simulation was set up. For this scenario the date February 2, 2019 was selected. For this date, measurements of the SSC at the Buffer Inflow were available (Inflowing SSC 52 mg/l), so that the simulation could be performed without use of the rating curves. This point is relevant since the RC1/RC2 deliver completely different SSCs when compared with the RC3 and hence consequently different models results would be obtained with different rating curves. For the selected date, measurements of the suspended concentration at the locations Buffer, Ferraria Bridge, PPA, Park, Center, Intake and Dam at different depths were available as well (see Figure 3.30). Two sediment groups were defined based on the granulometry of the suspended sediments measured at the Ferraria Bridge during the mentioned date (see Figure 3.37). They were defined as cohesive with the diameters of 13.6 (**group 1**) and 6.6 μm (**group 2**). The composition of the inflowing sediments, i.e. percentage of sediments of each group can also be defined according to the amount of grains found in the suspended sediment's granulometry.

No initial sediment layer at the bottom was added, to eliminate the possibility of erosion and also eliminate the parameters critical bed shear stresses for erosion as further uncertain variable. This simulation included wind as an average of the wind speed during the mentioned day and with the prevailing wind direction of the same period. The calculations were performed in the Sigma-grid, since this is the regular choice when modelling sediment transport. Several cases were run and they are summarized in Table 5.1.

The implemented simulations remained all within the range of physical realistic values based on the field measurements. **Sim1** depicts a situation for which all of the incoming sediments have a size of 13.6 μm, which corresponds to the D_{50} of the granulometric curve for the simulated day. The settling velocity of 0.05 mm/s was calculated using the formula after Winterwerp (see equation 2.47). **Sim2** represents a scenario where all of the incoming sediments have a size of 6.6 μm and an after Winterwerp's settling velocitiy of 0.02 mm/s. **Sim3** portrays a situation where both groups are present in the inflow with the coarsest fraction being dominant. Meanwhile for the **Sim4** both sediments groups are equally present in the inflowing sediments. **Sim5** represents an extreme case in which all sediments are extremely fine and have the lowest possible settling velocity according to the literature (Winterwerp and Van Kesteren, 2004). Notice that the defined sediment groups would correspond to highly cohesive materials (range 2 to 20 μm) according to the classification by Mehta and Lee (1994).

Table 5.1.: Steady state simulations for February 5th 2019

Simulation	% in infow		Settling velocity (mm/s)	
	Group 1	Group 2	Group 1	Group 2
Sim1	100	-	0.05	-
Sim2	-	100	-	0.02
Sim3	75	25	0.05	0.02
Sim4	50	50	0.05	0.02
Sim5	-	100	-	0.01

Figures 5.3 to 5.5 show the resulting SSCs at the observed positions in steady state and the measured quantities during the selected day. For all positions, the Sim1 delivered the lowest SSCs, which can easily be explained by the fact that this simulation presented the coarsest sediment composition and hence the sediments will settle earlier in the main inflow's proximity for this case. Following Sim1, Sim3, Sim4, Sim2 and Sim5 presented in that order increasing SSC for all positions. The explanation for this is the same: the content of fines in the inflowing sediments. In this order of ideas, Sim5 continuosly showed the highest SSCs, since this simulation introduced the lowest possible settling velocities for flocs structures.

Figure 5.2.: Positions of the measured SSCs.

Figure 5.2 shows the positions were the SSC were measured. As previously mentioned the SSC at the Buffer Inflow was used as boundary condition. At the Buffer the Sim4 depicted the best the measured SSC, meanwhile the Sim5 was the farthest away from the measurements. At a depth of 1 m below the water surface the Sim4 calculated a SSC 1 mg/l lower than measured. For deeper layers the simulated values could no be compared to measurements because of lack of data. Sim1, Sim3 and Sim4 presented lower SSCs gradients than the other two simulations, which can again be expained by the coarse of fine composition of the suspended sediments. For the Sim2 and Sim5 the turbulence primes over the gravitational forces due to the very fine composition of the grains.

For the position FB the measured SSCs are higher than the calculated ones for all simulations. Consequently, the simulation closest to the measurement was for this case the Sim5. Notice that according to the measurements the SSC at FB are higher than the inflow concentrations, which must mean than either further materials from the tributaries at the Buffer are contributing to these higher SSC or resuspension of the material from the bottom took place. Since the materials entering through the further tributaries does not sum up to the presented measured concentrations, it is likely than resuspension would be the reason. Also notice that the gradients for the measurements are evidently higher than the simulation results.

At PPA the gradients of all simulations are similar between each other and steeper than in the measurements. At the surface the simulation Sim1 was nearest tho the ground truth value, meanwhile at 1.5 m below the water surface the Sim4 performed the best. Following the gradient of the measurements, it could be possible than higher SSCs would be measured at deeper layers and even coninciding with the results of Sim5.

For the location Park the simulations Sim3 and Sim4 offered the nearest result to the measurements. Sim3 performed best at the upper layers and Sim4 at the bottom. For this position the measured SSC-gradient decreases in comparison to the to previous ones. For the locations Center, Intake and Dam, the measurements showed higher SSCs than the simulations with Sim5 being the nearest to the ground truth values for Center and Intake. The SSC for all simulations at the Dam are almost zero and hence far from the measurements. The fact that there is suspended sediment available at the most downstream position in the reservoir could be a hint for further sediments entering the reservoir trough the tributaries near the dam. Sediments which have not being quantified, since the only measurements of incoming SSCs were carried out at the main Inflow.

It can be noticed, that for the first four stations the simulated values are in the same range of the measurements but for the last three most downstream stations, the measured concentrations were always higher. If all over the stations the SSCs would be higher than the results of all simulations, one would be prone to assume than maybe the inflowing amount of sediments should be higher or than sediment resuspension at the inflow of the Buffer would contribute to the mismatch. But this in not the case here, the first stations show that the inflowing SSCs should be approximately right. The use of even lower settling velocities in order to get higher SSCs downstream, would be not reasonably from a physical point of view. Another hypothesis could explain the high SSCs downstream of the position Park: the tributaries downstream of it provide the reservoir with more sediments than the defined amounts and hence those sediments are not being accounted for. This could explain the SSCs being higher for Center than for Park even though the former one is closer to the main Inflow. As for the position Dam, which showed even higher concentrations at the bottom than the two inmediate upstream locations, it could be explained either by additional inflowing sediments through tributaries nearby or the measurements detected the presence of turbid water transported there as a turbidity current. Nevertheless, there is no further measurements of the tributaries different from the main Inflow to confirm this theory.

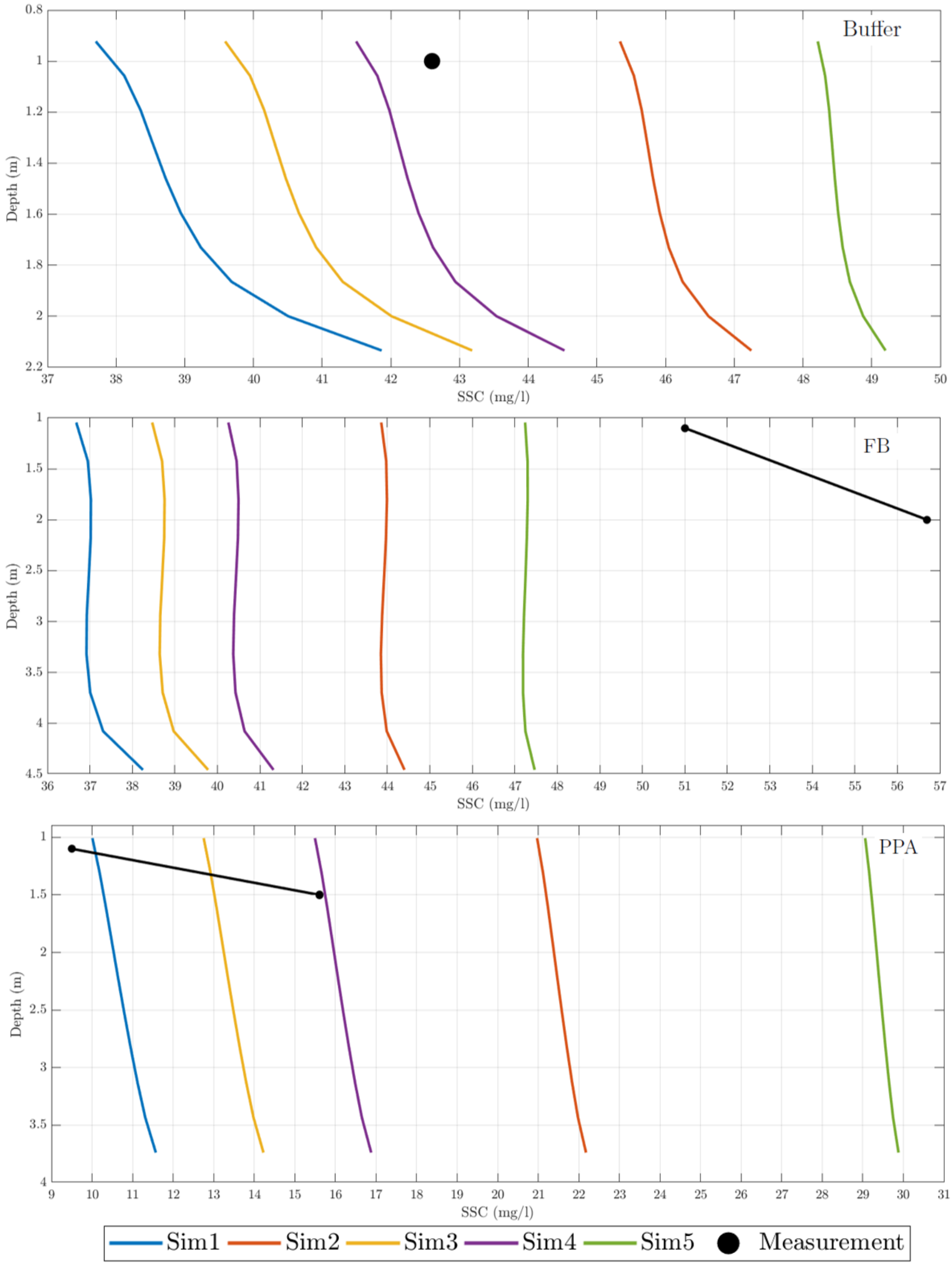

Figure 5.3.: Simulated steady SSCs at the positions Buffer, Ferraria Bridge and PPA and measured SSCs on February 5, 2019.

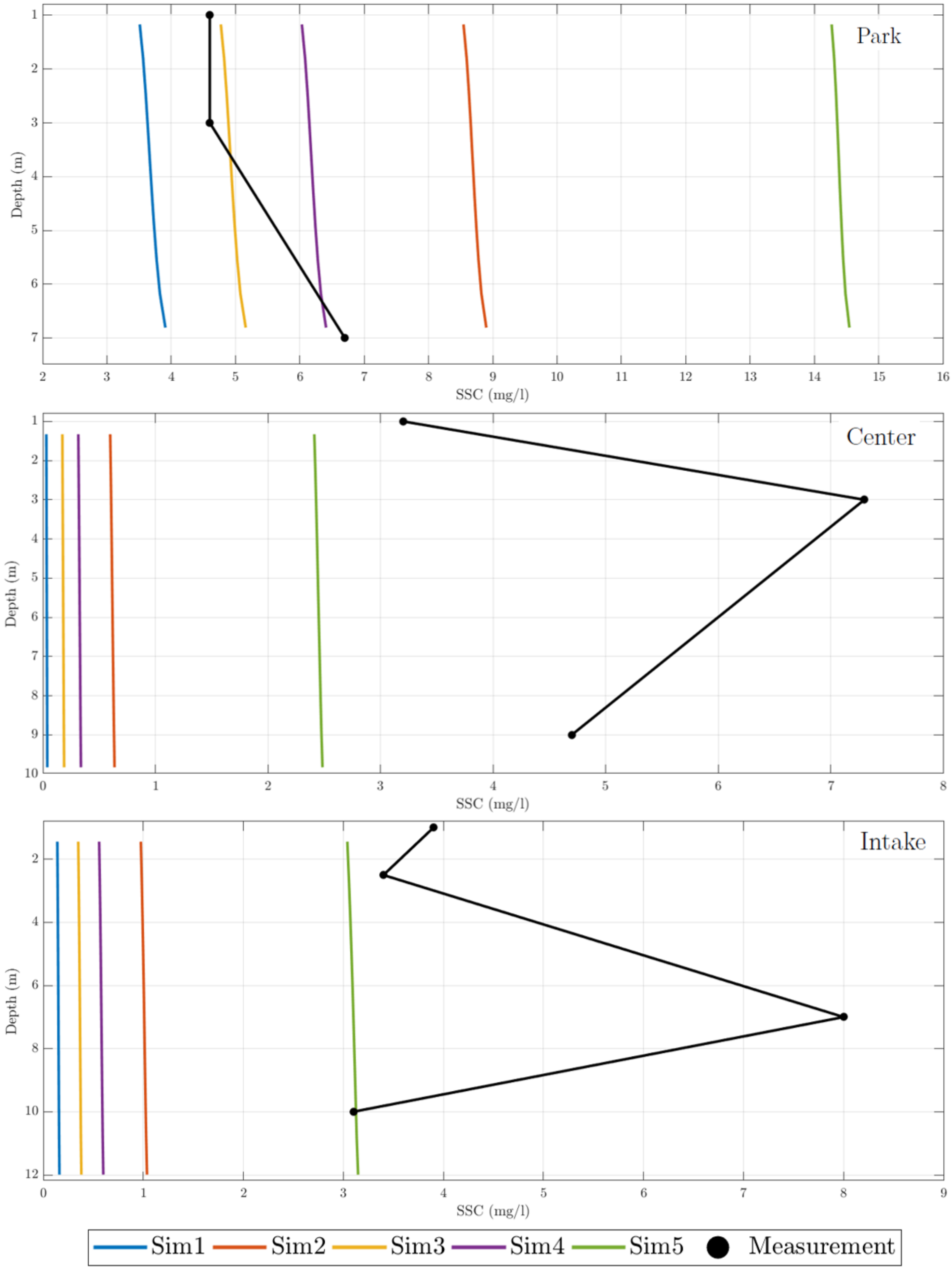

Figure 5.4.: Simulated steady SSCs at the positions Park, Center and Intake and measured SSCs on February 5, 2019.

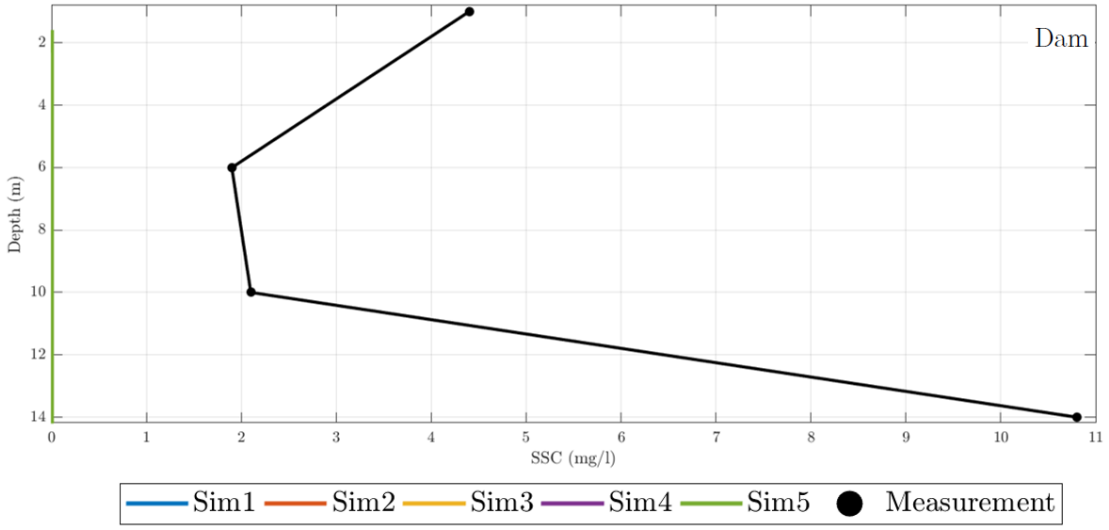

Figure 5.5.: Simulated steady SSCs at the position Dam and measured SSCs on February 5, 2019.

No simulation was able to match all measurements under the studied framework. For further studies, the sediment composition of Sim4 will be used, which for the first four points deliverd reasonable results and also includes the two sediment groups defined.

5.3.2. Calibration of Deposition Rates

For the calibration of the deposition rates, the results of the sediment traps will be used (see section 3.3.4). The reason to use the result of the traps and not the other sedimentation quantification methods, is that the results of the traps quantify the parameter for short periods of time for which hydro-morpohological data are available and reliable. On the other hand, the other methods (e.g. gravi-probe) presented the sedimentation for the whole life-span of the reservoir. Dividing the sediment layer magnitude found with the gravi-probe by 30 years to get an annual sedimentation rate would imply that the hydro-morphological processes during every year were almost the same, which is unlikely. Figure 3.44 in chapter 3 depicts the time spans covered by each campaign with the traps. The campaign four was selected for the calibration of the model since this comprehends the date that was used for the SSCs calibration (February 5, 2019). The campaign four corresponds to the period December 10, 2018 to February 12,2019, which makes for 64 days to be simulated with the morphological model. During this campaign, sedimentation rates of the points Center, Intake and Dam were measured. For the present study only the rates at the position Center will be considered. The reason to discard the information for the further two traps, is that as seen in the calibration of the SSCs it is likely that more sediment than the percentages determined with the RUSLE method by Sotiri (2020) is coming trough the tributaries downstream of the point Center and this additional sediment can not be quantified.

Notice that the position of the point Center for the traps (see map in Figure 3.44) is not the same than for the SSCs (see Figure 5.2) but the former is located upstream of the latter. Summarized, the deposition rate to be reached at the position Center is 9.27 g/m^2day for the mentioned period.

With the sediment composition of Sim4, the mentioned 64 days will be simulated, with no initial sediment layer at the bottom. The hydrological boundary conditions will be directly taken from the hydrodynamic model. For this simulation the use of a rating curve is necessary, since it is unsteady and no measurements of the inflowing SSC for each day of the mentioned period are available.

First, three different simulations are started using the three available rating curves. Those simulations are denominated **Sed1**, **Sed2** and **Sed3** and they employed the rating curves RC1, RC2 and RC3 respectively.

Simulation **Sed4** was set up using the RC3 and the sediment composition of Sim5, the aim of this simulation is to evaluate wether with the lowest physically plausible settling velocity and with the highest inflowing SSC delivered by RC3, the high measured sedimentation rate can be reached or not.

The simulations Sed1 to Sed3 showed all lower sdimentation rates at the position Center than measured (see Table 5.2). As can be observed and was expected the sedimentation rate was the highest for the simulation with the RC3. Nevertheless, it did not match the measured magnitude. Simulation Sed4 doubled the measured value. However, the use of the extremely low settling velocity and the high inflow concentrations derived in RC3 represents an extreme case. Simulation **Sed5** considered the half of the magnitude of the RC3's inflowing concentrations, delivering a sedimentation rate at the position Center of 9.71 g/m^2day, which matches the measured deposition rate. Still the SSCs entering the model through the main inflow for this simulation ranged between 832 and 1414 mg/l. In contrast to these magnitudes, at the station BR277 in the Passaúna River the highest ever registered SSC was 750 mg/l, which ignites the discussion of the use of sediment loads to calculate SSCs as was performed to create the RC3 (see 3).

In general, the simulation Sed5 showed that high inflowing SSCs are needed to get the measured sedimentation rates, concentrations that have not been registered, not even during a high flow event. Not to mention that the settling velocity would be in the lower boundary of physical plausibility. However, the unlikelihood of the measured sedimentation rate only holds if it is assumed that all sediment depositing in the trap comes from the sediment entering the reservoir during the simulation period. Sedimentation rates coming from sediment traps can be misleading, if they are used to quantify the amount of sediments entering the reservoir for a determined period. The reason for this is that previously deposited sediment in upstream regions like the Buffer could be eroded and end up in the trap and be erroneously accounted for the sediment that entered the reservoir.

For further simulations the RC2 was applied, since it is based in actual measurements of the SSCs and it delivers higher sediment loads than RC1 for the studied period. Simulation **Sed6** includes a 100 cm thick sediment layer all over the model to create a source of further sediment which could be at least partially eroded and contribute to the observed high deposition rates at the position Center. For this simulation the resulting deposition rate was two times higher than the measured value. For the simulations a critical bed shear stress for erosion of 0.1 N/m^2 was used. The lowest registered values go as low as 0.14 N/m^2 for cohesive sediments (Shi et al., 2015). In the model, the lower boundary for this parameter was used for the flow to be able to erode the sediments previously deposited in the Buffer, since the Reservoir in question is a low velocity system. In the case of cohesive sediments the critical bed shear stress for erosion depends not only on the grain size but also on the grade of consolidation of the bed materials, mineral composition, organic material, temperature, pH value and on the interaction between particles (Wu et al., 2018). The asssumption of the critical bed shear stress for erosion was feasible for the cohesive materials found at the bottom of the reservoir. The critical bed shear stress for deposition was asssumed as very low 0.001 N/m^2. The reason for this is to allow the sediments to be transported further downstream of the reservoir and not to most of them deposit at the Buffer region, almost inmediatly after entering the reservoir. The critical bed shear stress for deposition of cohesive sediments has been found to comprehend the range between 0.01 until 10 N/m^2 (Wu et al., 2018; Shi et al., 2015).

In order to reduce the high deposition rate calculated within the simulation Sed6, the critical bed shear stress for deposition was set up higher within the simulations **Sed7**, **Sed8**, **Sed9** and **Sed10** with the magnitudes of 0.04,0.02,0.005 and 0.003 N/m^2 respectively. With higher onset for the sediment deposition, more grains will be able to settle at the Buffer and hence not be available in the water column to be transported to downstream regions. Nevertheless, as can be observed in Table 5.2 the sedimentation rates produced within these simulations were much lower than 9.27 g/m^2day. This means that the bed shear stress at the Buffer was oft lower than those thresholds and hence sedimentation took place. Figure 5.6 shows the development of the bed shear stress at the numerical cell of the Buffer region with highest depsition. It is evident, that the bed shear stress was constantly lower than 0.005 N/m^2, which was the critical treshold in the simulation Sed9.

The further simulations kept the value of the critical thresholds as the simulation Sed6. Simulations **Sed10** and **Sed12**, included thiner sediment layers at the bottom: 50 cm and 30 cm respectively. Simulation Sed12 yielded a sedimentation rate that matched the measurement of this quantity at the position Center. The set up of this simulation will be used for the investigated scenarios that follow. Table 5.2 shows the sedimentation rates for all simulations set up within the framework of this section.

Table 5.2.: Sedimentation rates and sediment layer thickness at the position Center.

Simulation	Sedimentation rate ($g/m^2 day$)	Sediment layer (mm)
Sed1	0.12	0.006
Sed2	0.25	0.014
Sed3	4.42	0.253
Sed4	18.89	1.080
Sed5	9.71	0.560
Sed6	19.36	1.110
Sed7	1.05	0.06
Sed8	1.32	0.08
Sed9	2.64	0.15
Sed10	4.16	0.24
Sed11	14.76	0.84
Sed12	9.76	0.56

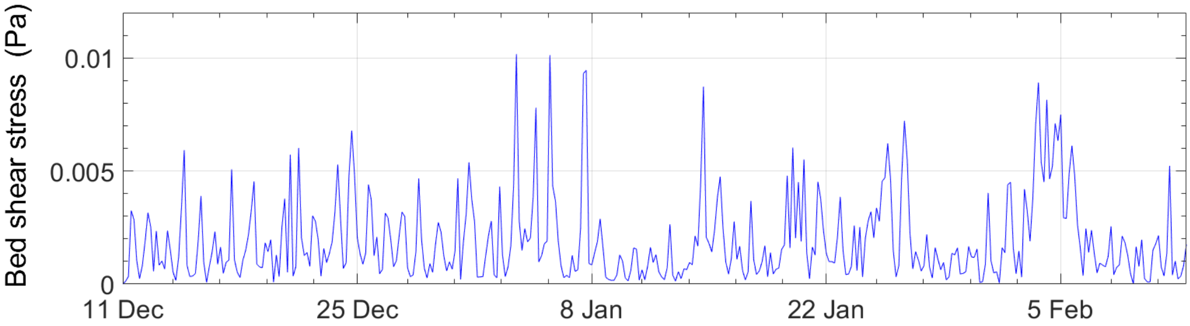

Figure 5.6.: Development of the bed shear stress for the cell with highest deposition at the Buffer within the period December 10, 2018 to February 12, 2019.

5.3.3. Effect of Wind on the Suspended Sediment Transport

Wind is a relevant factor affecting the hydrodynamics in the Passaúna Reservoir as analyzed in chapter 4. All morphological simulations up to this point included the effect of wind. To study the suspended sediment transport in the abscence of this forcing, two simulations were set up with morphological characteristics as the simulation Sed12 but for a different (longer) time period namely for August 1, 2017 to February 28, 2019. The model was vertically discretized with the Sigma-system using ten layers with a time step of 30 seconds. One of the simulations included the effect of wind (denominated **YW**) and the other one did not (denominated **NW**). Figure 5.7 shows the resulting deposition patterns.

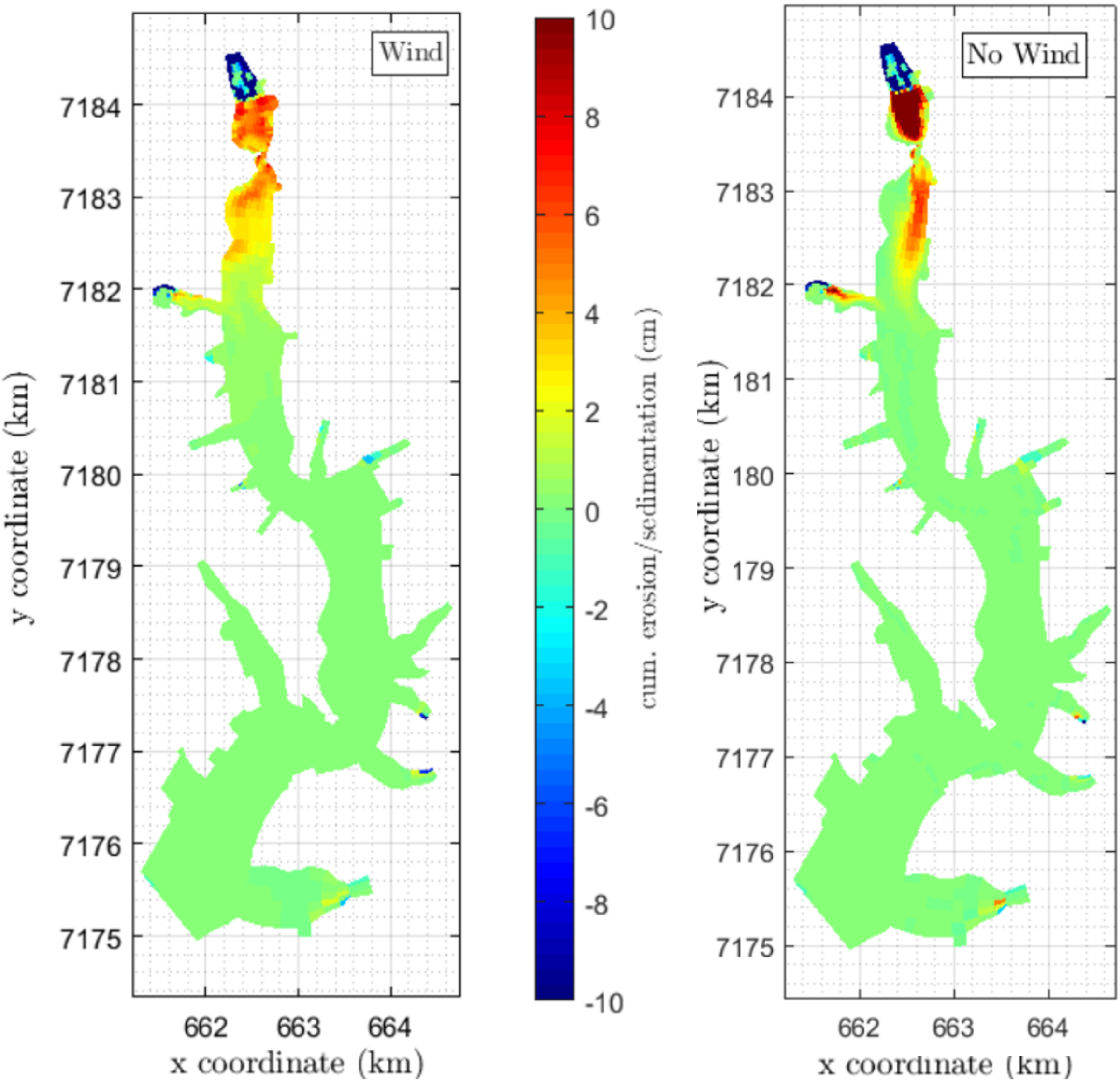

Figure 5.7.: Sedimentation patterns for the simulation with wind (left) and without wind (right).

The upper region of the Buffer where sediments are eroded remained similar for both scenarios. This was expected, since the hydrodynamics at the inflow are controlled by the momentum transfer from the incoming water to the impounded water body. From the whole reservoir area, at the inflow, the hydrodynamical conditions are the most similar to a river. In the case of rivers, wind is not an important forcing. For both scenarios the lower middle of the Buffer presents a depositional area with the thickest sediment layers. Nevertheless, in the scenario with wind the depositional sediment layer is observed all over the cross section even at the banks, which is not valid for the case with wind exclusion. At the Ferraria Bridge less sediments deposited for the simulation NW than for YW. Downstream this constriction and until the height of the side arm Ferraria River (y-coordinate 7182 km) the sedimentation patterns are remarkably different. For the scenario with wind the sediments are distributed

over the cross section more or less uniform with a light concentration at the right bank side of the reservoir. In contrast to this, the simulation wihtout wind shows a clear deposition region: the left bank side. At the Ferraria River side arm the erosive behaviour is similar for both simulations. The deposited sediment layer is thicker for the scenario NW and is concentraed towards the middle of the side arm, meanwhile for the scenario YW the sedimentation is higher at the left side bank of that arm.
Figure 5.8 depicts the differences between the erosion/deposition of both simulations. The differences were built substracting the results of the simulation NW from the simulation YW (i.e., YW-NW).

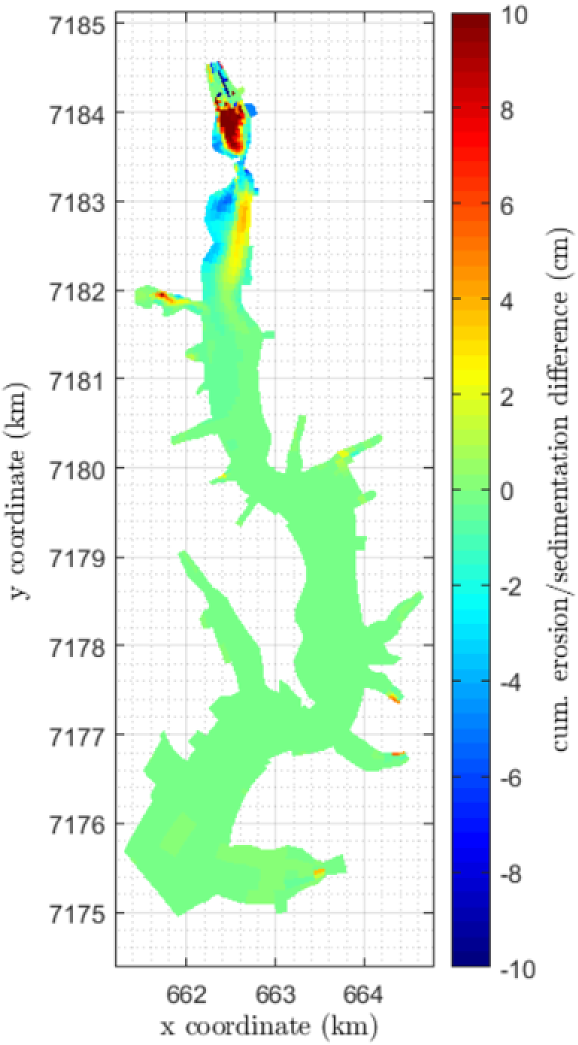

Figure 5.8.: Difference in the sedimentation patterns for the simulations with (YW) and without wind (NW). Legend: NW-YW.

At the Buffer inflow, it can be observed how the two simulations delivered similar results. The difference diagram correspondly depicts values near zero in this region. This can be explained as the velocities and hence transport capacity of the stream is governed by the momentum introduced by the Passaúna River's discharge (i.e. riverine region). Downstream of this area the differences in the sedimentation patterns are notorious. For the simulation with wind inclusion, the deposited layer is smaller than the layer for the case with no wind. This means that the flow in the former was able to keep transporting the sediment downstream. Downstream the Ferraria Bridge the sediments deposited mainly on the left side of the reservoir (looking in direction to the dam) for the simulation NW which is refelected in the positive values for that area. On the other hand, for the simulation YW the sediments deposited more uniformely over the cross-section. Figure 5.9 shows the deposition downstream of the Buffer for both simulations with a different scale, which allows to identify layers of sediments thinner than 3 cm. The differences downstream the Ferraria River become negative, which means that the deposition for the simulation YW was higher than for the simulation NW: sediments are trasnported further downstream in the reservoir when wind is considered as a forcing. Notice, tha the differences are in milimeter range (under 1 cm) for the area below the Ferraria River side arm. For both simulations the desposition prevailed over erosion. The deposited sediment volume for the simulation NW was 4.6 % higher than for the case YW, meanwhile the eroded volume was 2.3 % higher for the case with no wind. In total the resulting cummulative deposition (deposited volumen-eroded volume) when including wind was 8.3% lower than when this factor was omitted.

As already mentioned the total deposition was higher for the simulation without wind and it was concentrated specifically in the region upstream of the side arm of the Ferrarria River. In fact, the time averaged SSCs at the point Park (see Figure 5.2), located downstream of the side arm of the Ferraria River, were below 0.02 mg/l along the whole water column. For the scenario with wind, sediments also deposited all the way downstream of the mentioned side arm. The presence of sediments in the water column is reflected in the time averaged SSCs profiles along the depth for the positions Park, Center and Intake showed in Figure 5.10. Even at the Intake the SSCs are considerably over the magnitude of 0.02 mg/l available at Park in the scenario without wind.

At this point, it is evident that the inclusion of wind in the numerical modelling of the suspended sediments had an influence on the resulting deposited volume, the sedimentation patterns and the suspended sediment concentration profiles. A further study found similar results for the largest freshwater lake in China: the Poyang Lake. Wang et al. (2020a) identified than under weak currents the wind impact will be more notorious than for strong currents. A similar comparison would be the influence of the wind on the sediment transport in rivers and reservoirs, for the former this is not significant. Nevertheless, this study focused on the SSCs profiles and not the deposition amounts and patterns. Wang et al. (2020a) identified the influence of wind on both the vertical and horizontal dynamics of suspended solids and concluded that wind is determinant for lake's morphology.

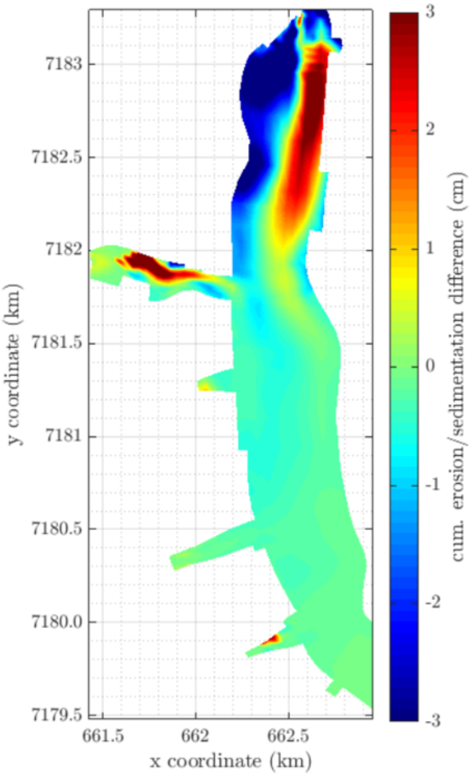

Figure 5.9.: Deposition difference downstream the Ferraria Bridge. Legend: NW-YW.

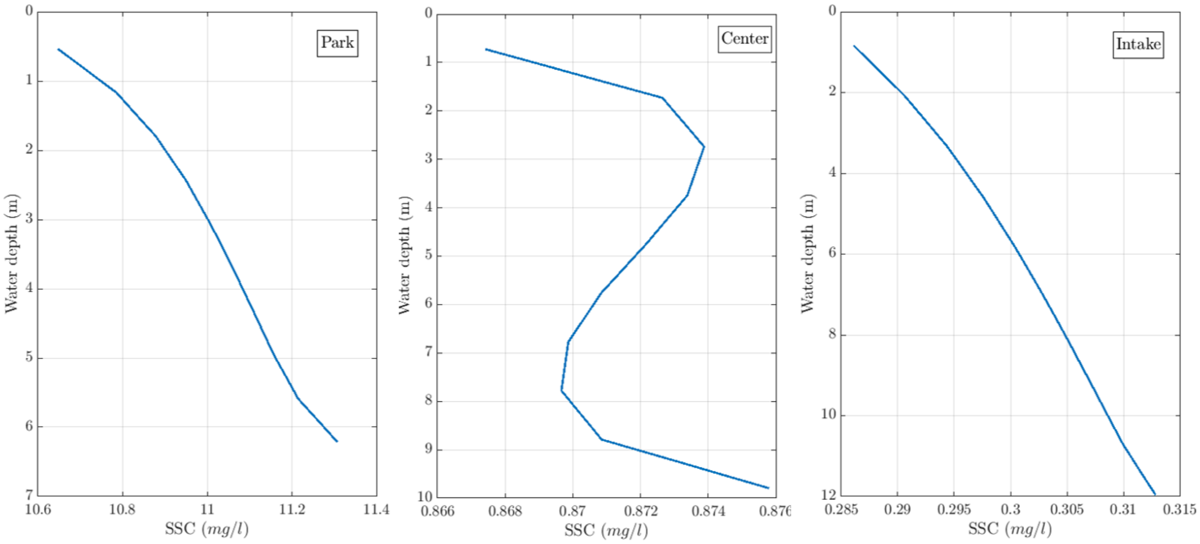

Figure 5.10.: Time averaged SSC for the simulation with wind.

Figure 5.11 compares the bed shear stresses over time for both scenarios. At the Buffer, it is observed that the inclusion of wind induced higher bed shear magnitudes than when omiting this forcing factor. Many peaks in this parameter for the simulation YW coincide with peaks in the simulation NW, if not in the magnitude they coincide in the moment they occur. Those peaks are probably due to increases in the discharge at the main inflow. The variations in the magnitude of this parameter or oscilations are higher in the scenario with wind. At the same time, the magnitude of it is more often over the threshold for deposition than in the case with wind. This explains the lower sedimentation in the Buffer area for the latter scenario. A similar scenario is to be observed for the position PPA downstream of the Ferraia Bridge. Figure 5.12 illustrates the bed shear stresses at the Intake for the simulations NW and YW. Even at this location where the water depths amounts to 12 m, the wind is able to induce oscilations in this parameter and the resulting bed shear stresses are two orders of magnitude higher for the simulation with wind ($10^{-5} vs. 10^{-3} N/m^2$).

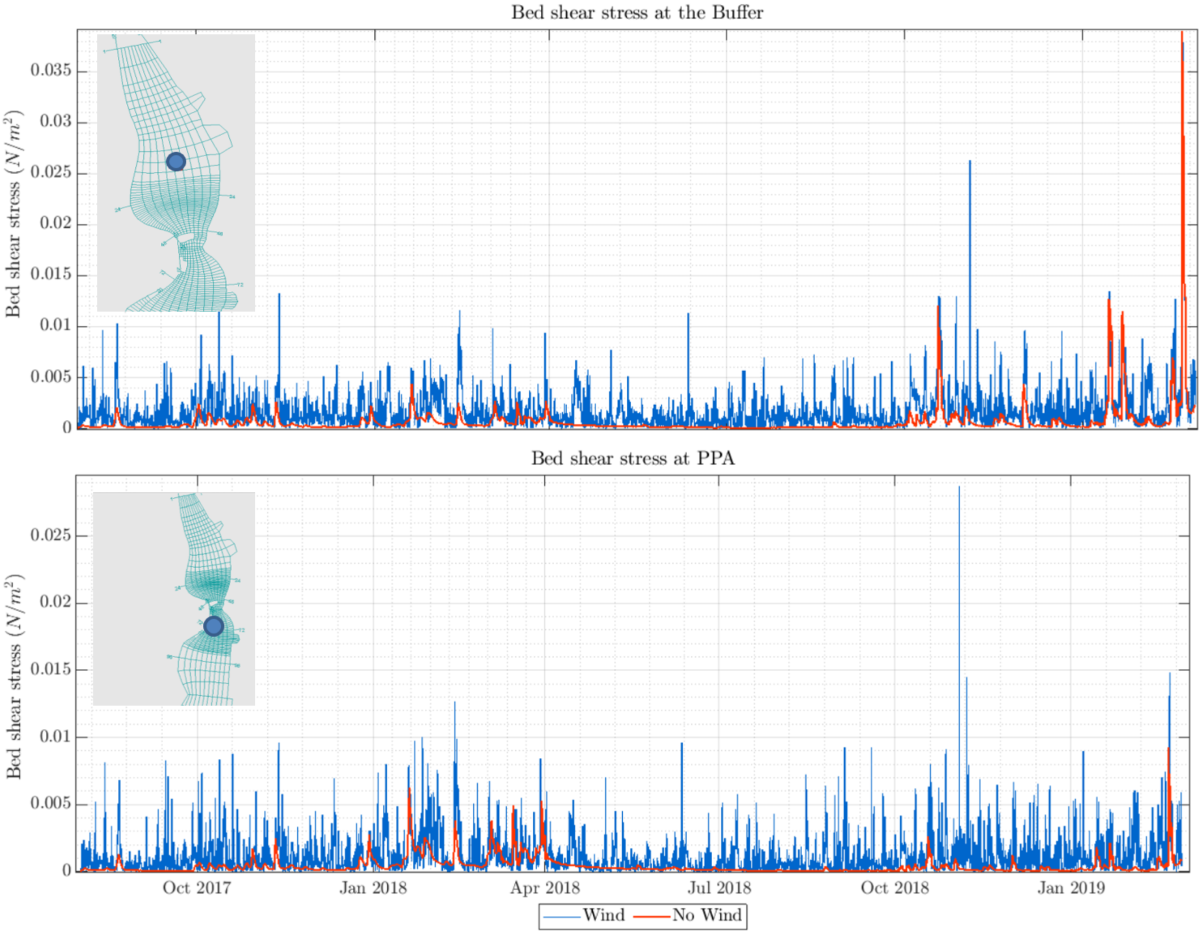

Figure 5.11.: Bed shear stresses at the Buffer and at PPA for the simulations with wind and wind exclusion.

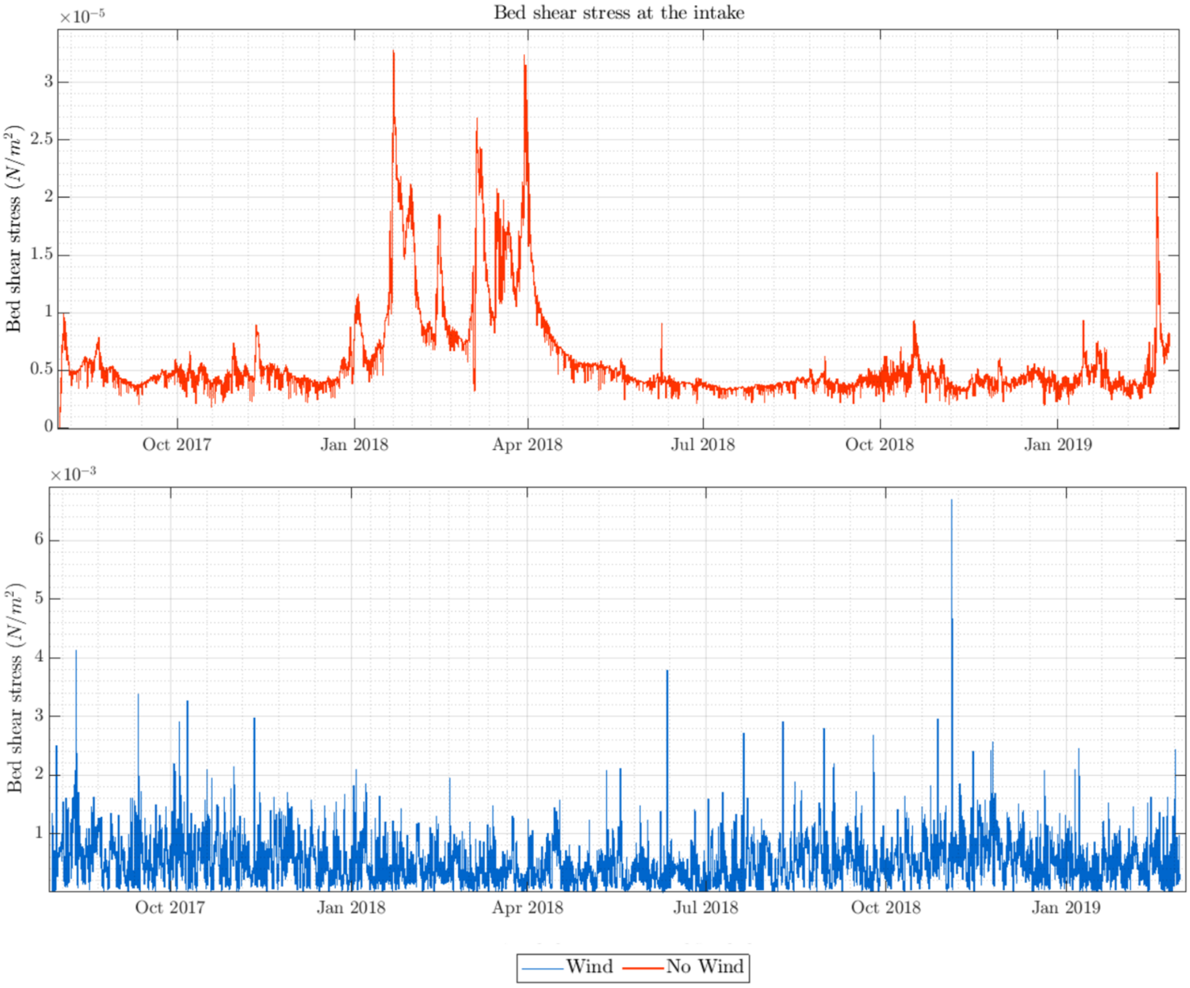

Figure 5.12.: Bed shear stresses at the Intake for the simulations with wind and wind exclusion.

Table 5.3 shows the time averaged bed shear stresses for different locations in the model area. It can be observed that on average the bed shear stresses were one to two orders of magnitude higher for the case with wind for all the positions. With the differences betwen both simulations being more accentuated the more downstream the studied location is.

Table 5.3.: Time averaged bed shear stresses and standard deviations (SD) at three positions in the model area with wind (YW) and without it (NW)

Position	NW		YW	
	Mean (N/m^2)	SD $(N/m2)$	Mean (N/m^2)	SD (N/m^2)
Buffer	$6.8 \cdot 10^{-4}$	$1.8 \cdot 10^{-3}$	$1.7 \cdot 10^{-3}$	$2.3 \cdot 10^{-3}$
PPA	$4.3 \cdot 10^{-4}$	$6.5 \cdot 10^{-4}$	$1.18 \cdot 10^{-3}$	$1.6 \cdot 10^{-3}$
Intake	$5.9 \cdot 10^{-6}$	$4.1 \cdot 10^{-6}$	$5.1 \cdot 10^{-4}$	$4.4 \cdot 10^{-4}$

The temporal oscilations of the bed shear stress represented by the SD are also more noteworthy for the simulation with wind. The difference between the SDs of the bed shear stress for the simulation NW and YW in percentage are more pronounced the father away a position is from the main inflow.

Figure 5.13 depicts the depth averaged velocities at the positios Buffer and Intake for both simulation YW and NW. At the Buffer the highest peaks in the depth averaged velocities coincide for both scenarios and the depth averaged quantities are in the same order of magnitude. Similar to the bed shear stresses, constant oscillations in the depth averaged velocity are introduced through the wind forcing. Further downstream at the water withdrawal, the behaviour of the oscillations is the same, nevertheless the magnitude of the depth averaged velocity is with a few exceptions, constantly higher for the simulation with wind inclusion. At the water surface, the horizontal flow velocities (see Figure A.12 in the Appendix sectioon) for the scenario with wind are observed to be higher than for the case excluding the effect of wind for both positions Buffer and Intake.

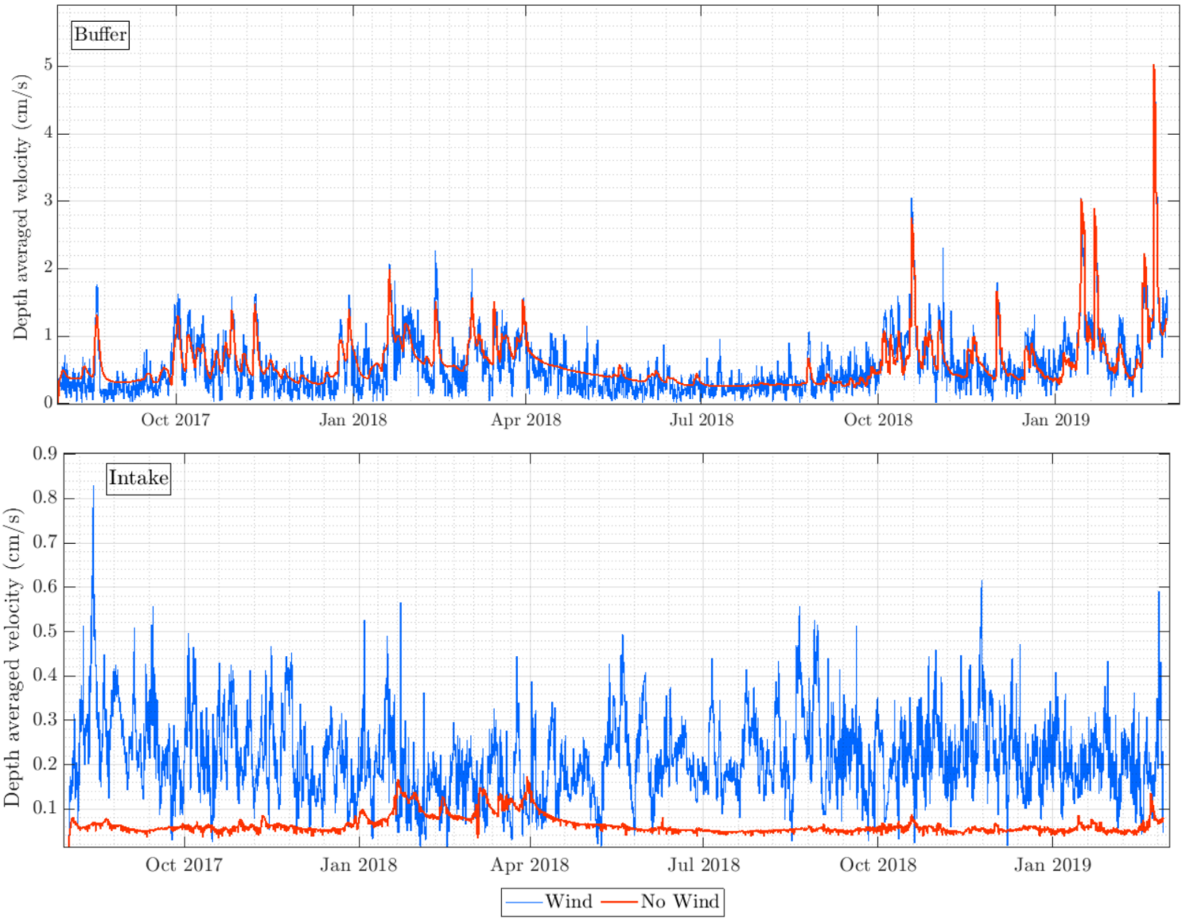

Figure 5.13.: Depth averaged velocities at the Buffer and Intake for the simulations with wind and wind exclusion.

Table 5.5 summarizes the time averaged horizontal flow velocities at the surface, at the

bottom and the depth averaged velocities for the positions Buffer, PPA, Center and Intake. All velocities in both scenarios exhibit a decreasing trend towards the downstream direction of the reservoir. For the case of the depth averaged velocities at the shallower positions Buffer and PPA are in the same order of manginutde for both simulations, with the simulation NW presenting even higher time averaged quantities for the Buffer than the simulation YW. For the further positions with higher water depths showed higher depth averaged velocities for the simulation with wind inclusion. The highest standard variation with respect to the mean was presented for the simulation YW at the position Buffer.
At the surface the mean of the horizontal velocities for the simulation with wind was one order of magnitude higher than the simulation with out wind. At the Bottom the inclusion of wind produced higher horizontal flow velocities at all positions, even for deep points like the Center and the Intake, the difference between both simulations was of one order of magnitude. The oscilations in the time averaged horizontal velocity at the surface and at the bottom were the highest with respect to the mean at the Buffer and Center both for the simulation without wind.

Table 5.4.: Time averaged velocities at four positions in the model area with wind (YW) and without it (NW)

Position	Depth averaged velocity (cm/s, $\cdot 10^{-1}$)				Horizontal velocity surface (cm/s, $\cdot 10^{-1}$)				Horizontal velocity bottom (cm/s, $\cdot 10^{-1}$)			
	NW		YW		NW		YW		NW		YW	
Position	Mean	SD	Mean	SD	Mean	SD	Mean	SD	Mean	SD	Mean	SD
Buffer	6	4.0	5.6	4.6	7.4	5.0	13	6.3	3.3	2.1	5.8	3.2
PPA	6.3	3.9	6.5	4.4	8.0	4.9	14	6.1	3.7	2.3	5.9	3.9
Center	0.14	0.13	4.0	2.3	10	5.1	10	5.1	0.14	0.13	6.8	3.9
Intake	0.64	0.21	2.1	0.94	0.64	0.22	10	5.4	0.63	0.20	5.8	2.7

For both simulations a conservative tracer was introduced with constant concentration through the main inflow at the Passaúna River. The tracer follows the fluid particles and offers an overview of the main transport paths for each scenario. Figure 5.14 presents the normalized tracer concentration for the simulations YW and NW for three different time steps. For the simulation without wind, it can be observed that the tracer is transported through an specific pathway on the left bank of the reservoir. For the scenario without wind at the 18th September, 2017 the highest concentrations are found at just one side of the reservoir between the Ferraria Bridge and the side arm of the Ferraria River. For this same reach at the end of the simulation, the tracer concentrations became more uniform over the cross section. Thus, among the three time instants the slower but present dispersion of the tracer can be observed. For the scenario with wind the concentrations are from the beginning more uniformly distributed. Nevertheless, a main transport path is recognisable during the first and second time steps presented, namely on the right bank. On the third time step slightly higher tracer concentrations are observable on the left bank of the reservoir at the height of the Ferraria River (y-coordinate 7182 km). Also interesting to notice is that for the second presented time instant, the tracer in the simulation with wind was able to reach several side arms (e.g. Ferraria River), meanwhile for the simulation without wind this was not possible, not even at the last time step presented.

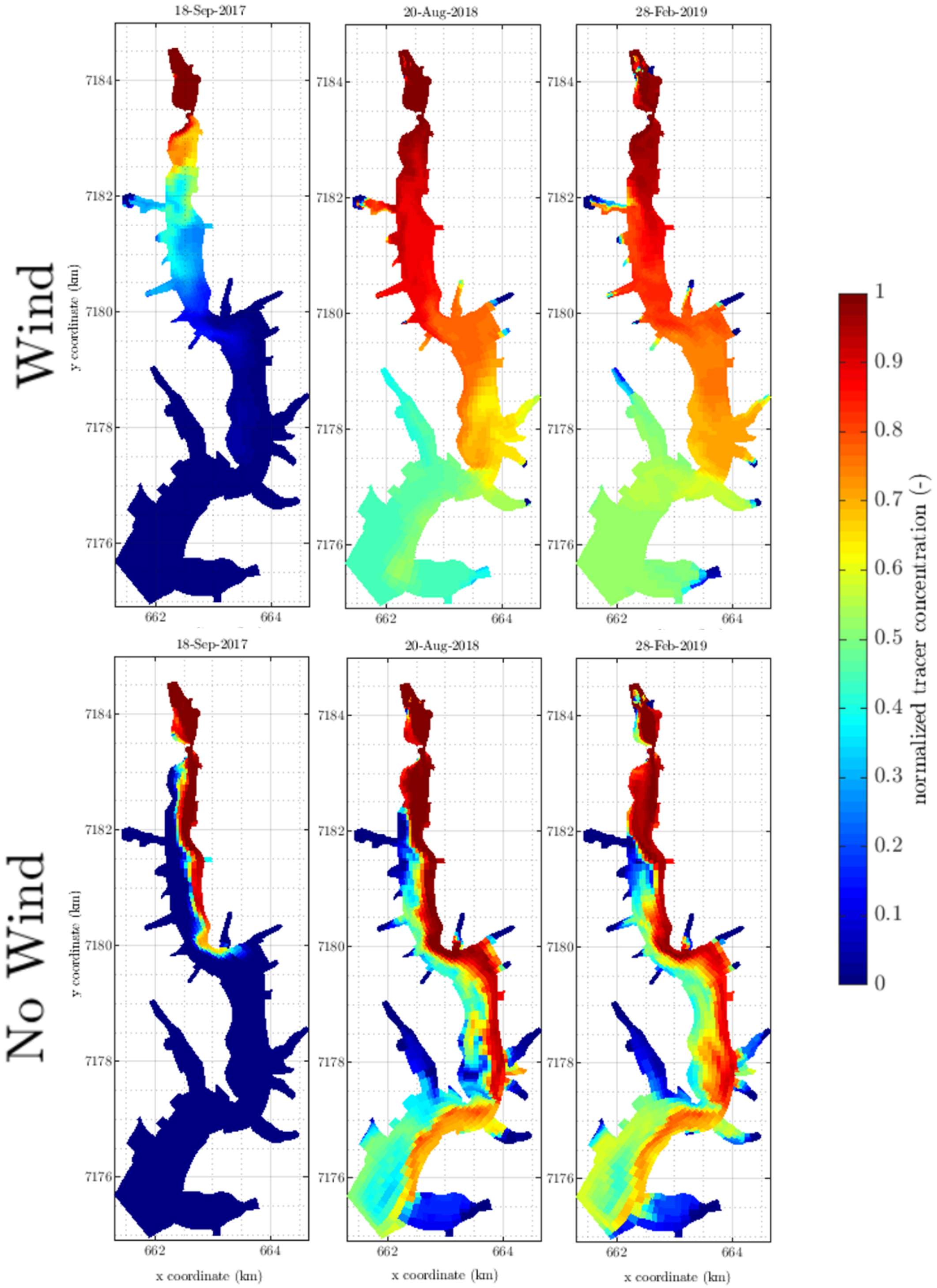

Figure 5.14.: Normalized tracer concentration for the simulations with wind and wind exclusion at layer 5.

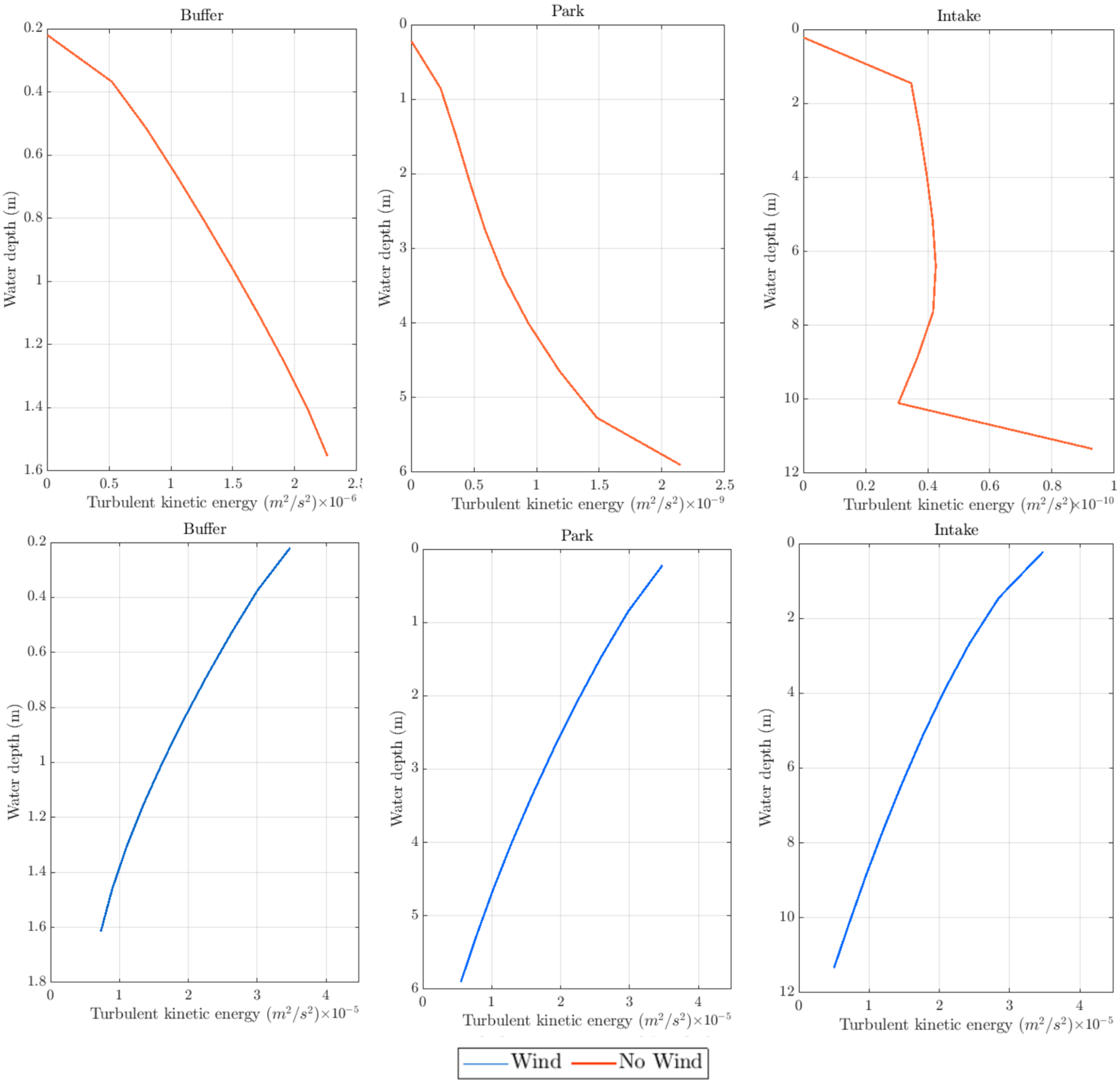

Figure 5.15.: Time averaged turbulent kinetic energy for the simulations with wind and wind exclusion.

The analysis of the turbulent kinetic energy (TKE) offers an overview of the locations where the temporal variations of the velocity are the highest and hence where is more feasible that the fine sediments will be maintained in suspension by the turbulence of the flow. Figure 5.15 shows time averaged turbulent kinetic energy profiles along the depth for three positions namely the Buffer, Park and Intake. The selection of those points should provide an idea about the turbulence at shallow and deep areas. The results for the simulation without wind show a decreasing trend in the TKE towards the downstream direction of the reservoir. The discussed parameter is five order of magnitude higher at the Buffer than at the Intake. For all three profiles the TKE increases towards the bottom of the reservoir and is nearly zero at the surface layer. For the scenario with wind inclusion, the time averaged TKE is of the same order of magnitde for all positions. Contrary to the behaviour in the previously analized scenario, the inclusion of wind produced decreasing profiles of TKE towards the bottom with a maximum at the surface layer. In general the energy was one to six order of magnitude higher for the scenario with wind inclusion than for the scenario without wind.

5.3.4. Effect of Water Temperature on the Suspended Sediment Transport

Today's practice in the field of morphological numerical modelling is to set up models for the simulation of suspended sediment transport without considering thermal stratification in the water body. As already mentioned, high computational costs and lack of data could be some reasons to it.

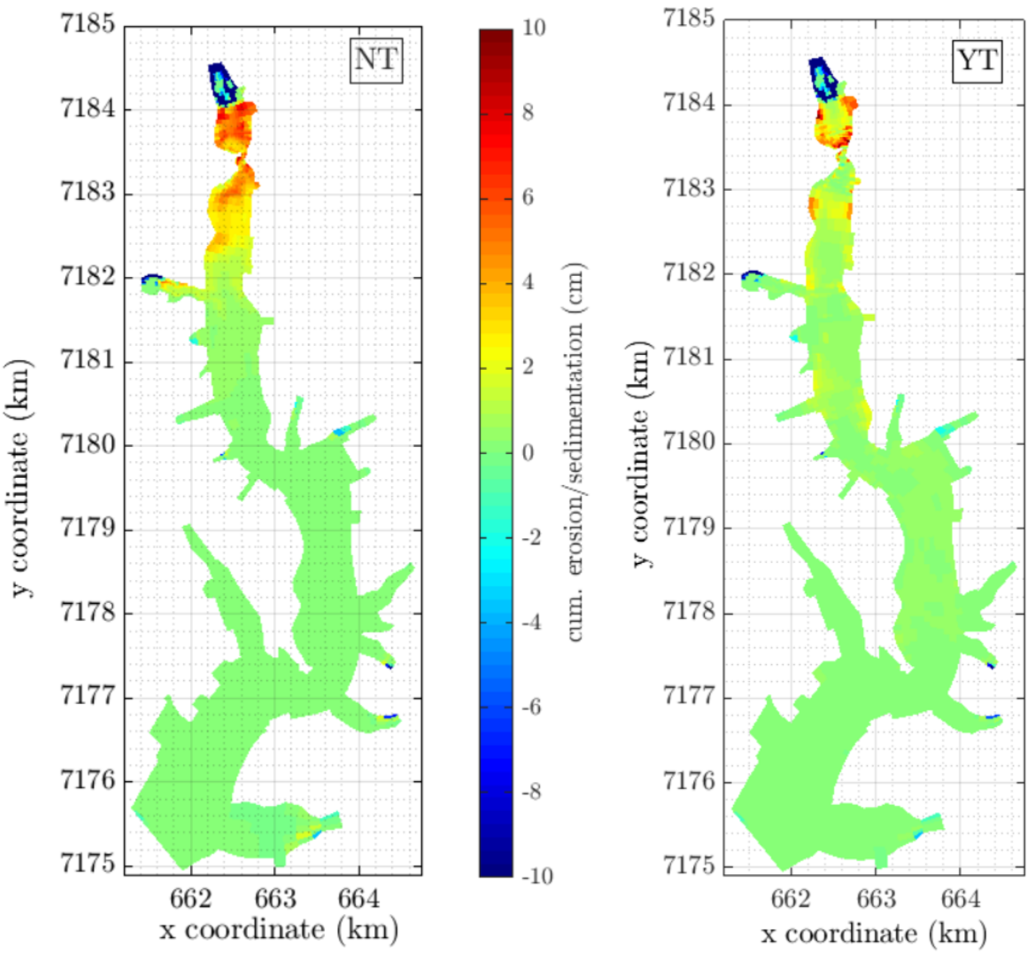

Figure 5.16.: Sedimentation patterns for the simulation without temperature (left) and with temperature (right).

To study the temperature effects on the sediment deposition and SSCs profiles a simulation practically identical to the simulation with wind in the previous section was set up. The only difference was the inclusion of the temperature of the inflows and a heat flux model for the heat exchange at the water-air interface. All the variables used in the heat flux model parametrization were the same as for the calibrated hydrodynamical model in chapter 4. The simulation with the inclusion of temperature will be denominated **YT** and the simulation without temperature **NT**, the latter is of course identical with the simulation YW from the previous section. After the simulated period of 19 months, the clearly different sedimentation patterns illustrated in Figure 5.16 were obtained. The sedimentation in the simulation without temperature is more equally distributed across the cross section than for the case with temperature. For the latter the depositional areas are more local like at the Buffer where the higher depositions took place at the bank. Downstream the Ferraria Bridge, the sedimentation patterns maintain their discrepances. This is also the case for the region of the Ferraria River's side arm where the deposition is lower for the scenario including temperature.

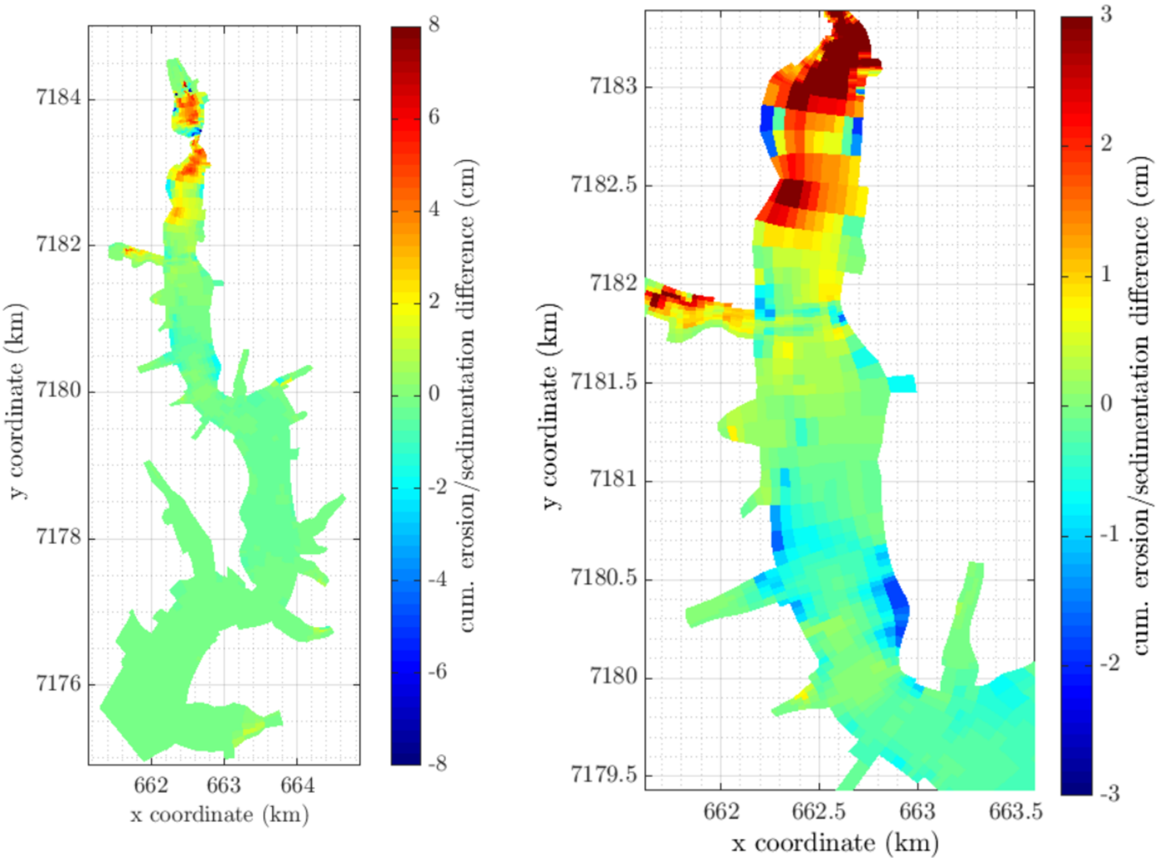

Figure 5.17.: Difference in the sedimentation patterns for the simulations without (NT) and with temperature (YT). Legend: NT-YT.

Figure 5.17 shows the difference between the two scenarios. The differences were built substracting the cummulative erosion/sedimentation of the scenario without temperature (NT) from the same quantity for the scenario with temperature inclusion (YT). On the left side of the mentioned figure, an overview of the whole reservoir is given and on the right side a zoom view to the region downstream the Ferraria Bridge is made with an appropiate selection of the shown limits in the color scale. Noteworthy, is the similarity between the two erosion areas at the upper half of the Buffer and at the entrance of the Ferraria River. In this region the differences are nearly zero. From the y-coordinate 7181.5 and downstream the differences are negative. This means that the deposition for the simulation with temperature were higher than for the simulation without it. In general the erosion was just 0.7% higher in the simulation with temperature inclusion. With regard to the deposition, this was 3.6 % higher for the simulation NT than for YT. For both simulations the deposition prevailed over the erosion. The difference between deposited and eroded sediment volume was 11% higher for the simulation with no temperature.

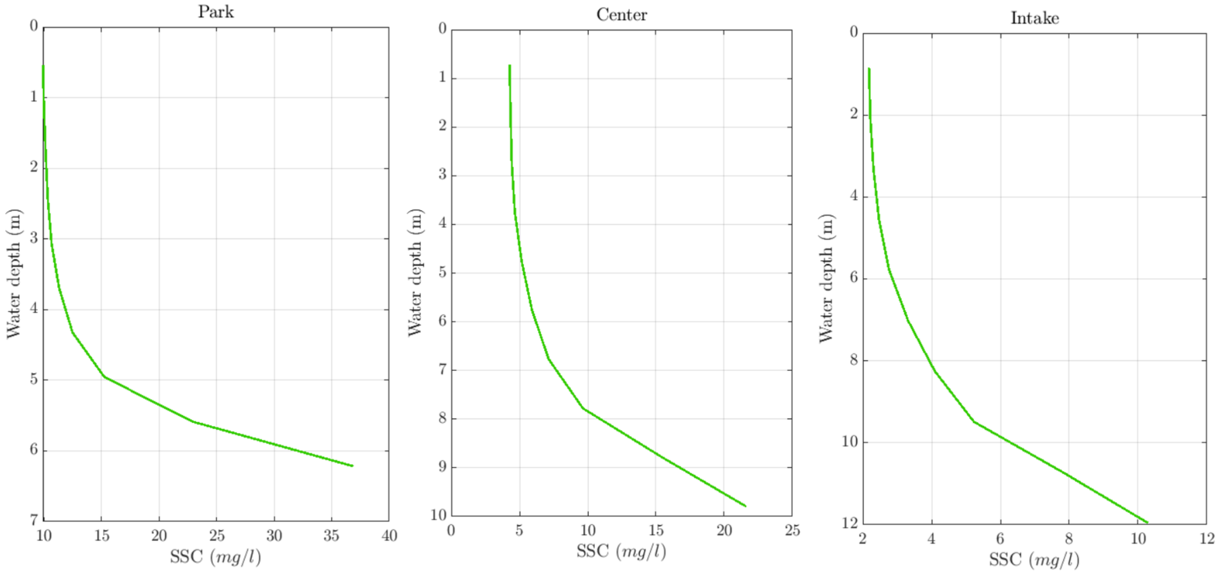

Figure 5.18.: Time averaged SSCs for the simulation with temperature.

Figure 5.18 depicts the time averaged SSCs profiles along the depth for the positions Park, Center and Intake for the scenario with temperature inclusion. Those can be compared to the profiles of the same type for the scenario without temperature in Figure 5.10. The profiles for both scenarios differ in their course and magnitude. For all three positions the time averaged SSCs are higher for the case with temperature than without its inclusion. Within the scenario with temperature, the flow was able to transport suspended sediments until the Intake in time averaged SSCs higher than 2 mg/l in comparison to the scenario with just ind inclusion, for which the SSCs were approximately ten times lower. The same is valid for the position Center. For the location Park the time averaged SSCs were similar at the water surface, nevertheless for the bottom layer this quantity was four times larger for the simulation with temperature. The gradients SSC_{Grad} between the highest SSC_{max} and lowest concentration SSC_{min} at each profile are calculated according to equation 5.1. This parameter is a measure of the uniformity of the SSCs profiles along the depht, the higher the value of it, the lower the uniformity of the profile.

$$SSC_{Grad} = \frac{(SSC_{max} - SSC_{min})}{SSC_{max}} * 100[\%] \tag{5.1}$$

The resulting gradients were always higher for the simulation with temperature inclusion in comparison to the case excluding this factor. For the positions Park, Center and Intake the gradients were of 73, 79.5 and 80% for the simulation YT and 6.2, 1, and 9.5% for the simulation NT.

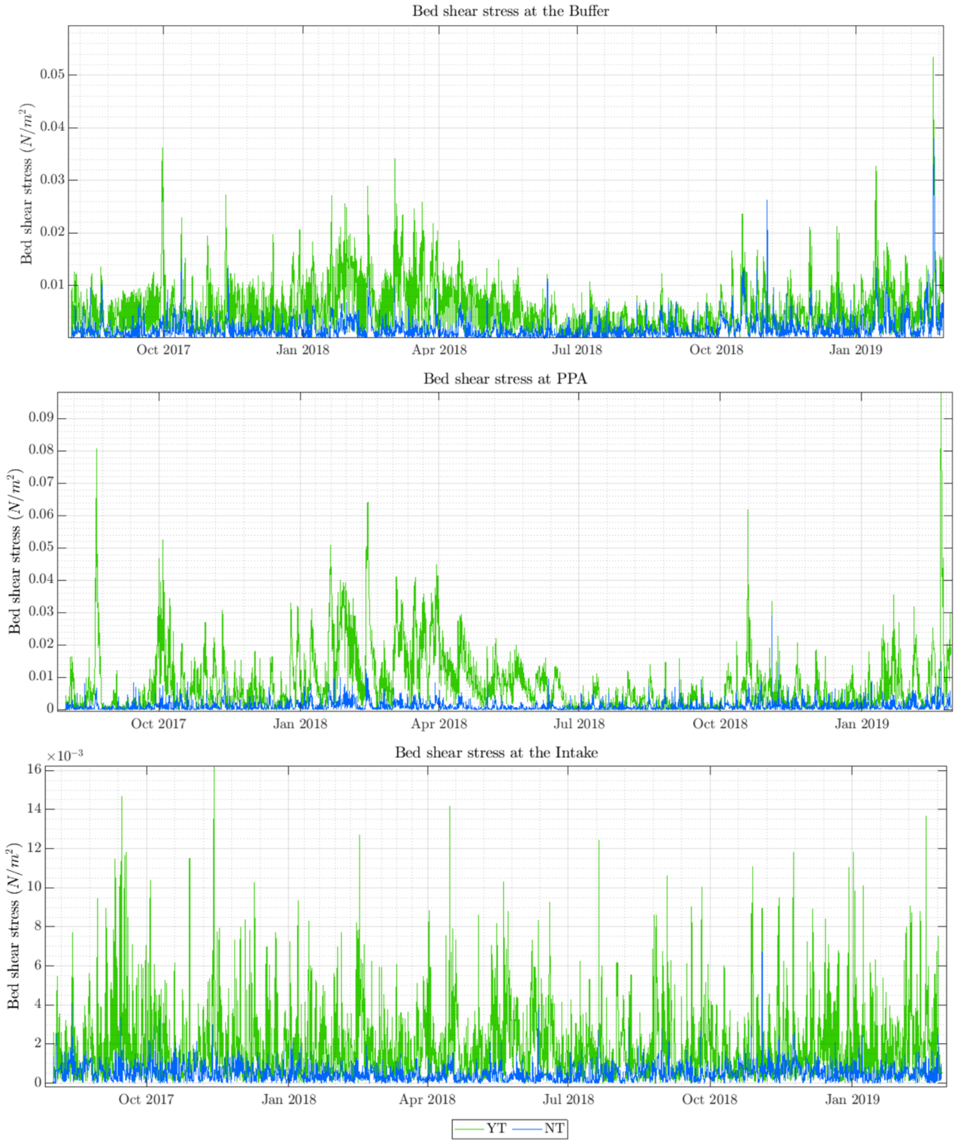

Figure 5.19.: Bed shear stresses at the Buffer, PPA and Intake for the simulations with temperature and temperature exclusion.

Figure 5.19 presents the bed shear stresses at the Buffer, PPA and at the Intake for the two studied cases. In general the inclusion of temperature resulted in higher magnitudes for this variable than when just wind was considered. It calls the attention that in spite of the differences between the bed shear stresses they have a similar order of magnitude for the same position. This was not the case for the comparison of the simulations with and without wind (see Figure 5.12). Table 5.5 presents the time averaged bed shear stresses for the simulations NT and YT. The time averaged quantities further show higher bed shear stresses for the scenario with temperature consideration. For both scenarios the lowest magnitudes of this parameter are reached at the Intake. The highest variations of the bed shear stress with respect to the mean value (i.e. $SD/Mean \cdot 100$) are present at the Buffer in the simulation NT.

A comparison between the depth averaged velocities for the positions Buffer and Intake is presented in Figure 5.20. For the Buffer, these quantities are in a similar range with slightly higher depth averaged velocities for the scenario with temperature inclusion. Regarding the Intake, the difference between both time series is more evident than at the previously mentioned shallower location. Again, the simulation with temperature produced the highest depth averaged velocities. For both scenarios, the highest magnitude of this parameter are reached at the position PPA and the lowest at the Intake. The highest variations with respect to the mean are found in the position Buffer for the simulation NT.

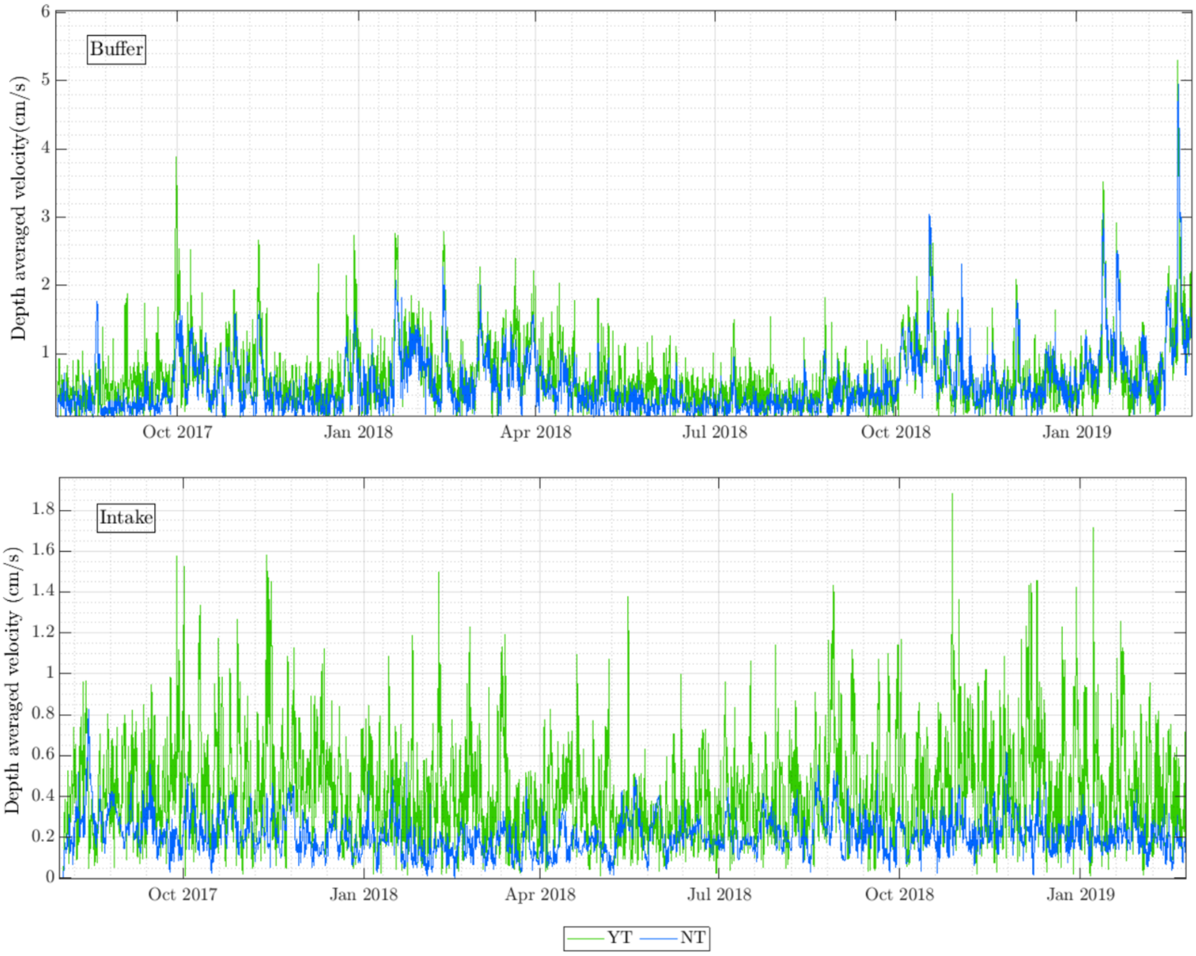

Figure 5.20.: Depth averaged velocities at the Buffer and Intake for the simulations with temperature and temperature exclusion.

Table 5.5.: Time averaged bed shear stresses and depth averaged velocities with temperature (YT) and without (NT).

Position	Bed shear stress (N/m^2, $\cdot 10^{-3}$)				Depth averaged velocity (cm/s, $\cdot 10^{-1}$)			
	YT		NT		YT		NT	
	Mean	SD	Mean	SD	Mean	SD	Mean	SD
Buffer	5.7	4.8	1.7	2.3	6.8	5.0	5.6	4.6
PPA	8.0	9.7	1.2	1.6	10	6.8	6.5	4.4
Intake	1.9	1.9	0.51	0.44	4.3	3.5	2.1	0.94

Not to forget, is that the amount of sediment suspended in the water column may also affect the amount of radiation entering to deepers layers into the water column, scattering the sun light and avoiding the rise in the water temperature (Schiebe et al., 1975). It would mean than presence of suspended sediment would also affect the thermal structure of the water. Regarding the TKE for the scenario with temperature inclusion, the time averaged quantities were in the same order of magnitud than the profiles for the simulation with just wind (see 5.15). The profiles along the depth are presented in the Figure A.14 in the Appendix section.

A further process which can not be simulated with the implementation of a model with just wind but not temperature are the gravity flows induced by temperature gradients i.e. underflow, interflow and overflow. In chapter 4 it was shown that the numerical model was able to simulate those different flow paths. In the following the influence of those density currents on the SSC-profiles is studied. Similar to the simulation with just wind inclusion, a conservative tracer was added to the main Inflow of the reservoir for the morphological simulation with temperature inclusion. The path of the tracer along the longitudinal axis of the reservoir should offer and idea about the main flow path of the fluid parcels. Figure 5.21 shows the longitudinal section of the reservoir for January 25, 2018. The figure shows the normalized tracer concentrations for the scenarios without (top) and with (bottom) temperature consideration. As can be appreciated the distribution of the tracer along the vertical dimension is uniform for the case with just wind, as it was expected. For the bottom diagram, the flow path is clearly concentrated at the bottom of the reservoir, indicating the presence of an underflow.

The SSCs profiles along the depth for the same date at four positions along the longitudinal axis are presented in Figure 5.22. The top row presents the results for the simulation NT and the bottom row for the simulation YT. For both scenarios the SSCs decrease along the longitudinal axis in direction to the dam. At the positions PPA and Park, the time averaged concentrations are found in approximately the same order of magnitude for both cases. What the positions Center and Intake concerns, the concentrations are two order of magnitude higher for the simulation with temperature inclusion. The calculation of the SSC_{Grad} using equation 5.1 allows to appreciate the stronger gradients for the simulation with temperature consideration and the pronounced non-uniformity of those SSCs along the depth. The gradients are presented in Figure 5.22 for each profile. The most pronounced non-uniformity is found at the Intake with a SSC_{Grad} of 93%. In general, for the simulation with temperature, it can be noticed how the sediments are mainly transported at the deeper layers which coincides with the main transport path depicted by the conservative tracer. Correspondly, the sediments are more uniformly distributed in the simulation without temperature inclusion as already hinted by the tracer. Since the sediments, in opposite to the tracer, have the action of the settling velocity affecting them, the SSCs profiles are not expected to be completely uniform like for the case of the conservative constituent.

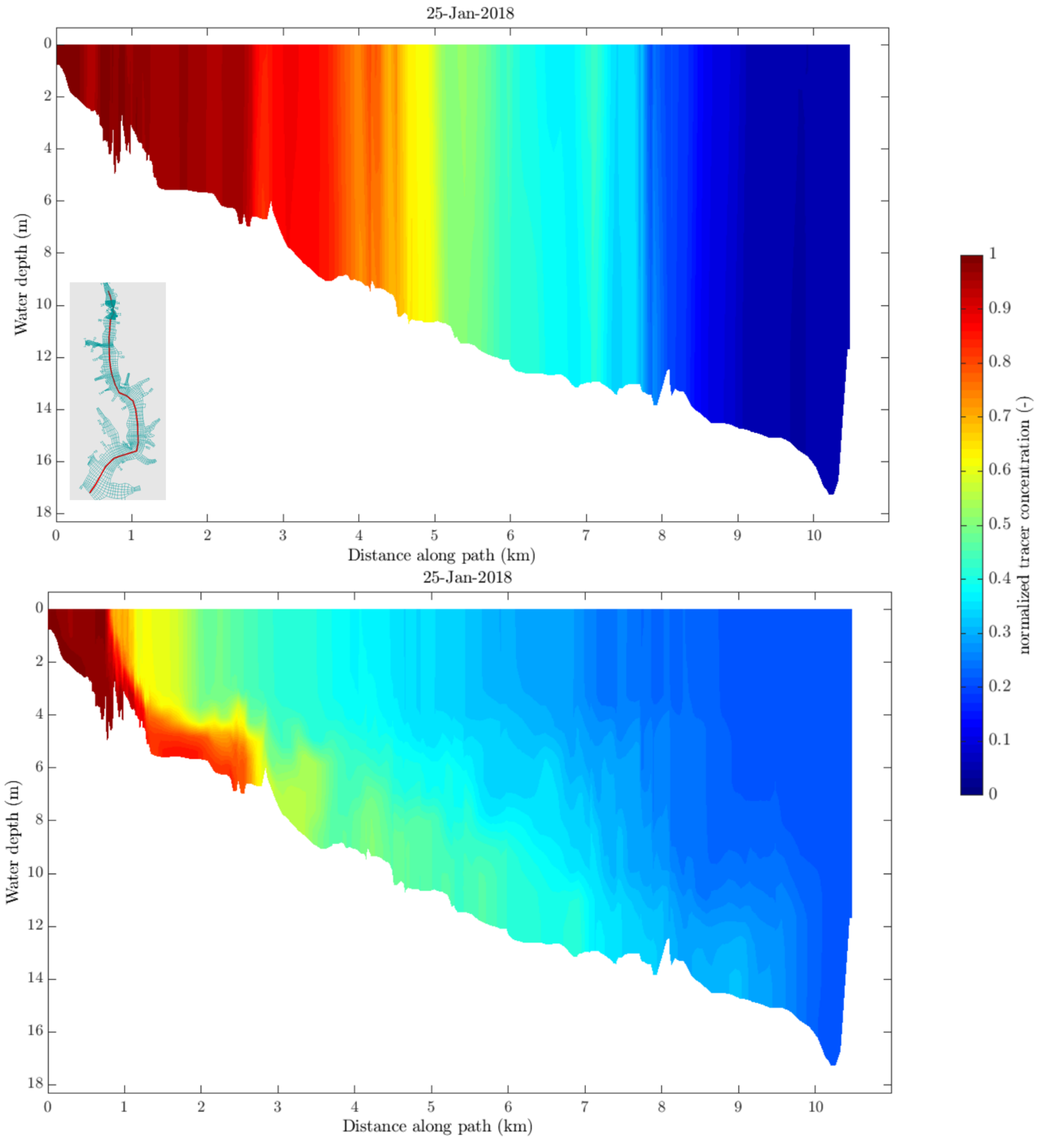

Figure 5.21.: Normalized tracer concentration along the longitudinal profile for the simulations with (bottom) and without temperature (top) for January 25, 2018.

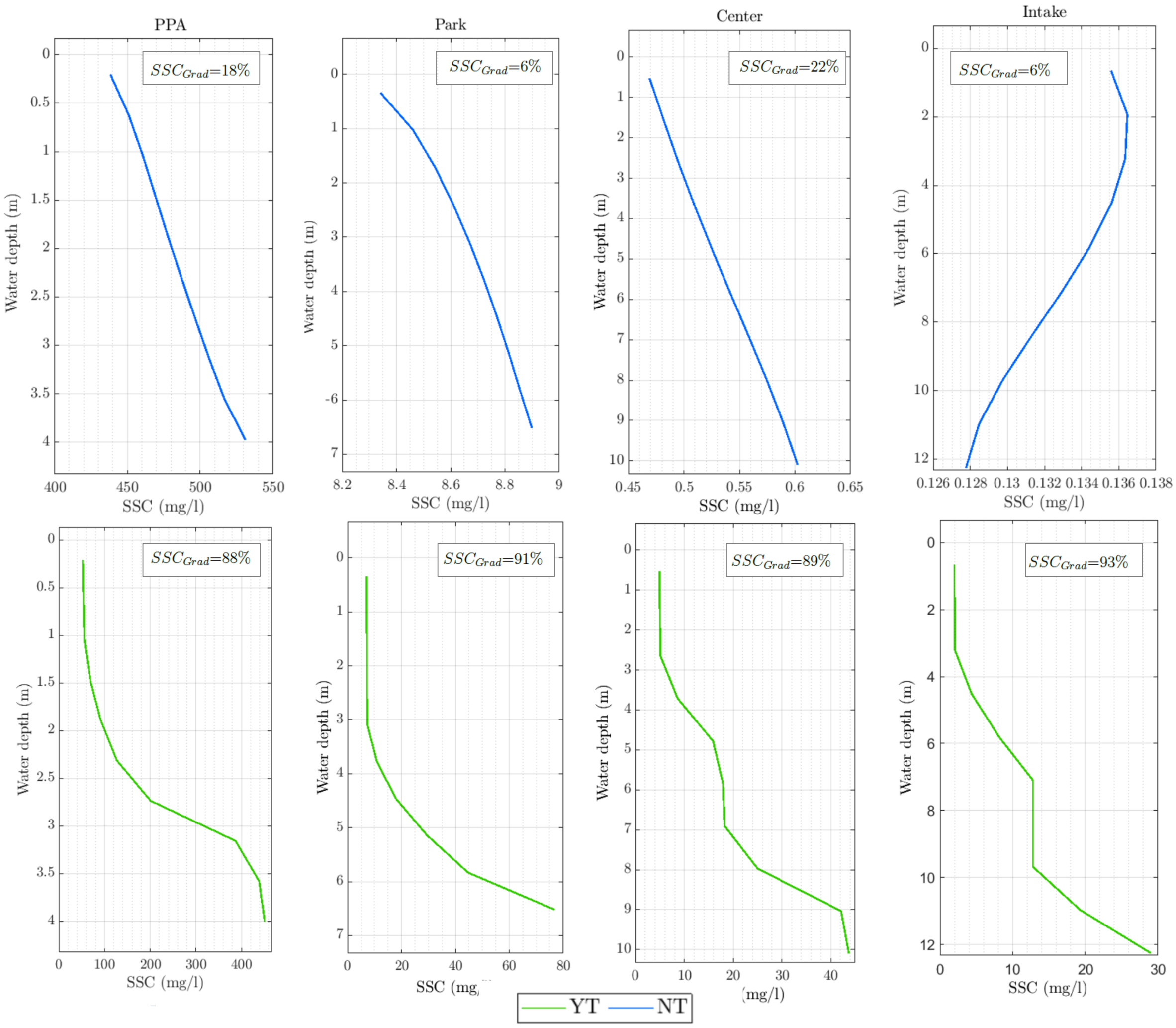

Figure 5.22.: SSCs at four stations along the longitudinal axis of the reservoir for the simulations with (bottom) and without temperature (top) for January 25, 2018.

Figure 5.23 presents the normalized tracer concentrations for a further date: December 12, 2018. The longitudinal profile shown is the same as for Figure 5.21. Again the concentratiosn of tracer are uniformly distributed along the depth for the scenario without temperature. As for the simulation with temperature effects, the main transport path can be located at the more superficial layers. The flow path can be identified as an overflow.
SSCs profiles along the depth for the above mentioned date are depicted in Figure 5.24. The SSCs for the positions PPA, Park and Center are in the same order of magnitude for the scenarios with and without temperature consideration. At the position Intake, the concentrations for the case with temperature are one order of magnitude higher than for the other considered situation. The difference between the highest and the lowest concentration along the depth for each profile is again reflected in the SSC_{Grad}. Which are higher for the simulation with temperature inclusion in comparison with the further case. It has to be considered, that the higest and lowest SSCs in a profile are not necessarily found at the bottom and the top of the water column respectively.

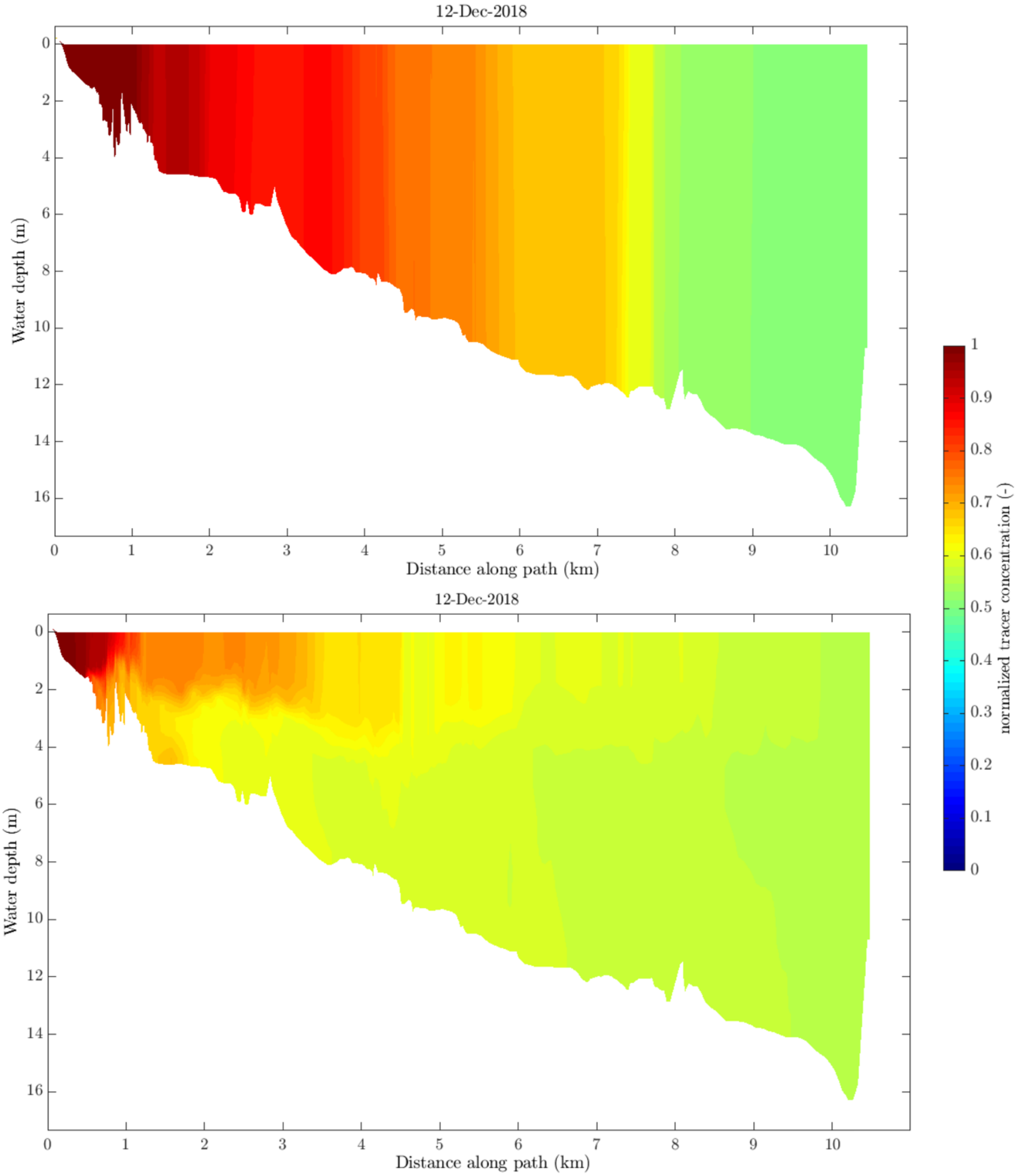

Figure 5.23.: Normalized tracer concentration along the longitudinal profile for the simulations with (bottom) and without temperature (top) for December 12, 2018.

For this date the non-uniformity of the SSCs profiles is increasing downstream for the scenario with temperature effects. A further trend can be identified for the simulation with temperature: at the first station the concentrations at the top of the water column are higher than at the bottom, this behaviour gradually changes until the most downstream profile, where the concentrations at the bottom porcentually much higher than at the top.

The behaviour depicted in the Figures 5.21to 5.24 is found in many dates where flow paths are clearly identified. The two selected dates here are not an exception. A further similar situation for an underflow is presented in Figure A.13 in the Appendix section.

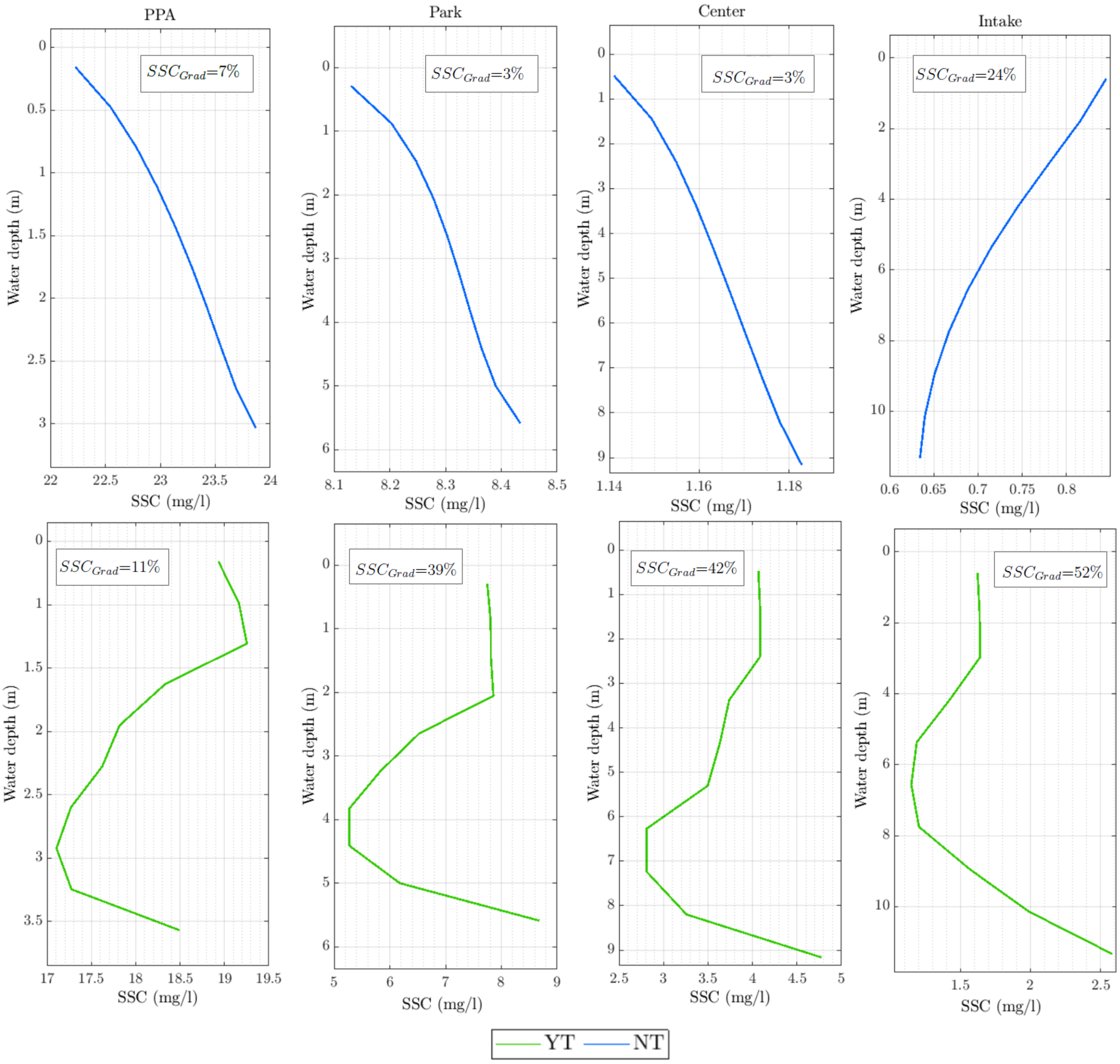

Figure 5.24.: SSCs at four station along the longitudinal axis of the reservoir for the simulations with (bottom) and without temperature (top) for December 12, 2018.

To generalize, Figure 5.25 presents a summary of the cummulative dispersive and advective transport of the suspended sediments. Here the differences in percentage between the simulations with and without temperature are shown for both kinds of transport. If the difference is positive, it means that that kind of transport was higher in the simulation with temperature and if the difference is negative, that kind of transport was higher for the simulation without temperature. The trasnport was accounted at the five cross sections shown in the map of Figure 5.25. Similar evaluations were performed by Polli and Bleninger (2019a) but for the tracer transport. Figure 5.25 shows higher magnitudes of the advective transport for the simulation with temperature for all cross section with exception of the Buffer, where this kind of transport was slightly lower than for the scenario without temperature. The dispersive transport also increased for the simulation with temperature in comparison to the case with just wind for all investigated cross sections with exception of the second cross section, where the transport was slightly higher for the further case.

Differences in the suspended sediment transport due to temperature effects have been already identified through field measurements. Elci (2008) studied the effects of thermal stratification and mixing on the water quality of a te Tahali Reservoir in Turkey including SSCs profiles. It was found that stratification drastically affected the flow velocity profiles and hence the water quality in the reservoir. The turbidity profiles were highly affected as well, with peaks in the SSCs at the thermocline. Akalin (2002) studied the suspended sediment dynamics in the Lower Mississippi River, finding out that changes in the water temperature introduced variations on the velocity profiles and on the vertical distribution of SSCs. To the author's of the present dissertation knowledge, there is no study published, which investigates the influence of thermal stratification on the suspended sediment transport for a study case of an existing water body through a numerical model fed with actual field measurements.

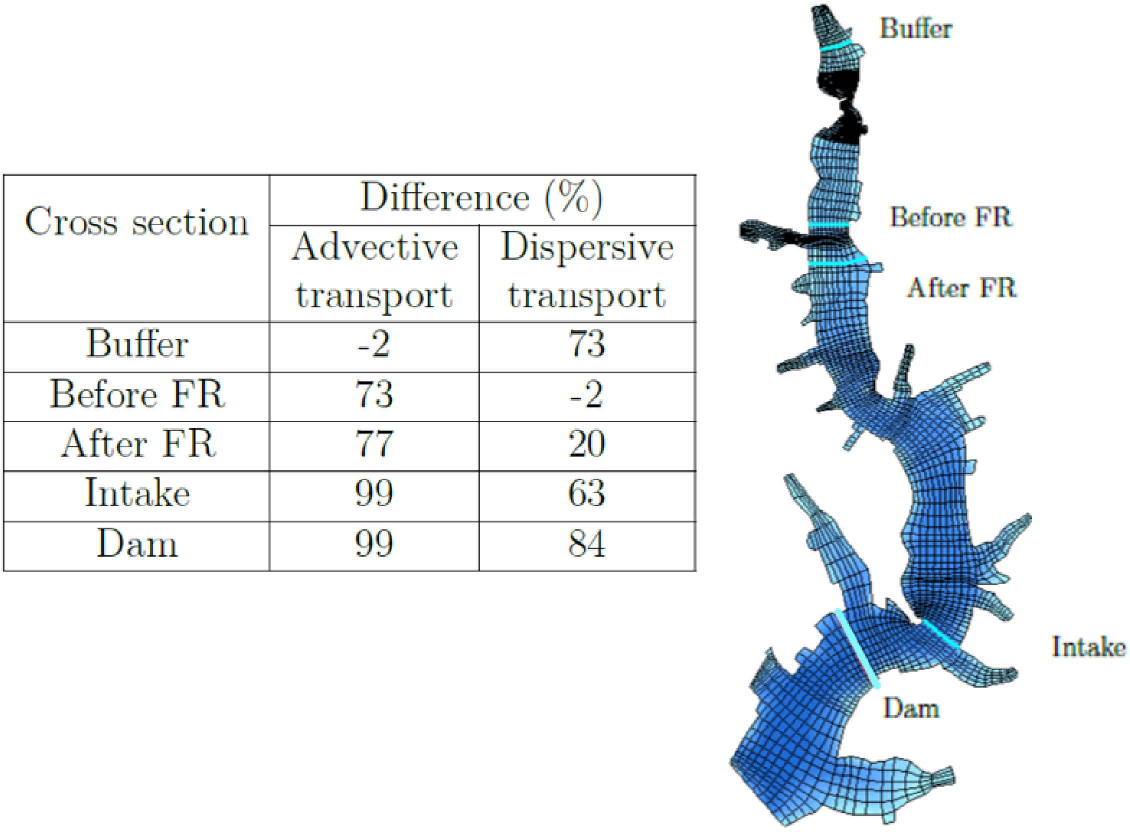

Cross section	Difference (%)	
	Advective transport	Dispersive transport
Buffer	-2	73
Before FR	73	-2
After FR	77	20
Intake	99	63
Dam	99	84

Figure 5.25.: Differences between the cummulative advective and dispersive transport of suspended sediments at the five cross sections shown in the map.

5.3.5. Effect of the Layering System

The selection of a layering system is a common decision to be made by modelers when the simulation of thermal stratification is going to be part of the study. Regarding the vertical structure of the grid two kind of scenarios will be investigated: the repercusion of the Sigma-model and the Z-model on the sdeimentation volume and pattern without the inclusion of temperature in any of the models. Secondly, both models will include temperature and the same kind of results will be evaluated. The aim of the first kind of scenario is to distinguish the impact of the layering system alone. Since, as shown in the previous section, the inclusion of temperature may introduce changes in the transport of suspended sediments. Nevertheless, the selection of a Z-model only makes sense when temperature is included. For a morphological model alone a layering of this kind would not be the traditional selection.

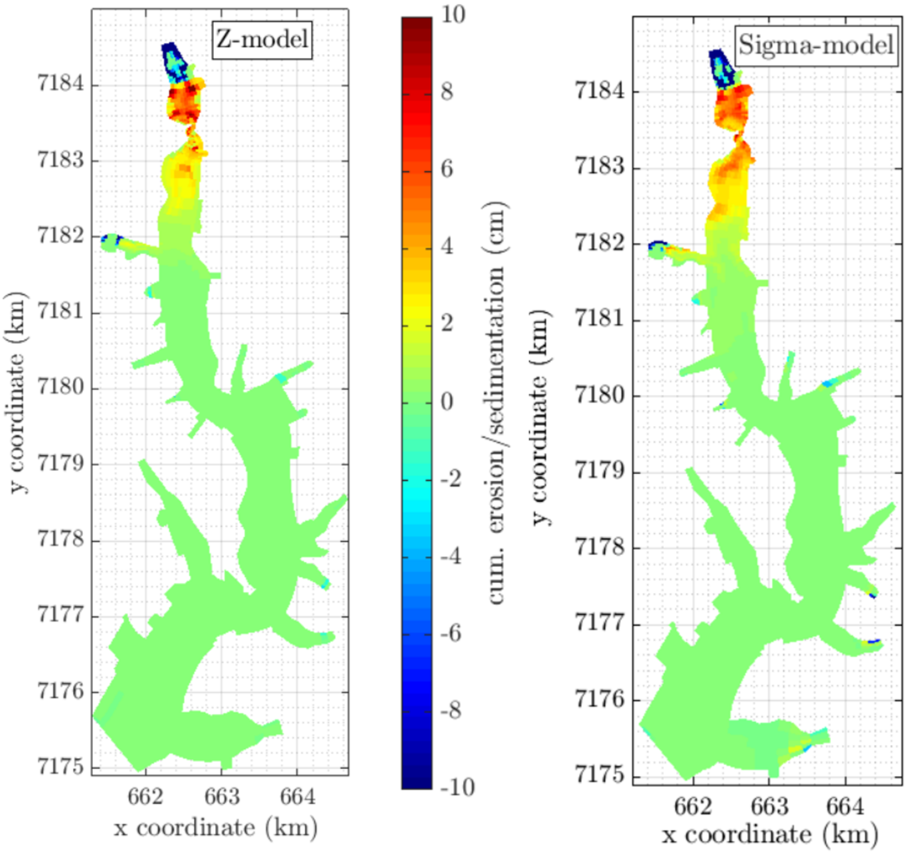

Figure 5.26.: Sedimentation patterns for the simulation with Z-model (left) and Sigma-model (right).

The obtained deposition patterns with the two layering systems without temperature inclusion are depicted in Figure 5.26. The erosional areas at the upper half of the Buffer are similar, nevertheless not identical. At the Ferraria River side arm the depositional areas for both scenarios are located in different regions and the deposition layer is higher for the Sigma-model. The depositional areas at the lower half of the Buffer are rather similar with local peaks for the Z-model. Inmediatly downstream of the Ferraria Bridge the present some discontinuities recognized by the local canges in colors (orange/yellow to green). Further downstream, the deposition with the Sigma-model seems to be higher than with the Z-model.

Figure 5.27 shows the differences between both models. Again, the local differences at a few numerical cells is observed at the Buffer and at the Ferraria Bridge. This is also the case for a few tributaries, which present local discrepancies. In general for both models deposition prevailed over erosion. In the Sigma model the eroded and deposited sediment volume was 16 and 26% higher than in the Z-model respectively. The total sedimentation was 43% hihger with the Sigma-model.

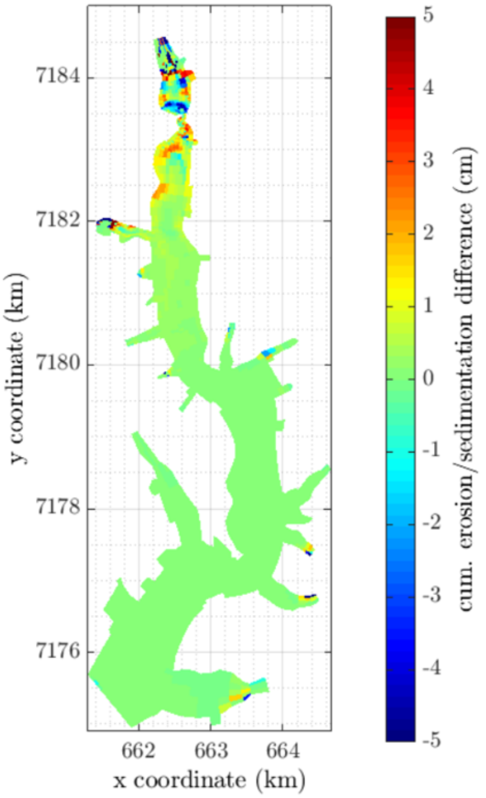

Figure 5.27.: Difference in the sedimentation patterns for the simulations with Z-model and Sigma-model. Legend: Sigma-Z.

The depth averaged velocities for both models resulted to be similar. The time series for the simulated period for the positions Buffer and Intake are presented in Figure A.16 in the Appendix section. The bed shear stresses at the Buffer were proven to be higher for the Sigma-layering system. At a deeper location like the PPA, the situation was similar (see Figure 5.28). For both positions the peaks of both models seems to coincide in time.

The time averaged SSCs for the Z-model without temperature are presented in Figure 5.29 and can be compared to the profiles presented in Figure 5.10, which correspond to the Sigma-model without temperature. The time averaged concentrations at all three investigated positions are higher for the Sigma-system. The differences are of one order of magnitude.

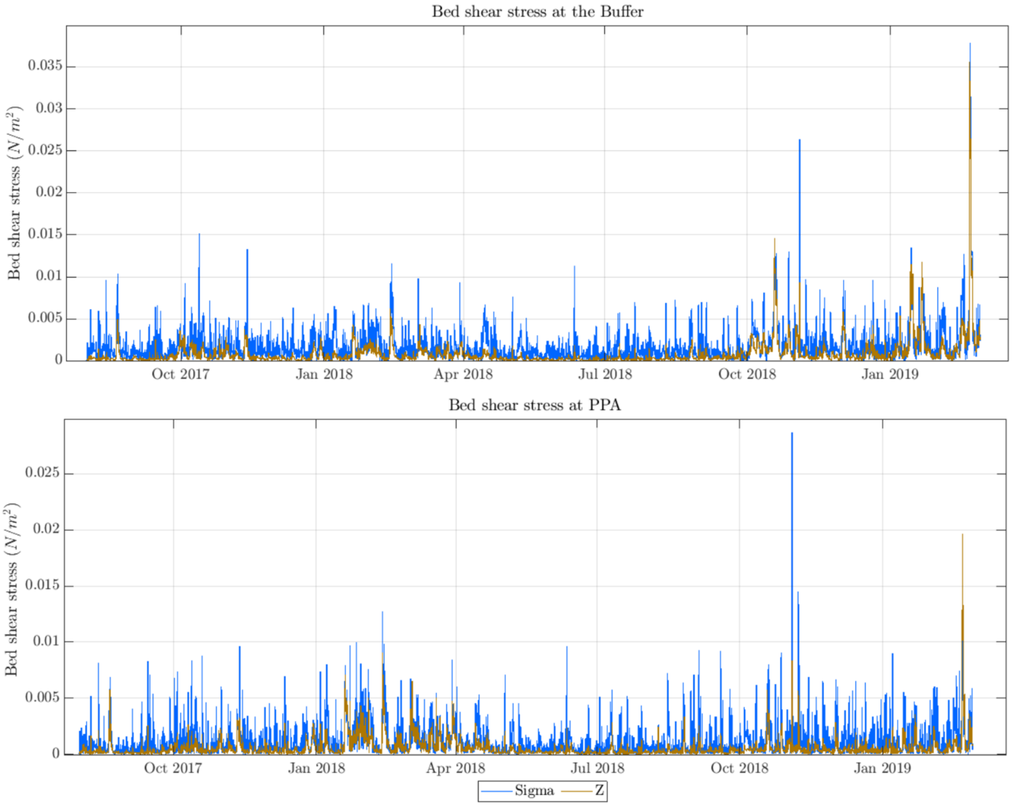

Figure 5.28.: Bed shear stresses at the Buffer and PPA for the simulations with Z-model and Sigma-model.

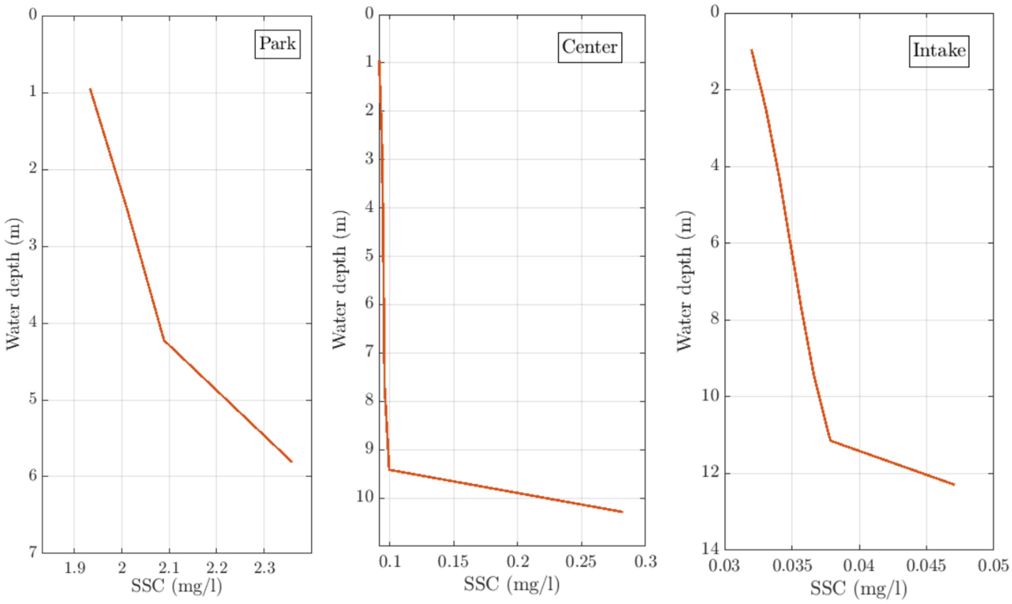

Figure 5.29.: Time averaged SSCs for the simulation with Z-model.

The inclusion of temperature in both models, delivered totally different sedimentation patterns. By comparison with Figure 5.27, for the Z-model the inclusion or exclusion of temperature just produced minor changes in the erosion-sedimentation patterns at the Buffer. A common characteristic: including temperature in both systems allowed the sediments not to be deposited right after the Ferraria Bridge but to be transported further downstream. In general, again sedimentation prevailed in both layering system also when temperature was included.

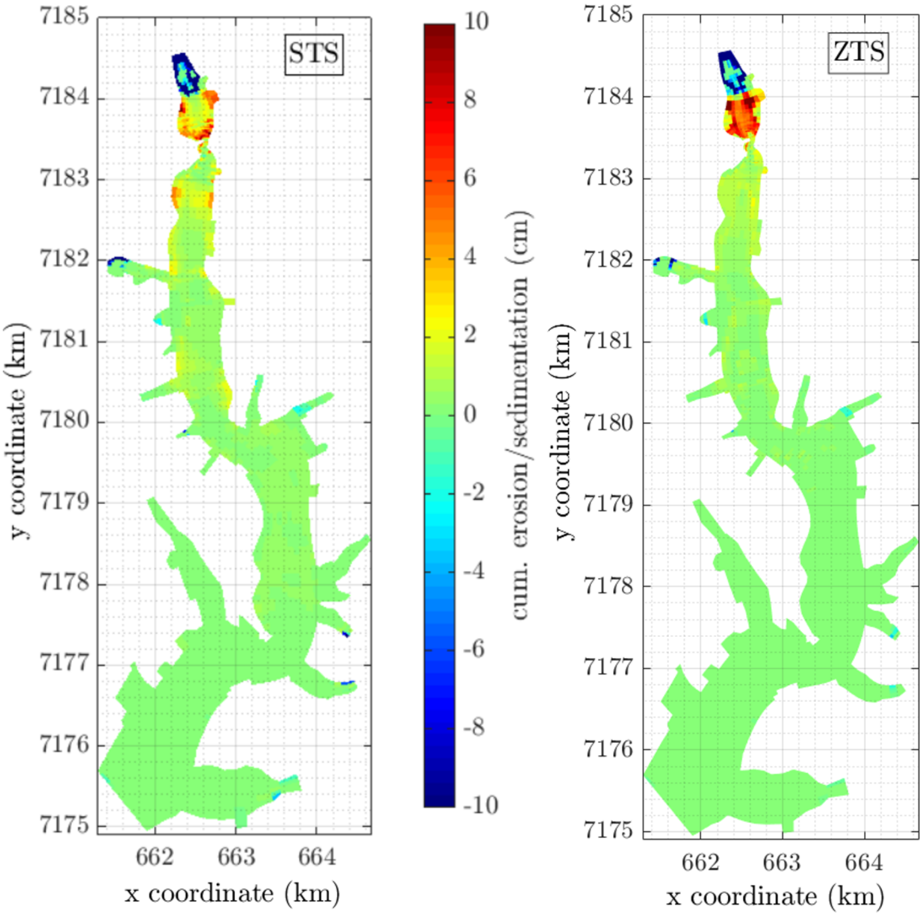

Figure 5.30.: Sedimentation patterns for the simulation with Sigma-model (left) and Z-model (right) both including temperature effects.

5.4. Conclusions

The model was first calibrated in a traditional way. By taking into account a steady state simulation and calibrating the simulated SSCs at several points over the longitudinal axis of the reservoir. Within this step two sediment groups in the cohesive particles range were defined with settling veloities of 0.05 and 0.02 mm/s. These settling velocities correspond to particles with diameters of 13.6 and 6.6 μm respectively. The low SSCs calculated at the Dam in comparison to the much higher measured quantities could be an indicator for unaccounted inflowing sediments entering the reservoir through tributaries near to that region. Since no measurements of the inflowing SSCs at southern tributaries are available, this theory can not be confirmed. The deposition rates were calibrated afterwards using the same model set up. Additional sediment had to be added through erosion of the sediment layer at the entrance of the Buffer and the use of the RC2 allowed to reach the sedimentation rates measured with the sediment trap. Since the wind was shown to be an important forcing for the Passaúna Reservoir, the calibration was performed with the inclusion of it.

The influence of wind on the morphological simulations was evident in the deposited sediment volumes, deposition patterns and SSCs-depth profiles by comparison with the scenario with wind exclusion. In total, the sedimentation in the simulation with no wind was 8.3 % higher than when including wind. More sediment remained in suspension in the simulation with wind inclusion, which is reflected in the time averaged SSCs profiles. The suspended sediments were able to reach the Intake position in the simulation includig wind, for the simulation without it, this was not the case. The more turbulent flow state over the water column for the scenario with wind was observed through the turbulent kinetic energy along the depth. Higher TKE were found for all studied positions when considering wind.

The inclusion of temperature in the model produced lower deposition than for the scenario without its consideration (11 % less deposited sediments). The resulting sedimentation patterns were considerably different for the two analyzed scenarios, with the suspended sediments reaching much further downstream in comparison to the simulation with just wind inclusion. The time averaged SSCs depth-profiles presented higher magnitudes for the simulation with temperature inclusion. At the Intake for example, the time averaged SSCs were ten times higher for the simulation with temperature than for the other case. Both the bed shear stresses and the depth averaged velocities were higher for the simulation with temperature inclusion. The presence of underflows and overflows, i.e. density currents induced by temperature changed the shape of the SSCs-profiles.

If the modelling of heat is going to be included, it is recommended to check the results of the two layering systems (Z- and Sigma-model) in comparison with measured sedimentation patterns and only to continue with Sigma-model if the results are much closer to reality. Given that the selection of a Z-model is more advantageous from a computational cost point of view.

6. Study on the Complexity Reduction of the Numerical Model

6.1. Introduction

[4] Reservoirs are used worldwide as water supply source, for hydropower generation and for the control of flood events. In regions with highly variable hydrological regimes, they are essential for a sustainable water supply for the community, where storing water for dry periods is necessary and requires a large volume for this aim (Annandale et al., 2016). In many countries the main source of energy is the hydropower generation e.g. in Brazil 70.1% of the produced energy (MME, 2013) and approximately 56% of the municipalities use superficial waters sources for consume (Sidagis Galli and Abe, 2010).

Ensuring the water quantity and quality of storages reservoirs is the most important management goal to be achieved by public water companies. Water quality parameters can be measured in any temporal resolution, as high as needed. If anomalies are detected in the measurements and they represent a risk for the human consume, immediate action must be taken. In the case that those actions do not produce a rapid impact on the reservoir water quality, it can happen that the supply of the community must be interrupted for long time periods.

Another process taking place in lakes and reservoirs is the density stratification. Vertical stratification affects negatively the quality of water in reservoirs and lakes. There is a decrease in vertical transfer of nutrients between the surface and deep layers, resulting in a light-abundant but nutrient-poor epilimnion and a light-poor but nutrient-rich hypolimnion (MacIntyre et al., 1999). A second aspect affecting both the water quality and quantity in reservoirs is the transport and deposition of sediments. The impoundment of water through the construction of dam reduces dramatically the flow velocities governing the once free flowing river. Those flow conditions allow sediment particles to deposit between the inflow and the dam of the reservoir. If no measures are taken, at some point the sediment will fill up the reservoir, occupying the space that had been planned for water storage and on this way affecting the capacity of providing enough water supply or flood control. It is widely agreed that between 1 to 2% of the world storage capacity of the reservoirs is lost each year (Schleiss et al., 2014). Sedimentation may also influence the water quality of a reservoir by the input of pollutants often attached to the sediment. Fine sediments have the capacity to absorb other substances as a consequence of their high specific surface area. For instance, the fine sediments at the Upper Rhine River in Germany are heavy loaded with the substance hexachlorobenzene (Klassen, 2017) , which is a persistent organic pollutant that may

---

[4] This section is based on the final report for the MuDak Project (MuDak-WRM, 2021) regarding the Work Package 3, which was written by the author of the present dissertation

cause some types of cancer. Also, heavy metals and nutrients can be attached to the fine sediments. Due to this fact, the sediment particles can be considered as a source of pollution for water bodies (Taveira-Pinto et al., 2014).

In the presented examples, the need for an instrument that helps to plan management strategies for the operation of reservoirs can be clearly seen. A hydrodynamic morphological numerical model can serve as a tool for this issue. The use of numerical models for the prediction and study of the processes that take place in water bodies is an established practice. The appropriate modelling of the hydrodynamics of a reservoir includes the simulation of its thermal structure, flow velocities, water residence time and density stratification (Chanudet et al., 2012b). In this order of ideas, it is necessary to build and calibrate the hydrodynamical model before it can be started with the investigations regarding further water quality parameters. It is important to keep in mind that the water temperature is a quality parameter as well.

The behavior of numerical models simulating the hydrodynamics of reservoirs has been widely investigated in different dimensionalities. Zhang et al. (2020) investigated the impact of rainfall, river inflow and wind on temperature stratification in the Tarago Reservoir in Australia using the software DHI MIKE 3. Polli and Bleninger (2019a) studied the thermal structure and the density currents present in the Vossoroca reservoir in Brazil using both a 3D and a 1D model. Chanudet et al. (2012b) set up and calibrated a 3D model of the Nam Theun 2 Reservoir in Lao using the software Delft 3D. (Ahlfeld et al., 2003) used the software CE-QUAL 2 to study the impact of the water column stratification on the interflow travel time through a laterally averaged 2D model.

Sedimentation in storage reservoir has also been widely simulated, since this is an important issue affecting the life span of these water bodies. Zhang and Wu (2019) analysed the high suspended sediment concentrations (SSC) interfiring with the water quality at the withdrawal location in the Deze Reservoir in China using a 3D model. Hillebrand et al. (2016) published their studies regarding the deposition of sediments at the run of river reservoir Iffezheim at the Rhine river in Germany. They employed the three dimensional software SSIIM3D. Omer et al. (2015) simulated the hydrodynamics and the sedimentation at the Roseires Reservoir in Sudan using Delft3D in order to optimize future field campaigns for the sediment core extractions of the bottom of the water body. Haun et al. (2013) built and calibrated a 3D model to compute SSC and sediment deposition patterns at the Angostura Reservoir in Costa Rica. The set up and calibration of numerical models require a high quantity of input data - in the highest possible resolution they can be obtained. The complexity and the amount of data required are rarely measured in regular campaigns or monitoring stations. The demand for data usually leads to the implementation of comprehensive measurement campaigns, which translates into personnel costs and time. In this vein, the main scientific objective of the present studies is the determination of the minimal complexity degree of the numerical model in order to still adequately represent the processes taking place in the water body.

6.2. Materials and Methods

For the studies presented in this chapter the software Delft3D was applied. All details regarding delft3d can be consulted in the sections 4.2.1 for the modelling of the hydrodynamics and heat transport and 5.2.1 for the morphological modelling. The possibilities to reduce the complexity of the hydrodynmaical numerical model are studied through the analysis of the effect of reducing the temporal resolution or changing the source of the input data in the modelling of the hyrodynamics and thermal stratification. Similarly the effect of the temporal resolution and data source is investigated for the morphological processes, making emphasis in the sedimentation patterns, sedimentation volumen and SSC.

The temperature of the inflows is a necessary variable when modelling the thermal structure of the water column. Within the MuDak Project the temperature of the water entering the reservoir coming from the Passaúna River was determined through direct field monitoring using a Mini-Dot (see chapter 3),these measurements were used for the 3D model with a 10-minutes resolution. Additionally, the model LARSIM-WT (Haag and Luce, 2008) was applied by further project partners in order to obtain not only the discharges, but also the temperature of them. With the calibrated water balance model in LARSIM-WT and in agreement with available data, the water temperatures of the main inflow and further 63 smaller tributaries were simulated. Figure 6.1 compares the results from both sources for the time period, where both data were available. The average absolute difference between the two sources is $0.53°C$, this value represents nothing more than the MAE of the LARSIM-WT temperatures with respect to the measurement with the Mini-Dot. As expected, the simulations results from LARSIM-WT with its daily resolution are not able to capture the peaks of the measurements, nevertheless the trends of both data sets are similar. The application of a model such as LARSIM-WT to obtain the water temperatures has the main advantage, that the temperatures of all tributaries can be estimated through one single model, meanwhile if ground truth values are wanted, multiple temperature loggers would have to be placed at the inflows. In the case of the present reservoir 64 loggers in total would be necessary.

The discharges predicted by LARSIM-WT have, like the inflow temperatures, a daily resolution. For the main inflow a further source of data is available for a fraction of the studied time period. They are measurements of the discharge at the BR277 with a temporal resolution of 15-minutes (see Figure 3.5). Comparing figures 3.3 and 3.5 can be observed in both data sets that on January 20, 2018 a high flow event took place in the Passaúna River. Figure 6.2 presents the discharge at the Passaúna River from various sources. The one-hour resolution curve was generated based on the 15-min resolution data by taking the measured discharge each hour. The daily averaged curve is based on the 15-min data as well. It is interesting how the peak discharge of the event differs between data sets: 10.9 m^3/s for the discharges modeled with LARSIM and 24.2 m^3/s for the 15-minutes resolution data gathered at the BR277. While taking the measured discharges with an hour resolution, a hydrogram can be obtaiend which is similar to the original one. The hydrogram resulting from the daily average discharges has a similar peak discharge to the LARSIM-hydrogram but the rising limb of the former present higher discharges than the LARSIM-data and the falling limb of the hydrogram presents the opposite behaviour.

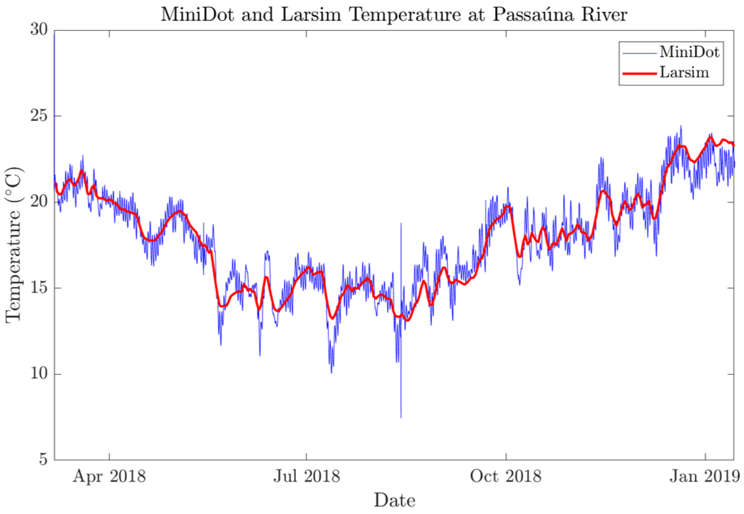

Figure 6.1.: Temperature of the water entering the reservoir through the main inflow provided by Mini-Dot and modelling with LARSIM.

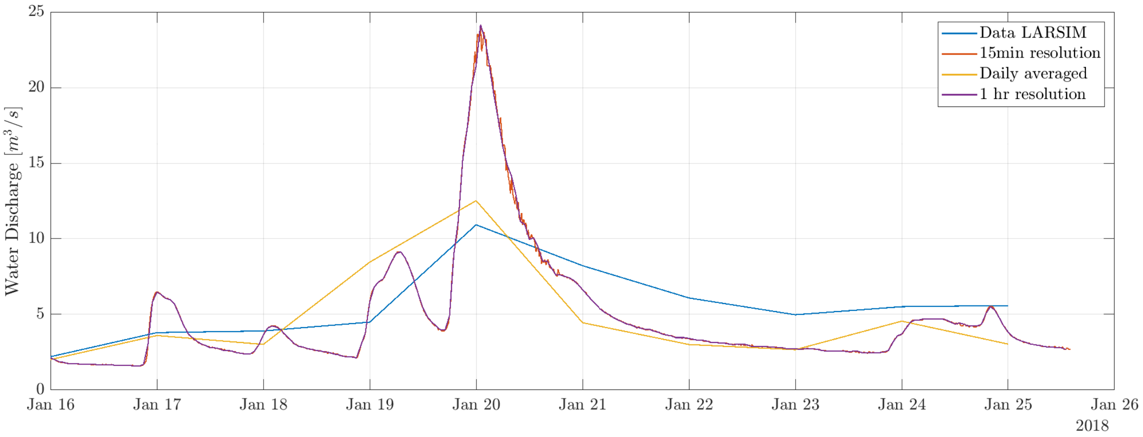

Figure 6.2.: High flow event in January 2018. Temporal variation of the discharge at the TGB154 based on two data sources and different temporal resolution.

Availability of field measurements and monitoring data are not the norm for most water bodies (not only in developing countries). For the modellers is therefore neccesary to consider further sources to obtain data to set up the model.In the case of meteorological data, one can try to obtain the data of the nearest station to the model area and in case of their unavailability optional sources like the ERA5 reanalysis data bank from the European Centre for Medium-Range Weather Forecasts ECMWF. The ERA5 provides hourly estimates of global meteorological parameters with a spatial resolution of 30 km. The meteorological variables are based on data going back to 1950 until today (Bell et al., 2021). Those data are available to the public and can be downloaded easily. Figure 6.3 shows the time series comparison for the calibrated reference model set up (SN1 in chapter 4) and the ERA5 data. The data presented arethe wind speed at 10m above ground U_{10}, air temperature T_{Air}, relative humidity RH, cloud coverage (CC) and solar radiation Q_s.

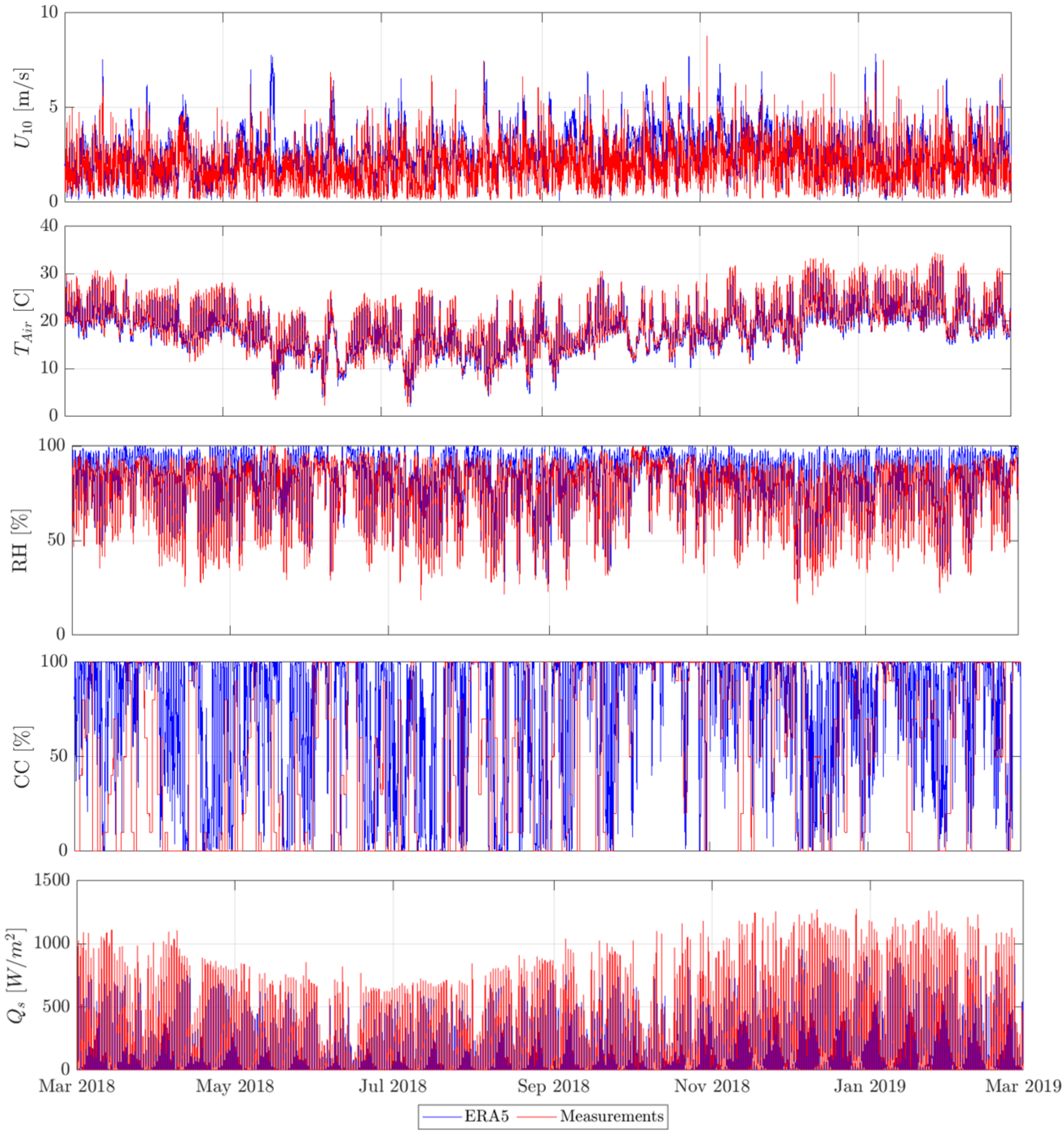

Figure 6.3.: Meteorological data comparison calibrated model setup SN1 and ERA5.

Figure 6.4 shows the wind roses for the four meteorological seasons based on the data from ERA5.

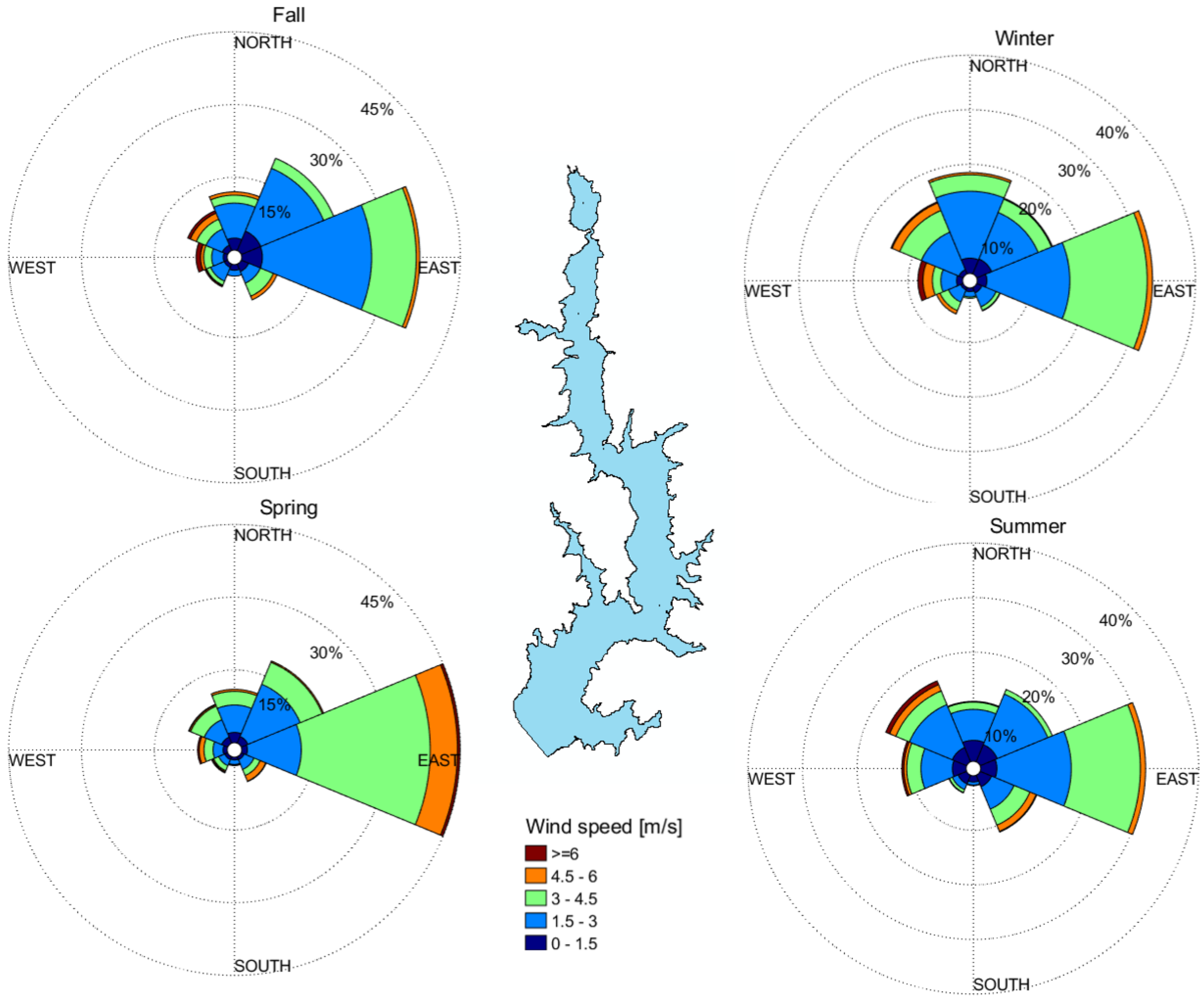

Figure 6.4.: Wind roses for the data originated with ERA5.

6.3. Results and Discussion

6.3.1. Complexity Reduction of the Input Data

Setting up a reliable model is normally a long process. Modelers often have difficulties finding input data, specially in developing countries. When the data are found, they usually have low resolution, which leads to the inveitable question: is the temporal resolution of the data adequate to simulate the hydrodynamics or the sedimentation processes in the reservoir? This practical matter will be handled in this section.

6.3.1.1. Effects on the Hydrodynamics

To set up the hydrodynamical model including heat transport requieres hydrological and meteorological data. The discharges of the tributaries contributing to the water balance of the reservoir can be measured with relatively low effort. It becomes a problem, when a reservoir has multiple tributaries, like in the case of Passaúna, 64 different tributaries and creeks. A reservoir operator, will normally not have a monitoring possibility for all of those inflows. The solution applied within the frame of the MuDak-Project, was the modelling of those inflows using the software LARSIM-WT. Nevertheless, LARSIM-WT requieres measured discharges of at least the main inflow in order to calibrate the model. The discharges from the further tributaries will be calculated according to the sub-catchment areas of each one of them. The resolution of the LARSIM-WT discharges depends on the resolution of the input data for this hydrological model.

To test the robustness of the simulation results with varying temporal resolution of the LARSIM-WT discharges, the simulations **RD3** and **RD7** were set up. For those simulations the resolution of all inflow's discharges are three and seven days respectively. For this, the discharges determined with LARSIM-WT were used taking the value for the discharges each three (RD3) or seven days (RD7). These simulations could represent two pratical cases: (1) field measurements of discharge values each three or seven days or (2) results from LARSIM-WT with these reduced resolutions, due to data unavailability. A further case was implemented using the available 15-minutes high resolution data for the Passaúna River, simulation **QM** notice that for this data set some short periods with missing values are present. The temperature of the inflows for the mentioned simulations had to be adjusted to the respective temporal resolution as well; using the temperature from the original set up.

As already mentioned, the temperature of the main Inflow for the Delft3D model came from the Mini-Dot measurements. Not often such high resolution measurement of the inflow temperature are available and many modelers are obligated to assume or somehow calculate those temperatures (Weber, 2017). In the simulation **TH** the temperatures modeled with LARSIM-WT are employed, this case should depict the lack of Mini-Dot measurements.

A further factor investigated was the resolution of the meteorological and wind data. In the simulation **M1** the mentioned original data sets were reduced to hourly-resolution, this means the values for the solar radiation, air temperature, air humidity, cloud coverage, wind speed and direction were considered for each hour. Often no meteorological data is avaiable at all, specially in developing countries or remote areas. Simulation **ERA5** considered an external source of meteorological data which is the ERA5 reanalysis data. Table 6.1 summarizes the simulations' characteristics for this section.

Within the framework of a master thesis by Varela (2020), which was supervised by the author of the present dissertation, similar simulations to RD3, RD7, M1 and ERA5 were set up. Nevertheless, the simulations presented here are not the same, further calibration of the hydromorphological model was performed and better quality data was gathered. Some results regarding the complexity reduction of the model were presented at the General Assembly of the European Geosciences Union EGU by the author of the dissertation (Gonzalez et al., 2021).

The results of each simulation are compared to the measurements regarding the thermal structure and the horizontal velocities at the water Intake. Table 6.2 describes the quality of the simulations in reproducing the measurements of the temperatures. It also includes the errors (MAE, ME and RMSE) for the calibrated simulation SN1, presented with detail in chapter 4. The simulations TH performed as good as the calibrated simulation. This implies that ground truth values of the temperature are not necesary to feed the model, as long as the LARSIM-WT results were calibrated based on measured water temperatures for a different period than the modeled. As it was the case within the frame of the MuDak-Project. The differences between the Mini-Dot records and the temperature serie of LARSIM-WT with a MAE of 0.57 $°C$ was not an obstacle to achieve equally good results in general and for the surface, middle and bottom layers.

Table 6.1.: Simulations for complexity reduction hydrodynamics

Simulation	Characteristic	Temporal resolution
RD3	River discharges	3 days
RD7	River discharges	7 days
QM	Discharge measured	15 minutes
TH	Temperature LARSIM-WT	1 day
M1	Meterorological and wind data	1 hour
ERA5	Use of data bank of the ECMWF	1 hour

A reduction of the temporal resolution of the meteorological data to one hour (M1), did not affect the quality of the simulation's results. The reduction of the temporal resolution of the discharges to three (RD3) and seven (RD7) days, produced slightly higher erros than SN1, with RD7 showing the highest error magnitudes. The use of measured discharges (QM) did not improved the simulation results, even though the measurements had a resolution of 15 minutes. The use of re-analysis data (ERA5) produced by far the worst results with respect to the measurements, with the highest MAE located at the surface layer and the lowest at the bottom. The opposite trend was found for all further simulations: the results were the poorest at the bottom and the best at the surface. On average, all simulations including SN1 overpredicted the measured temperatures at the water Intake, with exception of the simulation ERA5. A Wilcoxon signed rank test was performed for each simulation in order to check if the differences between each evaluated reduced simulation and the calibrated simulation SN1 were statiscally significant. There were statistical siginficative differences between each reduced simulation and the reference SN1, even for the simulations TH and M1, which had the same magnitude for the erros as SN1. The same statistical test performed individually for each one of the 11 computational layers at the position Intake resulted in siginificant differences at each layer for each simulation.

Table 6.2.: Comparison of the reduced simulations with the measured water temperature at the Intake.

Simulation	Total MAE (°C)	ME (°C)	RMSE (°C)	MAE (°C)		
				Surface	Middle	Bottom
SN1	0.38	0.12	0.48	0.34	0.34	0.48
RD3	0.40	0.17	0.52	0.32	0.40	0.51
RD7	0.43	0.21	0.58	0.27	0.46	0.56
QM	0.42	0.25	0.57	0.31	0.45	0.54
TH	0.38	0.12	0.48	0.34	0.35	0.48
M1	0.38	0.12	0.48	0.33	0.34	0.50
ERA5	1.99	-1.98	2.13	2.27	2.03	1.54

Table 6.3 shows the errors for the calculated horizontal velocities with respect to the measurements at the water Intake position. As for the temperatures, some simulations presented the same errors as the calibrated simulation SN1 including for the surface, middle and bottom layers, i.e. simulations RD3 and TH. The simulation TH showed the same behaviour regarding the calculated water temperatures. With higher error magnitudes performed the simulations QM, RD7 and M1. Notice that the simulation QM, included the measured discharges with a temporal resolution of 15 minutes. They include the peaks discharges that are not described by the daily discharges derived with LARSIM-WT. Thus the flow velocities for the simulation QM could be higher and hence more similar to the measurements than the calculation results of SN1. Nevertheless, the simulation QM did not performed better than the calibrated simulation. As for the modeled temperatures, the simulation with reanalysis data performed the poorest. Common characteristic for all simulations is the fact that the performance of the model was the best at the bottom and poorest at the water surface. All of the simulations underestimated the horizontal velocities at the water Intake. A Wilcoxon signed rank test showed that between the simulated horizontal velocities for SN1 and TH there was no significant statistical difference, with a p-value of 0.0769. All further reduced simulations produced statistically different results from the calibrated version.

Table 6.3.: Comparison of the reduced simulations with the measured horizontal flow velocities at the Intake.

Simulation	Total MAE (cm/s)	ME (cm/s)	RMSE (cm/s)	MAE (cm/s)		
				Surface	Middle	Bottom
SN1	1.01	-0.57	1.38	1.13	0.96	0.71
RD3	1.01	-0.57	1.38	1.13	0.96	0.71
RD7	1.03	-0.60	1.40	1.14	0.97	0.70
QM	1.02	-0.58	1.39	1.13	0.96	0.70
TH	1.01	-0.57	1.38	1.13	0.96	0.71
M1	1.08	-0.54	1.39	1.13	0.97	0.73
ERA5	1.16	-0.59	1.58	1.28	1.14	0.81

The behaviour of the velocities and temperature errors for further areas of the reservoir may differ for positions distant from the Intake. Further regions of the water body could be relevant depending on the issue in study. Figures 6.5 to 6.10 compare the results of each reduced simulation to the calibrated one by showing the values of the MAEs for the temperatures and horizontal velocities for the winter (June 16,2018 to September 1, 2018) and summer (Dezember 1, 2018 to February 28, 2019). The MAEs have been averaged in depth and in time. Using a resolution of three days for the tributaries discharges (see Figure 6.5 a and b), produced the highest discrepancies in the temperatures at the area of Buffer inflow. In general, the differences between the simulations RD3 and SN1 were on average higher during summer for the calculated temperatures. During winter, the region downstream from the FB showed differences smaller than 0.1 $°C$ and during summer lower than 0.3 $°C$. For the horizontal flow velocities (see Figure 6.5 c and d) the differences were more pronounced during winter than during summer and the regions with higher discrepancies are consistently concentrated downstream at the height of the Ferraria River side arm for winter and downstream of the position Center for summer. The lowest MAEs were found at the tributaries' inflows.

Using a temporal resolution of seven days for the liquid discharges (see Figure 6.6 a and b) produced the highest MAEs in the simulated temperature during the summer time period. For both studied seasons the MAEs than in general were under 0.4 $°C$ with the exception of the Buffer and the Ferraria River side arm, where this parameter reached its highest magnitude. For the summer the high values of the MAEs were extended all over the Buffer including the Ferraria Bridge. During Winter the mentioned region was restricted to the upper half of the Buffer. Regarding the erros for the horizontal velocities, in summer they were the highest being specially critical the area downstream of the Ferraria River side arm. In winter the MAEs were more attenuated with some peaks at the upper half of the Buffer but in general being maintained under 0.2 cm/s for most of the area of the water body.

Applying the measured discharges to the model, produced higher deviations from the simulaion SN1 during summer than during winter (see Figure 6.7 a and b). The highest magnitudes of the MAEs concentrated at the Buffer inflow during winter and at the lower half of the Buffer during summer. For most of the area of the reservoir the MAEs were lower than 0.1 $°C$ during winter and 0.38 $°C$ for the summer. On the other hand, for the horizontal velocities (see Figure 6.7 c and d), the most notable differencies (higher than 2.5 mm/s) were concentrated downstream of the Intake region for the winter and downstream of the position Center for the summer (higher than 4.5 mm/s)). Again, the lowest MAEs in the flow velocities were found at the tributaries' inflows for both seasons.

By making use of the water temperatures derived with LARSIM-WT for the reservoir's tributaries, the temperatures across the model for both configurations TH and SN1 remain similar for both winter and summer as depicted in Figure 6.8 a and b. The most notorious differences are found at the Buffer inflow and they become milder in the downstream direction for both seasons. Downstream the FB, the MAEs get values below 0.1 $°C$. The horizontal velocities showed a similar behaviour. The main differences are to be found in the Buffer for summer and winter. The errors are slightly larger for the summer period than for winter. For summer most of the reservoir's area presented MAEs lower than 1.8 mm/s and for winter lower than 1 mm/s.

When feeding the model with 1-hour resoution meteorological data, the mean absolute temperature differences with respect to SN1 result to be higher for the summer than for the winter (see Figure 6.9 a and b). For the winter period the MAEs remain for most of the reservoir below 0.1 $°C$, meanwhile for the summer below 0.3 $°C$. The highest differences concentrate at the upper half of the Buffer area. Figure 6.9 c and d shows the mean absolute errors for the calculated horizontal velocities. Those are evidently higher for the summer period than for the winter. Nevertheless, for both seasons the highest MAEs are located in the region of the water Intake and downstream of it.

Employing meteorological data coming from ERA5 - reanalysis data, produced from all reduced simulations, the largest differences in the calculated temperatures and horizontal velocities with respect to the calibrated simulation (see Figure 6.10). The vast majority of the reservoir area presents time and depth averaged absolute errors which are above of 1 $°C$ for both summer and winter. As for the horizontal velocities, the MAEs are mainly above 5 mm/s, except for the Buffer area and the regions dominated by the inflows of the tributaries.

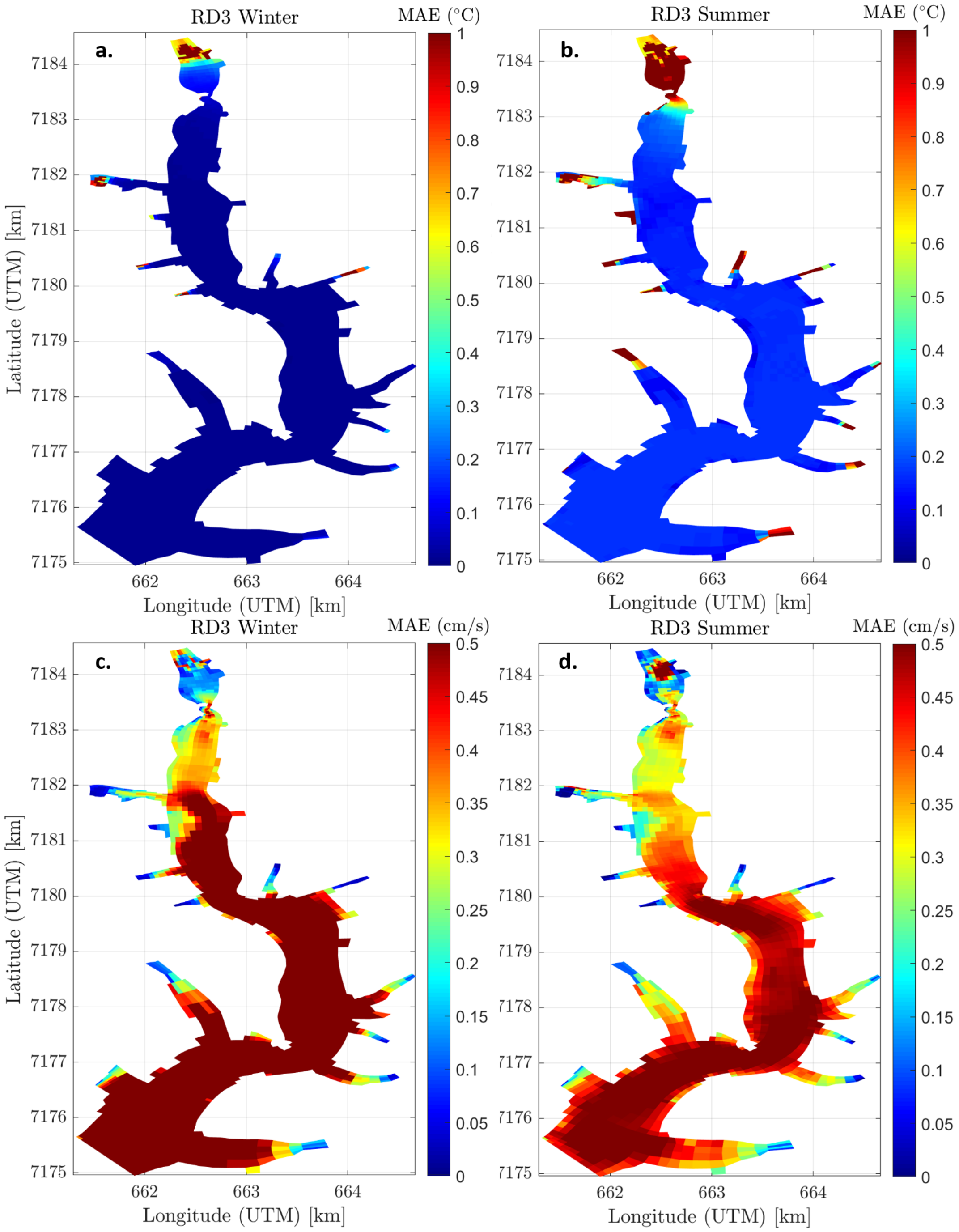

Figure 6.5.: Mean absoute error for the simulations RD3 and SN1 regarding the calculated temperatures (a and b) and horizontal velocities (c and d).

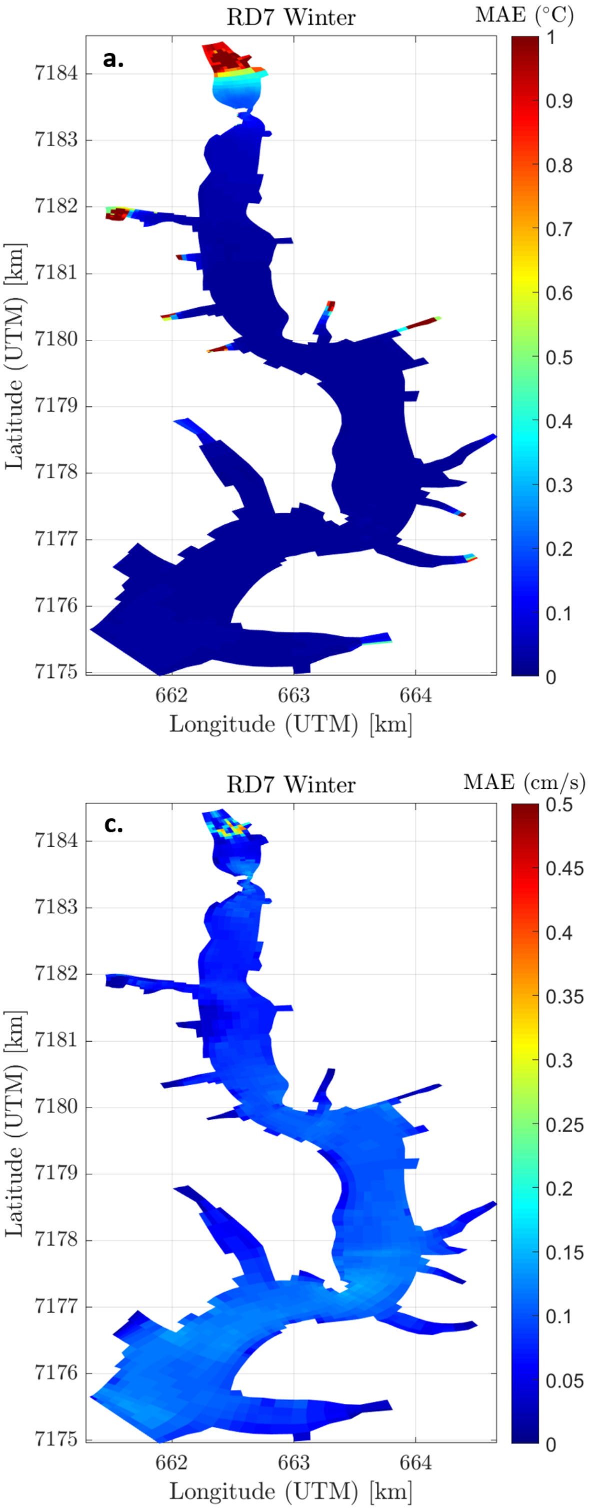

Figure 6.6.: Mean absoute error for the simulations RD7 and SN1 regarding the calculated temperatures (a and b) and horizontal velocities (c and d).

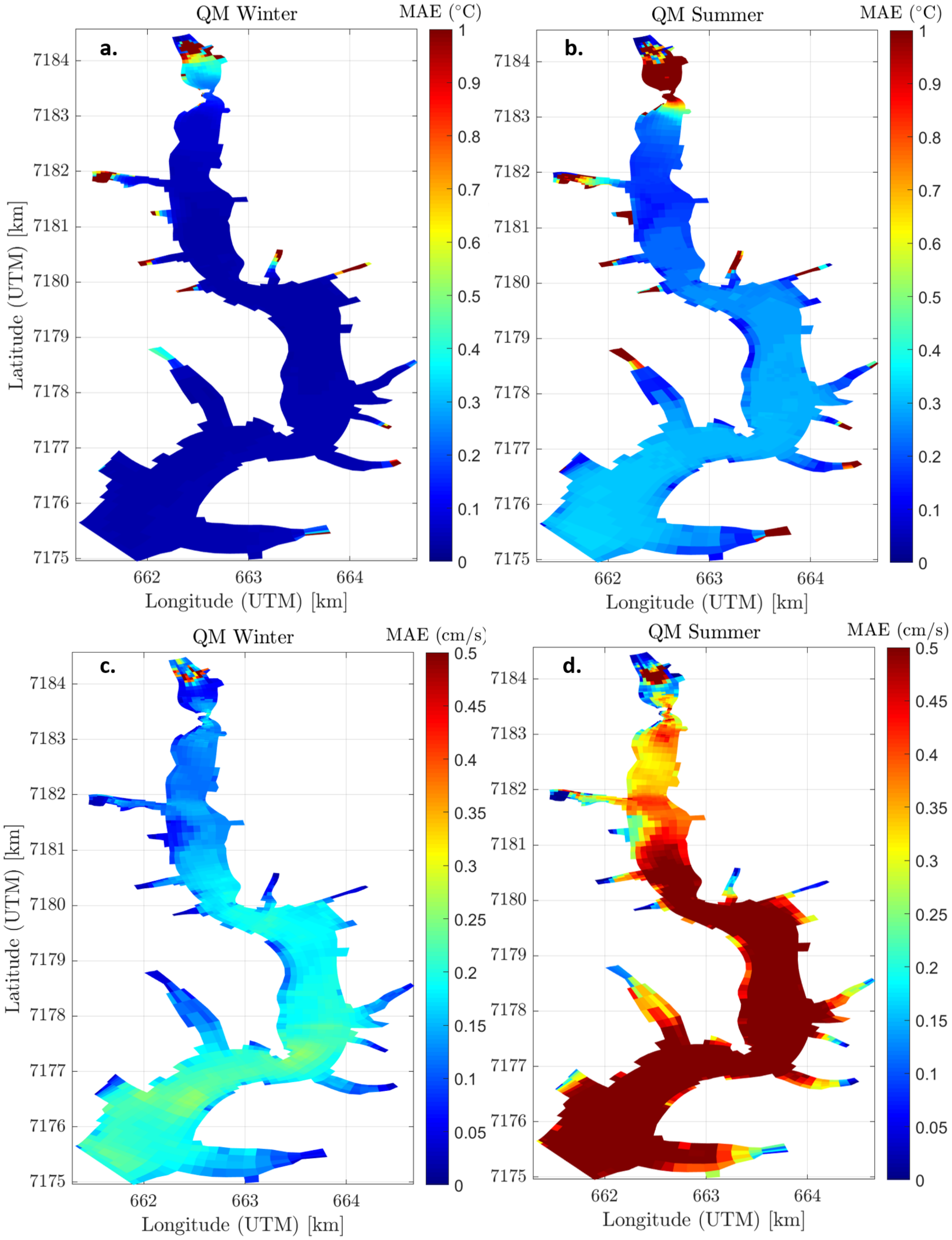

Figure 6.7.: Mean absoute error for the simulations QM and SN1 regarding the calculated temperatures (a and b) and horizontal velocities (c and d).

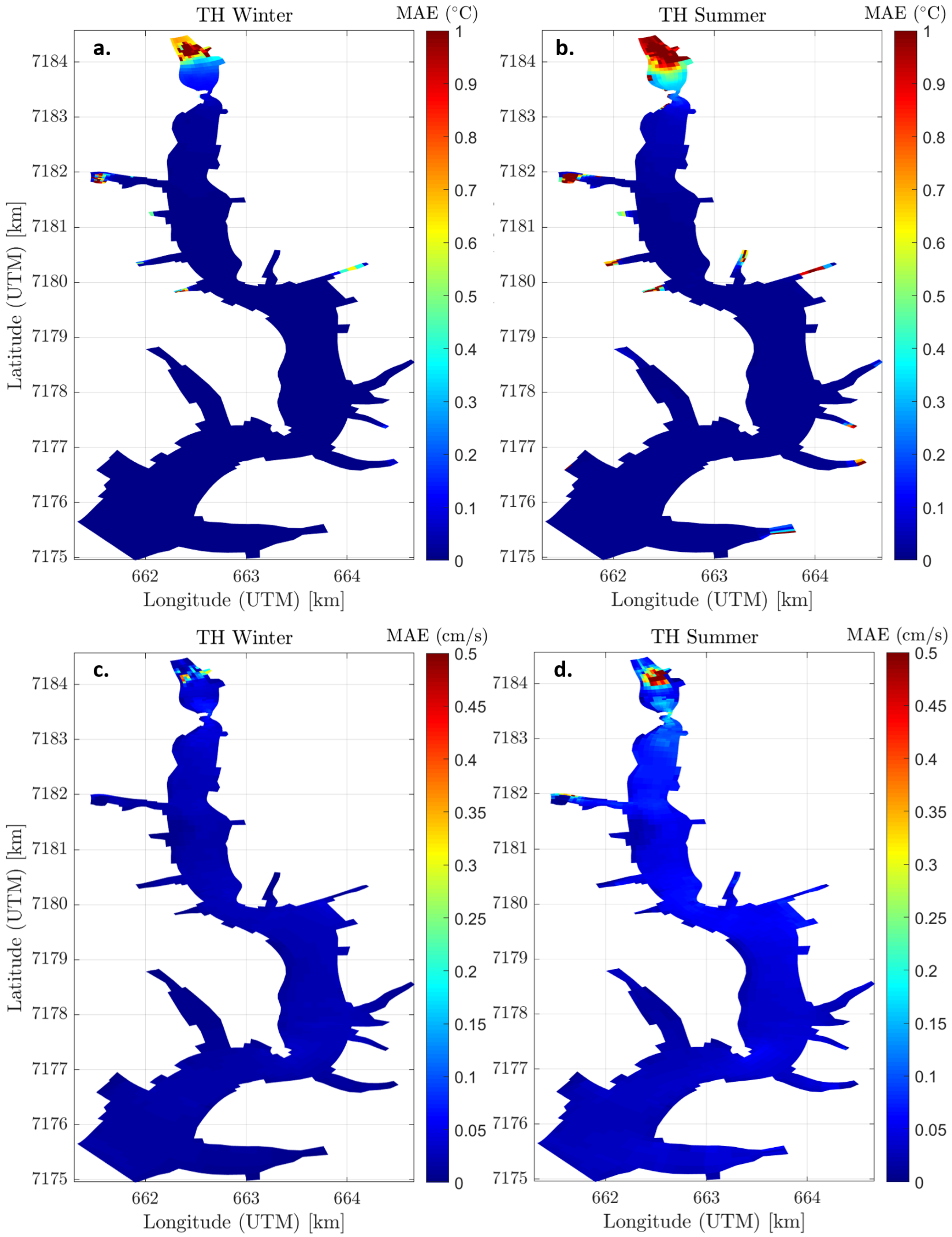

Figure 6.8.: Mean absoute error for the simulations TH and SN1 regarding the calculated temperatures (a and b) and horizontal velocities (c and d).

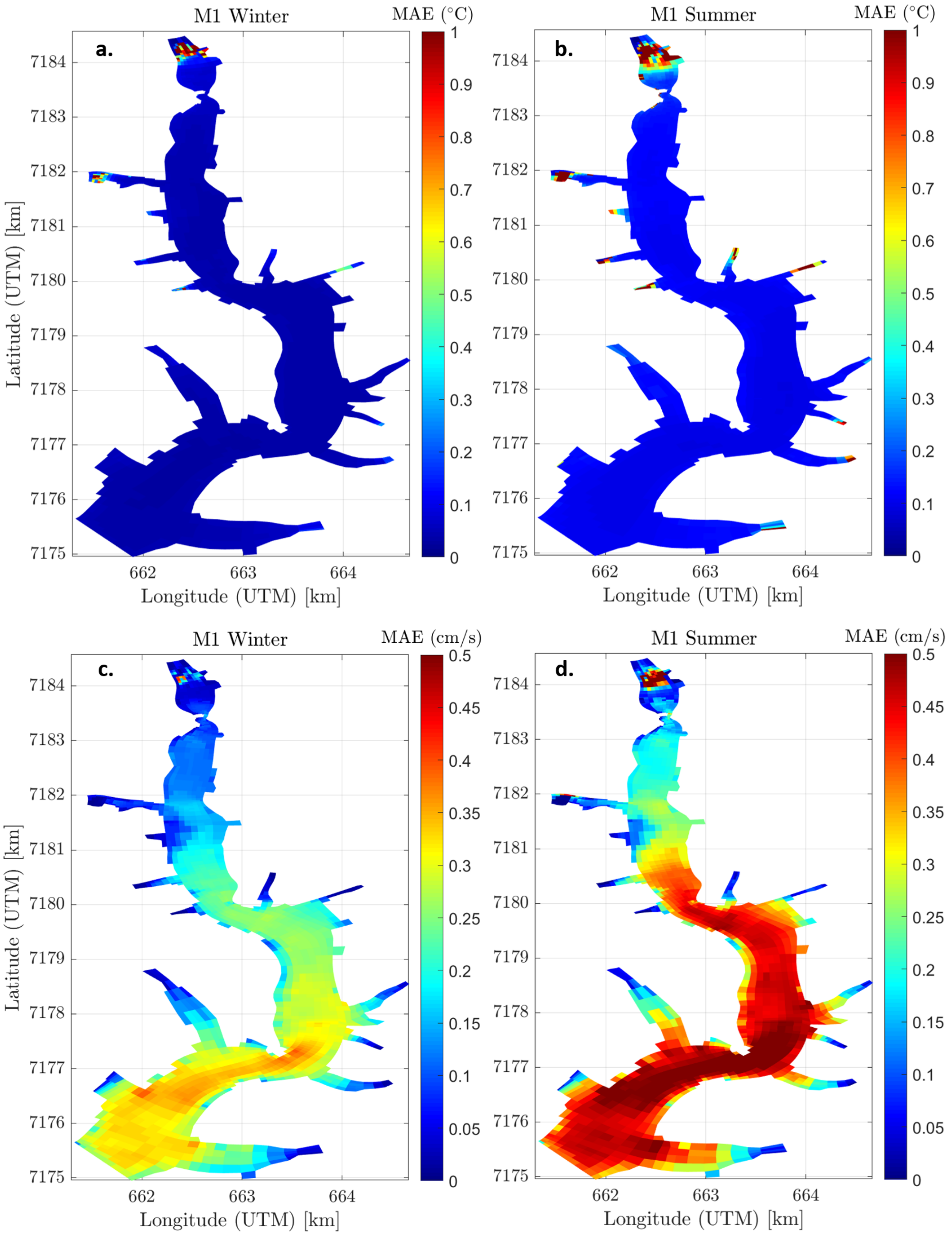

Figure 6.9.: Mean absoute error for the simulations M1 and SN1 regarding the calculated temperatures (a and b) and horizontal velocities (c and d).

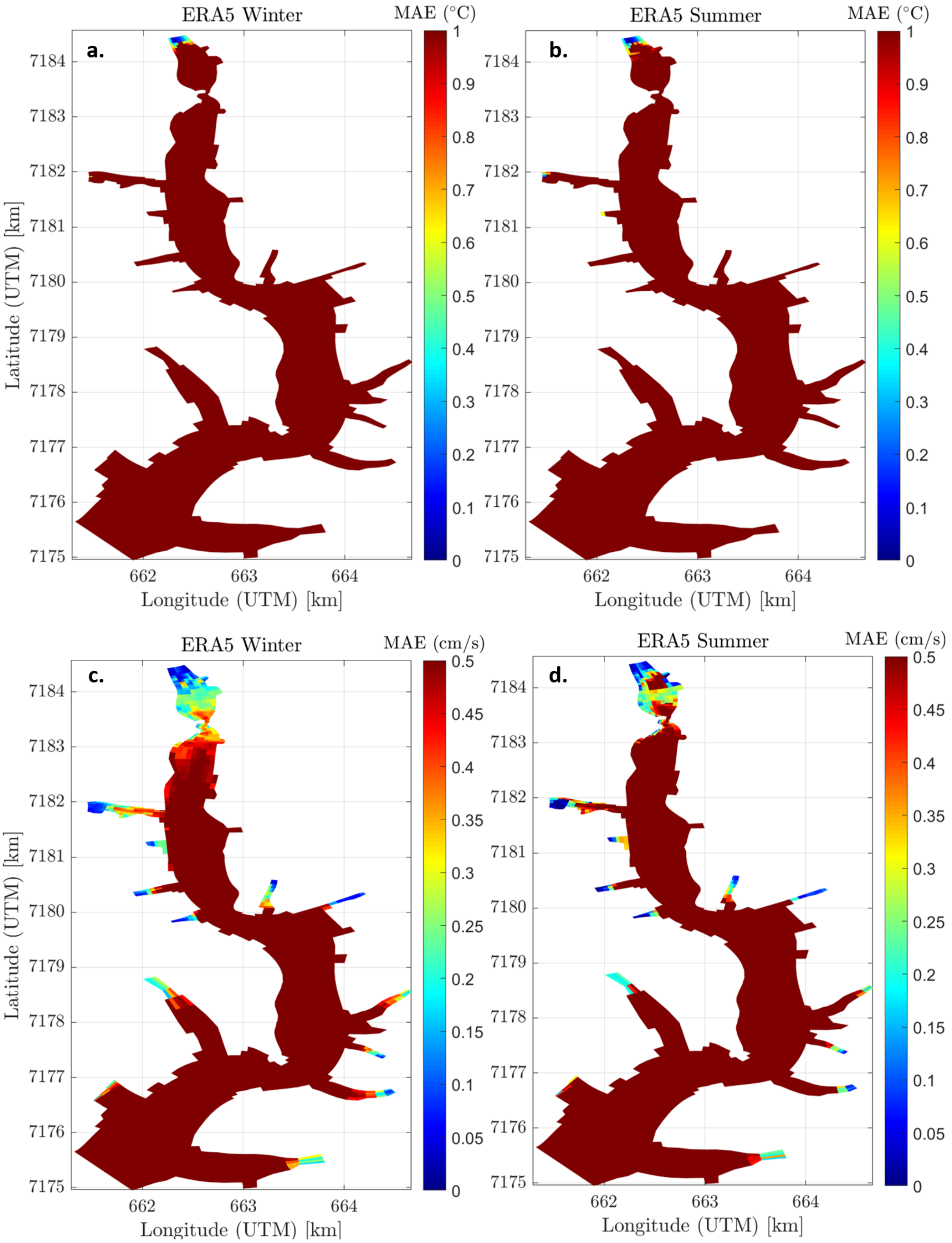

Figure 6.10.: Mean absoute error for the simulations ERA5 and SN1 regarding the calculated temperatures (a and b) and horizontal velocities (c and d).

6.3.1.2. Effects on the Suspended Sediment Transport

To investigate the effect of reducing the resolution of the simulation Sed12 (see chapter 5) on the deposited sediment volume, sedimentation pattern and SSCs in the reservoir, several simulations were set up. All simulations included wind. Nevertheless, the heat transport was not considered in order to avoid the double effect of the reduced resolution on the temperatures and on the sediment transport.

The modeled time period covers from December 11, 2018, to February 28, 2019. Table 6.4 shows a summary of the simulations studied within this section. Simulation **RC1** made use of the rating curve RC1 which is based in the work of Rauen et al. (2017) as described in section 3.3.1 of chapter 3. Similarly, simulations **Reference** and **RC3** employed the rating curves RC2 and RC3 derived from the high flow event in OCtober 2018 and from the work of Sotiri (2020) respectively. The RF simulation has the same set up as Sed12, the only difference resides in the simulated period which is longer for the former than for the latter. Simulations **RD3** and **RD7** used reduced temporal resolutions for the rivers discharges and hence a reduced resolution for the incoming sediment concentrations.

The simulation **QM** used the measured discharges at the main inflow with a 15-minutes resolution. For this simulation, the incoming SSCs were recalculated with the set of equations for the RC2 since they are a function of the discharge. This simulation comprehendeds nevertheless a different period than the other ones; from the 16th to the 26th of January 2018. The main reason is that for the period December 11, 2018, to February 28, 2019 no measured discharges were available. During the period in January 2018 a high flow event was observed in the Passaúna River, which was not good captured through the one-day resolution discharges derived with LARSIM-WT (see Figure 6.2). Simulation **QMrf**, was set up for the same period as QM but with the LARSIM-WT discharges in order to compare both simulations.

Simulation **M1** employed for the wind velocity and direction, data with a hourly-resolution in contrast to the 15 minutes resolution of the reference simulation. At last, simulation **ERA5** used for the wind data, information from reanalysis of the ECMWF.

Table 6.4.: Simulations for complexity reduction sediment transport.

Simulation	Characteristic	Temporal resolution
RF	Rating curve RC2	as inflows
RC1	Rating curve RC1	as inflows
RC3	Rating curve RC3	as inflows
RD3	River discharges	3 days
RD7	River discharges	7 days
QM	Discharge measured	15 minutes
QMrf	Discharge LARSIM-WT	daily
M1	Wind data	1 hour
ERA5	Wind data of the ECMWF	1 hour

Table 6.5 summarizes the results of the deposited and eroded sediment volumen. For the faster comparison of the results by side of the reader the deposited volume in the reference

simulation will be designated with the letter S and all other deposition and erosion quantities will be defined in function of it. For the simulation QM and QMrf the letter S_{rf} will be used as reference.

Table 6.5.: Results of reduced resolution simulations: deposited and eroded volumes.

Simulation	Deposition	Erosion	Difference
RF	S	$0.996{\cdot}S$	$0.004S$
RC1	$0.982 \cdot S$	$0.998{\cdot}S$	$-0.015 \cdot S$
RC3	$1.765 \cdot S$	$0.991{\cdot}S$	$0.774 \cdot S$
RD3	$1.002 \cdot S$	$0.998{\cdot}S$	$0.004 \cdot S$
RD7	$0.905 \cdot S$	$0.880{\cdot}S$	$0.025 \cdot S$
QM	$1.202 \cdot S_{rf}$	$0.872{\cdot}S_{rf}$	$0.330 \cdot S_{rf}$
QMrf	S_{rf}	$0.192{\cdot}S_{rf}$	$0.808 \cdot S_{rf}$
M1	$1.006 \cdot S$	$0.999{\cdot}S$	$0.007 \cdot S$
ERA5	$0.987 \cdot S$	$1.044{\cdot}S$	$-0.057 \cdot S$

In the reference simulation RF, the deposition prevailed over the erosion as indicated in Table 6.5. Nevertheless the two volumes were similar, resulting in a small total sedimentation volume. Using the rating curve based on historical data, induced to lower deposition and slightly higher erosion in comparison with the reference simulation. This had as result that erosion prevailed over deposition in this simulation and the total eroded volume was higher than the total deposited volume in the simulation RF. Applying the rating curve derived from data by Sotiri (2020), higher deposition rates were observed. In total he deposition was 76.5 % higher than in the reference simulation. On the other hand, the eroded volume was lower. Again, sedimentation prevailed over erosion. Simulation RC3 produced the highest total deposited volume of all reduced resolution simulations.

Reducing the resolution of the tributaries discharges to three days produced a slight increase in the deposited volume and decrease in the eroded volume. In total the difference between the deposition and erosion was the same as in the reference simulation. Regarding the simulation RD7, the results were the opposite to the simulation RD3. The erosion and the deposition were lower than for the reference simulation. The difference between deposition and erosion volume was positive and higher than the same difference for the simulation RF. Reducing the resolution of the wind data to one hour resulted in higher eroded volume than in the reference simulation. The deposited volume was just 0.6% higher than in the simulation RF. The total deposited volume was in the same oder of magnitude for both scenarios. The use of ERA5 data conduced to lower deposition rates and higher eroded volume. For this simulation the erosion prevailed over sedimentation.

The simulation of the high flow event in Jauary 2018 conducted to a prevailing deposition while using the standard resolution data of the calibrated model (simulation QMrf). The erosion was only 19.2 % of the deposited volume. The use of higher resolution discharge data conducted to higher deposition volume, in fact 20.2 % more sediment deposited in the simulation QM than in its reference simulation QMrf. Meanwhile the erosion was much higher for the former simulation.

Figure 6.11 shows the sedimentation pattern for the simulation RF. The upper half of the Buffer, where the bed shear stresses are the highest, presents erosion. Erosion is also found at the left bank of the Ferraria River's side arm. The highest deposited layers are found at the lower half of the Buffer. After the Ferraria Bridge, the deposited layer thickness gradually decreases. At the height of y-coordinate 7180.5 km the deposited layer thickness goes under 1 mm.

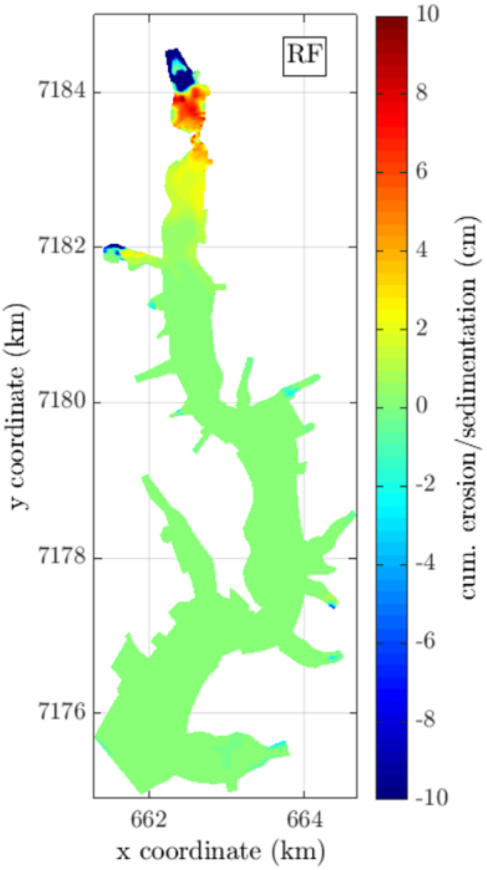

Figure 6.11.: Sedimentation pattern for the simulation RF.

The sedimentation patterns of the several reduced resolution simulations are compared to the reference case through maps showing the difference between the thickness of the deposited/erode sediment layer. The difference were always calculated with the simulation RF (or QMrf) as reference, i.e. substracting the magnitude of the deposited layer in a detrmined simulation from the RF scenario. Figure 6.12 shows the mentioned differences fo the simulation RC1 to RD7. It is important to notice, that the limits of the color scales are different and hece same color not necesarily have the same meaning for all diagrams. In the section a. of the figure, the simulation RC1 and RF are compared. The differences are mainly below 2 mm. The eroded enrace of the Buffer was similarly depicted with both simulations with a few local exceptions (red/orange points). From downstream of the Ferraria Bridge until the height of the Ferraria River the differences remain negative, indicating higher deposition for the RF simulation. Nevertheless, the differences are mostly below 1 mm. Donwstream of the Ferrari River side arm the differences decrease below 0.1 mm. Regarding the use of the RC3 rating curve, the difference are more notheworthy. They reach the 6 cm and the difference are not lower than 1 mm before the height of y-coordinate 7181 km, so much further downstream than in the simulation RC1.

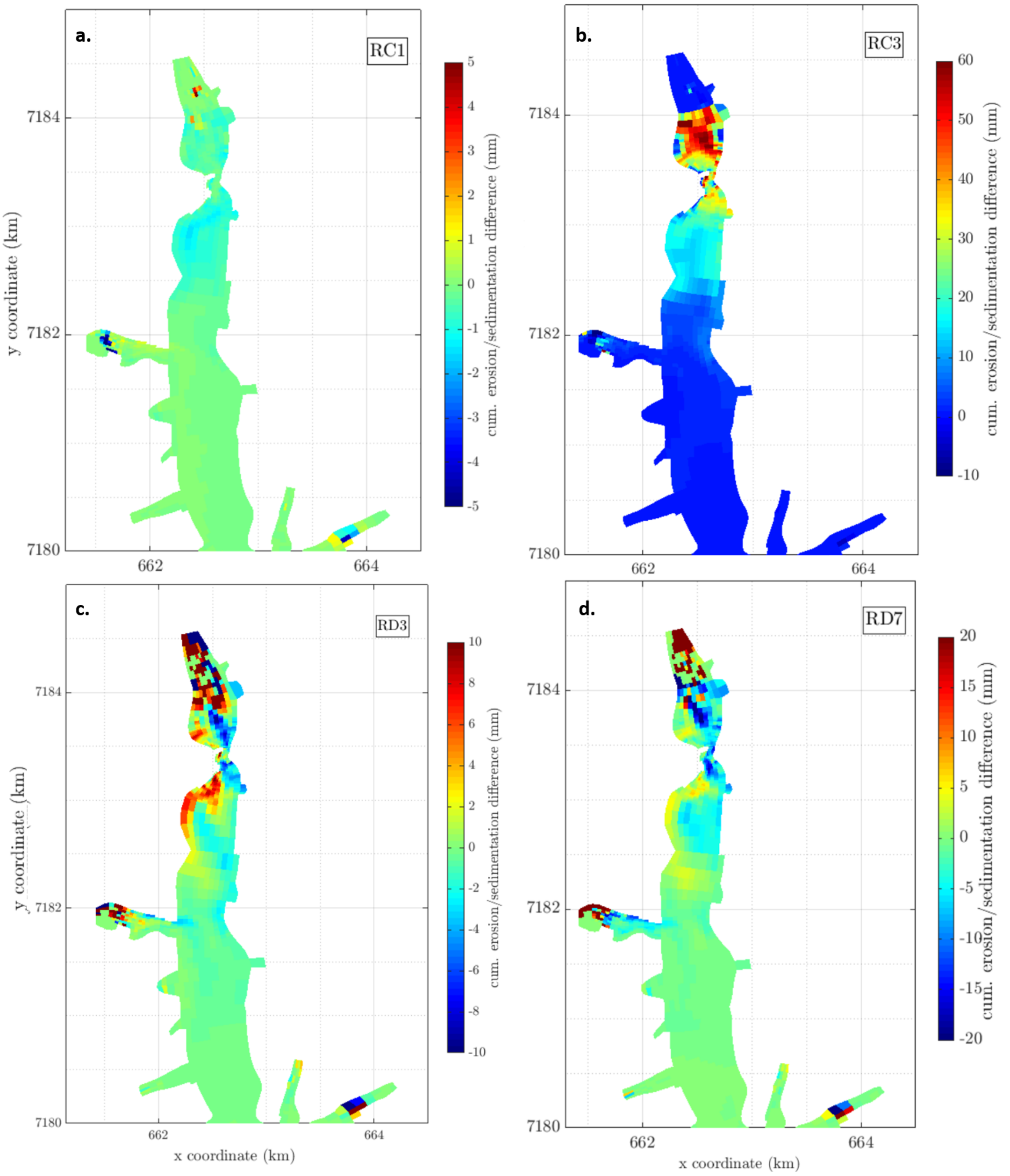

Figure 6.12.: Differences in the sedimentation pattern for the simulations RC1 (a), RC3 (b), RD3 (c) and RD7 (d) . Legend: Simulation-RF

For the simulation RD3 the major differences are concentrated in the Buffer and they are local rather tan continous. Inmediatly upstream and downstream of the Ferraria Bridge the differences are negative indicating higher sedimentation for the RF simulation. At the height of y-coordinate 7183 km, an rage region is identified where the deposition in the RD3 simulationwas notoriously larger than in the RF case. For the simulation RD7, the differences are even more pronounced (consider different color scales) but the general pattern in the differences is similar to the simulation RD3.

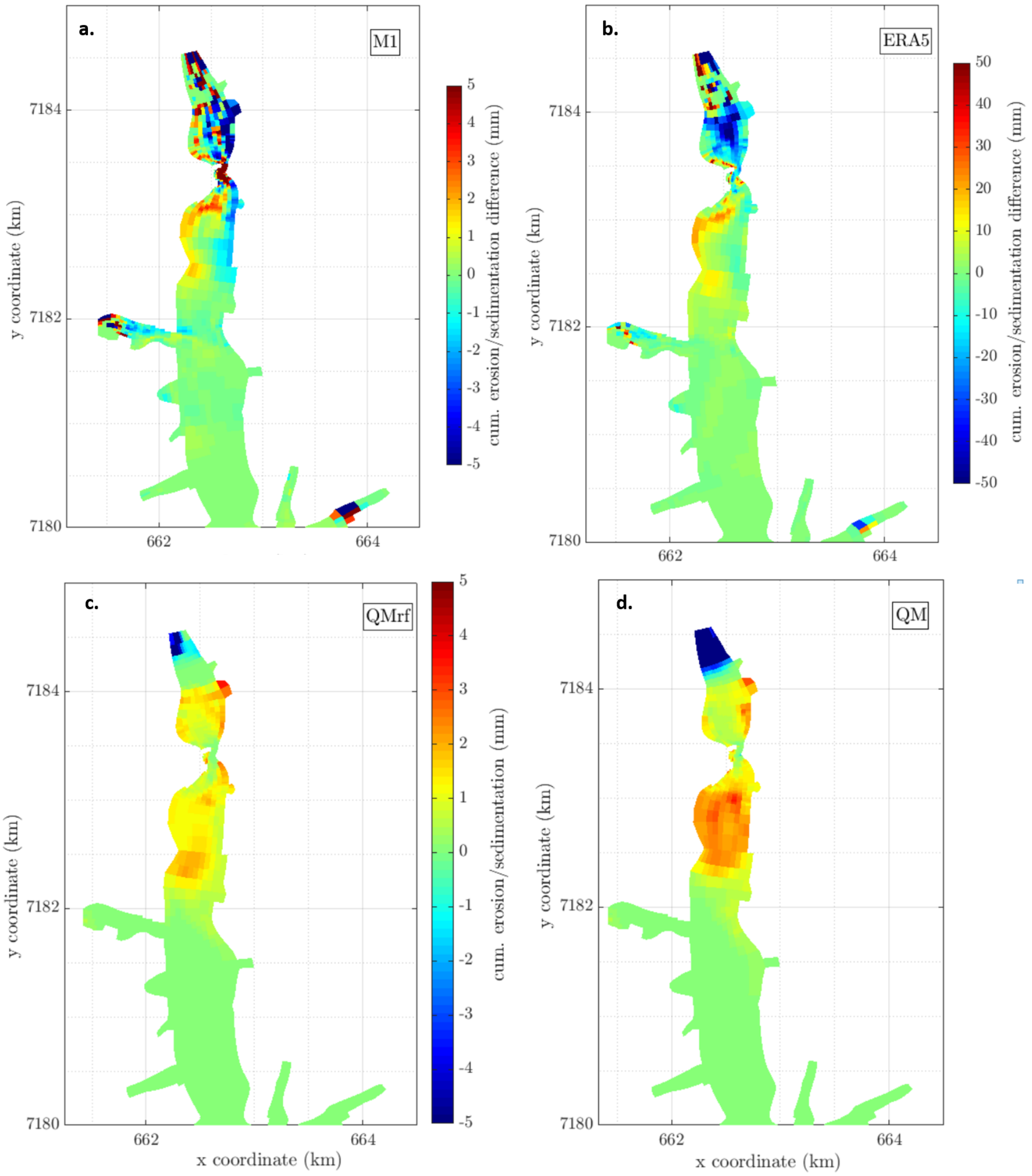

Figure 6.13.: Differences in the sedimentation patterns for the simulations M1 (a) ERA5 (b) and sedimentation patterns for the simulations QMrf (c) and QM (d).

Figure6.13 presents in the top row the difference in the sedimentation patterns for the simulation M1 (a) and ERA5 (b). Reducing the resolution of the wind data to one hour introduced changes in the erosion pattern at upper half of the Buffer. In the lower part of the same region, the changes were neither positive or negative over the entire region, showing for some cells lower sedimentation for the M1 simulation at the left bank of the Buffer. At the Ferraria Bridge the siulation M1 presented more deposition than RF. Downstream of the Bridge, the differences are again positive and negative with more depositionfor the M1 simulation at the left bank than for the case RF. Using reanalysis data from ERA5 produced a more consistent picture for the difference between both simulations. The eroded upper half of the Buffer showed differences (values different from zero) and the lower half of the Buffer presented lower sedimentation than the reference (RF) simulation. The bottom row of Figure 6.13 shows the sedimentation patterns for the simulation of the igh flow event in January 2018. The reference simulation for this special case showed some erosion at the entrance of the Buffer with sedimentation at the lower half of it. With the highest sediment thickness concentrated at the left bank of the Buffer. At the Ferraria Bridge little to non deposition took place. Downstream of this constriction deposition augmented in magnitude again. In contrast, the use of high resolution discharges delivered a much larger erosion area at the Buffers inflow and lower sedimentation at the lower half of the Buffer. Downstream of the Ferraria Bridge the sedimentation was also higher than in the respective reference simulation (QMrf).

In order to observe changes in the SSCs a general analysis of the a time average of this quantity was carried out. For it, three positions were considered Park, Center and Intake. Th results are summarized in Tables 6.6 to 6.8. At Park it is noteworhty, that for all comparable simulations, the SSCs were in the same order of magnitude with exception of the ERA5 simulation which was one order higher at all analyzed depths. For the further positions this simulation consistently showed the highest concentrations.
At Park all simulations showed similar gradients between the surface and bottom concentrations (around 8%). At Center the profiles were rather uniform with the exceptions of the profiles of the high flow event and ERA5. The simulations of the high flow event showed low SSCs for this position in the order $10^{-4} mg/l$. At the Intake the profiles presented higher SSCs towards the bottom with gradients of around 9%. The simulation of the high flow event showed higher SSCs when using the high temporal resolution discharges. Nevertheless, the SSCs were in the same order of magnitude.

Table 6.6.: Time and depth averaged SSCs at the position Park for the reduced simulations.

Simulation	SSC bottom (mg/l)	SSC middle (mg/l)	SSC surface (mg/l)
RF	46.13	44.12	42.29
RC1	45.09	43.13	41.36
RC3	76.93	73.56	70.43
RD3	36.68	35.23	33.86
RD7	39.44	37.81	36.25
QM	16.45	15.99	15.58
QMrf	10.18	9.83	9.60
M1	45.26	43.45	41.75
ERA5	117.48	112.06	107.74

Table 6.7.: Time and depth averaged SSCs at the position Center for the reduced simulations.

Simulation	SSC bottom (mg/l)	SSC middle (mg/l)	SSC surface (mg/l)
RF	1.84	1.85	1.87
RC1	1.90	1.89	1.90
RC3	2.23	2.43	2.27
RD3	1.90	1.90	1.91
RD7	2.90	2.93	2.97
QM	0.00048	0.00062	0.00077
QMrf	0.00041	0.00042	0.00043
M1	2.72	2.75	2.72
ERA5	6.23	5.92	5.66

Table 6.8.: Time and depth averaged SSCs at the position Intake for the reduced simulations.

Simulation	SSC bottom (mg/l)	SSC middle (mg/l)	SSC surface (mg/l)
RF	0.65	0.62	0.59
RC1	0.65	0.61	0.59
RC3	0.68	0.65	0.62
RD3	0.59	0.57	0.55
RD7	0.67	0.64	0.61
QM	0.00054	0.00054	0.00054
QMrf	0.00056	0.00055	0.00055
M1	0.75	0.72	0.69
ERA5	2.08	2.04	2.00

6.4. Conclusions

Values for the water temperature of the tributaries based on the hydrological simulations with LARSIM-WT produced simulations results with similar quality as the high resoluted simulation. The use of water discharges with a 3-day resolution showed also good results. The employment of discharges with 7 days resolution starts to be critical specially for other areas different to the Intake. The differences for the simulation ERA5 were the most notorious and the use of this kind of data should be carefully analyzed by the modeler. The prediction of the flow velocities was of similar quality than for the reference simulation using the lower 3-day resolution for the discharges and with the use of the temperatures modeled with LARSIM-WT. The differences for each reduced resolution simulation with respect to the reference simulation were also extended at further areas of the reservoir. The higher discrepances were obtained with the ERA5 simulation, those extending to the whole reservoir area for both parameters temperatures and horizontal flow velocities. The use of the temperatures provided by the hydrological model delivered the mildest differences all over the reservoir area.

Regarding the sedimentation volumes, all changes in resolution and data sources resulted in a change in the deposited/eroded sediment volumes. This is not only due to the different hydrodynamics resulting in the simulations but also to the changing amount of sediments entering the model for some of the simulations (RC1, RC3, RD3 and RD7). For those simulations the incoming sediments were different than for the reference simulation, i.e. different rating curves and different temporal resolution. Again, the influence of wind in the sedimentated volume and sedimentation patterns is shown here within the simulations M1 and ERA5, where different data for the wind parameters were used. The employment of high resolution data for a high flow event resulted in differences of 20 % in the deposited sediments and the amount of eroded sediments was much larger while using the high resolution data. The fact that peaks discharges are included and better described with the high resolution data could have caused peaks in the bed shear stress and hence higher erosion.

In solving the matter of which temporal resolution/ data source is adequate to get realiable model results, the context of the project matters. For example using ERA5 data for the wind characterization resulted in a deposition volume of just 1.3 % higher than when using the data of the nearest meteorological station and in a MAE which is by 1.6 $^{\circ}C$ worst than with the original simulation. Those differences will have to be put in context by the modeller. Weighing up if the mentioned differences are acceptable according to the aim of the study.

7. General Summary and Outlook

Reservoirs are designed to provide water supply, flood protection, hydropower generation and/or recreation. The construction of reservoirs around the world is constantly rising due to the increasing water scarcity and energy demand. Sedimentation threatens to decrease the storage capacity of these water bodies (Schleiss et al., 2014) and therefore it is essential to understand all the processes that may have an impact on it. A further aspect to take in to account in the field of reservoir management is the quality of the water which is directly affected by the water temperature and the suspended sediment concentrations (SSC). The aim of the present dissertation was to identify the main processes and parameters governing the quality of the results of the numerical modelling of the hydrodynamics and sediment transport in reservoirs including the relevance of considering thermal stratification and wind in the simulations. This dissertation was developed within the framework of the MuDak-Project (Multidisziplinäre Datenakquisition als Schlüssel für ein global anwendbares Wasserressourcenmanagement) at KIT funded by the Federal Ministry of Education and Research BMBF (MuDak-WRM, 2019).

The studied water body, the Passaúna Reservoir is a canyon-shaped reservoir in the west margin of the city of Curitiba in Brazil. The water body has its major tributary inflowing through the northern region of the reservoir: the Passaúna River. According to the hydrological modelling carried out with LARSIM-WT (Haag and Luce, 2008) within the frame of the MuDak-Project, the mean discharge of this tributary is of around 2 m^3/s. The highest ever registered discharge at the Passaúna River was 27 m^3/s. The highest registered wind speed at the reservoir's region was 9 m/s and the mean value of this parameter was found to be 2 m/s for the studied period of March 2018 to February 2019. Measured air temperatures ranged from 2 to 35 $°C$. The reservoir presented several mixing events during the mentioned period and is classified as a warm polymictic water body. Measurements of the horizontal flow velocity near the water intake, delivered time and depth averaged magnitudes of around 2 cm/s. The highest flow velocity was registered at the water surface and its magnitude was 14 cm/s. It is important to keep in mind, that those values are representative only for the lacustrine zone of the reservoir. The averaged Secchi depth for the Passaúna Reservoir was calculated to be 2 m, with the highest penetration of light measured to be 3.1 m and this parameter being variable over the reservoir's area and also as a function of time.

The amount of sediment entering the reservoir is a key point for the simulation of morphological changes in the reservoir, if not the most important parameter. A rating curve delivers this information as the SSC in function of the liquid discharge. For the Passaúna Reservoir, there were three rating curves (RC) available within the framework of the MuDak-Project. Two were derived from field measurements (RC1 and RC2) and the other one from the modelling of erosive processes in the catchment (RC3). RC1 and RC3 delivered similar results. RC3 delivered much higher concentrations and hence sediment loads. At this point the direct measurement of SSCs and liquid discharges on the field are strongly recommended.

The knowledge of the amount of sediments deposited in the reservoir and its pattern is a necessary information for the calibration of morphological models. For the modelling, the use of data coming from sediment cores can be useful regarding sediment composition at the reservoir's bed. Nevertheless, the information about sedimentation offered by the cores comprehends the whole morphological history of the reservoir. In the case of the Passaúna Reservoir, 30 years of sedimentation. This would mean that the modeller would have to model 30 years of sedimentation processes, since probably each year will be different from a hydrological and morphological point of view. Moreover, the data to feed up the model in order to simulate long periods will be difficult to gather and probably they would be also inaccurate. The sedimentation patterns coming from hydroacustic methods are a good source of information, only in the case that two bathymetries were measured: one measurement campaign at the beginning and one at the end of the modelled period. Knowing the two bathymetries, the difference between them will be a realiable approximation of the sedimentation volume.

Sediment traps are a good and low-cost alernative to measure the deposition rates in the reservoir. The deployment of several sediment traps combined with reliable rating curves provides an excelent basis for the calibration of the numerical model. However, sediment traps are not a good source to determine how much sediments are entering the reservoir in a defined period of time. The information they deliver, refers to how much sediment is reaching the trap. This could include eroded sediment from deposited layers upstream of the trap, which did not necessarily entered the reservoir in the studied time period.

The modelling of the hydrodynamics and suspended sediment transport in reservoirs represents a valuable tool to study those systems, not only for scientist but also for practitioners and engineers to support their decision making. Regarding the number of layers in the numerical model, not always the highest vertical resolution implies the best choice. The modeler should consider smaller resolutions, those may deliver similar results at lower computational costs. In this way, additional time resources will be gained to study further scenarios. In the case of the Passaúna Reservoir, the implementation of a 20-layered model for the hydrodynamics delivered a prediction of the temperatures in the reservoir, which were on average 0.01 $°C$ (averaged in time and in the vertical dimension) closer to the measured parameter than the 15-layered model. Nevertheless, the computer had to calculate one day longer to obtain such similar results.
The relevance of meteorological parameters collected near the water body and if possible above the water surface was evident over the course of the performed studies. Diverging wind speeds and directions could lead to a misprediction of the flow velocity, the thermal stratification and consequently of the mixing processes in the reservoir. The Background viscosity and diffusivity in vertical and horizontal directions introduced additional mixing which resulted in changes of 0.5 to 2.5 $°C$ in the averaged temperature profiles, accentuated at the bottom layers. In general, at the water intake the parameters affecting the most and the least the time averaged temperatures along the depth were the Dalton number and the Manning's coefficient respectively. Concerning the horizontal flow velocities, the user defined background vertical viscosity and the number of layers affected the most and the least the simulation results respectively. It is necessary to point out, that these affirmations

are valid for the studied range of the investigated parameters. The thermal stratification at the water intake could be well reproduced with a mean absolute error of 0.38 $°C$ (RMSE 0.48 $°C$) and the horizontal velocities at the same position were modeled with a value of 1.01 cm/s (RMSE 1.38 cm/s) for the same parameter. Similar magnitudes for the errors were reached within the framework of several studies regarding the three dimensional numerical modelling in reservoirs (Mi et al., 2020; Dissanayake et al., 2019; Soulignac et al., 2017; Chanudet et al., 2012b; Marti et al., 2011). The quality of the predictions of the temperature decreased towards the bottom of the reservoir, the opposite was true for the simulated horizontal velocities. At further positions in the reservoir like the Ferraria Bridge, the Side Arm Laggus (SAL) and Park, the model was able to predict the magnitudes and course of the measured temperatures. With the highest deviations being found at the Ferraria Bridge (MAE 0.9 $°C$) and the lowest at Park (MAE 0.36 $°C$). Analysing the thermal structure over all the water body, the highest vertical temperature gradients were present at the Dam.

The Passaúna Reservoir with its Buffer owns an special morphology, which can introduce changes in the temperature of the water reaching the main body of the reservoir (downstream from the Ferraria Bridge) when compared to the temperature at the main inflow. In the analysis of density currents, it was observed that the water gets warmer at this pre-bay, specially in the warm months. This requieres to consider the temperature of the water at the Ferraria Bridge and not at the main inflow, when studying the diffents flow paths caused by gravity driven flows. In the simulations, interflows prevailed over underflows and overflows werer rarely observed. The addition of a conservative tracer at the main inflow of the reservoir and by finding the position of the layer with the highest concentration at the intake the modelers can have a notion of which flow path was followed by the constituent from the inflow to the intake. In the present study this analysis showed the presence of constantly occurring overflows, in contrast to the results produced with the analysis of the simulated temperatures and matching the analysis based on the measurements. In general the Z-model depicted better the thermal stratification at the intake producing a MAE of 0.38 $°C$ in comparison to a MAE of 0.8 $°C$ when using the Sigma-model. The main discrepancies between the models are presented at the lower part of the water column where the Sigma-model presents artificial mixing and the temperatures are higher than for the Z-model. The distribution of the time averaged MAE over the depth for the Z-model remains fairly under 0.5 $°C$ over the whole depth. On the other hand, the Sigma-model even reaches the 1.8 $°C$ at the bottom part of the water column. For the upper 4 m, the predictions with the two layering-systems present almost the same quality. For the lower part the quality of the performance of the Z-model remains almost constant and for the Sigma-model the quality of the predictions becomes poorer towards the bottom, probably due to the artificial mixing introduced by this layering system. The exclusion of wind in the simulations led to different thermal structures of the resevoir which were more notorious at the water surface than at the bottom, with differences in the calculated temperatures ranging from 1.2 to 3 $°C$ at the intake. This can be explained by the changes in the evaporative and wind driven convection fluxes, since those fluxes are a function of the wind speed at 10 m above the water surface. The differences propagated all over the water column. The discrepancies in the temperature of both scenarios were more accentuated at deeper than at shallow locations over the reservoir's area. The flow velocities, were higher for the scenario without wind in comparison to the case with wind inclusion at deep lacustrine positions like the intake. The mean horizontal flow velocities for the simulation with wind were 2.19, 1.39 and 0.95 cm/s at the surface, middle and bottom layers in contrast to 0.73, 0.5 and 0.38 cm/s for the same layers in the simuation without wind. On the other hand, for shallower regions, e.g. at the Buffer the flow velocities were slightly higher for the case with no wind. Nevertheless, the oscillations in the flow velocity were higher for the simulation with wind at all positions. This means, than the wind should be considered as an important factor contributing to the magnitude of the turbulent kinetic energy in reservoirs. These results should remind the modellers, how immportant the wind can be for the simulation of the hydrodynamics in reservoirs. Hence, it should be considered when settling a numerical model, specially for a low flow velocities system like the Passaúna Reservoir.

The simulation of the SSCs and deposition rates could match the measurements performed on the field. Two sediments groups in the cohesive particles range were defined with settling veloities of 0.05 and 0.02 mm/s. These settling velocities correspond to particles with diameters of 13.6 and 6.6 μm respectively. The calibration of the morphological model highlights the importance of a reliable rating curve, preferably constructed based on ground truth data. It is also important to evaluate the incoming SSCs through several tributaries and not only through the main one, performing field measurements. Considering just the subcatchment area as the only key parameter for the amount of sediments a tributary is delivering can lead to sub/overestimation of the sediment budget.

The inclusion and exclusion of wind conducted to divergent sedimentation patterns between the simulations. The total deposited volume was 8.3 % lower in the case with wind than in the simulation without it. The zones of maximum deposition were in different locations for both scenarios. The suspended sediments in the water column could reach further downstream regions in the reservoir in the presence of wind. The inclusion of this forcing produced higher bed shear stresses not only at shallow locations but also at positions as deep as at the bottom of the water withdrawal. According to the results presented here, it is advised to set up the numerical model considering wind as a forcing. It introduces turbulent kinetic energy to the system, which is transfered to the whole water column and the transport of constituents (conservative tracers, heat and suspended particles) will be affected by its inclusion. The inclusion of temperature in the numerical model resulted in lower deposited sediment volume than for the scenario without its consideration: in total, 11 % less deposited sediments. The resulting sedimentation patterns were considerably different for the two analyzed scenarios, with the suspended sediments reaching much further downstream in comparison to the simulation with just wind and no temperature. The time averaged SSCs depth-profiles presented higher magnitudes for the simulation with temperature inclusion. At the intake for example, the time averaged SSCs were ten times higher for the simulation with temperature than for the other case. Moreover, the gradients between the highest and lowest SSC when considering vertical profiles were more pronounced for the scenario with temperaure. Both the bed shear stresses and the depth averaged velocities were higher for the simulation with temperature inclusion. The presence of underflows and overflows, i.e. density currents induced by temperature changed the shape of the SSCs-profiles: the highest suspended SSCs being transported through the same path in the vertical dimension as the conservative tracer. The inclusion of temperature resulted in higher advective and dispersive transport in comparison to the scenario with just wind. The advective transport showed higher changes than the dispersive one when comparing the two scenarios. The influence of temperature in the suspended sediment transport has been underestimated, probably due to the high additional effort to calibrate the thermal structure of the reservoir, in the first place. Since this implies the gathering of meteorological data and temperatures for the tributaries, information that is not be necessary when not modelling temperature. Nevertheless, as shown in the present study, gravity currents driven by temperature can redefine the transport path of the suspended sediments and hence change the shape and the magnitudes of the concentration profiles. In low flow velocity systems like the Passaúna Reservoir (flow velocities in the order of magnitude of 2 cm/s), wind and temperature were shown to play an important role in the morphological changes in the water body. The selection of a Sigma- or Z-layered model will have an impact on the deposited sediment volume and on the sedimentation patterns. When modelling sediment transport, the selection of a Z-model would only make sense if the thermal structure of the water column should be modeled. A test with both model configurations is advised and the selection of the layering system should be done based on field measurements. An advantage of the Z-model over the Sigma-model is the much lower computational time. Due to its structure a Sigma-model posses the same number of layers at all positions in the reservoir, meanwhile the Z-model will have less layers, depending on the water depth and bathymetrie of the water body.

The employment of data in different temporal resolution and from different sources to feed up the model, produced differences in the simulation results. They were the most notorious for the usage of meteorological reanalysis data from ERA5 in the predictions of the temperatures and horizontal flow velocities. In the case of the suspended sediment transport the largest differences were found while using the rating curve derived from the erosion catchment modelling data. In solving the matter of which temporal resolution/ data source is adequate to get realiable model results, the context of each project matters. For example using ERA5 data for the wind characterization resulted in a deposition volume of 1.3 % higher than when using the data of the nearest meteorological station and in a MAE for the simulated temperature which is 1.6 $°C$ worst than for the original simulation. Those differences will have to be put in context by the modeller. Weighing up if the mentioned differences are acceptable according to the aim of the study.

According to the literature studies within the framework of this dissertation, the influence of wind and temperature on the suspended sediment transport needs to be further investigated both in the field and through numerical modelling. Additional aspects that should be studied would be the influence of the wind in resuspension processes of the sediments at the bottom of a reservoir/lake which have not been long consolidated and hence present low critical bed shear stresses for erosion. Regarding the inclusion of temperature, this could also affect in some measure the settling velocities of the sediment particles. The settling velocity is in fact a function of the kinematic viscosity of the water (among other factors). At the same time the kinematic viscosity is a function of the water temperature. It could be evaluated, which changes are produced in the settling velocities within the range of the temperatures present in the water column for stratified conditions.

Bibliography

(2022). *GraviProbe Rheology version GP-R01.* Ocean nautical innnovations, Belgium.

Ahlfeld, D., Joaquin, A., Tobiason, J., and Mas, D. (2003). Case study: Impact of reservoir stratification on interflow travel time. *Journal of Hydraulic Engineering*, 129:966–975.

Akalin, S. (2002). *Water temperature effect on sand transport by size fraction in the Lower Mississippi River.* PhD thesis, Colorado State University.

Annandale, G. W., Morris, G. L., and Karki, P. (2016). *Extending the life of reservoirs sustainable sediment management for dams and run-of-river hydropower.* World Bank Group.

BAČA, P. (2008). Hysteresis effect in suspended sediment concentration in the rybárik basin, slovakia / effet d'hystérèse dans la concentration des sédiments en suspension dans le bassin versant de rybárik (slovaquie). *Hydrological Sciences Journal*, 53(1):224–235.

Bell, B., Hersbach, H., Simmons, A., Berrisford, P., Dahlgren, P., Horányi, A., Muñoz-Sabater, J., Nicolas, J., Radu, R., Schepers, D., Soci, C., Villaume, S., Bidlot, J.-R., Haimberger, L., Woollen, J., Buontempo, C., and Thépaut, J.-N. (2021). The era5 global reanalysis: Preliminary extension to 1950. *Quarterly Journal of the Royal Meteorological Society*, 147(741):4186–4227.

Bergen, e. a. (1999). *Numerische Modelle von Flüssen, Seen und Küstengewässern.* Deutscher Verband für Wasserwirtschaft und Kulturbau e.V. (DVWK).

Boegman, L. (2009). Currents in stratified water bodies 2: Internal waves. *Encyclopedia of Inland Waters*, 1:539–558.

Bogucki, D. J., Jones, B. H., and Carr, M.-E. (2005). Remote measurements of horizontal eddy diffusivity. *Journal of Atmospheric and Oceanic Technology*, 22(9):1373–1380.

Burchard, H. and Baumert, H. (1995). On the performance of a mixed-layer model based on the k-epsilon closure. *Journal of Geophysical Research - Oceans.*

Carneiro, C., Kelderman, P., and Irvine, K. (2016). Assessment of phosphorus sediment–water exchange through water and mass budget in Passaúna Reservoir (Paraná State, Brazil). *Environmental Earth Sciences*, 75(7):564.

Chai, T. and Draxler, R. R. (2014). Root mean square error (rmse) or mean absolute error (mae)? – arguments against avoiding rmse in the literature. *Geoscientific Model Development Discussions*, 7(3):1247–1250.

Chanudet, V., Fabre, V., and [van der Kaaij], T. (2012a). Application of a three-dimensional hydrodynamic model to the nam theun 2 reservoir (lao pdr). *Journal of Great Lakes Research*, 38(2):260 – 269.

Chanudet, V., Fabre, V., and van der Kaaij, T. (2012b). Application of a three-dimensional hydrodynamic model to the Nam Theun 2 Reservoir (Lao PDR). *Journal of Great Lakes Research*, 38(2):260–269.

Chow, V. T. (1959). *Open-channel hydraulics.* McGraw-Hill, New York, USA.

Constantin, A. (2006). The trajectories of particles in stokes waves. *Inventiones mathematicae*, 166(3):523–535.

Cuthbertson, A., Dong, P., King, S., and Davies, P. (2008). Hindered settling velocity of cohesive/non-cohesive sediment mixtures. *Coastal Engineering*, 55:1197–1208.

Deltares (2014). *Delft3D-FLOW Simulation of multi-dimensional hydrodynamic flows and transport phenomena, including sediments.*

Dey, S. (2014). *Fluvial hydrodynamics*, volume 818. Springer.

DIN19661-2 (2000). Deutsche norm: Richtlinie für wasserbauwerke -sohlenbauwerke.

Dissanayake, P., Hofmann, H., and Peeters, F. (2019). Comparison of results from two 3D hydrodynamic models with field data: Internal seiches and horizontal currents. *Inland waters*, 9(2):239–260.

Eadie, B. J. (1997). Probing particle processes in lake michigan using sediment traps. *Water, Air and Soil Pollution*, 99(1-4):133–139. Copyright - Kluwer Academic Publishers 1997.

Eckart, C. (1958a). Properties of water, part ii. the equation of state of water and sea water at low temperatures and pressures. *American Journal of Science*, 256:225–240.

Eckart, C. H. (1958b). The equation of state of water and sea water at low temperatures and pressures, part 2 of properties of water. *American Journal of Science*, 256(4):225–240.

Elci, S. (2008). Effect of thermal stratification and mixing on reservoir water quality. *Limnology*, 9:135–142.

Feng, Z., Tan, G., Xia, J., Shu, C., Chen, P., and Yi, R. (2020). Two-dimensional numerical simulation of sediment transport using improved critical shear stress methods. *International Journal of Sediment Research*, 35(1):15–26.

Fierro, P. and Nyer, E. (2007). *The Water Encyclopedia: Hydrologic Data and Internet Resources.* CRC Press.

Geernaert, G. L., Davidson, K. L., Larsen, S. E., and Mikkelsen, T. (1988). Wind stress measurements during the tower ocean wave and radar dependence experiment. *Journal of Geophysical Research: Oceans*, 93(C11):13913–13923.

GHASEMLOUNİA, R. and KABDAŞLI, S. (2021). Numerical study on suspended sediment transport under the effect of water temperature in reservoirs and lakes. *Academic Platform-Journal of Engineering and Science*, 9(3):415–426.

Gill, A. E. and Adrian, E. (1982). *Atmosphere-ocean dynamics*, volume 30. Academic press.

Gonzalez, W., Delfes Varela, D. M., and Seidel, F. (2021). Study on the complexity reduction of the input data for 3d numerical modeling of the hydrodynamics and sediment transport in a brazilian reservoir. In *vEGU21*.

Gonzalez, W., Klassen, I., Seidel, F., and Franca, M. J. (2022). Numerical modelling of the suspended sediment transport in a reservoir under the influence of wind and temperature. In *Proceedings of the 39th IAHR World Congress (Granada, 2022)*.

Haag, I. and Luce, A. (2008). The integrated water balance and water temperature model LARSIM-WT. *Hydrological Processes: An International Journal*, 22(7):1046–1056.

Harcourt-Baldwin, J. and Diedericks, G. (2006). Numerical modelling and analysis of temperature controlled density currents in tomales bay, california. *Estuarine, Coastal and Shelf Science*, 66(3):417–428.

Haun, S., Kjærås, H., Løvfall, S., and Olsen, N. R. B. (2013). Three-dimensional measurements and numerical modelling of suspended sediments in a hydropower reservoir. *Journal of Hydrology*, 479:180 – 188.

Hillebrand, G. (2008). *Transportverhalten kohaesiver Sedimente inturbulenten Stroemungen – Untersuchungen imoffenen Kreisgerinne*. PhD thesis, Universitaet Fridericiana zu Karlsruhe (TH).

Hillebrand, G., Klassen, I., and Olsen, N. (2016). 3d cfd modelling of velocities and sediment transport in the iffezheim hydropower reservoir. *Hydrology Research*.

Hirsch, R. M. (2012). Flux of nitrogen, phosphorus, and suspended sediment from the susquehanna river basin to the chesapeake bay during tropical storm lee, september 2011, as an indicator of the effects of reservoir sedimentation on water quality. *Scientific Investigations Report*.

Horowitz, A. J., Clarke, R. T., and Merten, G. H. (2015). The effects of sample scheduling and sample numbers on estimates of the annual fluxes of suspended sediment in fluvial systems. *Hydrological Processes*, 29(4):531–543.

Horowitz, J. (2002). The use of rating (transport) curves to predict suspended sediment concentration: a matter of temporal resolution. In *Turbidity and other sediment surrogates workshop*.

Hu, X., Zhang, L., and Zhang, H. (2018). Vortex cascade and dissipation features of turbulent flow in hydro-turbine blade passage. *Shuili Fadian Xuebao/Journal of Hydroelectric Engineering*, 37:1–7.

ICOLD (2009). Sedimentation and sustainable use of reservoirs and river systems. draft bulletin 147. Technical report, International Commission on Large Dams, Paris, France.

ICOLD (2019). General synthesis. In *International Commission on Large Dams: World register of dams.*

Imberger, J. and Patterson, J. C. (1989). Physical limnology. *Advances in applied mechanics*, 27:303–475.

Imboden, D. M. and Wuest, A. (1995). *Physics and Chemistry of Lakes*, chapter 4. Mixing Mechanisms in lakes, pages 83–138. Springer Verlag.

InMeteo (2019). Ventusky. `http://www.ventusky.com/`. Accessed: 2019-06-15.

Ishikawa, M., Bleninger, T., and Lorke, A. (2021). Hydrodynamics and mixing mechanisms in a subtropical reservoir. *Inland Waters*, 11.

Ishikawa, M., Gonzalez Otero, W., Golyjeswski, O., Sales, G., Rigotti, J., Bleninger, T., Mannich, M., and Lorke, A. (2022). Effects of dimensionality on the performance of hydrodynamic models for stratified lakes and reservoirs. *Geoscientific Model Development*, 15:2197–2220.

Jenzer Althaus, J. M., Cesare, G. D., and Schleiss, A. J. (2015). Sediment evacuation from reservoirs through intakes by jet-induced flow. *Journal of Hydraulic Engineering*, 141(2):04014078.

Johnson, B. H. (1981). A review of numerical reservoir hydrodynamic modeling. Technical report, U.S. Army Engineer Waterways Experiment Station. http://hdl.handle.net/11681/4503.

Juez, C., Hassan, M., and Franca, M. (2018). The origin of fine sediment determines the observations of suspended sediment fluxes under unsteady flow conditions: The origin of fine sediment and suspended sediment fluxes. *Water Resources Research*, 54.

Köhler, K. (2010). *Simultanes Emulgieren und Mischen.* PhD thesis, Karlsruher Institut für Technologie.

Kirillin, G. and Shatwell, T. (2016). Generalized scaling of seasonal thermal stratification in lakes. *Earth-Science Reviews*, 161:179–190.

Klassen, I. (2017). *Three-dimensional Numerical Modeling of CohesiveSediment Flocculation Processes in Turbulent Flows.* PhD thesis, Karlsruher Institut für Technologie.

Komar, P. D. and Cui, B. (1984). The analysis of grain-size measurements by sieving and settling-tube techniques. *Journal of sedimentary research*, 54(2):603–614.

Lai, Y. and Wu, K. (2019). A three-dimensional flow and sediment transport model for free-surface open channel flows on unstructured flexible meshes. *Fluids*, 4:18.

Lane, A. (1989). The heat balance of the North Sea. Technical Report Report N° 8, Bidston Observatory, Birkenhead, UK.

Lara, J. and Pemberton, E. (1963). Initial unit weight of deposited sediments. In *Proc. Federal Interagency Sedimentation Conf.*

Laurien, E. and Oertel, H. (2013). *Numerische Strömungsmechanik Grundgleichungen und Modelle –Lösungsmethoden – Qualität und Genauigkeit.* Springer Vieweg.

Lee, S., Moon, J.-W., and Moon, H.-S. (2004). Heavy metals in the bed and suspended sediments of anyang river, korea: Implications for water quality. *Environmental geochemistry and health*, 25:433–52.

Lin, S., Boegman, L., and Rao, Y. (2021). Characterizing spatial and temporal distributions of turbulent mixing and dissipation in lake erie. *Journal of Great Lakes Research*, 47(1):168–179.

MacIntyre, S., Flynn, K. M., Jellison, R., and Romero, J. R. (1999). Boundary mixing and nutrient fluxes in mono lake, california. *Limnology and Oceanography*, 44(3):512–529.

Mahmood, K. (1987). Reservoir sedimentation : impact, extent, and mitigation (english). Technical report, Washington, D.C.

Malcherek, A. (2001). *Hydromechanik der Fliessgewässer.* Hannover: Institut für Strömungsmechanik und Elektronisches Rechnen im Bauwesen.

Marti, C. L., Mills, R., and Imberger, J. (2011). Pathways of multiple inflows into a stratified reservoir: Thomson reservoir, australia. *Advances in Water Resources*, 34(5):551–561.

Mehta, A. J. and Lee, S.-C. (1994). Problems in linking the threshold condition for the transport of cohesionless and cohesive sediment grain. *Journal of Coastal Research*, 10(1):170–177.

Mi, C., Shatwell, T., Ma, J., Xu, Y., Su, F., and Rinke, K. (2020). Ensemble warming projections in germany's largest drinking water reservoir and potential adaptation strategies. *Science of The Total Environment*, 748:141366.

Milano, M., Reynard, E., Muniz-Miranda, G., and Guerrin, J. (2018). Water supply basins of São Paulo metropolitan region: hydro-climatic characteristics of the 2013–2015 water crisis. *Water*, 10(11):1517.

MME (2013). Brazilian energy balance 2013. Technical report, Ministry of Mines and Energy.

Monismith, S. and MacIntyre, S. (2009). The surface mixed layer in lakes and reservoirs. In Likens, G. E., editor, *Biogeochemistry of inland waters*, pages 636–650. Academic Press, Millbrook, New York, USA.

Morris, G. L. and Fan, J. (1998). *Reservoir Sedimentation Handbook: Design and Management of Dams, Reservoirs and Watersheds for Sustainable Use.* New York: McGraw-Hill.

MuDak-WRM (2019). Multidisciplinary data acquisition as the key for a globally applicable water resource management(mudak-wrm). Online: https://www.mudak-wrm.kit.edu/.

MuDak-WRM (2021). Multidisciplinary data acquisitionas the key for a globally applicable waterresource management - final report. Technical report, Karlsruhe Institute of Technology.

Murakami, M., Oonishi, Y., and Kunishi, H. (1985). A numerical simulation of the distribution of water temperature and salinity in the Seto Inland Sea. *Journal of the oceanographical society of Japan*, 41(4):213–224.

Murali, M. K., Hipsey, M. R., Ghadouani, A., and Yuan, Z. (2020). Sewersedfoam: A model for free surface flow, sediment transport, and deposited bed morphology in sewers. *Water*, 12(1).

Musall, M. (2011). *Mehrdimensionale hydrodynamisch-numerische Modelle im praxisorientierten und operationellen Einsatz.* PhD thesis, Karlsruher Institut für Technologie.

OECD (2015). *Governança dos Recursos Hídricos no Brasil.* OECD Publishing, Paris, France.

Omer, A. Y. A., Ali, Y. S. A., Roelvink, J. A., Dastgheib, A., Paron, P., and Crosato, A. (2015). Modelling of sedimentation processes inside roseiresreservoir (sudan). *Earth Surface Dynamics*, 3(2):223–238.

Ono, G. (2020). Monitoramento e analise da sedimentacao no reservatorio passauna-pr. Master's thesis, Universidade Federal do Parana, Curitiba, Brazil.

Partheniades, E. (1965). Erosion and deposition of cohesive soils. *Journal of the Hydraulics Division*, 91(1):105–139.

Peeters, F., Wüest, A., Piepke, G., and Imboden, D. M. (1996). Horizontal mixing in lakes. *Journal of Geophysical Research: Oceans*, 101(C8):18361–18375.

Platzek, F. W., Stelling, G. S., Jankowski, J. A., and Pietrzak, J. D. (2014). Accurate vertical profiles of turbulent flow in z-layer models. *Water Resources Research*, 50(3):2191–2211.

Polli, B. (2017). *Modeling of heat transport in lakes: spatial and temporal characterization.* PhD thesis, Federal University of Parana.

Polli, B. and Bleninger, T. (2019a). Comparison of 1d and 3d reservoir heat transport models and temperature effects on mass transport.

Polli, B. A. and Bleninger, T. (2019b). Comparison of 1D and 3D reservoir heat transport models and temperature effects on mass transport. *RBRH*, 24.

Postma, L., G. and Boon, J. (1999). Three-dimensional water quality and hydrodynamic modelling in hong kong. stratification and water quality. In *Proceedings of the 2nd international Symp. on Environmental hydraulics, Hong Kong.*

Raudkivi, A. J. (2020). *Loose boundary hydraulics.* CRC Press.

Rauen, W., Castro, C., and da Silva, M. (2017). Caracterização hidrossedimentológica do riopassauna, pr, brasil, a partir de dados históricos. In *XX Simpósio Brasileiro de Recursos Hídricos,Associação Brasileira De Recursos Hídricos*.

Read, J. S., Hamilton, D. P., Jones, I. D., Muraoka, K., Winslow, L. A., Kroiss, R., Wu, C. H., and Gaiser, E. (2011). Derivation of lake mixing and stratification indices from high-resolution lake buoy data. *Environmental Modelling & Software*, 26(11):1325–1336.

Robertson, D. M. and Imberger, J. (1994). Lake number, a quantitative indicator of mixing used to estimate changes in dissolved oxygen. *Internationale Revue der gesamten Hydrobiologie und Hydrographie*, 79(2):159–176.

SANEPAR Companhia de Saneamento do Paraná (2013). Plano Diretor SAIC: Sistema de Abastecimento de Água Integrado de Curitiba e Região Metropolitana. Technical report, Proensi.

Saunitti, R. M., Fernandes, L. A., and Bittencourt, A. (2004). Estudo do assoreamento do reservatÓrio da barragem do rio passaÚna - curitiba - pr. *Boletim Paranaense de Geociências*, 54(0).

Schiebe, F. R., Ritchie, J. C., and Mchenry, J. R. (1975). Influence of suspended sediment on the temperatures of surface waters of reservoirs. *SIL Proceedings, 1922-2010*, 19(1):133–136.

Schillereff, D. N. (2015a). 3.7. 1. a review of in situ measurement techniques for investigating suspended sediment dynamics in lakes.

Schillereff, D. N. (2015b). *Lake sediment records of flood frequency and magnitude*. PhD thesis.

Schleiss, A. J., Cesare, G. D., Franca, M. J., and Pfister, M., editors (2014). *Reservoir Sedimentation: River Flow 2014*.

Selge, F. and Gunkel, G. (2013). Water reservoirs: worldwide distribution, morphometric characteristics and thermal stratification processes. In Gunkel, G., da Silva, J. A. A., and Sobral, M. C., editors, *Sustainable Management of Water and Land in Semiarid Areas*. Editora Universitária UFPE, Recife-PE, Brasil.

Sheng, Y. P. and Lick, W. (1979). The transport and resuspension of sediments in a shallow lake. *Journal of Geophysical Research: Oceans*, 84(C4):1809–1826.

Shi, B., Wang, Y. P., Yang, Y., Li, M., Li, P., Ni, W., and Gao, J. (2015). Determination of critical shear stresses for erosion and deposition based on in situ measurements of currents and waves over an intertidal mudflat. *Journal of Coastal Research*, 31:1344–1356.

Sidagis Galli, C. and Abe, D. (2010). *Disponibilidade, poluição e eutrofização das águas.*, pages 165–174.

Simon, A., Kocsis, O., Stips, A., and Wuest, A. (2002). Momentum and turbulent kinetic energy balance in the surface boundary layer of developing waves. Unplished data.

Smith, S. and Banke, E. (1975). Variation of the sea surface drag coefficient with wind speed. *Quarterly Journal of the Royal Meteorological Society*, 101(429):665–673.

Sotiri, K. (2020). *Integrated Sediment Yield and Stock Assessment for the Passaúna Reservoir, Brazil.* PhD thesis, Karlsruher Institut für Technologie (KIT).

Sotiri, K., Hilgert, S., and Fuchs, S. (2019). Sediment classification in a Brazilian reservoir: Pros and cons of parametric low frequencies. *Advances in Oceanography and Limnology*, 10(1).

Soulignac, F., Vinçon-Leite, B., Lemaire, B., Martins, J. R., Bonhomme, C., Dubois, P., Mezemate, Y., Tchiguirinskaia, I., Schertzer, D., and Tassin, B. (2017). Performance assessment of a 3d hydrodynamic model using high temporal resolution measurements in a shallow urban lake. *Environmental Modeling & Assessment*, 22:1–14.

Stokes, G. G. (2009). *On the Effect of the Internal Friction of Fluids on the Motion of Pendulums*, volume 3 of *Cambridge Library Collection - Mathematics*, page 1–10. Cambridge University Press.

Taveira-Pinto, F., Lameiro, L., Moreira, A., Carvalho, E., and Figueiredo, N. (2014). Global analysis of the sedimentation volume on portuguese reservoirs.

UNESCO (1981). Tenth report of the joint panel on oceanographictables and standards. Technical Report 36, UNESCO.

Unesco, Ices and SCOR, IAPSO (1981). Background papers and supporting data on the international equation of state of seawater 1980.

Urban, N. R., Lu, X., Chai, Y., and Apul, D. S. (2004). Sediment trap studies in lake superior: Insights into resuspension, cross-margin transport, and carbon cycling. *Journal of Great Lakes Research*, 30:147–161. Exploring Superior.

van Rijn, L. (1993). *Principles of Sediment Transport in Rivers, Estuaries and Coastal Seas.* Number Teil 1 in Principles of Sediment Transport in Rivers, Estuaries, and Coastal Seas. Aqua Publications.

Varela, D. (2020). Complexity reduction of three-dimensional numerical modelling of the hydrodynamics and sediment transport in water reservoirs considering the heat transport. study case: Passaúna resevoir in brazil. Master's thesis, Karlsruhe Insttitute of Technology.

Vercruysse, K., Grabowski, R. C., and Rickson, R. (2017). Suspended sediment transport dynamics in rivers: Multi-scale drivers of temporal variation. *Earth-Science Reviews*, 166:38–52.

Verstraeten, G. and Poesen, J. (2001). Variability of dry sediment bulk density between and within retention ponds and its impact on the calculation of sediment yield. *Earth Surface Processes and Landforms*, 26:375 – 394.

Wagner, A. (2020). *Event-Based Measurement and Mean Annual Flux Assessment of Suspended Sediment in Meso Scale Catchments.* PhD thesis, Karlsruher Institut für Technologie (KIT).

Wahl, B. and Peeters, F. (2014). Effect of climatic changes on stratification and deep-water renewal in Lake Constance assessed by sensitivity studies with a 3D hydrodynamic model. *Limnology and oceanography*, 59(3):1035–1052.

Wang, H., Kaisam, J. P., Liang, D., Deng, Y., and Shen, Y. (2020a). Wind impacts on suspended sediment transport in the largest freshwater lake of China. *Hydrology Research*, 51(4):815–832.

Wang, X., Zhang, H., Bertone, E., Stewart, R., and O'Halloran, K. (2020b). Numerical study of the hydrodynamic and sediment transport process in a subtropical water reservoir: the impacts of storms and winds. *Environmental Modeling and Assessment*, 25.

Weber, M. (2017). *Optimizing withdrawal from drinking water reservoirs to combine downstream river demands with a sustainable raw water management.* PhD thesis, Universität Koblenz-Landau.

Wetzel, R. (2001). *Limnology.* Saunders College Publishing, Philadelphia, 3rd edition.

Wiberg, P. L., Hornberger, G. M., Raffensperger, J. P., and D'Odorico, P. (2014). *Elements of physical hydrology.* Johns Hopkins University Press.

Winterwerp, J. (2007). On the sedimentation rate of cohesive sediment. In *INTERCOH 2003: 7th International Conference*, pages 209–226. Elsevier.

Winterwerp, J. and Van Kesteren, W. (2004). *Introduction to the Physics of Cohesive Sediment Dynamics in the Marine Environment.* ELSEVIER.

Winterwerp, J., Van Kesteren, W., Van Prooijen, B., and Jacobs, W. (2012). A conceptual framework for shear flow–induced erosion of soft cohesive sediment beds. *Journal of Geophysical Research: Oceans*, 117(C10).

Wosiacki, L. (2020). *Surrogate technologies for suspended solid dynamics assessment in surface waters.* PhD thesis, Universidade Federal do Paraná.

Wright, D. G. (1997). An equation of state for use in ocean models: Eckart's formula revisited. *Journal of atmospheric and oceanic technology.*

Wu, J. (1982). Wind-stress coefficients over sea surface from breeze to hurricane. *Journal of Geophysical Research: Oceans*, 87(C12):9704–9706.

Wu, W., Perera, C., Smith, J., and Sanchez, A. (2018). Critical shear stress for erosion of sand and mud mixtures. *Journal of Hydraulic Research*, 56(1):96–110.

Wuest, A. and Lorke, A. (2003). Small-scale hydrodynamics in lakes. *Annual Review of Fluid Mechanics*, 35:373–412.

Wüest, A. and Lorke, A. (2003). Small-scale hydrodynamics in lakes. *Annual Review of fluid mechanics*, 35(1):373–412.

Wuest, A. and Lorke, A. (2009). *Small-Scale Turbulence and Mixing: Energy Fluxes in Stratified Lakes*, volume 1, pages 628–635.

Wuest, A., Piepke, G., and Senden, D. (1388). Turbulent kinetic energy balance as a tool for estimating vertical diffusivity in wind-forced stratified waters. *Limnol. Oceanogr. American Society of Limnology and Oceanography*, 45:1388–1400.

Wunderlich, W. (1971). *The Dynamics of Density-stratified Reservoirs.* Tennessee Valley Authority, Division of Water Control Planning, Engineering Laboratory.

Xavier, C., Neiva, L., and Brunkow, R. (2017). Qualidade das águas dos reservatórios do estado do Paraná. Technical report, Governo do estado do Paraná, Secretaria de estado do meio ambiente e recursos hídricos, IAP – Instituto Ambiental do Paraná.

Xu, Y. (1998). *Numerical Modelling of Suspended Sediment Transport in Rivers.* PhD thesis, Institut für Wasserbau der Universität Stuttgart.

Yelland, M., Moat, B., Taylor, P., Pascal, R., Hutchings, J., and Cornell, V. (1998). Wind stress measurements from the open ocean corrected for airflow distortion by the ship. *Journal of Physical Oceanography*, 28:1511–1526.

Zamani, B. and Koch, M. (2020). Comparison between two hydrodynamic models in simulating physical processes of a reservoir with complex morphology: Maroon reservoir. *Water*, 12(3).

Zanke, U. (1982). *Grundlage der Sedimentbewegung.* Springer-Verlag.

Zarfl, C., Lumsdon, A. E., Berlekamp, J., Tydecks, L., and Tockner, K. (2015). A global boom in hydropower dam construction. *Aquatic Sciences*, 77(1):161–170.

Zhang, F., Zhang, H., Bertone, E., Stewart, R., Lemckert, C., and Cinque, K. (2020). Numerical study of the thermal structure of a stratified temperate monomictic drinking water reservoir. *Journal of Hydrology: Regional Studies*, 30:100699.

Zhang, R. and Wu, B. (2019). Environmental impacts of high water turbidityof the niulan river to dianchi lake water diversion project. *Journal of Environmental Engineering.*

Zhiyin, Y. (2015). Large-eddy simulation: Past, present and the future. *Chinese Journal of Aeronautics*, 28(1):11 – 24.

Zhong, Y., Qiao, L., Song, D., Ding, Y., Xu, J., Xue, W., and Xue, C. (2020). Impact of cold water mass on suspended sediment transport in the south yellow sea. *Marine Geology*, 428:106244.

Zhu, Q., Van Prooijen, B., Wang, Z., Ma, Y., and Yang, S. (2016). Bed shear stress estimation on an open intertidal flat using in situ measurements. *Estuarine, Coastal and Shelf Science*, 182:190–201.

Zhu, Y., Yang, J., Hao, J., and Shen, H. (2009). Numerical simulation of hydrodynamic characteristics and water quality in Yangchenghu Lake. In *Advances in Water Resources and Hydraulic Engineering*, pages 710–715. Springer.

A. Appendix

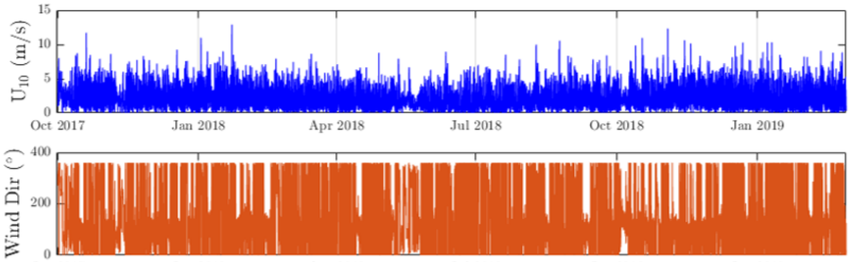

Figure A.1.: Wind speed and direction at the meteorological station TECPAR for the period August 2017 - February 2019.

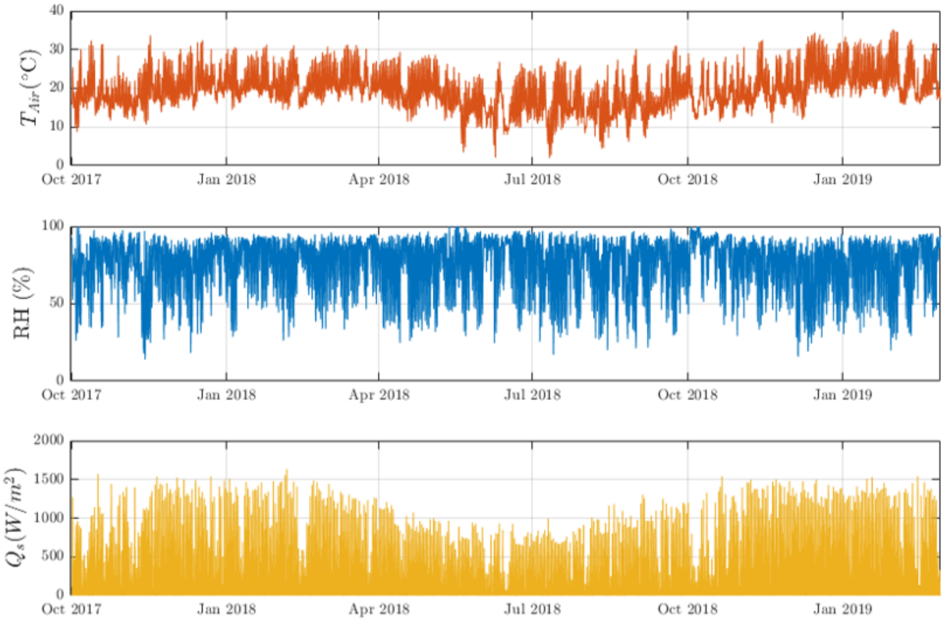

Figure A.2.: Air temperature, relative air humidity and solar radiation at the meteorological station TECPAR for the period August 2017 - February 2019.

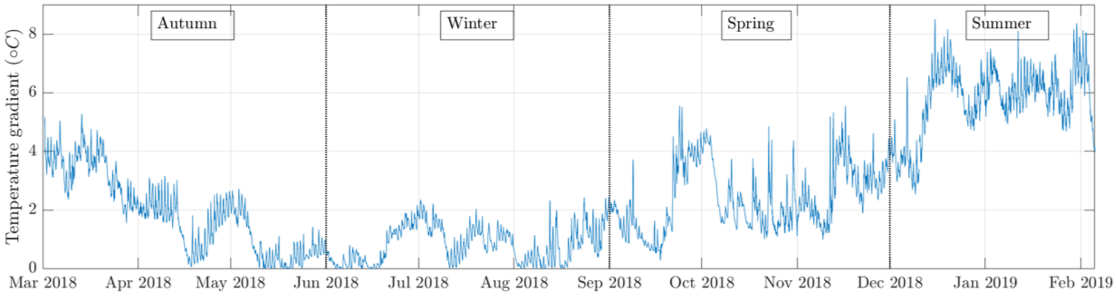

Figure A.3.: Temperature gradient between the thermistors at the surface and bottom at the intake position.

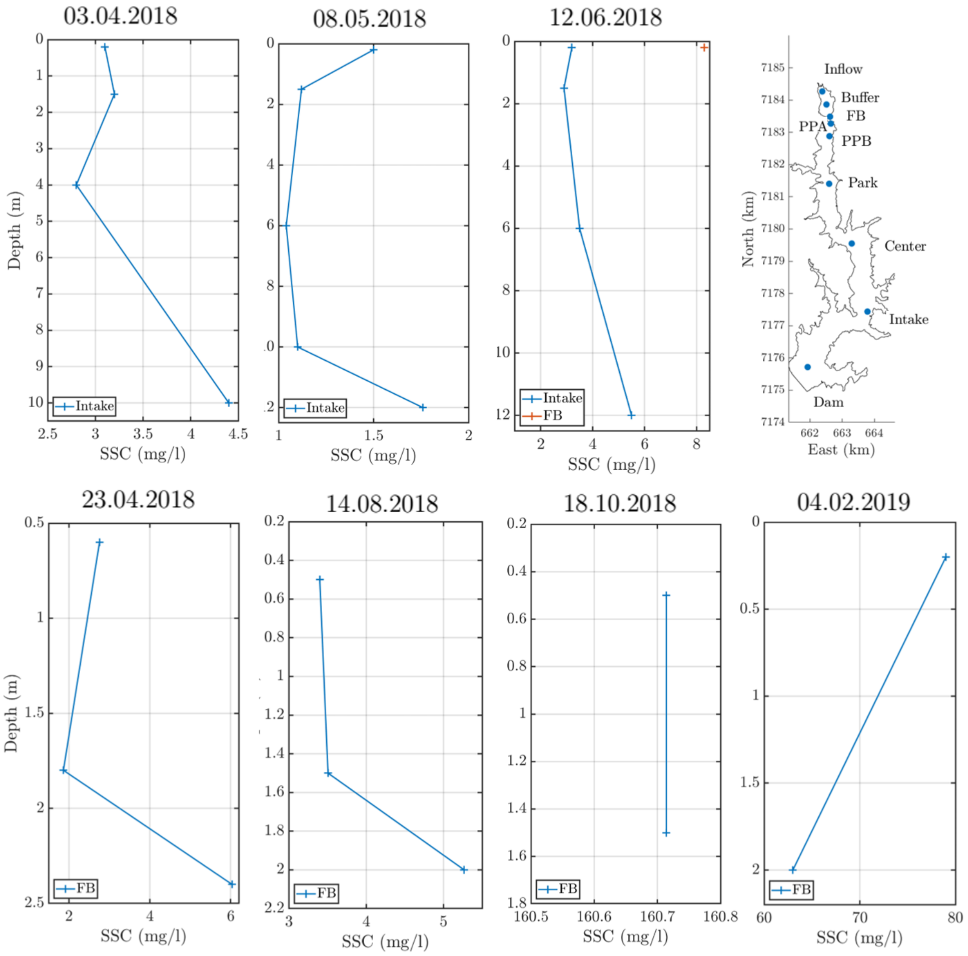

Figure A.4.: Measured SSC-profiles at the Passaúna Reservoir for the indicated dates.

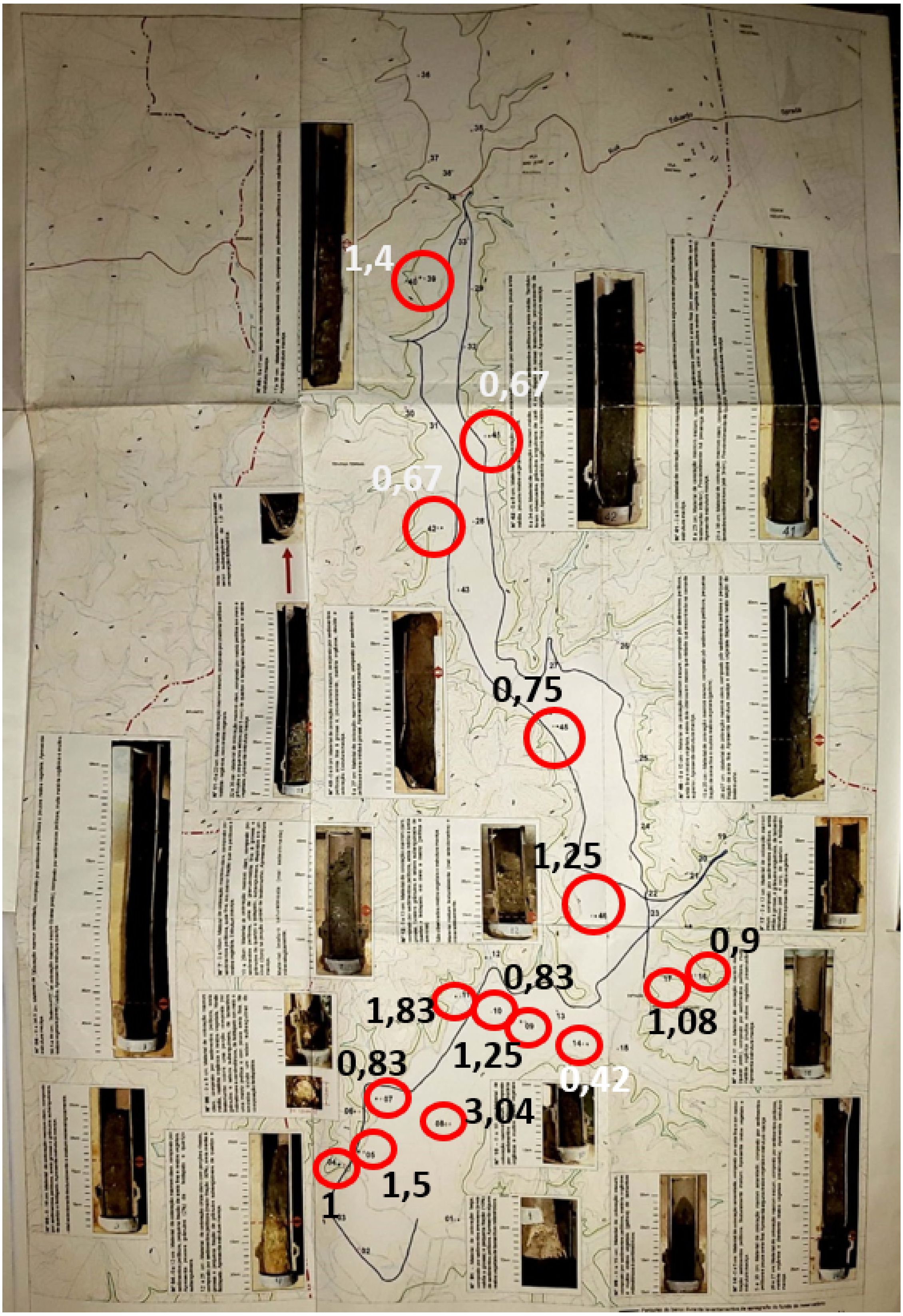

Figure A.5.: Position of the cores and sedimentation rates in cm/year (numbers in the figure) (adapted from Saunitti et al. 2004).

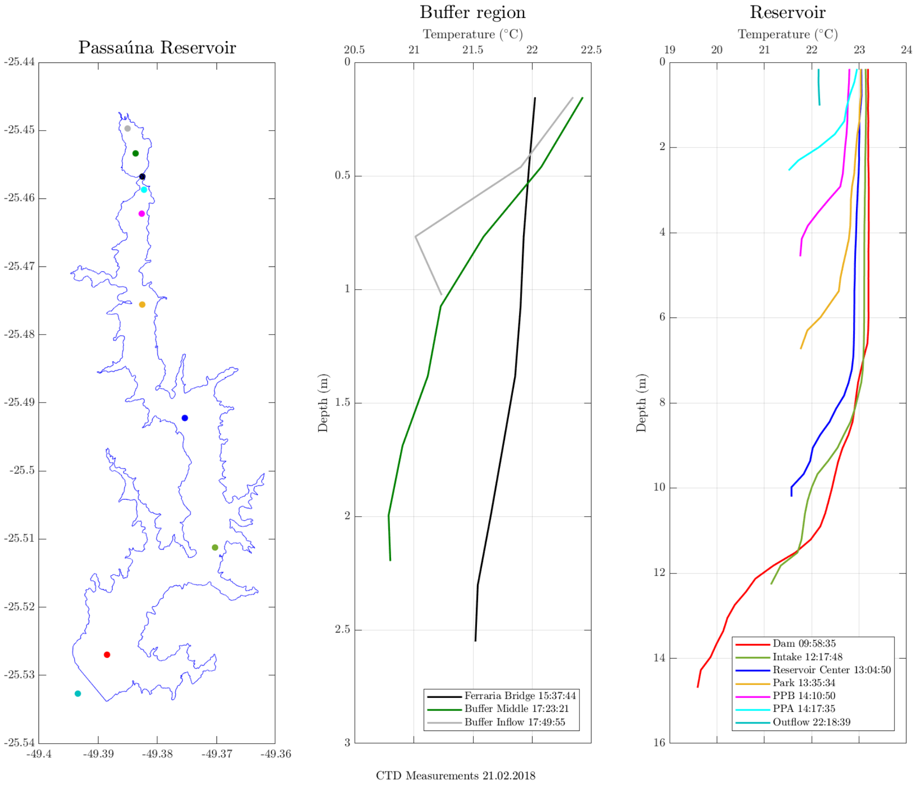

Figure A.6.: Temperature profiles derived from CTD-measurements on the 21.02.2018.

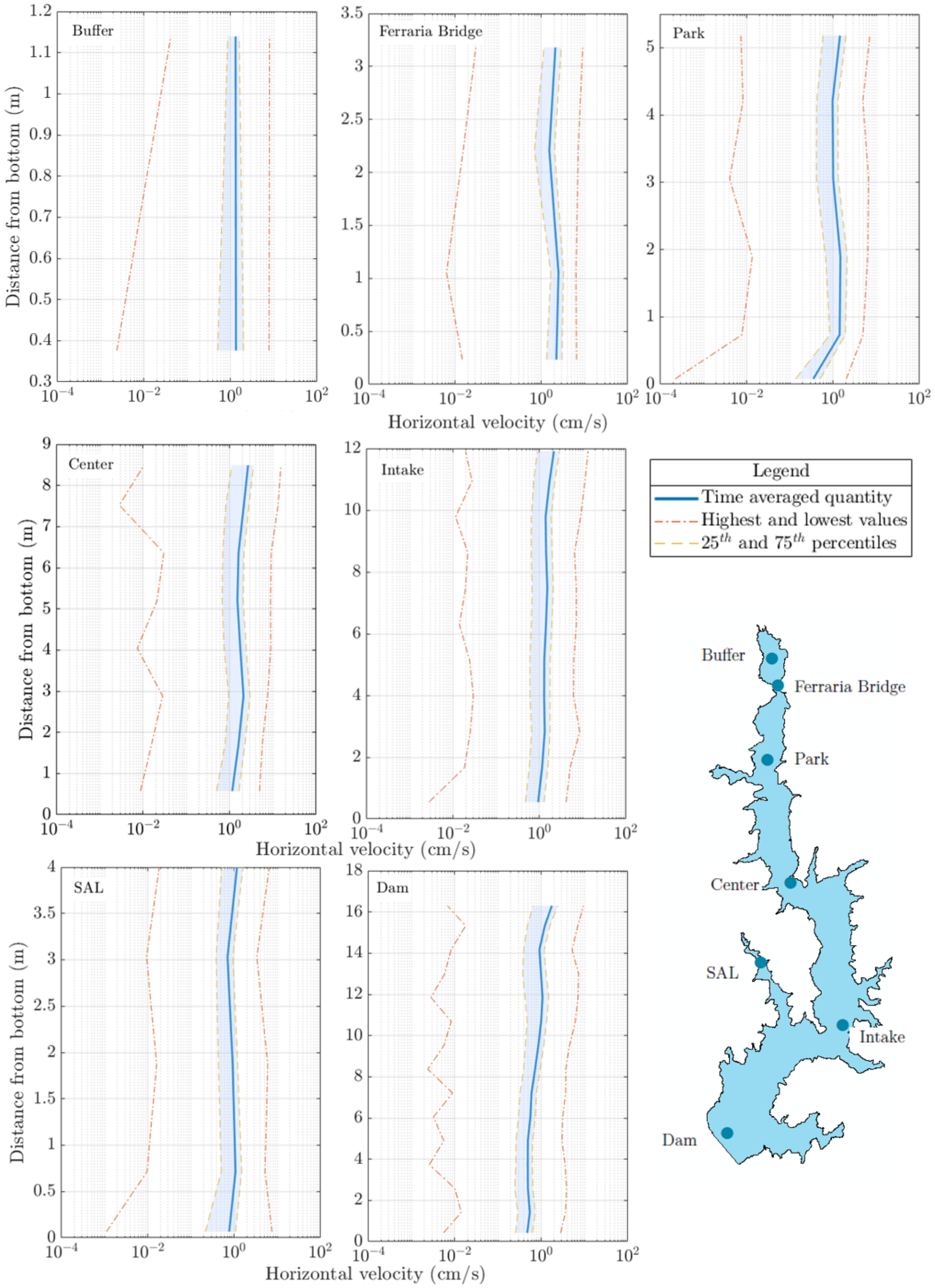

Figure A.7.: Simulated time averaged horizontal velocity profiles along the depth, lowest and highest simulated horizontal flow velocites (orange dash-dotted lines) and its ranges of variation (blue shaded area: its limits correspond to the $25th^{th}$ and $75th^{th}$ percentiles) for the indicated positions at the reservoir. Notice the use of a logarithmic scale for the horizontal axis.

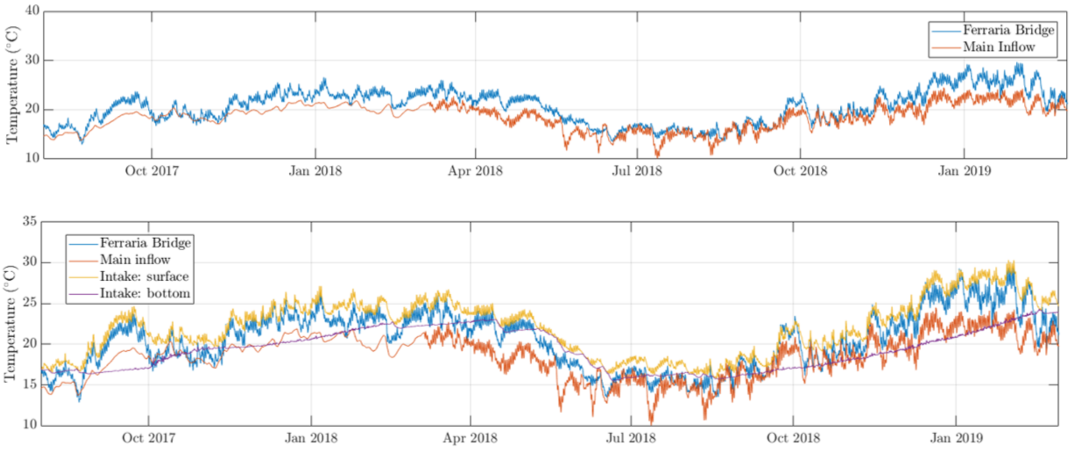

Figure A.8.: Analysis of possible density currents based on simulated temperatures at the Inflow, Ferraria Bridge and at the Intake for the whole simulation period. Top: comparison of the temperatures at the Ferraria Bridge and the main Inflow. Bottom: comparison of the three relevant locations.

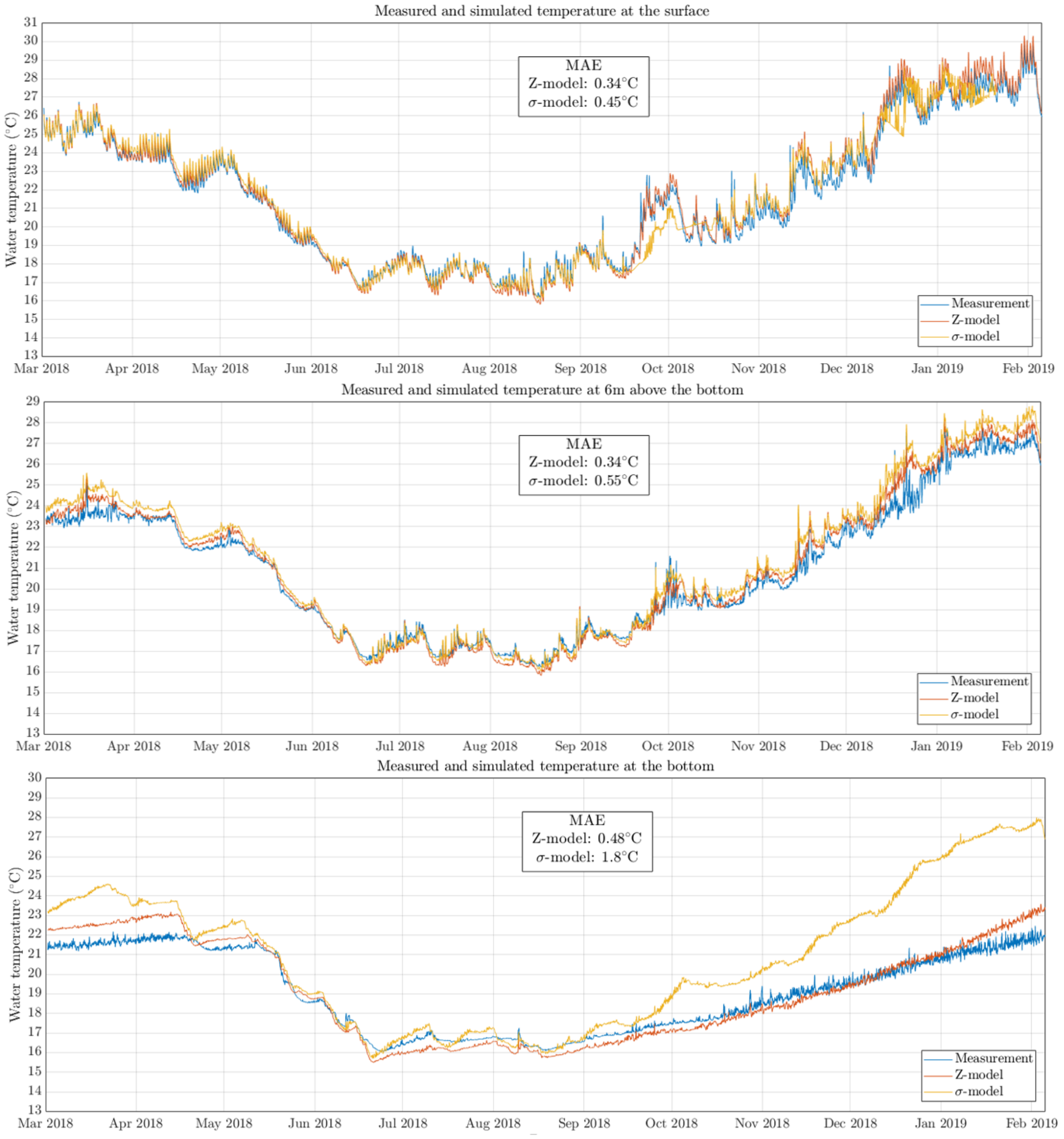

Figure A.9.: Comparison of the performance of the Z- and Sigma models at three different depths: water surface, middle and bottom.

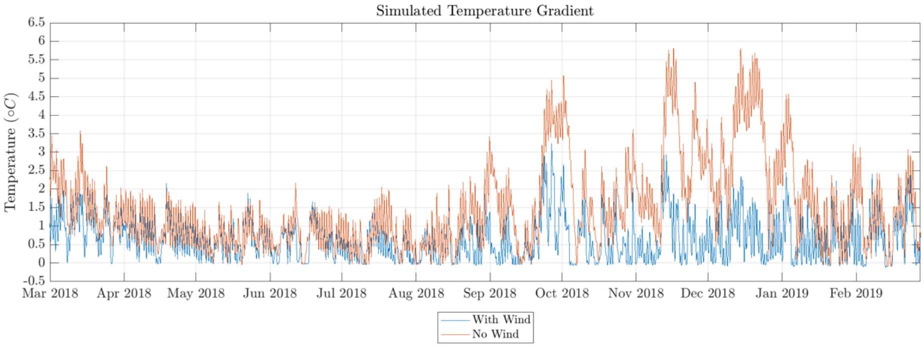

Figure A.10.: Simulated water temperature gradient at Park with inclusion of wind (blue line) and neglecting wind (orange line).

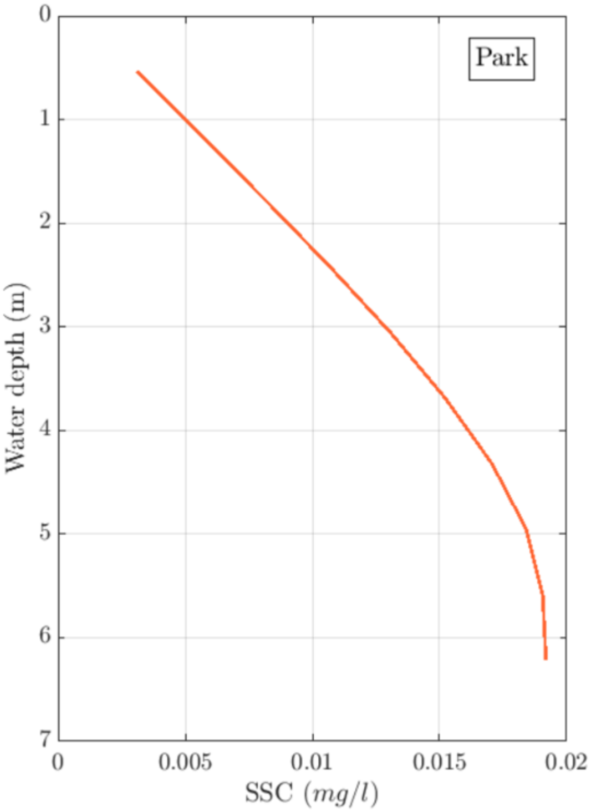

Figure A.11.: Time averaged SSC for the simulation without wind at Park.

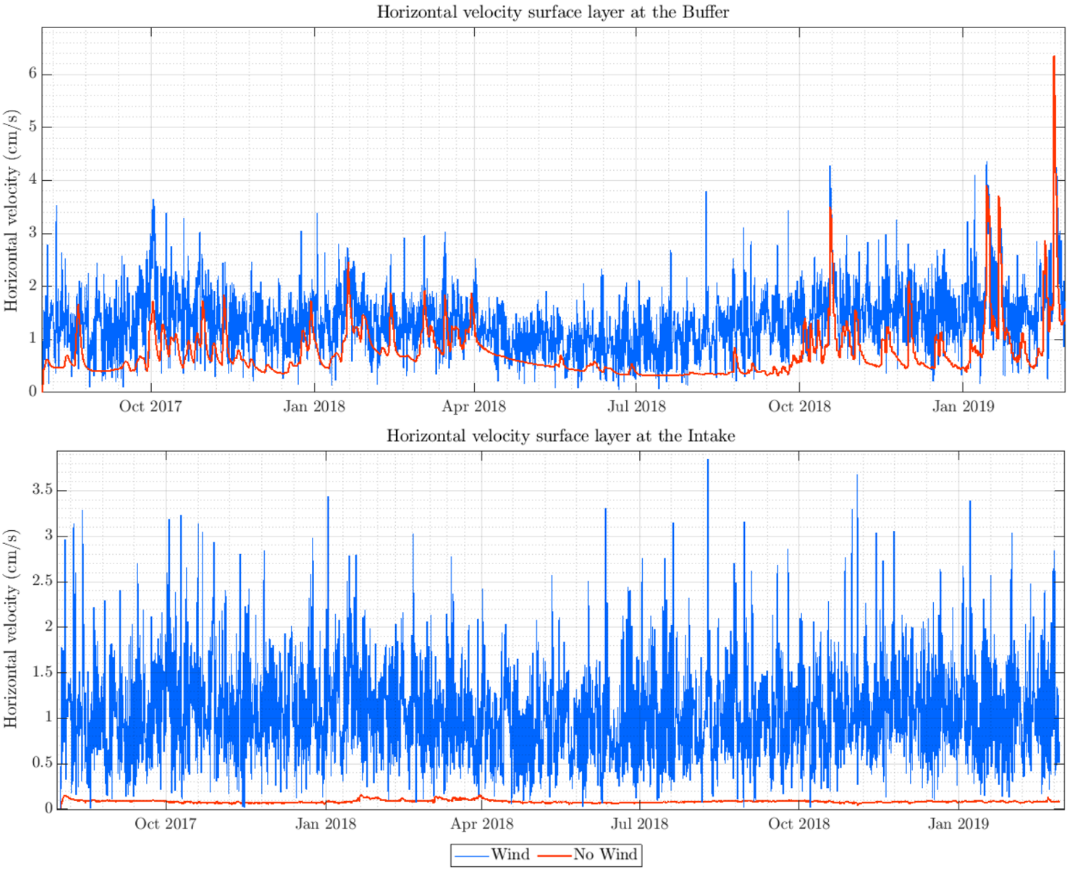

Figure A.12.: Horizontal velocities surface layer at the Buffer and Intake for the simulations with wind and wind exclusion.

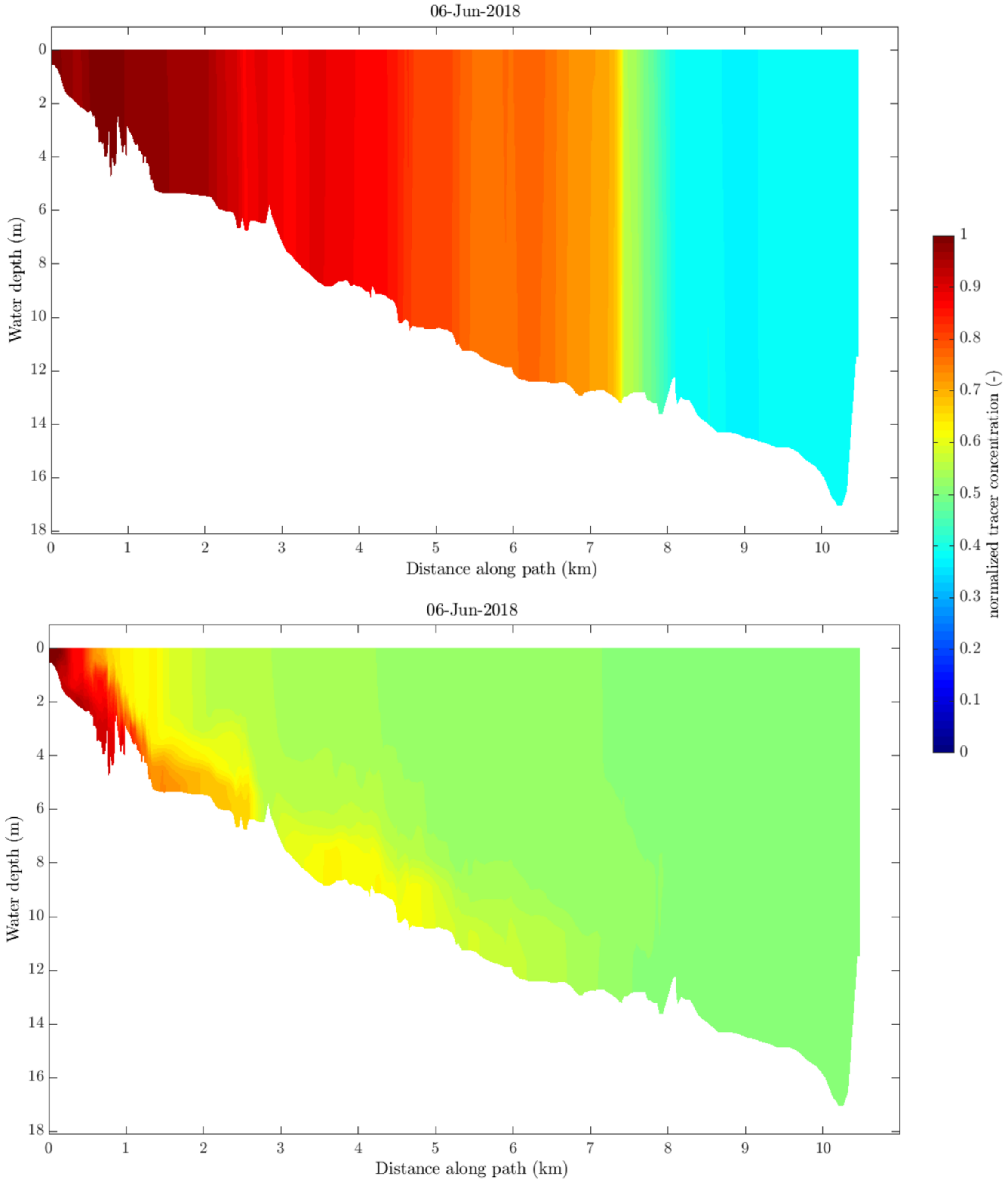

Figure A.13.: Normalized tracer concentration along the longitudinal profile for the simulations with (bottom) and without temperature (top) for June 6, 2018.

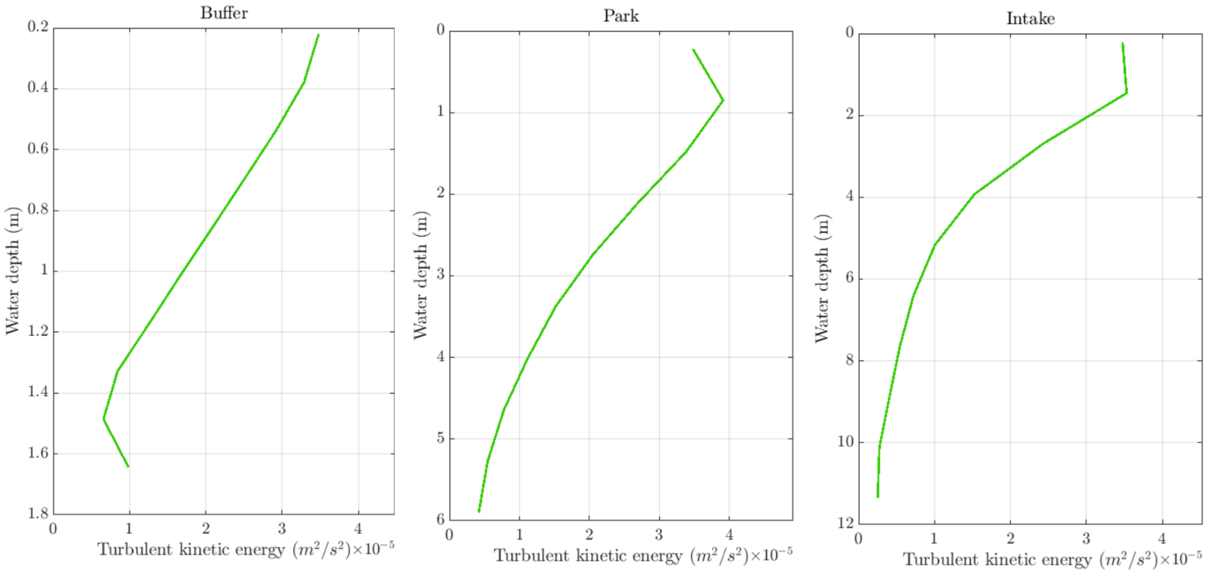

Figure A.14.: Turbulent kinetic energy for the simulation with temperature inclusion.

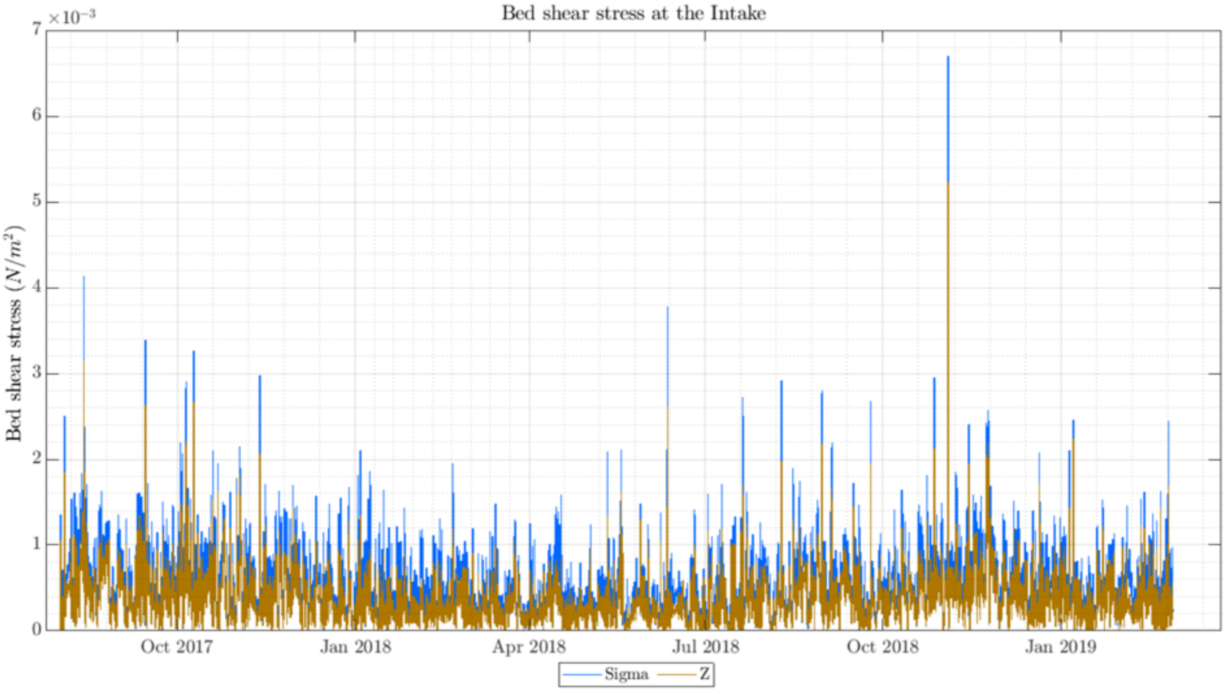

Figure A.15.: Bed shear stresses at the Intake for the simulations with Z-model and Sigma-model. Legend: Sigma-Z

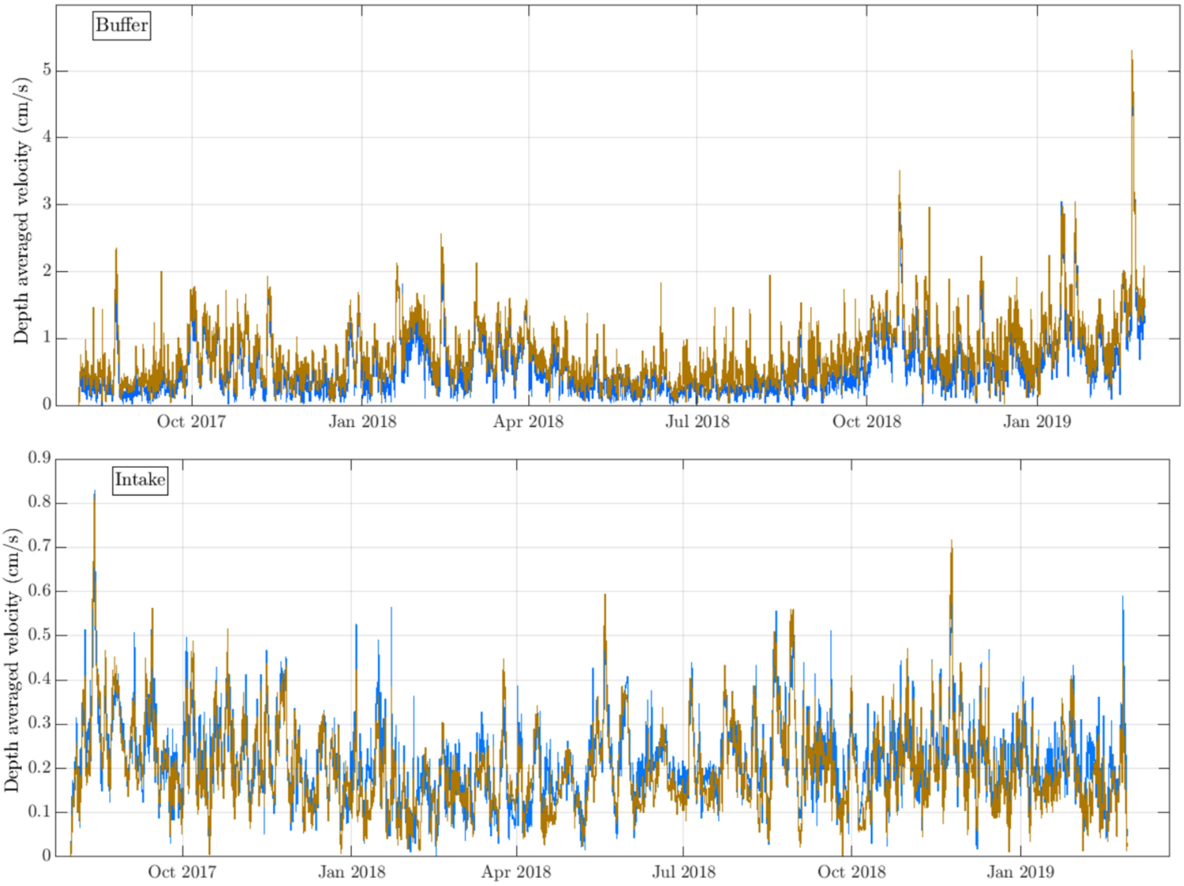

Figure A.16.: Depth averaged velocity at the Buffer and at the Intake for the simulations with Z-model and Sigma-model. Legend: Sigma-Z

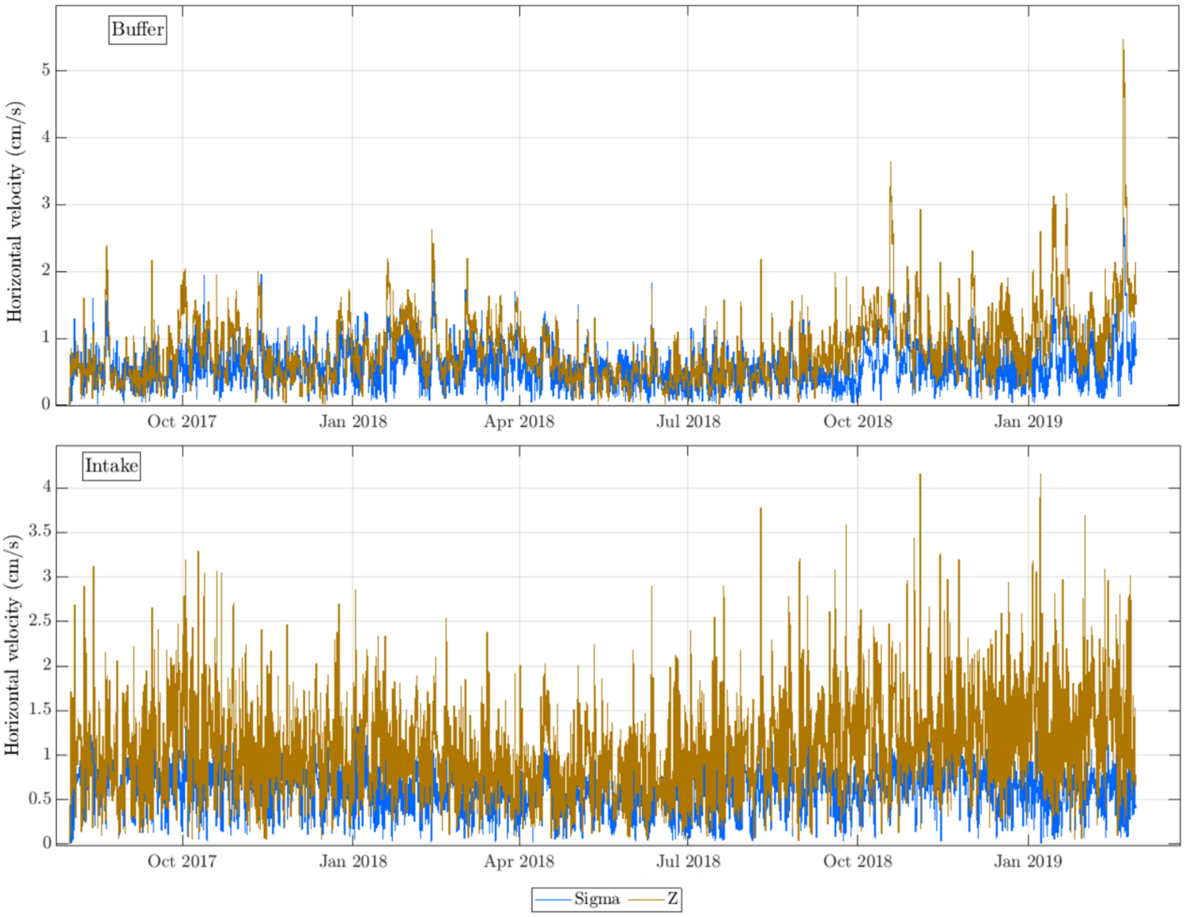

Figure A.17.: Horizontal velocities bottom layer at the Buffer and at the Intake for the simulations with Z-model and Sigma-model.